Diffusion Concept in Phase Stability of High Temperature Composites

by

Dr. Ji-Cheng Zhao
Dr. Melvin R. Jackson

AFOSR FINAL REPORT

February 2003

20030613 092

REPORT DOCUMENTATION PAGE

Form Approved
OMB No. 0704-0188

Public reporting burden for this collection of information is estimated to average 1 hour per response, including the time for reviewing instructions, searching existing data sources, gathering and maintaining the data needed, and completing and reviewing this collection of information. Send comments regarding this burden estimate or any other aspect of this collection of information, including suggestions for reducing this burden to Department of Defense, Washington Headquarters Services, Directorate for Information Operations and Reports (0704-0188), 1215 Jefferson Davis Highway, Suite 1204, Arlington, VA 22202-4302. Respondents should be aware that notwithstanding any other provision of law, no person shall be subject to any penalty for failing to comply with a collection of information if it does not display a currently valid OMB control number. **PLEASE DO NOT RETURN YOUR FORM TO THE ABOVE ADDRESS.**

1. REPORT DATE	2. REPORT TYPE	3. DATES COVERED *(From - To)*
02-27-2003	Final Technical Report	01-Dec-00 to 30-Sep-02

4. TITLE AND SUBTITLE
Diffusion Concept in Phase Stability of High Temperature Composites

5a. CONTRACT NUMBER
F49620-99-C-0026

5b. GRANT NUMBER

5c. PROGRAM ELEMENT NUMBER

6. AUTHOR(S)
Ji-Cheng Zhao and Melvin R. Jackson

5d. PROJECT NUMBER
FQ8671-00010152306/AX

5e. TASK NUMBER

5f. WORK UNIT NUMBER

7. PERFORMING ORGANIZATION NAME(S) AND ADDRESS(ES)

General Electric Company
GE Global Research Center
P.O. Box 8
Schenectady, NY 12301

8. PERFORMING ORGANIZATION REPORT NUMBER

9. SPONSORING / MONITORING AGENCY NAME(S) AND ADDRESS(ES)
USAF, AFRL
AF Office of Scientific
Research
4015 Wilson Blvd., Room 713
Arlington, VA 22203

10. SPONSOR/MONITOR'S ACRONYM(S)
AFOSR/PK4

11. SPONSOR/MONITOR'S REPORT NUMBER(S)

12. DISTRIBUTION / AVAILABILITY STATEMENT

Distribution Statement A. Approved for public release; distribution is unlimited.

13. SUPPLEMENTARY NOTES

14. ABSTRACT

A high-efficiency "diffusion multiple" approach was employed to determine the phase diagrams of nine ternary systems Nb-Ti-Si, Nb-Cr-Si, Nb-Cr-Ti, Ti-Cr-Si, Nb-Si-Al, Nb-Cr-Al, Nb-Ti-Al, Ti-Si-Al, and Ti-Cr-Al. These phase diagrams are very important for the design of Nb silicide based composites and their coatings for advanced military aircraft engines. Most of these ternary systems are very complex – some contain up to 14 phases, thus they also serve as excellent examples to test the applicability of the diffusion multiple approach to such complex systems. A total of seven different diffusion multiples were made to map the phase diagrams of these nine ternary systems. It would take more than a thousand individual alloys to accomplish the same amount of phase diagram mapping. All the equilibrium phases reported in these systems were observed in the diffusion multiples and an extremely large amount of phase equilibrium information was obtained to construct isothermal section phase diagrams. The results clearly demonstrate the applicability of this novel approach to very complex phase diagrams. We have gained extensive experience on how to make diffusion multiples and how to most efficiently analyze such complex systems. The experimental data were used to model thermodynamic parameters for extrapolating the ternary data into multicomponent alloys to provide critical data for computational design of alloys. Our results provide a much clearer picture of the phase equilibria in the Nb-Si-Ti-Cr-Hf-Al composites.

15. SUBJECT TERMS
High temperature composites; phase stability; phase diagrams; Nb-Si-Ti-Cr-Hf-Al; Laves phases; silicides

16. SECURITY CLASSIFICATION OF: Unclassified			17. LIMITATION OF ABSTRACT	18. NUMBER OF PAGES	19a. NAME OF RESPONSIBLE PERSON J-C Zhao
a. REPORT	b. ABSTRACT	c. THIS PAGE	UU		19b. TELEPHONE NUMBER *(include area code)* (518) 387-4103

Standard Form 298 (Rev. 8-98)
Prescribed by ANSI Std. Z39.18

GE Global Research

Diffusion Concept in Phase Stability of High Temperature Composites

by

Dr. Ji-Cheng Zhao
Dr. Melvin R. Jackson

AFOSR FINAL REPORT

February 2003

Diffusion Concept in Phase Stability of High Temperature Composites

Ji-Cheng Zhao and Melvin R. Jackson

GE Global Research Center, P.O. Box 8, Schenectady, NY 12110

Abstract

A high-efficiency "diffusion multiple" approach was employed to determine the phase diagrams of nine ternary systems Nb-Ti-Si, Nb-Cr-Si, Nb-Cr-Ti, Ti-Cr-Si, Nb-Si-Al, Nb-Cr-Al, Nb-Ti-Al, Ti-Si-Al, and Ti-Cr-Al. These phase diagrams are very important for the design of Nb silicide based composites and their coatings for advanced military aircraft engines. Most of these ternary systems are very complex – some contain up to 14 phases, thus they also serve as excellent examples to test the applicability of the diffusion multiple approach to such complex systems. A total of seven different diffusion multiples were made to map the phase diagrams of these nine ternary systems. It would take more than a thousand individual alloys to accomplish the same amount of phase diagram mapping. All the equilibrium phases reported in these systems were observed in the diffusion multiples and an extremely large amount of phase equilibrium information was obtained to construct isothermal section phase diagrams. The results clearly demonstrate the applicability of this novel approach to very complex phase diagrams. We have gained extensive experience on how to make diffusion multiples and how to most efficiently analyze such complex systems. The experimental data were used to model thermodynamic parameters for extrapolating the ternary data into multicomponent alloys to provide critical data for computational design of alloys. Our results provide a much clearer picture of the phase equilibria in the Nb-Si-Ti-Cr-Hf-Al composites.

Research Objective

The overall objective of this research is to create an efficient methodology for determining phase stability in multicomponent systems by combining the results from novel diffusion multiple experiments with state-of-the-art thermodynamic modeling procedures. This methodology will provide phase stability information quickly enough to make up-front predictions and to enable accelerated design approach for new classes of composite materials. The novel approach will provide the scientific basis for rapid and low-cost development of Nb silicide composites and will serve as an exemplar for future materials design.

Results / Accomplishment / New Findings

Niobium silicide-based composites show great promise for applications as the next generation turbine airfoil materials with significantly higher operating temperatures than current generation advanced Ni-base superalloys [1-6]. The Nb-Si binary composites have excellent creep strength, but poor oxidation resistance and poor room temperature fracture toughness [1-2]. Alloying with Cr can significantly improve the oxidation resistance by stabilizing the Cr-rich Laves phase $NbCr_2$. The potential application of these composites at very high temperatures requires a balance of high creep resistance, high oxidation resistance, and good low-temperature damage tolerance (fracture toughness). To achieve such a property balance, elements such as Cr, Ti, Hf and Al are added to the composites and significant progress has been made in improving the properties of the composites. Some of the alloying concepts were discussed by Zhao *et al.* [7]. The advanced design of the composites requires a fair understanding of the phase equilibria in the Nb-Si-Ti-Cr-Hf-Al system. Since a reasonable definition of the Nb-Hf-Si system has been achieved [8-10], our effort under the current AFOSR program has been focused on the ternary systems Nb-Cr-Si, Nb-Si-Al, Nb-Cr-Al, Ti-Si-Cr, Ti-Si-Al, Ti-Cr-Al, Nb-Ti-Si, Nb-Ti-Cr, and Nb-Ti-Al. Other ternary systems related to the six-element system such as Nb-Ti-Hf, Nb-Cr-Hf, Nb-Hf-Al, Ti-Si-Hf, Ti-Cr-Hf, and Cr-Hf-Al have either good data or are less critical for the design of the Nb silicide composites.

A high-efficiency "diffusion multiple" approach [11-14] was employed as part of this AFOSR program, and especially extended to very complex systems such as Nb-Cr-Si. It would take thousands of alloys to determine these nine ternary systems using the traditional one-alloy-at-a-time (equilibrated alloy) approach. For instance, it took Goldschmidt and Brand [15] about 220 alloys to map just the Nb-Cr-Si ternary system and similarly about 135 alloys were employed by Lysenko *et al.* [16] to determine the Ti-Cr-Si system. These alloys have very high melting temperatures and are difficult to make and to homogenize. Extra effort also needs to be taken to avoid interstitial (oxygen, nitrogen, carbon, etc.) contamination during alloy casting and heat treatment. In contrast, the diffusion multiple approach needs only a few cast alloys and the samples were easy to make, and safe-guarding against the interstitial contamination can be very easily implemented as will be discussed later. The general diffusion multiple approach is discussed in detail previously [11-14] and has been successfully applied to many alloy systems.

Seven kinds of diffusion multiples with the cross-section view shown schematically in the Fig. 1(a) were made. For samples AF-1 to AF-4, the inner and outer circle diameters were 15.6 and 25.4 mm respectively. We later changed the inner components of the diffusion multiples in AF-5 to AF-7 to square shapes with the dimension of 7 x 7 x 25 mm for each square for the ease of sample preparation. These dimensions were designed to guarantee that the dimensions of the pure element and alloy pieces are much larger than the diffusion distance, thus there will be pure elements left after the long term diffusion anneal. To avoid the low melting region of the ternary phase diagram, we used $NbSi_2$, $NbAl_3$, $TiSi_2$, and $TiAl_3$ compounds as members of the diffusion multiples. All these compounds were made by arc-melting. They were then cut into square bars of 7 x 7

x 25 mm using electro-discharge machining (EDM). High purity Nb, Cr, Si and Ti were machined into the proper shapes (quarter pies, square bars and round shells, Fig. 1(a)) by electro-discharge machining (EDM). The re-cast layer on the EDM'ed surfaces was removed by mechanical grinding to make clean surfaces. The pieces were ultrasonically cleaned in methanol and then assembled into the geometry shown in Fig. 1(a). The height of all pieces was 25 mm. The assembled diffusion multiples were then loaded into cans made of commercial purity Ti (schematically shown in Fig. 1(b)), and subjected to hot isostatic pressing (HIP) 1204 °C, 200 MPa for 4 hours. A 25-μm thick layer of Ta foil was placed between the diffusion multiples and the HIP cans to isolate any interstitial contaminants that may diffuse into the HIP can from the quartz capsule during long term annealing. The top and bottom caps of the HIP can were electron beam welded. The HIP cans containing the diffusion multiples were then encapsulated in evacuated quartz tubes backfilled with pure argon. Since both Nb and Ti are susceptible to oxygen and nitrogen contamination, it is critical to keep the diffusion multiples from interstitial elements. To further absorb any oxygen that might diffuse into the quartz tube, a packet of pure yttrium was wrapped in Ta foils and was then placed inside each quartz tube. Thus, the diffusion multiples were protected from the interstitials (O, N, C, etc.) by the quartz tube, the pure yttrium absorber, the Ti HIP can, and the Ta diffusion barrier. The encapsulated samples were then annealed in argon at different temperatures (1200°C for 1000 hrs, 1150°C for 2000 hrs, and 1000 °C for 2000 or 4000 hrs). Identical diffusion multiples were made and each was annealed at one temperature. After the heat treatment, the diffusion multiples were taken from the furnace and cooled down to ambient temperature by breaking the quartz tube and quenching the diffusion multiples into water. The diffusion multiples were then cut into halves parallel to the ends using wire EDM, ground and polished.

The samples were first examined using scanning electron microscopy (SEM), especially the backscatter electron (BSE) imaging. Most phases could be seen (although not identified explicitly) in the BSE images due to the differences in their average atomic weight. Quantitative EPMA analysis was performed on a CAMECA (Paris, France) microprobe using 15 kV voltage, 40 nA current and a 40° take-off angle. Electron backscatter diffraction (EBSD) analysis was performed to obtain crystal structure information of the phases formed in the diffusion multiple. Phase identification was accomplished by a direct match of the diffraction bands in the experimental backscatter pattern with simulated patterns generated using known structure types and lattice parameters. A detailed discussion on this powerful EBSD technique can be found in Schwartz *et al.* [17].

Several SEM backscatter electron images are shown in Fig. 2 as examples of the formation of all the intermetallic compounds by thermal interdiffusion. By performing EPMA analysis in the tri-junction areas, extremely large amounts of phase equilibrium information were obtained. Based on the compositional information from EPMA, EBSD analysis was performed to identify the crystal structure of most phases that were difficult to define based on the composition alone. EBSD is extremely useful for this system since several phases have compositions very close to one another and EPMA data alone would not be enough to differentiate them. For instance, the compositions of the phases $(Cr,Nb)_6Si_5$ and $(Cr,Nb)_{11}Si_8$ in the Nb-Cr-Si ternary system are very similar, without

EBSD it would require time-consuming transmission electron microscopy (TEM) and electron diffraction analysis to tell them apart. Also, the ternary NbCrSi phase sits right on the same Nb concentration as the C14 Laves phase, it would have been very easy to mistakenly plot the C14 Nb(Cr,Si)$_2$ Laves phase region (line) all the way to the NbCrSi composition. The EBSD results helped us correctly interpret the data. Some EBSD patterns of the intermetallic phases are shown in Fig. 3.

The phase diagrams obtained from the seven diffusion multiples are shown in Fig. 4. These phase diagrams have been compared to the available results in the literature and the detailed comparisons can be found in the attached papers detailing the results of individual systems.

We found that diffusion multiples make it easier to form equilibrium phases especially for alloys with very sluggish decomposition kinetics. This is somewhat counter-intuitive: one would think that the equilibrated alloy method (melting, casting and heat treatment of individual alloys) is the ultimate "gold-standard" for equilibrium. However, since it involves the process of solidification and heat treatment, true equilibrium can be difficult to reach if the solid-state decomposition process is sluggish for some of the phases (as in the case of several Nb-base systems). For instance, the βNb$_5$Si$_3$ which was formed directly from solidification (from its primary liquidus surface) and which is not an equilibrium phase for the Nb-Cr-Si ternary system at 1000°C, did not decompose to the equilibrium phases after annealing at 1000°C for 336 hours [see the attached Nb-Cr-Si paper for detail]. Alternatively, to avoid the solidification phase formation / segregation, to shorten diffusion distances, and to equilibrate more quickly, a powder metallurgy (solid state reaction of elemental powders) approach would be preferred. We found an excellent example to illustrate this case during our study of the Nb-Cr-Al system. Hunt and Raman [18] used the melting and annealing method whereas Mahdouk and Gachon [19] employed solid-state reaction of fine powders (without melting) to determine the same ternary phase diagram. Both groups annealed the samples at 1000°C for 168 hours (1 week). The alloys of Mahdouk and Gachon reached equilibrium near the C14 Laves phase, whereas the off-stoichiometric alloys near the C14 Laves phase melted by Hunt and Raman did not decompose into the equilibrium phases. This clearly shows the advantage of the power metallurgy route in reaching equilibrium for very high temperature alloys. The powder metallurgy route also has its drawbacks. It is very easy to introduce oxides or nitrides or moisture at fine particle surfaces, thus contaminating the samples and potentially causing interstitial stabilization of non-equilibrium phases. Here again the diffusion-multiple method can be superior.

In the diffusion multiples, there are no problems associated with melting or powder contamination since all the phases form by diffusion reactions of bulk constituents at the temperature of interest (heat treatment). The phases formed should all be equilibrium phases and local equilibrium at the phase interface would give the equilibrium phase diagram. However, the diffusion-multiple approach is not fool-proof either: in rare occasions one of the phases does not form by interdiffusion reactions. The exact reason for this is still not well understood. However, for phases with narrow stoichiometry surrounded by phases with broad stoichiometry and higher diffusivity, the phases with

4

narrow stoichiometry may be reduced to interfacial phases (near zero thickness) for lower temperatures. Fortunately, all these instances occurred at temperatures below half of the homologous melting points. Even though the occurrence was very rare, when using diffusion couples and diffusion multiples in mapping phase diagrams one should always be watchful for the possibility of missing phases (especially at low temperatures). In all our nine ternary systems, we are very confident that the phase diagrams we obtained are equilibrium ones since all the binary phases appeared and all the confirmed ternary compounds were observed. It is always a good check to see whether all the binary phases and reported ternary phases appear.

The efficiency gain we obtained from the diffusion multiples was tremendous which was clearly shown in Fig. 4. It would take more than a thousand individual alloys to map these phase diagrams. Based on our very positive experience of this AFOSR program, we have now extended the diffusion multiples to even higher efficiency. For instance, we can now map 10 phase diagrams from a single diffusion multiple [13-14]. The experience we gained from this AFOSR program is the base for such advancement.

The results shown in Fig. 4 give us a much clearer understanding of the phase stability in Nb silicide based composites, especially for phase stability of Laves phases and silicides. We have have mapped all the ternary systems (except for Al-Cr-Si) related to the four quaternary systems: Ti-Si-Cr-Al, Nb-Ti-Si-Cr, Nb-Ti-Si-Al, and Nb-Ti-Cr-Al, as schematically shown in Fig. 5. Our work has cleared much confusion in these systems and makes the work of thermodynamic modeling much more straight-forward.

Our results serve as the base for constructing a thermodynamic database for the Nb-Si-Ti-Cr-Al-Hf system at the University of Wisconsin [10,20,21].

Acknowledgment/Disclaimer

References

1. M.G. Mendiratta and D.M. Dimiduk, *Mat. Res. Soc. Symp. Proc.*, 133 (1989), 441-446.
2. M.R. Jackson, B.P. Bewlay, R.G. Rowe, D.W. Skelly, and H.A. Lipsitt, *JOM*, 48 (1996), 39-44.
3. P.R. Subramanian, M.G. Mendiratta, and D.M. Dimiduk, *JOM*, 48 (1996), 33-38.
4. B.P. Bewlay, J.J. Lewandowski, and M.R. Jackson, *JOM*, 49 (1997), 44-45.
5. S.J. Balsone, B.P. Bewlay, M.R. Jackson, P.R. Subramanian, J.-C. Zhao, A. Chatterjee, and T. Heffernan, in *Structural Intermetallics 2001* (K. Hemker, D.M.

Dimiduk, H. Clemens, R. Darolia, H. Inui, J.M. Larsen, V.K. Sikka, M. Thomas, and J.D. Whittenberger, eds.), TMS, Warrendale, PA, 2001, 99-108

6. B.P. Bewlay, M.R. Jackson, J.-C. Zhao, and P.R. Subramanian, *Metallurgical and Materials Transactions,* Accepted November 2002.
7. J.-C. Zhao, B.P. Bewlay, M.R. Jackson, and L.A. Peluso, in *Structural Intermetallics 2001* (K. Hemker, D.M. Dimiduk, H. Clemens, R. Darolia, H. Inui, J.M. Larsen, V.K. Sikka, M. Thomas, and J.D. Whittenberger, eds.), TMS, Warrendale, PA, 2001, 483-491.
8. B.P. Bewlay, R.R. Bishop, and M.R. Jackson, *Z. Metallkde.,* 90 (1999), 413-422.
9. J.-C. Zhao, B.P. Bewlay, and M.R. Jackson, *Intermetallics,* 9 (2001) 681-689.
10. Y. Yang, Y.A. Chang, J.-C. Zhao, and B.P. Bewlay, *Intermetallics,* Accepted November 2002.
11. J.-C. Zhao, *Adv. Eng. Mater.,* 3 (2001), 143-147.
12. J.-C. Zhao, *J. Mater. Res.,* 16 (2001), 1565-1578.
13. J.-C. Zhao, M.R. Jackson, L.A. Peluso, and L. Brewer, *MRS Bulletin,* 27 (2002) 324-329.
14. J.-C. Zhao, M.R. Jackson, L.A. Peluso, and L. Brewer, *JOM,* 54 (7) (2002) 42-45.
15. H.J. Goldschmidt and J.A. Brand, *J. Less-Common Met.,* 3 (1961), 34-43.
16. L.A. Lysenko, V.Ya. Markiv, O.V. Tsybukh, and E.I. Gladyshevskii, *Inorganic Mater.,* 7(1) (1971), 157-159.
17. *Electron Backscatter Diffraction in Materials Science,* edited by A.J. Schwartz, M. Kumar, and B.L. Adams (Kluwer Academic / Plenum Publishers, New York, 2000).
18. C.R. Hunt and A. Raman, *Z. Metallkde.,* 59 (1968), 701-707.
19. K. Mahdouk and J.C. Gachon, *J. Alloys Compounds,* 321 (2001), 232-236.
20. H. Liang and Y.A.Chang, *Intermetallics,* 7 (1999) 561.
21. Y. Yang and Y.A. Chang (University of Wisconsin – Madison), private communication, 2002.

Personnel Supported

Dr. Ji-Cheng Zhao,	Staff Materials Scientist, GE Global Research Center
Dr. Melvin R. Jackson,	Staff Metallurgist, GE Global Research Center
Mr. Louis A. Peluso,	Staff Physicist, GE Global Research Center
Dr. Y. Austin Chang,	Professor, University of Wisconsin-Madison
Ms. Ying Yang,	Graduate Student, University of Wisconsin-Madison

Publications

1. J.-C. Zhao, **Advanced Engineering Materials**, vol. 3, p. 143-147 (2001) "A Combinatorial Approach for Structural Materials"
2. J.-C. Zhao, **Journal of Materials Research**, vol.16, p. 1565-1578 (2001) "A Combinatorial Approach for Efficient Mapping of Phase Diagrams and Properties"
3. J.-C. Zhao, B.P. Bewlay, and M.R. Jackson, **Intermetallics,** vol. 9, p. 681-689 (2001) "Determination of Nb-Hf-Si Phase Equilibria"

4. J.-C. Zhao, B.P. Bewlay, M.R. Jackson, and L.A. Peluso, in **Structural Intermetallics 2001** (K. Hemker, D.M. Dimiduk, H. Clemens, R. Darolia, H. Inui, J.M. Larsen, V.K. Sikka, M. Thomas, and J.D. Whittenberger, eds.), TMS, Warrendale, PA, 2001, p. 483-491 "Alloying and Phase Stability in Niobium Silicide In-Situ Composites"

5. S.J. Balsone, B.P. Bewlay, M.R. Jackson, P.R. Subramanian, J.-C. Zhao, A. Chatterjee, and T. Heffernan, in **Structural Intermetallics 2001** (K. Hemker, D.M. Dimiduk, H. Clemens, R. Darolia, H. Inui, J.M. Larsen, V.K. Sikka, M. Thomas, and J.D. Whittenberger, eds.), TMS, Warrendale, PA, 2001, p. 99-108 "Materials Beyond Superalloys - Exploiting High-Temperature Composites"

6. J.-C. Zhao, M.R. Jackson, L.A. Peluso, and L. Brewer, **MRS Bulletin**, vol. 27, p.324-329 (2002) "A Diffusion Multiple Approach for Accelerated Design of Structural Materials"

7. J.-C. Zhao, L.A. Peluso, L. Brewer, and M.R. Jackson, in **High Throughput Analysis: A Tool for Combinatorial Materials Science**, to be published by Kluwer Academic / Plenum Publishers. Accepted "Diffusion Multiples for High Efficiency Alloy Design"

8. J.-C. Zhao, M.R. Jackson, and L.A. Peluso, to be submitted "Mapping of the Nb-Cr-Si Phase Diagram Using Diffusion Multiples"

9. J.-C. Zhao, M.R. Jackson, and L.A. Peluso, to be submitted "Phase Diagram of the Nb-Cr-Al Ternary System"

10. J.-C. Zhao, M.R. Jackson, L.A. Peluso, and L. Tan, to be submitted "Phase Diagram of the Nb-Al-Si Ternary System"

11. J.-C. Zhao, M.R. Jackson, L.A. Peluso and L. Tan, to be submitted "Mapping of the Nb-Ti-Al Phase Diagram Using a Diffusion Multiple"

12. J.-C. Zhao, M.R. Jackson, and L.A. Peluso, to be submitted "Mapping of the Ti-Cr-Si Phase Diagram Using Diffusion Multiples"

13. J.-C. Zhao, M.R. Jackson, and L.A. Peluso, to be submitted "Mapping of the Ti-Si-Al Phase Diagram Using a Diffusion Multiple"

14. J.-C. Zhao, M.R. Jackson, and L.A. Peluso, to be submitted "Mapping of the Nb-Cr-Ti Phase Diagram Using Diffusion Multiples"

15. J.-C. Zhao, M.R. Jackson, and L.A. Peluso, to be submitted "Mapping of the Nb-Ti-Si Phase Diagram Using Diffusion Multiples"

16. J.-C. Zhao, M.R. Jackson, and L.A. Peluso, to be submitted "Mapping of the Ti-Cr-Al Ternary Phase Diagram using a Diffusion Multiple"

The work published under the support of this AFOSR contract was featured on the front cover of *Advanced Engineering Materials* (March 2001) and *MRS Bulletin* (April 2002), in the "News and Views" section of *Nature* (April 5, 2001, vol. 410, p. 643-644, by R.W. Cahn), in the "Research/Researchers" section of *MRS Bulletin* (July 2001, vol. 26, p. 495), and in a cover story of *Chemical and Engineering News* (August 27, 2001, vol. 79, no. 35, p. 59-63).

Dr. Zhao was invited to give lectures at the Gordon Conference on Physical Metallurgy (July 23-27, 2000) and Gordon Conference on Combinatorial and High Throughput Materials Science (June 30-July 5, 2002). He has also been invited to give seminars at NIST, the University of Central Florida, and the Pennsylvania State University. In

addition, Dr. Zhao was invited to serve as a Guest Editor for the April 2002 issue of *MRS Bulletin* on Combinatorial Materials Science. He has also been invited to write two book chapters but has accepted only one due to time constraints. All these were largely based on the AFOSR work.

Awards

Dr. Zhao was awarded the 2001 *Albert W. Hull Award* that is presented annually to an early-career researcher (across all disciplines at GE Global Research Center) who exhibits outstanding technical achievement and positive influence on fellow technologists. Zhao also obtained the *2001 Alfred H. Geisler Award* from the Eastern New York Chapter of ASM International as recognition of an outstanding young engineer in the field of materials science and engineering having significant achievement in the fields of education, research, manufacturing or distribution. The AFOSR work is an important part of these awards.

Transitions

The results were used for alloy and coating design for the IHPTET III Advanced Intermetallic Blade (AIMB) program at GE Global Research. Point of contact is Dr. Melvin R. Jackson, GE Global Research Center, P.O. Box 8, Schenectady, NY 12301, Phone: 518-387-6362.

Primary Contact:

J.-C. Zhao
GE Global Research Center
PO Box 8, K1-MB239
Schenectady, NY 12301
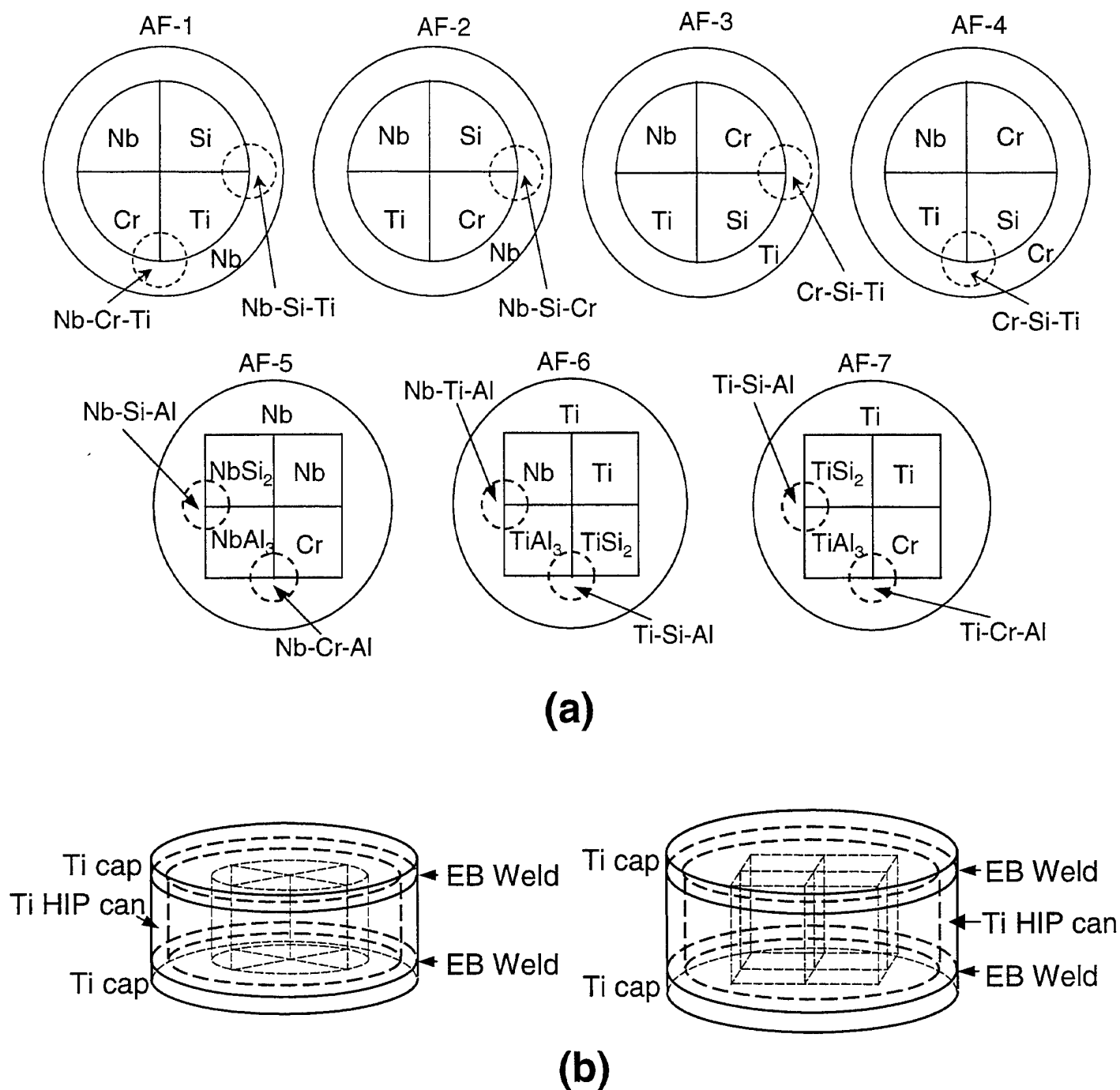Tel: 518-387-4103 (-6232 Fax)
Email: zhaojc@research.ge.com

Figure 1. Diffusion multiple for efficient mapping of ternary phase diagrams critical to the design of Nb silicide composites: (a) cross-sectional view of 7 different diffusion multiples; and (b) perspective view. See text for the size of the sample. All the results reported here were obtained from the tri-junction areas circled in (a).
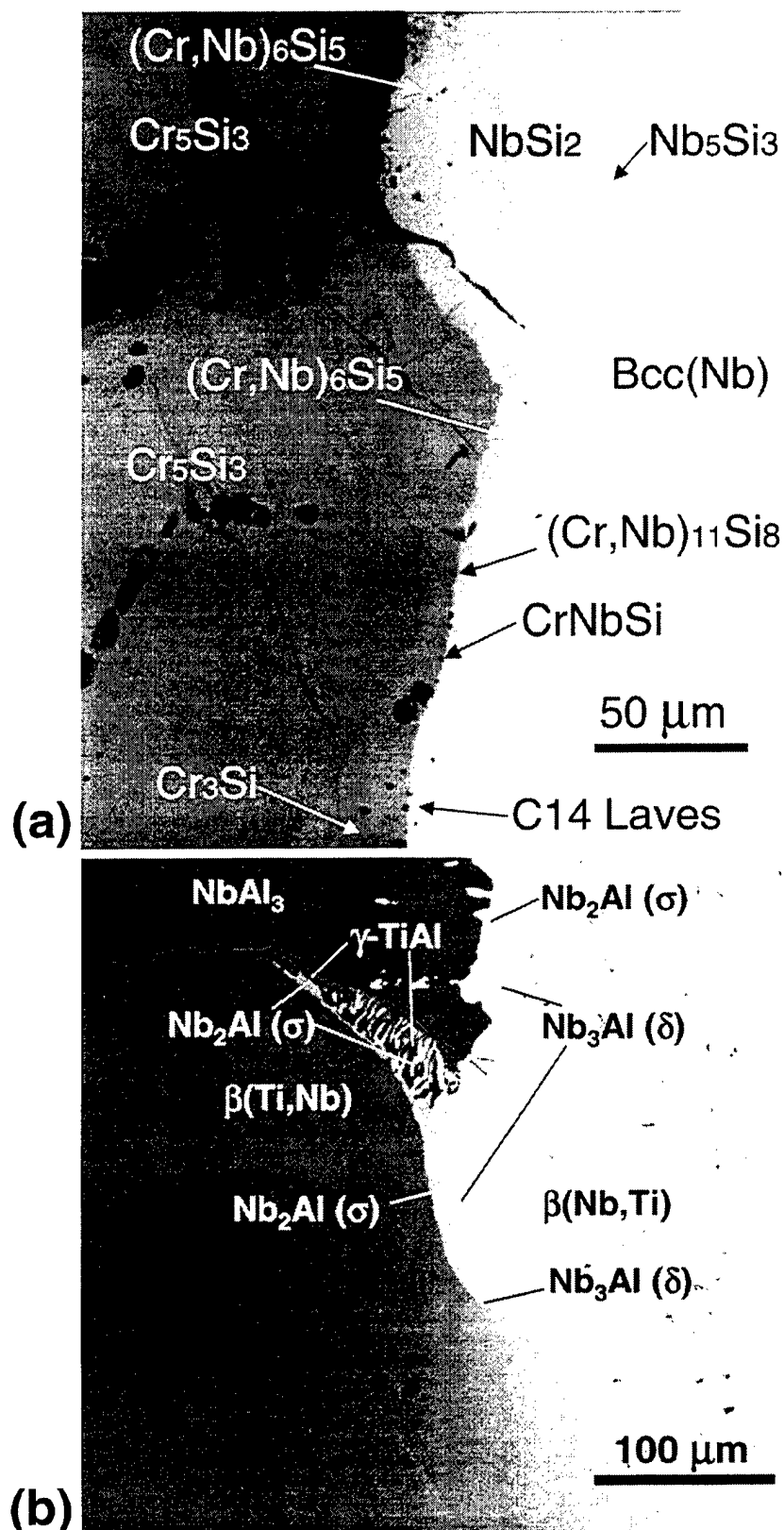
Figure 2. Backscatter electron SEM images of tri-junction areas of the diffusion multiples (Fig. 1) annealed at various temperatures for extended periods of time showing the formation of many different phases and intermetallic compounds: (a) Nb-Cr-Si tri-junction of a diffusion multiple annealed at 1000°C for 4000hrs; (b) Nb-Ti-NbAl$_3$ tri-junction of a diffusion multiple annealed at 1200°C for 1000hrs; (c) Nb-Ti-Si tri-junction of a diffusion multiple annealed at 1150°C for 2000hrs; (d) Nb-Ti-Cr tri-junction of a diffusion multiple annealed at 1150°C for 2000hrs; (e) Ti-Cr-Si tri-junction of a diffusion multiple annealed at 1200°C for 1000hrs; and (f) Nb-NbSi$_2$-NbAl$_3$ tri-junction of a diffusion multiple annealed at 1000°C for 2000 hrs
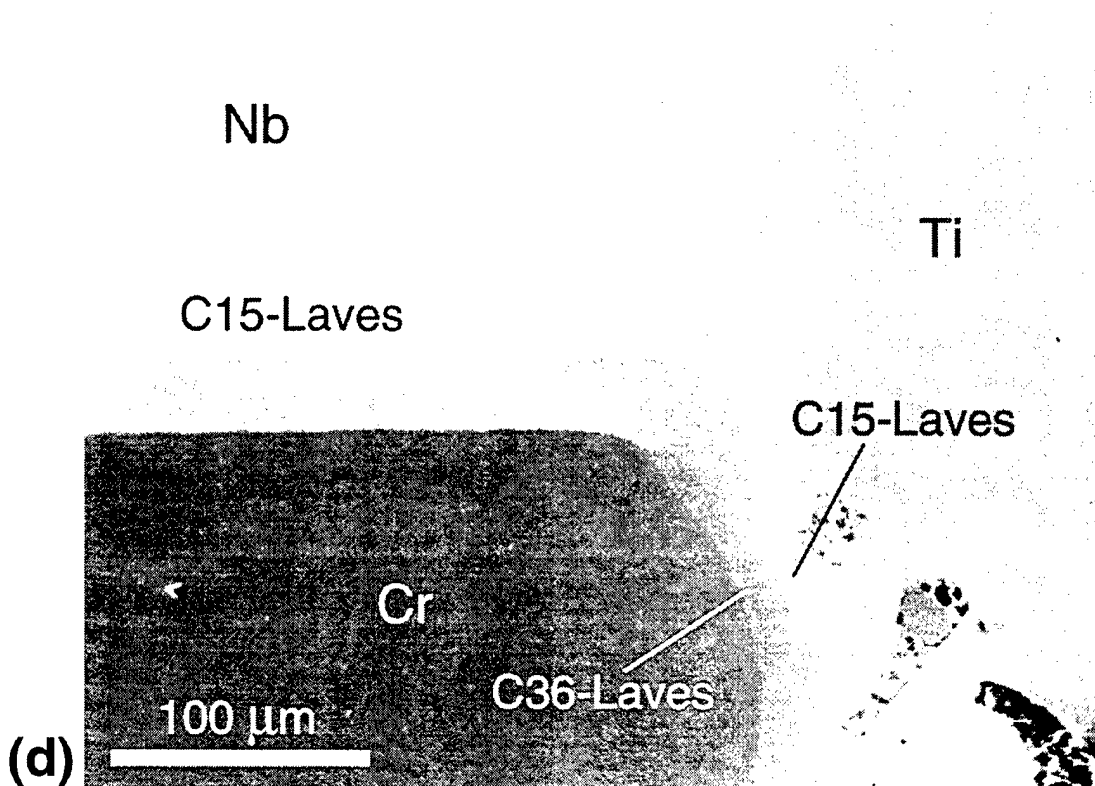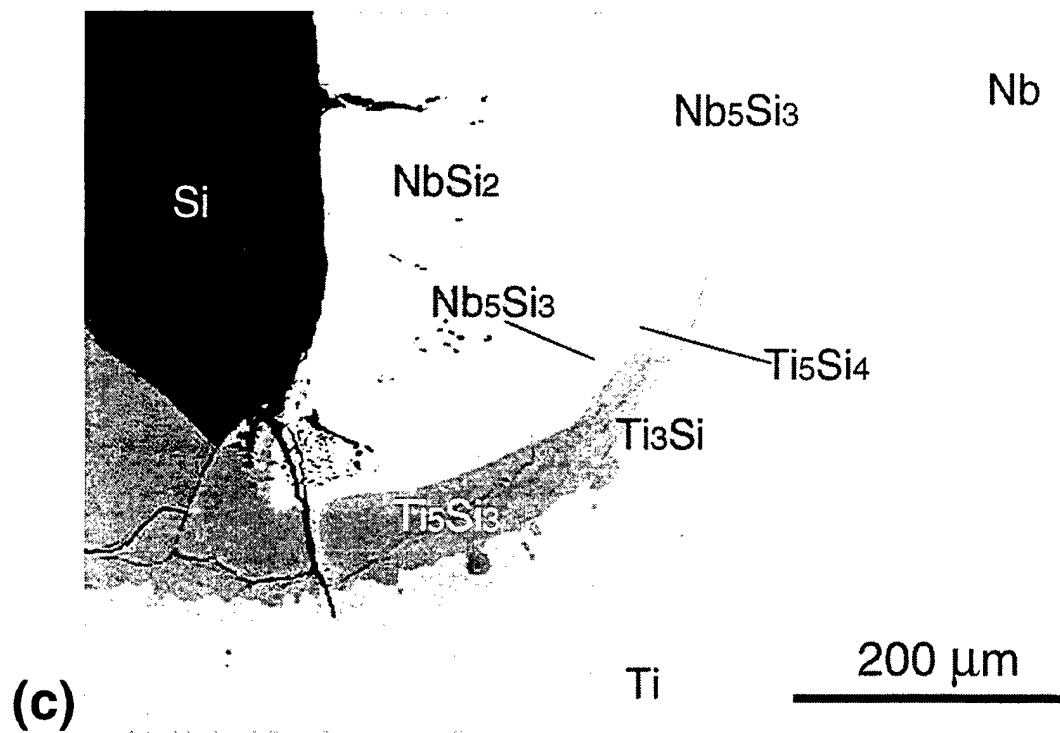
10

(c)

Si
Nb₅Si₃
Nb
NbSi₂
Nb₅Si₃
Ti₅Si₄
Ti₃Si
Ti₅Si₃
Ti
200 μm

(d)

Nb
Ti
C15-Laves
C15-Laves
Cr
C36-Laves
100 μm

Figure 2. Continued

(e)

50 μm

(Cr,Ti)$_6$Si$_5$

Ti

Ti$_5$Si$_3$

Laves

Cr$_5$Si$_3$

Cr

Cr$_3$Si

NbSi$_2$

αNb$_5$Si$_3$

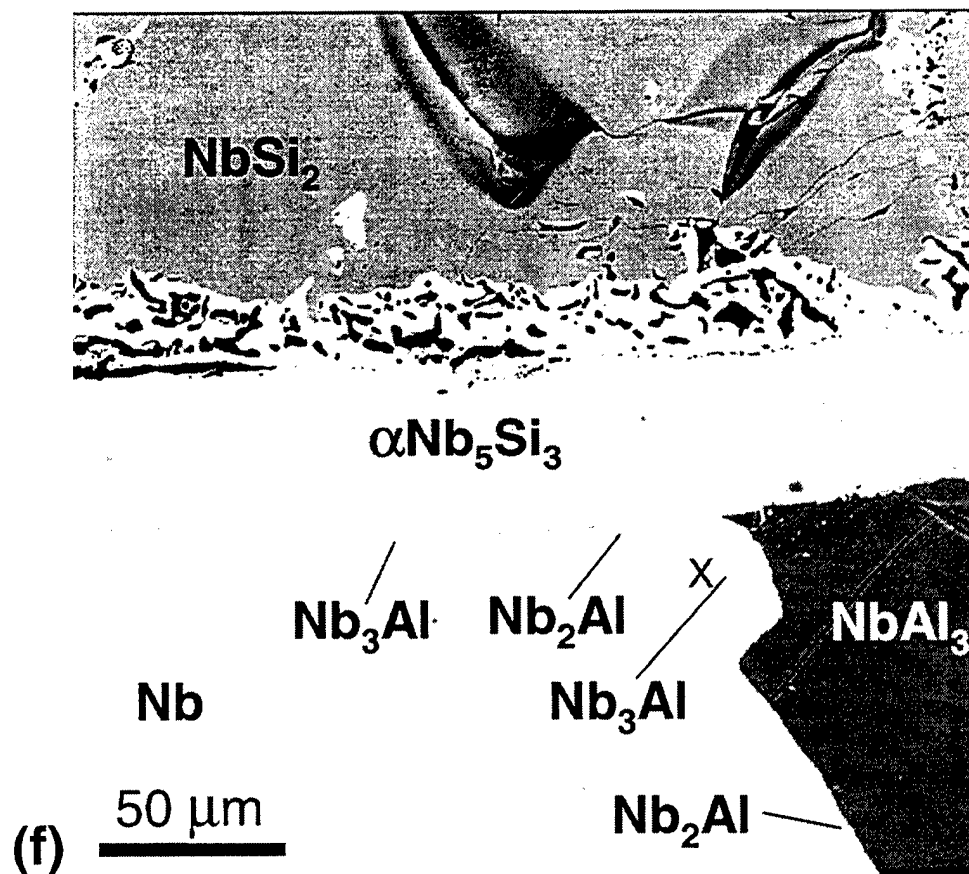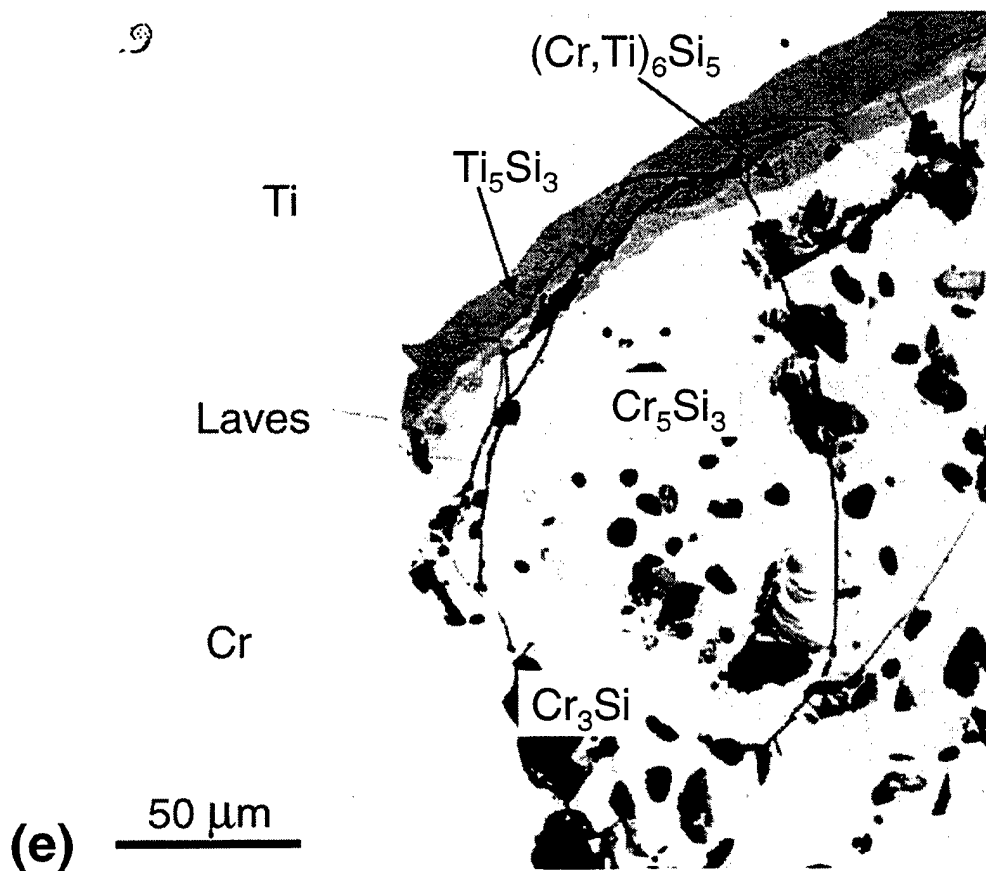Nb$_3$Al   Nb$_2$Al   X   NbAl$_3$

Nb

Nb$_3$Al

Nb$_2$Al

(f)

50 μm

Figure 2. Continued
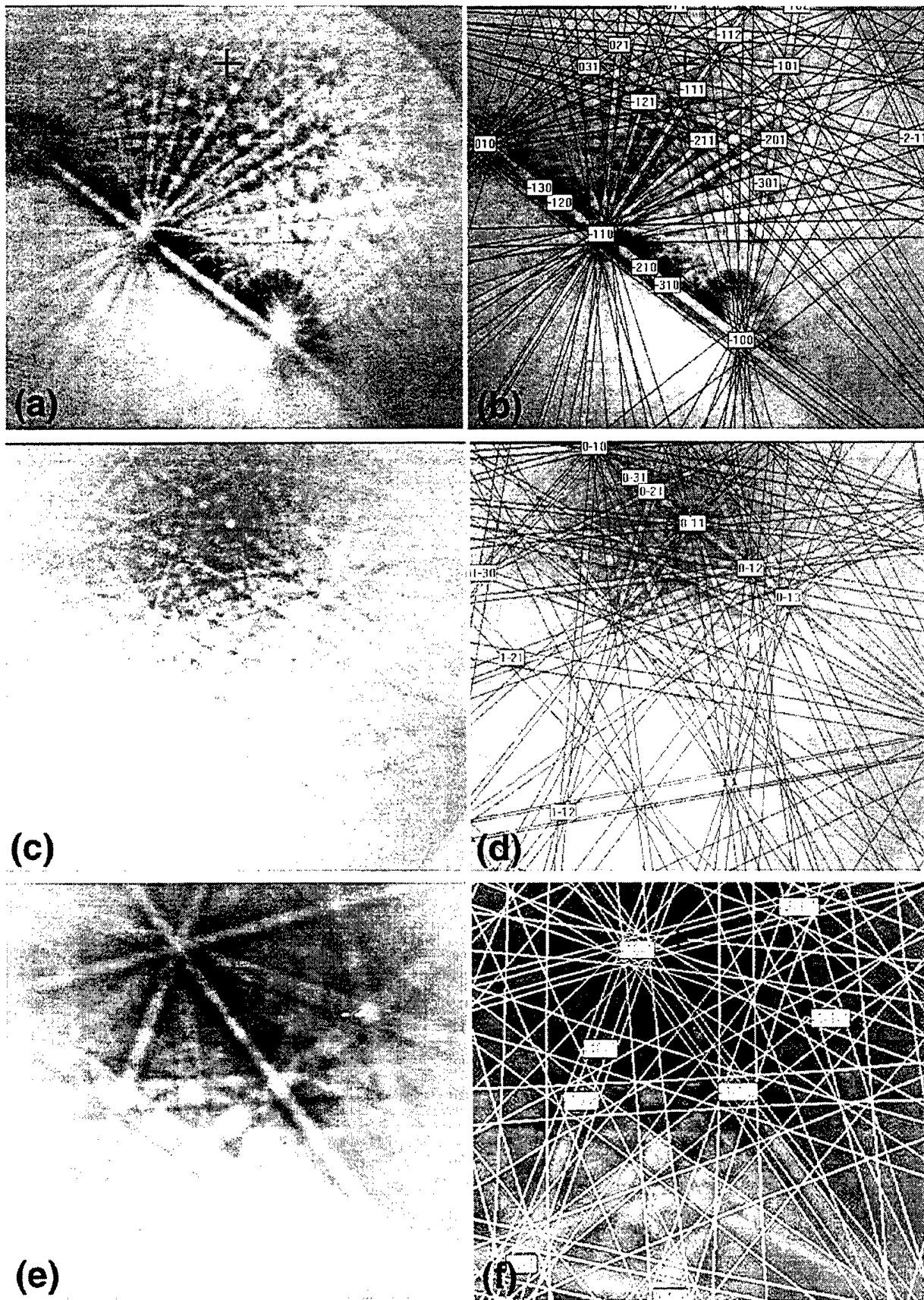
Figure 3. EBSD patterns of several intermetallic compounds: (a) and (b): $NbSi_2$; (c) and (d): $(Cr,Nb)_6Si_5$; and (e) and (f): τ-$L1_2$ (Ti_2CrAl_5). The un-indexed patterns are on the left and the indexed patterns on the right. EBSD is a very critical tool for crystal structure identification.
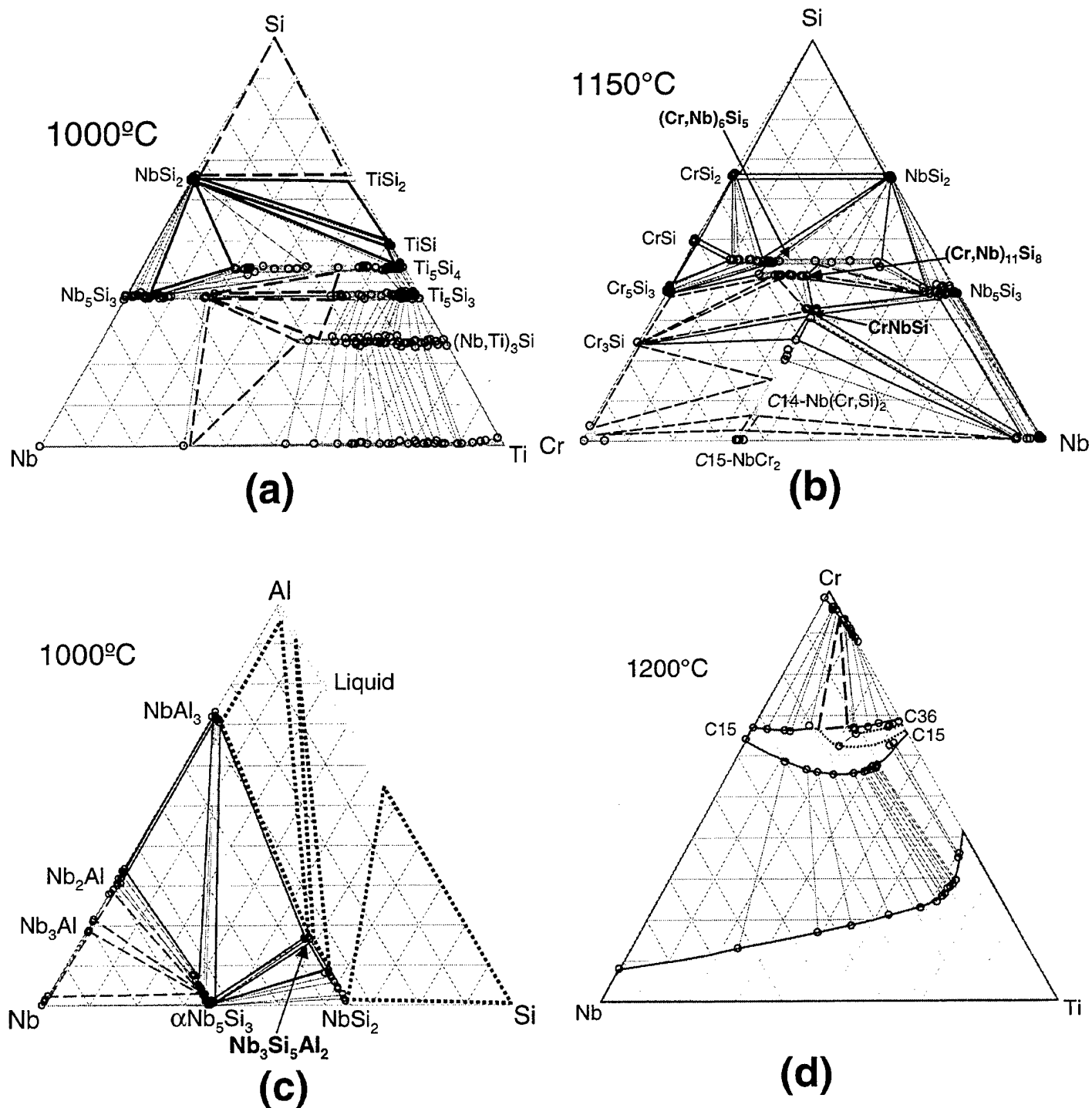
13

Figure 4. Isothermal sections of the nine ternary systems obtained from the tri-junction areas of the seven diffusion multiples shown in Fig. 1. The phase diagrams are plotted in atomic percent axes with the numbers removed for simplicity. The solid triangles indicate well-defined three-phase equilibria and the open circles show the tie-line compositions. The tie-lines are shown with dotted lines. The dashed triangles are hypothesized three-phase equilibria.
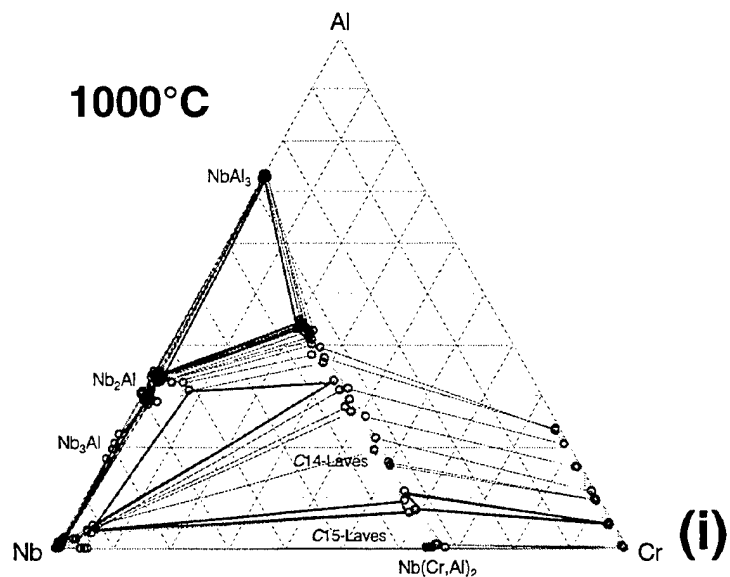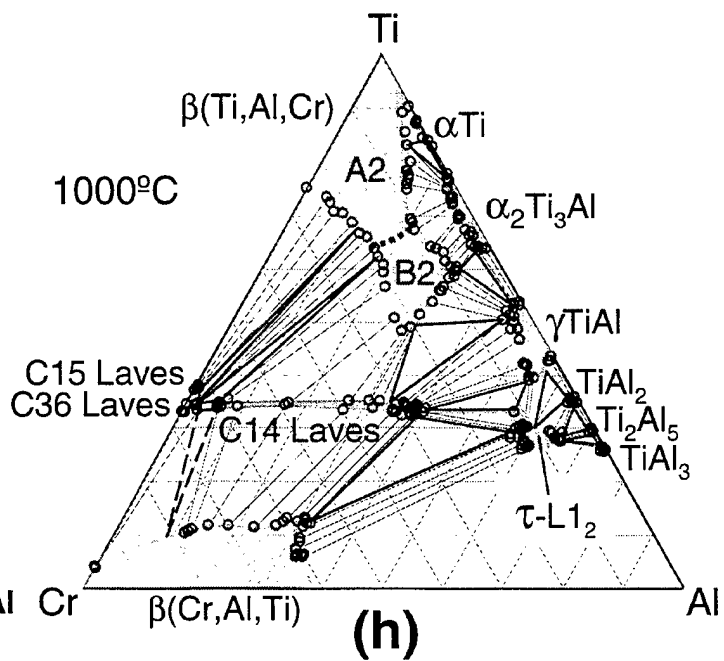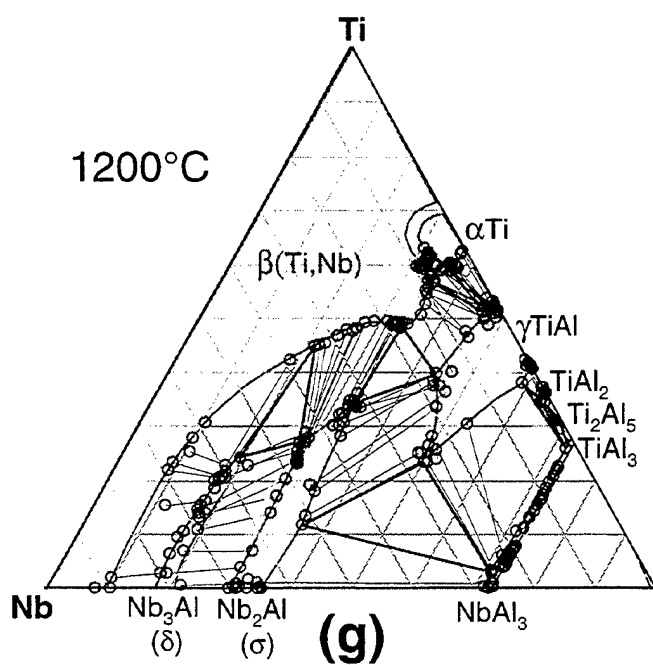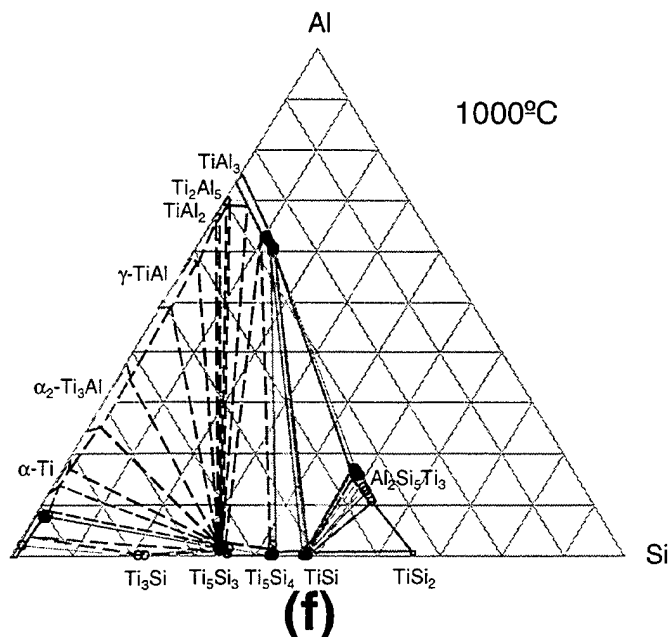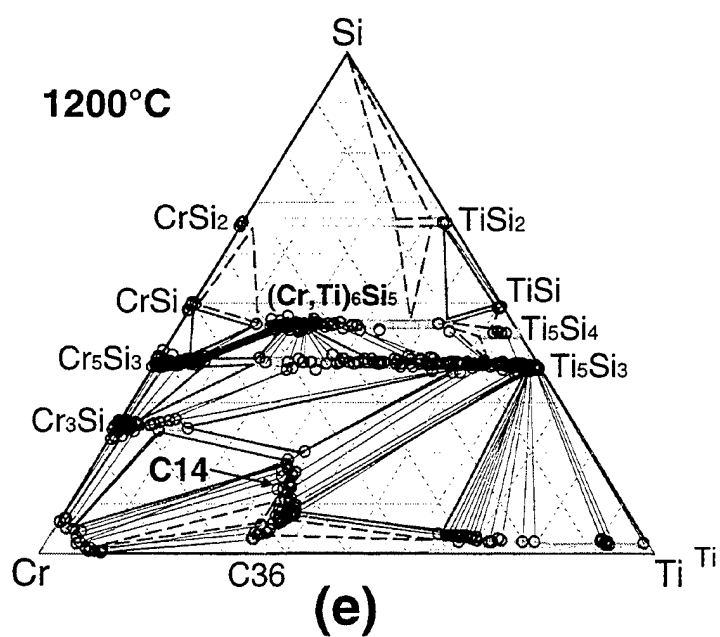
Figure 4. Continued
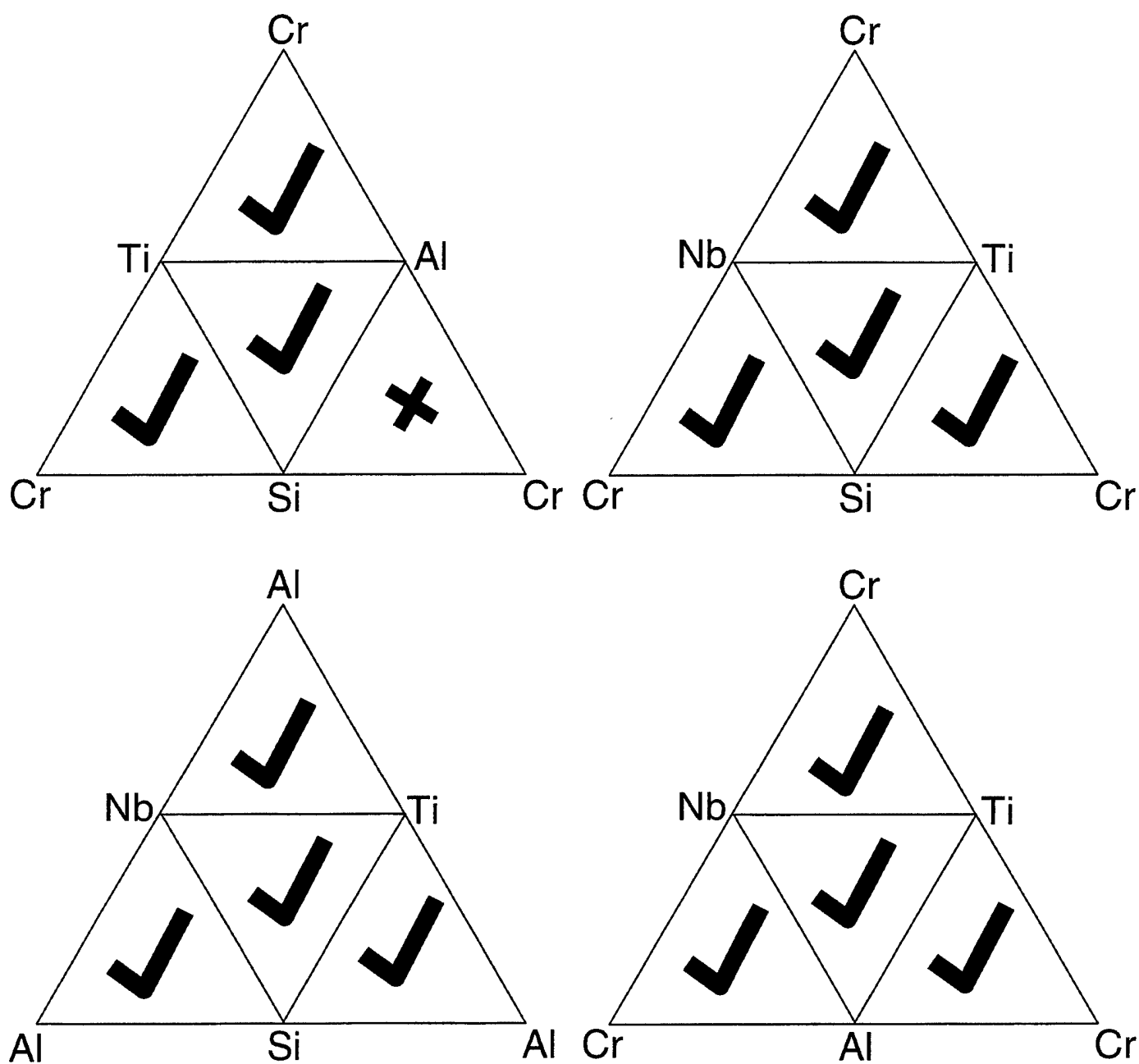
Figure 5. Schematic diagrams showing that we have mapped all the ternary systems (except for Al-Cr-Si) related to four quaternary systems: Ti-Si-Cr-Al, Nb-Ti-Si-Cr, Nb-Ti-Si-Al, and Nb-Ti-Cr-Al.

A Combinatorial Approach for Structural Materials

J.-C. Zhao

Advanced Engineering Materials, March 2001

ENGINEERING
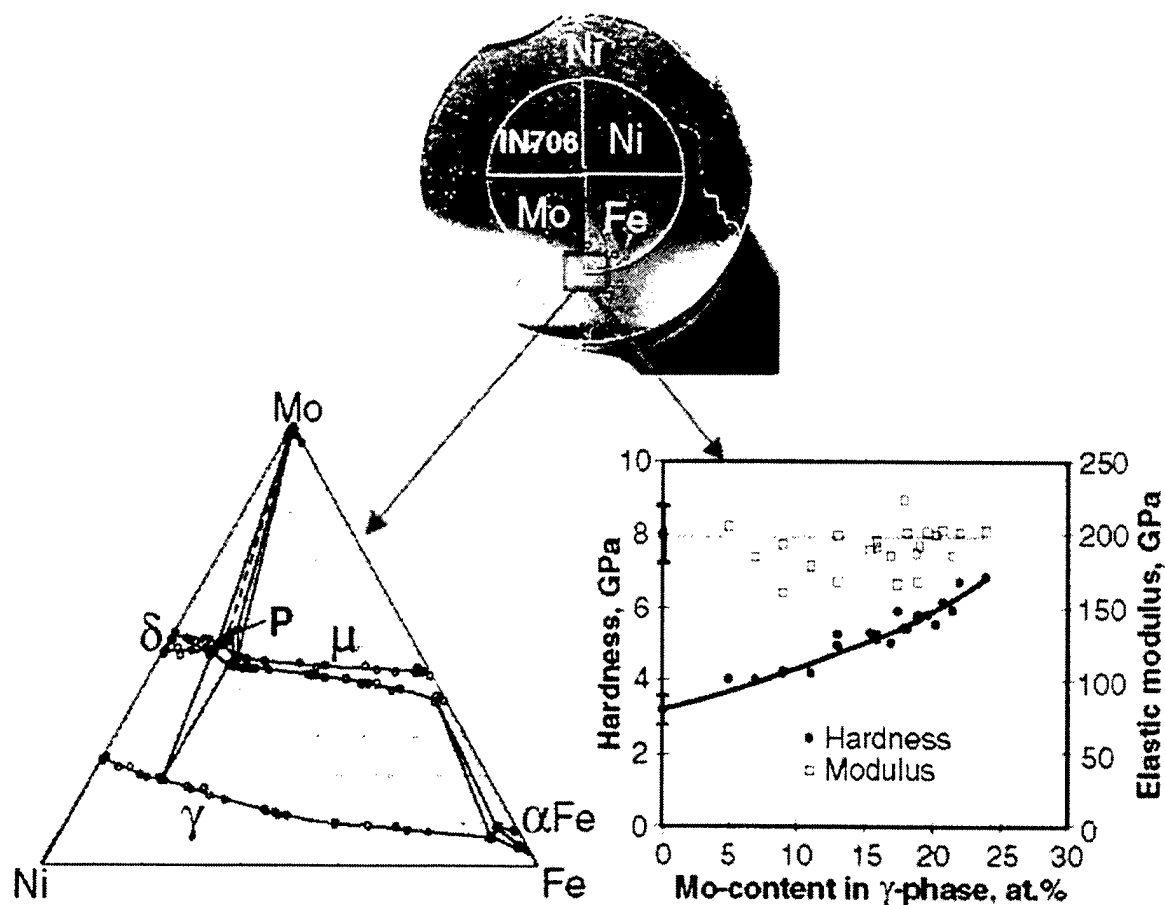
Combinatorial Approach for Structural Materials

Testing of Thin Films and Small Structures

High-T Superconducting Tapes

DLC Coatings

This journal is online
WILEY InterScience®
www.interscience.wiley.com

A Combinatorial Approach for Structural Materials**

By *Ji-Cheng Zhao* *

Structural materials such as superalloys and steels provide the mechanical properties for building jet engines, power generation turbines, cars, etc. that are everywhere in our lives. Structural materials development work is currently very time-consuming and expensive by handling one composition at a time for synthesis and testing of properties. The high-efficiency combinatorial approaches used for parallel synthesis and screening of large composition libraries of drugs[1] and functional materials[2-6] inspire the possibility of rapid screening of structural materials. Because bulk properties are required for structural materials, the existing approaches for solid-state functional materials using thin film deposition[2-6] are difficult to apply to structural materials screening. Here I describe a different methodology—the "diffusion multiple"—that generates large, multicomponent composition variations (libraries) in bulk samples through thermal interdiffusion. The coupling of diffusion multiples with micro-scale composition–phase–property measurements constitutes a powerful combinatorial approach for structural materials research and development.

A diffusion couple is simply a pair of metal (or ceramic) blocks of different composition, placed in intimate interfacial contact, and subjected to interdiffusion at a high temperature under the imposed chemical potential gradient. It has long been used to determine phase diagrams and evaluate diffusion coefficients.[7] An illustrative example of a diffusion couple is shown in Figure 1a for pure Ni in contact with $Ni_{0.5}Al_{0.5}$ (NiAl). It was made by physically placing a 3 mm thick Ni piece against a 3 mm thick single-crystal of NiAl. The two blocks were intimately joined together by hot isostatic pressing (HIP) at 1204 °C for 4 h under a 200 MPa of argon pressure. After heating the diffusion couple for another 100 h in vacuum at 1204 °C, substantial interdiffusion between Ni and Al took place and a reaction phase, Ni_3Al (γ'),

[*] Dr. J.-C. Zhao
General Electric Company, Corporate Research and Development
P.O. Box 8, Schenectady, NY 12301 (USA)
Email: zhaojc@crd.ge.com

was formed. Figure 1b shows the concentrations of Ni and Al as a function of distance as measured by the electron probe microanalysis (EPMA) method.[8] Pure Ni has a face-centered cubic lattice and forms a solid solution with Al called the γ-phase. Similarly, NiAl has an ordered body-centered cubic lattice and forms a solid solution with excess Ni called the β-phase. The formation of the γ'-phase between γ and β created two interfaces, one between γ and γ' and the other between γ' and β phases, which can be understood by looking at points 0 to 5 in Figure 1b and comparing them with the known phase diagram shown in Figure 1c. The local phase equilibrium at the interfaces is the basis for using diffusion couples to determine phase diagrams.[7] The libraries of single-phase compositions created in diffusion couples by interdiffusion, e.g., 0 to 18 at.-% of Al for the γ-phase in Figure 1b, have been used in the past for evaluating phase diagrams and diffusion coefficients but have not been employed for combinatorial surveys of properties.

In this light, I performed a systematic survey of mechanical properties on the composition libraries generated in the Ni–NiAl diffusion couple by taking advantage of the improved micro-mechanical testing equipment with a nano-sized indenter. This nano-indentation test monitors both load and displacement, and can evaluate both hardness and elastic modulus simultaneously.[9,10] A plot of hardness as a function of Al-concentration in the different phases is shown in Figure 1d. The hardness of the γ-phase increased from ~3.3 to 4.5 GPa as the Al-concentration increased from 0 to ~13 at.-% and was caused by a solution-hardening effect, a situation where dissimilar atoms distort the crystal lattice and make dislocations difficult to move. A further significant increase in hardness was observed for the Al-rich compositions (13 to 18 at.-% Al) of the γ-phase. This is highlighted in Figure 1d and is related to precipitation hardening where fine γ' particles, formed in the γ-matrix when the diffusion couple was cooled from 1204 °C to room temperature in the vacuum furnace, obstruct the movement of dislocations. Precipitation hardening is an important mechanism for structural materials design. It provides most of the strength to advanced Ni-based superalloys and requires the condition of supersaturation, i.e., where the Al solubility in the γ-phase decreases with lowering temperatures (e.g., 18 and 13 at.-% at 1204 and 800 °C respectively), Figure 1c. By varying the cooling rate and/or subsequent heat treatment of the diffusion couples, valuable information on precipitation kinetics may be obtained simultaneously for a library of compositions. This new combinatorial way of evaluating precipitation kinetics is significant since such information would be very time-consuming and expensive to obtain using the conventional one-alloy-at-a-time approach. Although not shown in Figure 1, the elastic modulus of the γ-phase was also measured and found to be ~200 GPa, and it did not vary significantly with Al-content.

Extending the concept from binary systems into multicomponent systems, a "diffusion multiple" was employed to generate libraries of multicomponent compositions for combina-
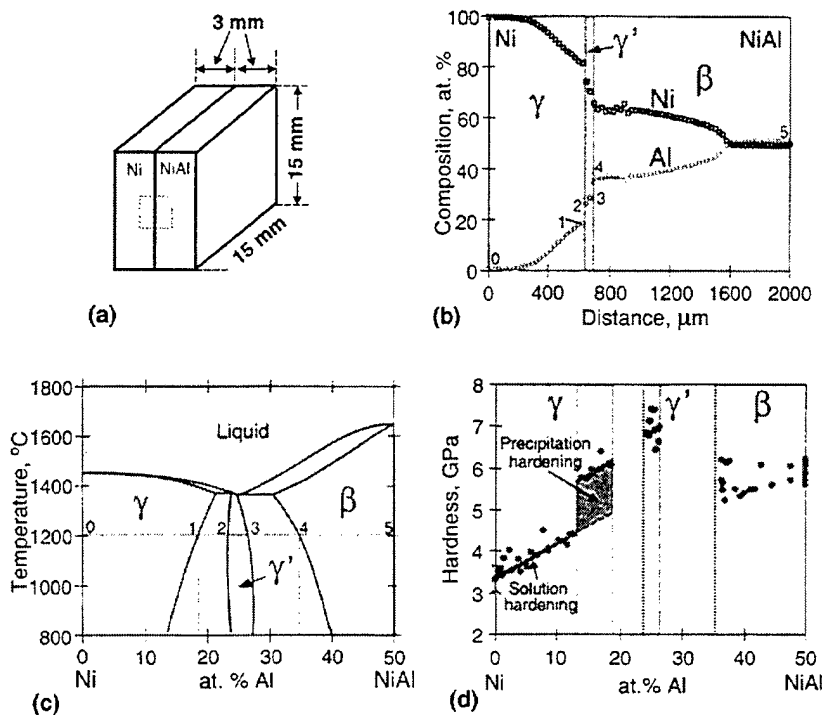
Fig. 1. Application of a diffusion couple to create libraries of single-phase compositions for combinatorial surveys of precipitation kinetics, phases and properties: a) a diffusion couple made up of Ni and NiAl, b) composition profiles of the diffusion couple after heat treated at 1204 °C for 100 h, c) Ni-rich side of the Ni–Al phase diagram (Points 0 to 5 correspond to these same points in b in composition), and d) the composition–phase–property (hardness) data obtained by performing nano-indentation tests on the composition libraries, showing the solution hardening and precipitation hardening effects.

Figure 2b. The welded assembly was treated by HIP for 4 h at 1100 °C under a 200 MPa pressure to provide good contacts among the elements and the alloy. The assembly was then heated for 1500 h at 1100 °C to cause extensive interdiffusion. Finally the diffusion assembly was cut through its central region parallel to the end caps and the cut surfaces polished flat for quantitative microchemical analyses and mechanical property surveys.

The results from the Ni–Mo–Fe triple at the rim of the diffusion multiple (highlighted in Fig. 2a) are shown in Figures 2c–e. All the intermetallic compounds, both binary and ternary, NiMo (δ), Fe_7Mo_6 (μ) and $Fe_{11}Ni_{36}Mo_{53}$ (P phase[15]), formed by diffusion reactions, Figure 2c (All these compounds have previously been observed in cast, equilibrated alloys[15]). By performing EPMA over the Ni–Mo–Fe triple region (Fig. 2c), the entire isothermal section of this ternary phase diagram was obtained, Figure 2d. For instance, the left-hand edge (points 0 to 5) of the diffusion triple (Fig. 2c) is a binary Ni–Mo dif-

torial surveys of critical materials properties. A diffusion multiple is an assembly of three or more different metal (or ceramic) blocks, in intimate interfacial contact, arranged as a triple, quadruple, etc. and subjected to a high temperature to allow thermal interdiffusion. Diffusion triples (introduced by Hasebe and Nishizawa[11] for simple ternary systems and demonstrated by Jin et al.[12,13] for complex systems with intermetallic compounds) and quadruples[14] have been used before to efficiently map ternary and quaternary phase diagrams; however, they were not widely adopted, partly due to the difficulty in making good contacts at the tri-junctions and quadri-junctions. A new five-part assembly like the one shown in Figure 2a was designed to overcome the sample-making difficulty and to combine diffusion couples (dotted lines), triples (dashed square), and a quadruple (dashed circle) into one sample. This assembly greatly increases the efficiency of generating composition libraries, Figure 2a. The use of alloy IN706 as one component of the diffusion multiple was intended to study the effect of Mo, Ni, and Fe modifications of composition on the properties of the alloy. IN706 is a Ni-based superalloy having a composition [in at.-%] of 40.06 Ni–38.0 Fe–17.4 Cr–2.1 Ti–1.8 Nb–0.5 Al–0.14 C. The pure elements of Ni, Mo and Fe and IN706 were cut into quarter-pie shapes and placed into four different quadrants as shown in Figure 2a. This assembly was placed inside a pure Ni tube with Ni caps and welded in vacuum using an electron beam,

fusion couple, since Fe could not reach there by diffusion. Similarly, points 5 to 12 at the top edge of the triple gave binary Mo–Fe equilibria, and points 12 to 14 at the right-hand edge gave the binary Fe–Ni information (Fe and Ni are completely soluble at 1100 °C). Closer to the centre of the triple, more interdiffusion of the three elements was achieved, thus ternary phase equilibrium information was obtained. Therefore, only one triple is needed to map a whole isothermal section of a ternary phase diagram.[11–13] The Ni–Mo–Fe phase diagram obtained from the diffusion multiple agrees very well with that measured from equilibrated alloys.[15] Since a diffusion triple maps all the phases in a ternary system, it can be used to effectively screen for the possible appearance of new intermetallic compounds and to map phase diagrams for alloy design.

Again a very important, but unexplored, feature of a diffusion triple is its ability to generate full libraries of all the single-phase compositions. It is clear that points 0–1–15–16–11–12–13–14–0 in Figure 2c correspond to those same points in Figure 2d in composition and they envelop the entire composition region of the γ-phase. I note and demonstrate that this full-composition library of single-phase regions can be employed for efficient and systematic surveys of properties and precipitation microstructures and kinetics. For instance, by performing nano-indentation tests,[9,10] the composition–phase–property data were obtained for the Ni–Mo–Fe ternary system. Figure 2e shows the collected hardness and modulus
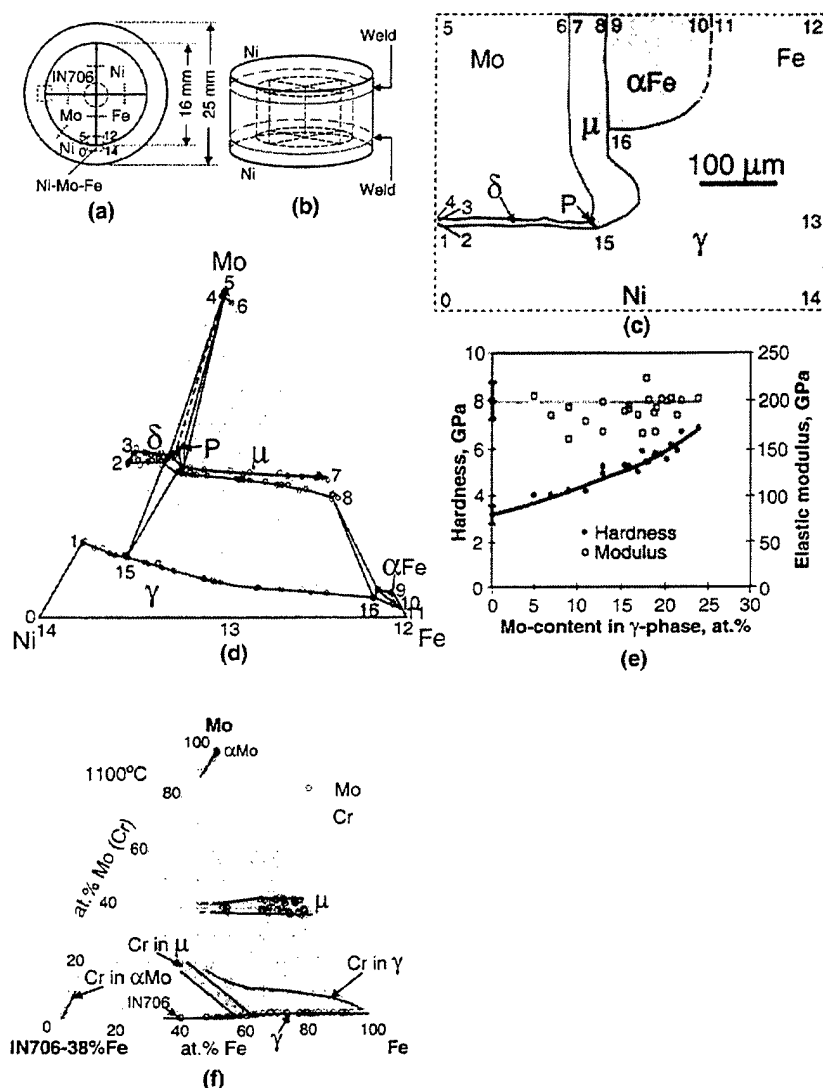
(a) **(b)**

(c)

(d)

(e)

(f)

Fig. 2. *Diffusion multiple to generate large multicomponent composition libraries in a bulk sample for combinatorial surveys of phases, crystal structures, phase diagrams, properties, and composition–phase–property data: a) geometry of a diffusion multiple (cross-sectional view) consisting of diffusion couples (dotted lines), triples (dashed squares), and a quadruple (dashed circle), b) method of making the diffusion multiple using electron beam welding and HIP, c) intermetallic compounds and solid–solution phases formed by interdiffusion reactions among the elements in the Ni–Mo–Fe diffusion triple (highlighted in a) after heat treatment at 1100 °C for 1500 h, d) the whole 1100 °C isothermal phase diagram of Ni–Mo–Fe (composition scale in at.-%) obtained from the diffusion triple (Points 0 to 16 corresponds to these same points in composition in c), e) variation of hardness and elastic modulus with Mo content in the γ-phase as measured by nano-indentation, and f) IN706–Fe–Mo (with Cr superimposed) pseudo-ternary section of a multicomponent phase diagram obtained from a IN706-Fe-Mo diffusion triple (the composition of all other elements were obtained but not plotted for simplicity).*

data of different Fe and Mo concentrations in the γ-phase plotted against Mo-content only. The degeneration of all the hardness data into a single curve indicates that Fe has little effect on the hardness and modulus of the γ-phase, whereas Mo is a potent solution hardener (but has little effect on modulus). For solid solutions, there is a strong correlation between hardness and yield strength (more precisely flow stress), thus Mo should be a potent strengthener for the γ-phase. The average hardness values of the δ and μ phases

were 15.1 and 13.7 GPa respectively (much higher than that of γ, <7 GPa), but their moduli (235 and 238 GPa respectively) were only slightly higher than that of γ. Such composition–phase–property relations are very valuable for structural materials design.

A multicomponent alloy—the 7-element alloy IN706 as an example—can be used as a member of a diffusion multiple to directly map multicomponent phase diagrams and to generate multicomponent composition libraries for rapid surveys of critical mechanical and compositional properties. An IN706–Fe–Mo–Ni diffusion multiple was made to evaluate the possibility of further strengthening IN706 by adding Mo. The obtained IN706–Mo–Fe pseudo-ternary multicomponent phase diagram is shown in Figure 2f (The lower-left corner of the phase diagram represents a hypothetical composition where the 38 at.-% Fe in IN706 is replaced by 38 at.-% Ni, i.e., a hypothetical IN706 composition without Fe so that the diagram can be plotted from 0 at.-% Fe to 100 at.-% Fe in the horizontal axis). The result shows that no Mo could be directly added to IN706 without forming the brittle μ-phase. Only when the Cr content is reduced to ~10 at.-% and the Fe content increased to ~60 at.-%, will 1 at.-% Mo addition become possible (at 1100 °C). The maximum Mo addition is 2 at.-% and further reduction of Cr and increase of Fe do not change the Mo solubility in the γ-phase. This kind of multicomponent phase diagram can be directly used for alloy design, and it can also be used to test and improve thermodynamic modeling parameters for computational design of materials.[16,17] In addition, precipitation ki-

netics and composition–property data can be efficiently evaluated from the multicomponent composition libraries created in the diffusion multiples in a similar way as demonstrated with the Ni–NiAl diffusion couple and the Ni–Mo–Fe diffusion triple.

An automated electron backscatter diffraction (EBSD) technique was employed to identify the crystal structures of phases in the diffusion couples and multiples. EBSD is an electron diffraction technique used in scanning electron

microscopy (SEM). Phase identification was accomplished by a direct match of the diffraction bands (similar to Kikuchi bands) in the experimental pattern with simulated patterns generated using known structure types and lattice parameters.[18] Recent advancement in algorithms and computer programs in automated EBSD systems makes it possible to perform rapid pattern collection and recognition (indexing) from small (~2 μm) areas at about 5000 points an hour.

Useful tensile strength of structural materials is a combination of three properties: plastic hardness (i.e., resistance to yielding), elastic stiffness (i.e., elastic modulus), and toughness (i.e., resistance to crack failure).[19] Recent advancement in nano-indentation tests enables rapid evaluation of hardness and modulus, and even fracture toughness[20] of brittle phases from small areas (~10 μm) in bulk samples. Pharr et al.[20] found that the cube-corner indenter greatly reduces the load required to generate cracks in brittle phases as compared to the regular Vickers indenter. If the indentation-generated cracks are within the dimensions of individual intermetallic phases formed in diffusion multiples, then the fracture toughness can be evaluated using the simple equation developed by Lawn et al.[21,22] This kind of combinatorial survey has its advantage since sometimes it takes quite some effort to synthesize macro-scale samples of these brittle intermetallics through casting or powder metallurgy routes. As more understanding is achieved on the elasto-plastic behavior of nano-indentation, it is even possible to extract yield strength of materials from the load and displacement curves.[23,24]

Compared to the conventional one-alloy-at-a-time approach, rapid analyses on the composition libraries generated in parallel by diffusion multiples greatly reduce the time in each step of making an ingot of individual composition, homogenizing it, preparing a sample, and loading it into different testing systems. The efficiency gain is especially large for measurement systems with a vacuum, such as SEM, EPMA, EBSD, etc. The time to change samples and to wait until the desired vacuum level is attained can amount to a significant part of the analysis time.

The multicomponent compositional libraries generated in the diffusion multiples are continuous for single-phase compositions. Thus, it is difficult to compare the size of this continuous library size to that of the discrete combinatorial methods.[2-4] The intermetallic compounds and solid solution phases formed by thermal interdiffusion in the diffusion multiples range in size from several microns to hundreds of microns in width (and several mm in thickness—the thickness of the bulk sample), depending on the heat treatment temperature and time, thus allowing at least several nano-indentation measurements to be made in each phase (in each scan). The indents on all the phases are less than 2 μm in size. The size of all the phases is also sufficiently large for reliable EPMA and EBSD measurements for composition and crystal structure determination to map phase diagrams. One limitation of the diffusion multiple technique is that, to avoid melting, the highest temperature for diffusion heat treatment is

limited by the lowest liquidus temperature of the multicomponent system which may not be known a priori. When the liquidus is low, it may take a long time to promote sufficient interdiffusion for a reliable evaluation of properties.

The properties of structural materials are microstructure dependent, and desired microstructures can be difficult to achieve in thin films, especially when the scale of the microstructure is larger than the film thickness. Moreover, phase precipitation kinetics and diffusivities are usually very different in bulk samples than in thin films due to surface effects, thus data evaluated from thin films cannot be directly used to design bulk structural materials. In addition, the usually small grain size of thin film samples may produce additional (microstructural) hardening to confound the solution hardening and precipitation hardening effect. All these properties can be efficiently evaluated from the bulk diffusion multiples. Note that the intermetallic compounds formed in diffusion multiples are equilibrium phases; whereas those in thin films can sometimes be metastable phases and it would take some effort to promote equilibrium phase formation by varying the deposition and heat treatment temperatures and sequences.[6]

In summary, multicomponent composition libraries can be generated in bulk diffusion multiples through high-temperature thermal diffusion for a combinatorial development of materials. This technique can be used to map multicomponent phase diagrams, search for novel compounds in multicomponent systems, determine diffusion coefficients from the composition profiles, evaluate precipitation kinetics, study effects of compositional modification of complex alloys, and map composition–structure–property data.

[1] R. A. Houghten, Proc. Natl. Acad. Sci. USA 1985, 82, 5131.
[2] X.-D. Xiang, X. Sun, G. Briceno, Y. Lou, K.-A. Wang, H. Chang, W. G. Wallace-Freedman, S.-W. Chen, P. G. Schultz, Science 1995, 268, 1738.
[3] G. Briceno, H. Chang, X. Sun, P. Schultz, X.-D. Xiang, Science 1995, 270, 273.
[4] E. Danielson, H. Golden, E. W. McFarland, C. M. Reeves, W. H. Weinberg, X. D. Wu, Nature 1997, 389, 944.
[5] R. B. van Dover, L. F. Schneemeyer, R. M. Fleming, Nature 1998, 392, 162.
[6] X.-D. Xiang, Annu. Rev. Mater. Sci. 1999, 29, 149.
[7] F. J. J. van Loo, Prog. Solid State Chem. 1990, 20, 47.
[8] J. I. Goldstein, Scanning Electron Microscopy and X-Ray Microanalysis, Plenum, New York 1992.
[9] M. F. Doerner, W. D. Nix, J. Mater. Res. 1986, 1, 601.
[10] W. C. Oliver, G. M. Pharr, J. Mater. Res. 1992, 7, 1564.
[11] M. Hasebe, T. Nishizawa, in Applications of Phase Diagrams in Metallurgy and Ceramics (Ed: G. C. Carter), NBS Special Publ. #496, Vol. 2 1978, p. 911.
[12] Z. Jin, Scand. J. Metall. 1981, 10, 279.
[13] J.-C. Zhao, Z. Jin, Z. Metallkd. 1990, 81, 247.

[14] J.-C. Zhao, Z. Jin, P. Huang, *Scr. Metall.* **1988**, *22*, 1825.

[15] F. J. J. van Loo, G. F. Bastin, J. W. Q. A. Vrolijk, J. J. M. Hendriks, *J. Less-Common Met.* **1980**, *72*, 225.

[16] G. B. Olson, *Science* **1997**, *277*, 1237.

[17] N. Saunders, A. P. Miodownik, *CALPHAD*, Elsevier Science, New York **1998**.

[18] C. J. Harland, P. Akhter, J. A. Venables, *J. Phys.* **1981**, *E14*, 175.

[19] A. Cottrell, *MRS Bull.* **2000**, *25*, 43.

[20] G. M. Pharr, *Mater. Sci. Eng. A* **1998**, *253*, 151.

[21] B. R. Lawn, A. G. Evans, D. B. Marshall, *J. Am. Ceram. Soc.* **1980**, *63*, 574.

[22] G. R. Anstis, P. Chantikul, B. R. Lawn, D. B. Marshall, *J. Am. Ceram. Soc.* **1981**, *64*, 533.

[23] T. A. Venkatesh, K. J. van Vliet, A. E. Giannakopoulos, S. Suresh, *Scr. Mater.* **2000**, *42*, 833.

[24] A. E. Giannakopoulos, S. Suresh, *Scr. Mater.* **1999**, *40*, 1191.

Autopassive Wrought Magnesium Alloys[**]

By *Paloma Adeva-Ramos, Simon B. Dodd, Peter Morgan, Franz Hehmann,* * *Pierre Steinmetz, and Ferdinand Sommer*

In order for magnesium to compete more effectively with aluminum in weight-sensitive wrought applications, the magnesium bulk alloy should i) develop a naturally and

[*] Dr. F. Hehmann
     NEMP
     Iburger Strasse 151, D-49082 Osnabrück (Germany)

     Dr. P. Adeva-Ramos
     Departamento de Metallurgia Fisica, CENIM
     Av. de Gregorio del Amo 8, E-28040 Madrid (Spain)

     Dr. S. B. Dodd
     Structural Materials Centre, DERA
     Farnborough, Hants., GU14 0LX (UK)

     Dr. P. Morgan
     British Aerospace Systems, Sowerby Research Centre
     Filton, Bristol, BS34 7QW (UK)

     Dr. P. Steinmetz
     Laboratoire de Chimie du Solide Minéral, University of Nancy
     B.P. 239, F-54506 Vandœuvre (France)

     Dr. F. Sommer
     Institut für Metallkunde, University of Stuttgart
     Seestrasse 75, D-70174 Stuttgart (Germany)

spontaneously protecting alloy surface when exposed to the environment, for example by damage via a scratch on the surface of an aircraft component, and ii) exhibit an enhanced plasticity relative to prior art by having an increased number of active crystal slip systems.

Both attributes require the manufacture of magnesium-based solid solution alloys showing greatly extended solid solubilities without undue increase in density, toxicity, or susceptibility to thermal decomposition as a result of alloying elements. "Autopassivity" is an engineering property which requires that the environment of the alloy always sees a statistically identical alloy microstructure, regardless of whether the surface is intact or damaged. It is obvious that such magnesium-based solid solution alloys must be resistant to microstructural degradation, such as by coarsening upon thermomechanical processing, and to creep. Conventional alloying using ingot metallurgy or spray-formed precursor product forms is restricted to alloying elements that involve an undue increase in density, toxicity and/or susceptibility to thermal degradation while in equilibrium αMg-based solid solution (e.g., In, Pb, Sn, Bi, Dy, etc. / Tl, Cd, Th, Pu / Li, Al, Zn, Ag) or they are unaffordable (Sc).

A summary of the observed terminal solid solubility extensions (TSSEs) of binary alloying elements in αMg is reproduced in Table 1. Although quite remarkable extensions of solid solubilities by melt spinning or splat cooling a magnesium alloy melt have been reported,[1,2] through-thickness of the homogeneous TSSE microstructural zone was usually limited to a few micrometers, beyond which a plane solidification front or solute trapping broke down into an equilibrium (e.g., dendritic) microstructure. The TSSE of Al in αMg was reported to decompose within some months at room temperature and the decomposition rate increased with increasing levels of aluminum in a magnesium-based solid solution. The attempt to achieve thermally more stable TSSE in a magnesium-based solid solution by rapid quenching from the liquid phase was usually frustrated by the release of latent heat, imposing severe dimensional limits on the undivided volume of interest. The need to develop autopassive magnesium alloys calls for a fresh look at manufacturing technology for continuous production of unlimited volume TSSE Mg alloys.

Physical vapor deposition (PVD) has been shown[3] to result in partitionless growth scales of TSSE even exceeding

Table 1. Selected terminal solid solubility extensions (TSSE) in rapidly solidified Mg-alloys (in [at. %]). After [10].

Solute in Mg	Max. equil. solid solubility	TSSE	RSP-method employed
Al	11.5	22	melt spinning
Y	3.5	9.7	piston-and-anvil splats
Ca	0.98	7	rotating wing splats
Sm	1	5.8	rotating wing splats
Zn	2.8	4.8	rotating wing splats
Pd	0.23	3.4	rotating wing splats
Ce	0.09	3.15	rotating wing splats
Mn	1	2.2	rotating wing splats
Ni	0.04	1.7	rotating wing splats

A Combinatorial Approach for Efficient Mapping of Phase Diagrams and Properties

J.-C. Zhao

A combinatorial approach for efficient mapping of phase diagrams and properties

Ji-Cheng Zhao
*General Electric Company, Corporate Research and Development, P.O. Box 8, K1-MB231,
Schenectady, New York 12301*

A methodology is developed which extends the combinatorial approaches to structural materials research and development. This high-efficiency methodology employs diffusion couples and "diffusion multiples" to create large variations (libraries) of compositions in bulk samples for fast and systematic surveys of bulk properties. These composition libraries coupled with microanalytical techniques such as electron probe microanalysis, electron backscatter diffraction analysis, and nanoindentation tests can be used for efficient surveys of phases, equilibria, diffusion coefficients, precipitation kinetics, properties, and composition–phase–property relations (such as solution hardening and strengthening effect) for accelerated design of multicomponent alloys.

I. INTRODUCTION

Compared to the conventional one-alloy-at-a-time approach, the combinatorial approaches dramatically increase the efficiency of materials discovery by coupling parallel syntheses of large libraries of compositions with an effective screening for desired properties.[1–6] The combinatorial approaches are being aggressively pursued to develop new functional materials with novel physical and chemical properties.[1–6] These approaches using thin-film deposition, however, have yet to find applications in developing structural materials for improved mechanical properties. Since the approaches usually generate only a very small volume of thin film for each composition, it is difficult to evaluate properties critical to structural materials design. For instance, the properties of structural materials are microstructure dependent, and desired microstructures can be difficult to achieve in thin films, especially when the scale of the microstructure is larger than the film thickness. In addition, phase precipitation kinetics, which is also critical for structural materials design, is usually very different in bulk samples than in thin films; thus, the kinetic information obtained from thin-film samples cannot be used for bulk structural materials design.

To overcome the thin-film limitations, a different combinatorial approach has been developed which creates composition libraries in bulk diffusion couples and "diffusion multiples" by thermal interdiffusion.[7] Diffusion multiple is an assembly of three or more different metal blocks, in intimate interfacial contact, arranged as a triple, quadruple, etc., and subjected to a high temperature

to allow thermal interdiffusion. The concept is an extension of a diffusion triple method introduced by Hasebe and Nishizawa[8] for simple ternary systems and demonstrated by Jin et al.[9–11] for complex ternary systems with intermetallic compounds. The coupling of the composition libraries generated in diffusion multiples with microscale composition, structure, and property evaluation techniques constitutes an efficient methodology for mapping phase diagrams and properties.

The idea of this combinatorial approach can be illustrated using a hypothetical binary A–B system with a miscibility gap, schematically shown in Fig. 1. When a diffusion couple made up of pure A and pure B [Fig. 1(b)] is exposed to a temperature, T_1 (above the miscibility gap), for an extended time period, a continuous binary composition spectrum (library) from 0 at.% B to 100 at.% B can be obtained by thermal interdiffusion, Fig. 1(c). The composition profile that correlates composition with location (position) can be determined using electron probe microanalysis (EMPA).[12] Such composition profiles have long been used to evaluate diffusion coefficients. What has not been taken full advantage of is the composition library generated in diffusion couples. This composition library can be used to survey precipitation kinetics and properties. For instance, by heat-treatment of the already T_1-exposed diffusion couple at a lower temperature, T_2, for different time periods, the isothermal transformation kinetics can be evaluated simultaneously for a wide range of compositions. This can be accomplished by examining the microstructure (morphology, size, distribution, etc.) at different composition
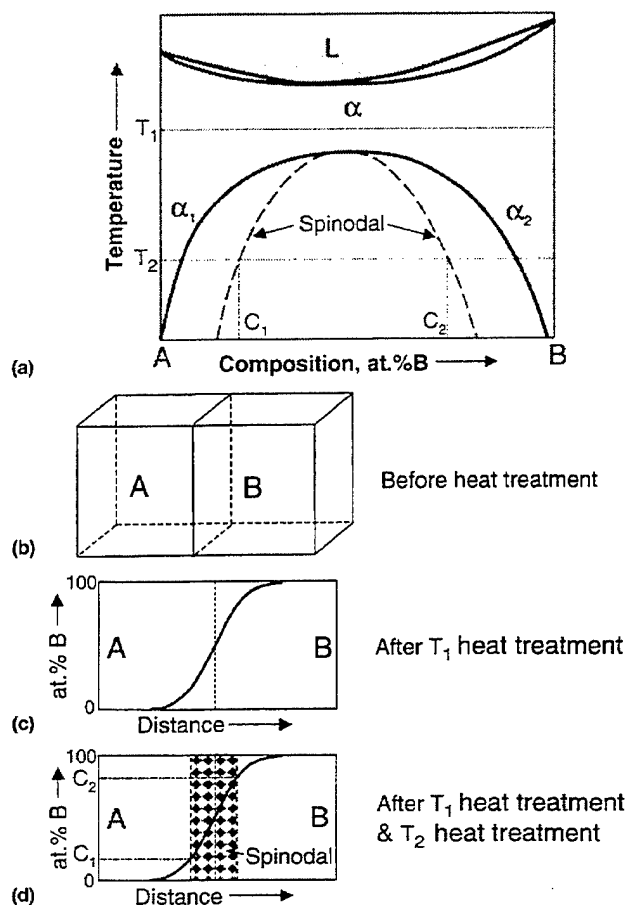
FIG. 1. Application of a diffusion couple to generate a binary composition library (spectrum) for an efficient evaluation of precipitation kinetics, diffusivity, and properties: (a) a hypothetical binary A–B phase diagram; (b) a schematic diffusion couple; (c) schematic composition profile after an extended heat-treatment at T_1; (d) schematic microstructure after an extended heat-treatment at T_1 and a short time exposure at T_2 to determine the spinodal decomposition compositions and kinetics.

regions (different locations) in the diffusion couple. For instance, by exposure at T_2 for a short time period, the spinodal decomposition compositions and kinetics [Fig. 1(d)] can be determined since the nucleation and growth type transformations take a much longer time period. Alternatively, by cooling of the T_1-exposed diffusion couple at different cooling rates, the continuous cooling transformation kinetics can be evaluated, again by examining the microstructure and properties (such as hardness) at different locations (compositions) of the diffusion couple. In addition to surveying precipitation kinetics and diffusion coefficients, the composition library created in the diffusion couple can be used for localized determination of mechanical properties. For instance, the load- and displacement-sensing nanoindentation tests allow simultaneous evaluation of hardness and elastic modulus from very localized (e.g., approximately 2 µm)

regions.[13–16] Such a survey of properties and precipitation kinetics is much more efficient and systematic than the conventional one-alloy-at-a-time approach.

With extension of the technique, a diffusion triple[8–11] can be employed for a combinatorial survey of ternary systems. A diffusion triple is an assembly made up of three components in the geometry like the one shown in Fig. 2(a). In most cases there exists only an interface between two phases (as in most diffusion couples) and a line (perpendicular to the cross-sectional plane) among three phases in a triple after a long-term heat-treatment at a given temperature [Fig. 2(c)]. By quantitative EPMA across the interfaces and at the three-phase trijunction, both tie-lines and tie-triangles can be obtained to construct an isothermal section of the corresponding ternary phase diagram. For instance, points 1 and 2 in Fig. 2(c) are basically a binary diffusion couple since element B cannot reach there by diffusion even after a long-term heat-treatment; thus, EPMA across points 1 and 2 can give tie-line 1–2 in Fig. 2(b). Moving from points 1 and 2 to points 3 and 4 to points 5 and 6, more and more B has been diffused into the α- and γ-phases, thus tie-lines with higher concentrations of B can be obtained, corresponding to tie-lines 3–4 and 5–6 in Fig. 2(b). Similarly, points 7 and 8 give tie-line 7–8 of the A–B binary system. Points 5, 6, and 9 can provide the tie-triangle of the α–β–γ three-phase region. Thus, for most systems, only one triple is needed to survey the whole isothermal section of a ternary system.[8–11] By exposure of the diffusion triples at different temperatures, several isothermal sections can be obtained to construct a ternary phase diagram.

It is clear that points 0–1–3–5–7–0 in Fig. 2(a) correspond to those same points in Fig. 2(c) in composition, and they envelop the entire composition region of the α-phase. Thus, a diffusion triple can generate full-composition libraries for all the single-phase regions of a ternary system. These composition libraries can be employed for combinatorial surveys of properties and precipitation kinetics in a similar way as discussed for the binary A–B diffusion couple, Fig. 1.

The aim of this work is to explore the feasibility of using such a combinatorial approach to efficiently map multicomponent phase diagrams, properties (such as hardness and modulus), and precipitation kinetics for accelerated design of structural materials. This paper complements a previous short communication[7] by providing more detailed examples and discussions.

II. EXPERIMENTAL PROCEDURES

The starting pure elements were 25-mm diameter bars with a purity of 99.95% for Fe, 99.98% for Ni, and 99.95% for Mo (all in wt.%), respectively. A high-purity
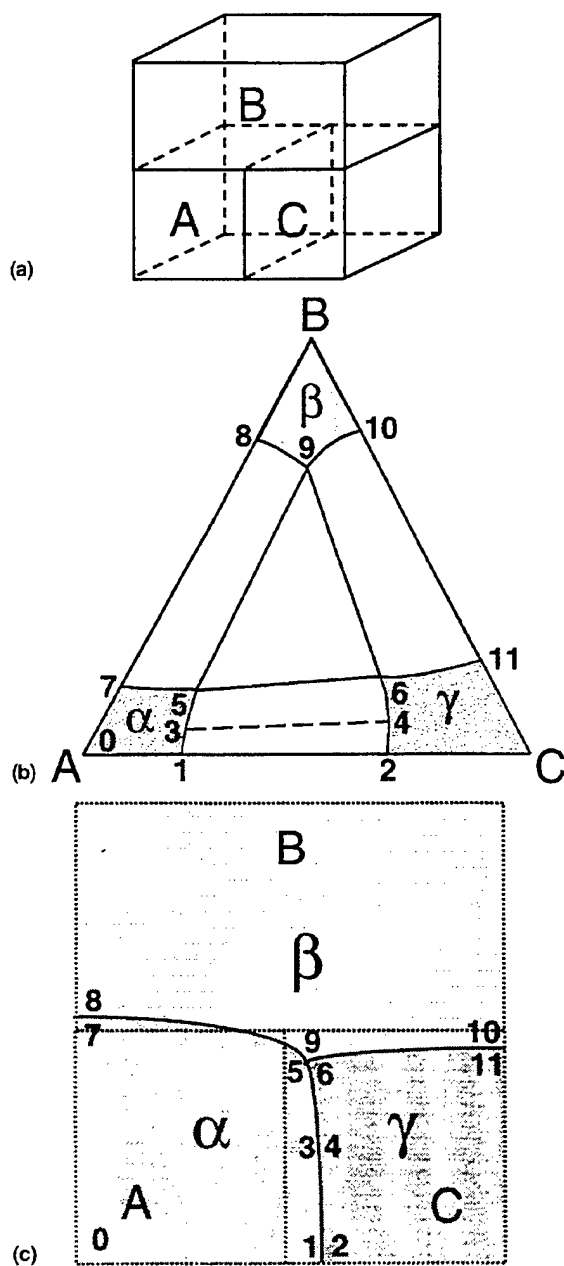
(a)

(b)

(c)

FIG. 2. Schematic diagrams explaining how a diffusion triple can be used to map a whole isothermal section of a ternary phase diagram and to generate full libraries of single-phase compositions for an efficient survey of properties: (a) diffusion triple; (b) phase diagram; (c) cross-sectional view of the diffusion triple after heat treatment showing phase boundary locations and their correspondence with the phase diagram.

stoichiometric NiAl single-crystal bar was used as the starting NiAl stock. An Inconel 706 (IN706) superalloy bar of 25-mm diameter was purchased commercially. The composition of IN706 is the following: 41.62 Ni–37.5 Fe–16.0 Cr–0.20 Al–1.75 Ti–1.45 Ta–1.45 Nb–0.03 C (wt.%).

A diffusion couple of Ni–NiAl was made by placing 3-mm-thick slices of Ni and a single-crystal NiAl in a pure Ni hot isostatic pressing (HIP) can. The HIP can containing the diffusion couple was electron beam (EB) welded, and the HIP was performed at 1204 °C and 200 MPa for 4 h. The HIP can was then heat-treated at 1204 °C for 100 h in a vacuum furnace and then furnace cooled to ambient temperature. The heat-treated can was then cut into halves parallel to the diffus-ion direction using electrodischarge machining (EDM) to prepare metallography samples for microprobe and nanoindentation tests. A Ni–Pt diffusion couple was made by sandwiching a 0.75-mm-thick pure Pt piece (99.99 wt% purity) between two, 3-mm-thick, pure Ni slices. The diffusion couple underwent a HIP run of 1100 °C and 200 MPa for 4 h and was then heat-treated at 900 °C for 1650 h. After the heat-treatment, the sample was quenched into water by breaking the quartz tube.

A five-part "diffusion multiple" assembly[7] was de-vised that combines diffusion couples (dotted lines), triples (dashed squares), and a quadruple[17] (dashed circle) in one sample, as shown in Fig. 3(a) using the Fe–Cr–Mo–Ni system as an example. To make this diffusion multiple, pure elements of Fe, Cr, Ni, and Mo were cut into quarter-pie shapes using EDM. The recast layer formed on the EDM cut surfaces was re-moved by glass beading using SiO_2 particles accelerated by a compressed air gun, followed by mechanical grind-ing. The quarter-pie pieces were placed into four differ-ent quadrants as shown in Fig. 3. This assembly was placed inside a pure Ni tube of 25-mm outer diameter and 16-mm inner diameter. Two pure Ni caps were EB-welded in vacuum onto the Ni tube. The welded assem-bly underwent a HIP run of 4 h at 1100 °C under a 200 MPa pressure to provide good contacts among the components. The size of the sample was designed such that the dimensions of the pure elements were much larger than the diffusion distances. The multiples were then sliced to approximately 6-mm-thick disks [Fig. 3(c)] and sealed individually in evacuated quartz tubes (ap-proximately 1×10^{-6} torr) for heat treatment at 1100 °C for 1500 h.

All the samples were first examined using scanning electron microscopy (SEM), especially the backscatter elec-tron (BSE) imaging. Most phases could be seen in the BSE images due to the differences in their average atomic number density. Quantitative EPMA analysis was performed on either CAMECA (Paris, France) micro-probe using 15–kV voltage, 40-nA current and a 40° take-off angle or a JEOL 733 Superprobe (Japan Electron Optics Ltd., Tokyo, Japan) operated at 20 kV, 60 nA, and also a 40° take-off angle.

Crystal structure identification of phases was made by electron backscatter diffraction (EBSD),[18,19] which is an electron diffraction technique in SEM (and which is
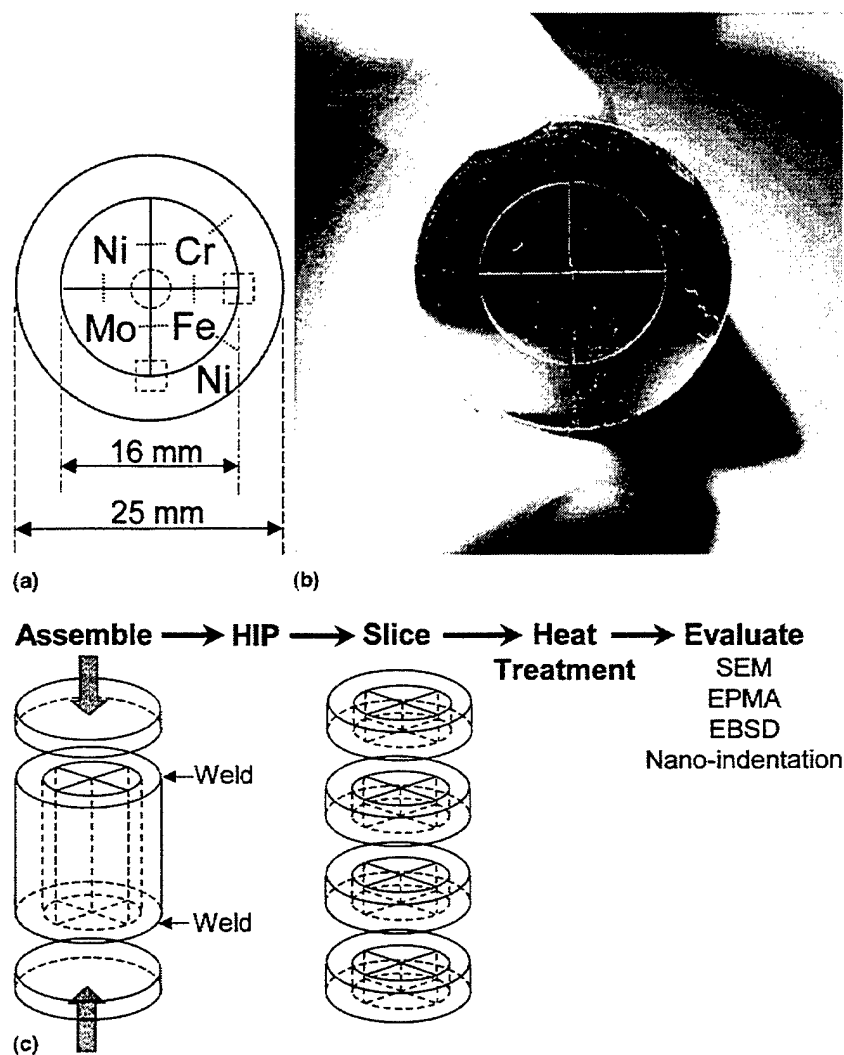
FIG. 3. (a) Geometry, (b) appearance, and (c) procedure for making a diffusion multiple.

different from the BSE imaging). This technique allows rapid electron diffraction pattern collection from small (e.g., 2 μm) microstructural features in bulk samples (not thin foils). Phase identification was accomplished by a direct match of the diffraction bands in the experimental backscatter pattern with simulated patterns generated using known structure types and lattice parameters. The crystal structure identification for the Ni–Pt diffusion couple was carried out using a Siemens GADDS (Siemens AG, Munich, Germany) microdiffractometer with a collimated x-ray beam of 0.3-mm diameter.

Nanoindentation tests were performed using a NanoTest 550 tester manufactured by Micro Materials Ltd., Wrexham, U.K. This tester monitors both the load and the displacement during indentation tests and thus allows both hardness and elastic modulus to be evaluated.[13–16] The tests were performed at room temperature with a load of 10 milli-newton (mN).

III. RESULTS

The first example illustrating the idea is shown in Fig. 4 for the Ni–NiAl diffusion couple that was heat-treated at 1204 °C for 100 h. The composition profiles based on EPMA measurements are shown in Fig. 4(b), which can be used to evaluate diffusion coefficients of various phases and their compositional dependence.[20] The diffusion coefficients evaluated from the composition profiles are shown in Fig. 4(c), and they agree very well with previous literature results.[21–23] Such diffusion coefficients are essential for simulating the precipitation and coarsening kinetics.

The composition profiles, Fig. 4(b), show that significant interdiffusion took place in the diffusion couple and that the γ′ (Ni_3Al) phase was formed, creating two interfaces—one between γ and γ′ (points 1 and 2) and the other between γ′ and β (points 3 and 4). The local
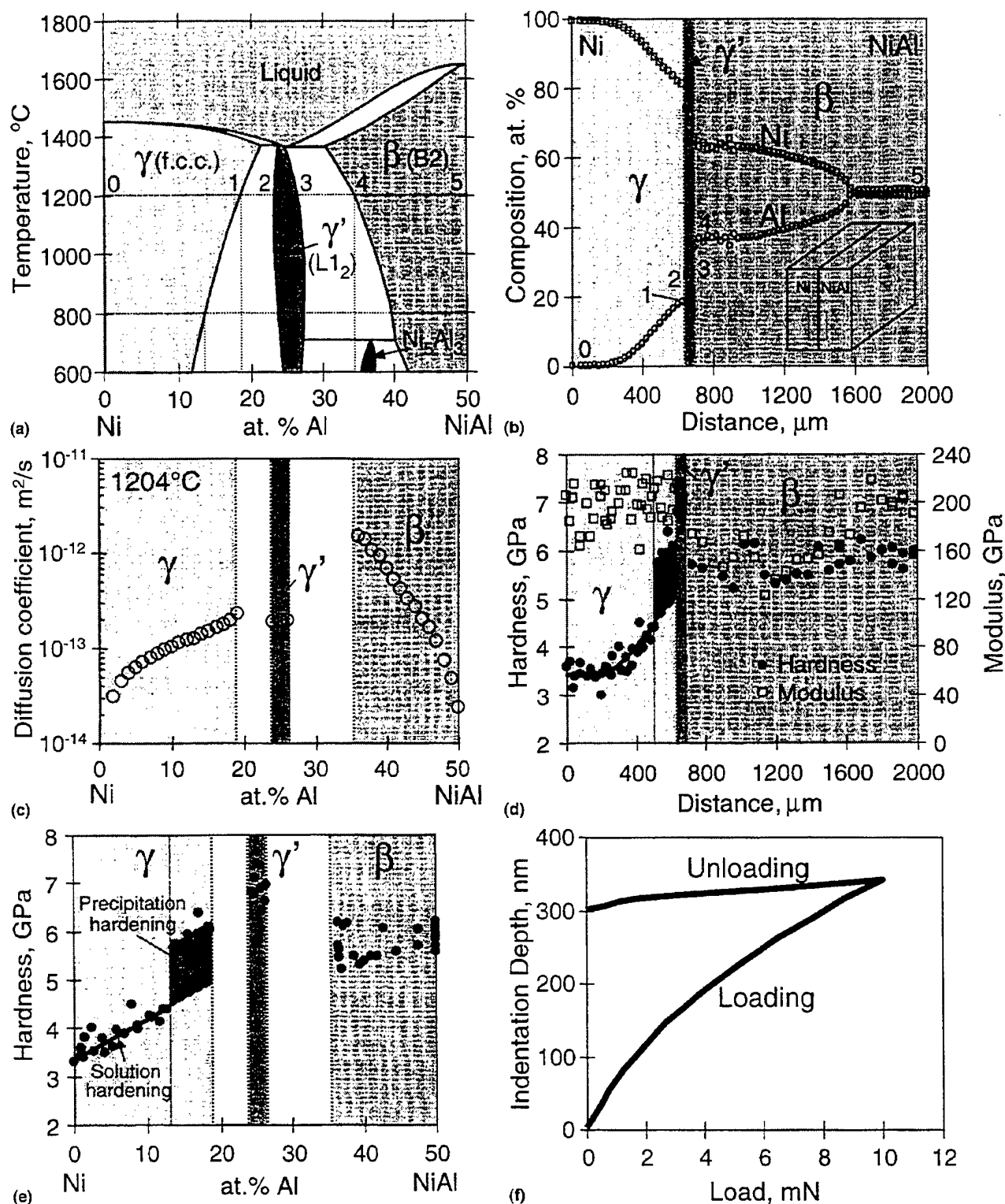
FIG. 4. Application of a diffusion couple to create spectra of single-phase compositions for an efficient evaluation of phases, equilibria, and properties: (a) Ni-rich side of Ni–Al phase diagram; (b) composition profiles of a Ni–NiAl diffusion couple after annealing at 1204 °C for 100 h; (c) diffusivity of various phases evaluated from the diffusion profile of (b); (d) hardness and modulus profiles obtained from nanoindentation tests; (e) hardness variation with compositions and phases; (f) a typical load–displacement curve (for pure Ni) from a load and displacement sensing nanoindentation test for hardness and modulus evaluation.

equilibrium at the interfaces is the basis for the wide application of diffusion couples in determination of phase diagrams.[24,25] This can be appreciated by looking at correspondence of points 1 to 4 in the composition profiles [Fig. 4(b)] to these same points in the phase diagram [Fig. 4(a)]. This phase diagram is based upon a recent assessment by Huang and Chang[26] and the recent results from Ootoshi et al.[27]

It can be seen from the composition profiles shown in Fig. 4(b) that a full composition variation (library) of all the single-phase regions between Ni and NiAl was obtained, e.g., 0 to 18 at.% Al (points 0 to 1) for the γ-phase. The composition libraries generated in the diffusion couple, shown in Fig. 4(b), can be used for localized surveys of critical materials properties. For instance, by performance of nanoindentation tests on the diffusion couple using the load- and displacement-sensing "mechanical properties microprobe,"[13–16] the hardness and modulus variation with distance was obtained as shown in Fig. 4(d) which was the combined results of several parallel indentation scans. The hardness and modulus profiles [Fig. 4(d)] can be converted into composition–phase–property data [Fig. 4(e)] since the composition of each location is known from Fig. 4(b). The hardness of the γ-phase increased from approximately 3.3 to 4.5 GPa as the Al concentration increased from 0 to approximately 13 at.%, which was caused by the solution-hardening effect. The further significant increase of hardness in the Al-rich compositions (13 to 18 at.%) of the γ-phase [highlighted in Figs. 4(d) and 4(e)] came from precipitation hardening, where fine γ' particles formed in the γ matrix (when the diffusion couple was cooled from 1204 °C to room temperature) obstructed the movement of dislocations. Such precipitation hardening provides most of the strength for advanced Ni-based superalloys, and it is an important mechanism for structural materials design. Precipitation hardening requires a supersaturation—a decreasing solubility with lowering temperature [e.g., 18 and 13 at.% Al in γ at 1204 and 800 °C respectively, Fig. 4(a)]. Therefore, both phase diagrams and precipitation kinetics information are critical for designing precipitation-hardened alloys.

By cooling of the 1204 °C exposed diffusion couple at different cooling rates and by examining the hardness and microstructures at different locations (compositions) in the diffusion couple, the continuous cooling transformation kinetics of γ' precipitation can be evaluated simultaneously for a range of γ compositions. Alternatively, by quenching of the 1204 °C exposed diffusion couple to ambient temperature (to retain the high-temperature γ-phase), exposure of the couple at lower temperatures (e.g., 800 °C) for different time periods, and then examining the microstructure and hardness at different locations (compositions), the isothermal precipitation kinetics of the γ'-phase can be evaluated

simultaneously for a library of γ compositions. Such precipitation kinetics information would be much more time-consuming and expensive to obtain using the conventional one-alloy-at-a-time approach.

The average elastic modulus of pure Ni evaluated from 33 nanoindentations is 201 ± 22 GPa, which agrees very well with the literature values ranging from 197 to 207 GPa.[28,29] A typical load and displacement curve of the nanoindentation is shown in Fig. 4(f). Both hardness and modulus were evaluated from such a curve without the need of measuring the indentation size.[13–16]

When the 1204 °C exposed Ni–NiAl diffusion couple was cooled from 1204 °C to room temperature in a vacuum furnace, the composition region of the β-phase with 35 to 37 at.% Al had precipitates in the β-phase matrix, as shown in Fig. 5. The precipitates can be γ' (L1$_2$), Ni$_5$Al$_3$ (oC16; space group Cmmm), or the martensitic phase (L1$_0$, P/4mmm).[30,31] EMPA analysis found that the precipitates had an average Al concentration of 27.9 at.%. Thus, they were unlikely to be the martensitic phase—martensitic transformation is composition-invariant—therefore, the martensitic phase composition should be similar to the parent β-phase, i.e., >35 at.% Al. The crystal structure identification of the precipitation phase was made using EBSD, as shown in Fig. 6. The EBSD pattern matched only to that of γ', not Ni$_5$Al$_3$ nor the L1$_0$ martensite. By cooling of the diffusion couple at different cooling rates, continuous cooling transformation kinetics of the β-phase can be measured
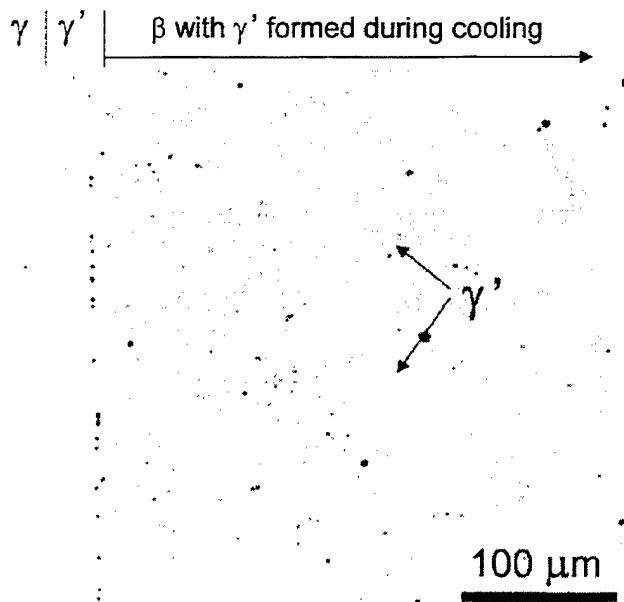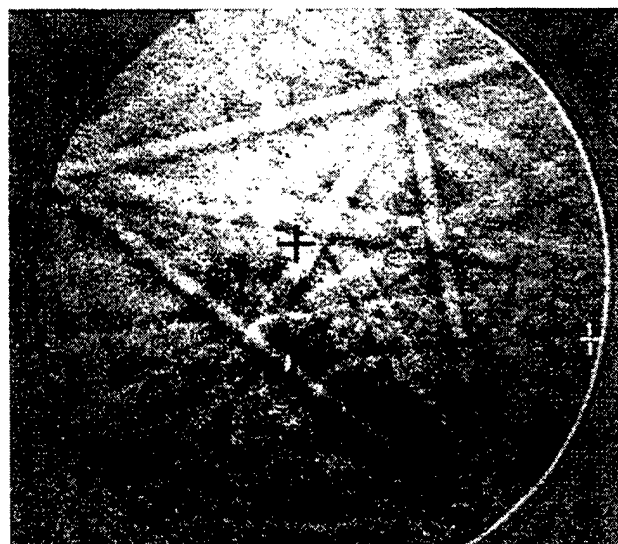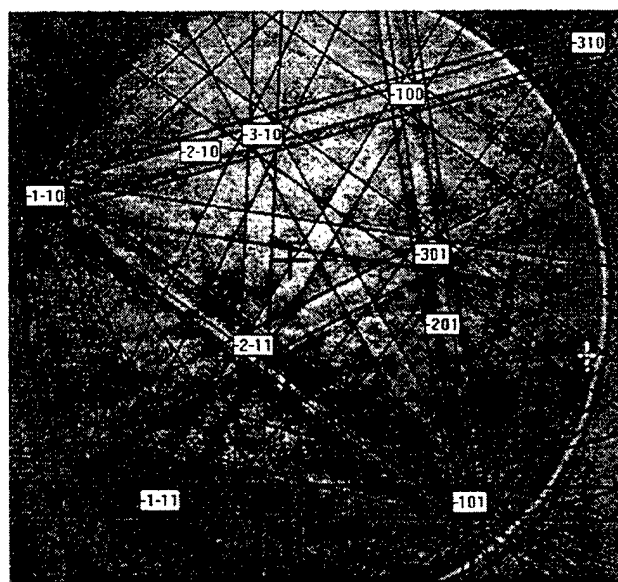

FIG. 5. SEM image showing the γ' precipitates formed in the Al-lean region of the β-phase in the Ni–NiAl diffusion couple during cooling from 1204 °C in a vacuum furnace.
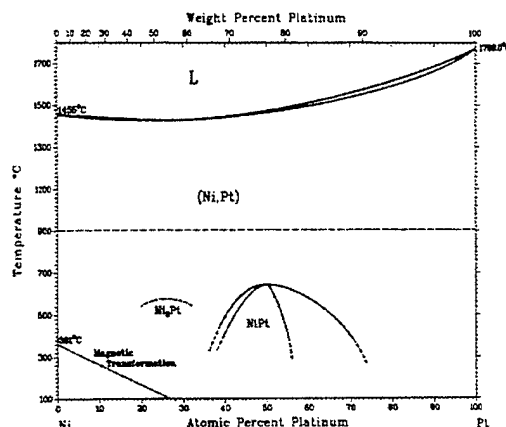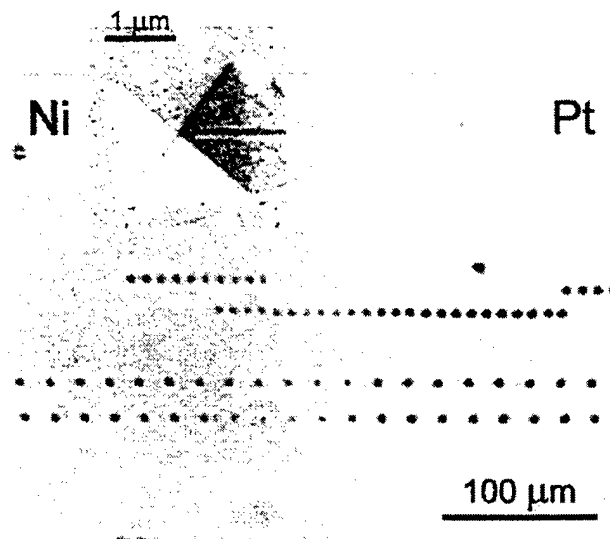
(a)

(a)

(b)

FIG. 7. Application of a Ni–Pt diffusion couple to create a full composition library (from 0 to 100% Pt) for an efficient evaluation of the hardening effect: (a) phase diagram of Ni–Pt; (b) optical micrograph with a high-resolution SEM image as an insert showing the nanoindents on the diffusion couple.

(b)

FIG. 6. EBSD patterns taken from the precipitates shown in Fig. 2: (a) un-indexed pattern; (b) indexed pattern with the γ'-phase crystal structure.

simultaneously for a range of compositions. For instance, by water quench, martensitic transformation may take place in the Al-lean composition regions of the β-phase.[30,31]

The second example is shown in Figs. 7 and 8 for the Ni–Pt binary system. The Ni–Pt phase diagram is shown in Fig. 7(a), indicating that Ni and Pt are completely soluble at temperatures between approximately 650 and approximately 1400 °C.[32] At temperatures <650 °C, there are two ordered phases, Ni_3Pt ($L1_2$) and NiPt ($L1_0$). Nanoindentation tests were performed on a Ni–Pt diffusion couple exposed at 900 °C for 1650 h. The average

elastic modulus of pure Pt based on 33 nanoindentation measurements is 179 ± 16 GPa, which is in excellent agreement with the literature data, 168 to 173 GPa.[28,33] The average hardness of pure Pt is 2.2 ± 0.1 GPa again based on the same 33 measurements. It is clear that the hardness of pure Pt is much lower than that of pure Ni, 3.3 ± 0.3 GPa. Figure 8 shows that the hardness values of concentrated Ni–Pt compositions (e.g., Ni–50 at.% Pt) are much higher than those of pure Ni and pure Pt. To see whether the significant hardening comes from the formation of the ordered phases (Ni_3Pt or NiPt) or the solution-hardening effect, or both, x-ray diffraction analysis was performed using a Siemens GADDS microdiffractometer with a collimated x-ray beam of 0.3-mm diameter. By systematically moving of the beam across
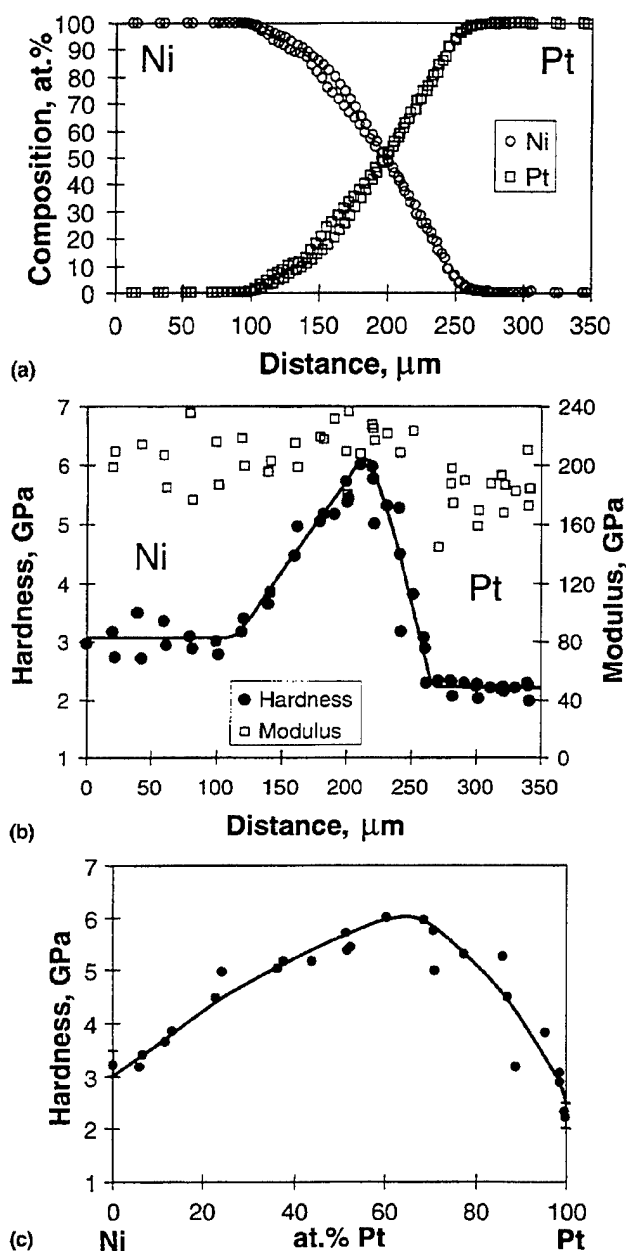
(a)

(b)

(c)

FIG. 8. Evaluation of the solution hardening effect from a Ni–Pt diffusion couple heat-treated at 900 °C for 1650 h: (a) composition profiles from EPMA; (b) the nanoindentation profile; (c) the solution-hardening effect evaluated from both the composition and nanoindentation profiles.

the entire the Ni–Pt diffusion couple and taking the x-ray diffraction patterns (spectra), no $L1_0$ (NiPt) or $L1_2$ (Ni_3Pt) phase was found; i.e., no [001] and [011] reflections were observed. Therefore, the significant increase in hardness for concentrated Ni–Pt alloys is from the solution-hardening effect. For solid solutions, there is a strong correlation between hardness and yield strength (more precisely flow stress); thus, Pt should be a potent

strengthener for the γ-phase. This result is consistent with the observation of Corti et al.[34] that Pt is a strong strengthener for Ni-based superalloys.

The full composition library (from 0 to 100% Pt) generated in the diffusion couple can also be used to study the ordering transformation kinetics in Ni–Pt alloys. For instance, by exposing the diffusion couple at 500 °C, it would be possible to study the ordering transformation kinetics for both the Ni_3Pt and NiPt phases over a wide range of compositions in a similar way as discussed in relation to Figs. 1 and 4.

The results described in Figs. 4 to 8 clearly show that diffusion couples can be used to generate composition libraries for binary alloys for combinatorial surveys of phase, phase equilibria, diffusion coefficients, mechanical properties, composition–phase–property (i.e., hardness and modulus) data, and precipitation kinetics. Similarly, a diffusion triple can be employed for combinatorial surveys of a ternary system as shown in Fig. 9 using the Ni–Mo–Fe system as an example. A Ni–Mo–Fe diffusion triple, Fig. 9(a), was exposed at 1100 °C for 1500 h, during which time all the intermetallic compounds, both binary and ternary, NiMo (δ), Fe_7Mo (μ), and $Fe_{11}Ni_{36}Mo_{53}$ (P-phase[35]), formed by diffusion reactions, Figs. 9(b) and 9(c). By performance of EPMA across the interfaces and at the three-phase junctions, both tie-lines and tie-triangles were obtained to construct the entire isothermal section of the ternary phase diagram, Fig. 9(d). For instance, the left-hand edge of the triple [points 0 to 5 in Fig. 9(b)] was a binary Ni–Mo diffusion couple since Fe could not reach there by diffusion. EPMA analysis along points 0 to 5 gave tie-lines 1–2 and 3–4 in Fig. 9(d). Similarly, points 5 to 12 at the top edge of the triple gave binary Mo–Fe equilibria and points 12 to 14 at the right-hand edge gave the binary Fe–Ni information (Fe and Ni are completely soluble at 1100 °C). Closer to the center of the triple, more interdiffusion of the three elements was achieved; thus, ternary tie-lines were obtained. For instance, EPMA analysis from position X to position Y in Fig. 9(c) gave composition profiles of Fig. 9(e) which show significant diffusion of Fe into the δ- and γ-phases. The local equilibrium compositions at the phase interfaces in Fig. 9(e) gave tie-lines T1 and T2 in Fig. 9(d). At three-phase junctions such as locations 15 and 16 in Fig. 9(b), the respective tie-triangles γ–δ–μ and γ–αFe–μ were obtained. Therefore, only one diffusion triple is needed to survey all the phases and equilibria in the whole isothermal section.[8–11] In this connection, the diffusion triple method is much more efficient in mapping of phase diagrams than traditional equilibrated alloys and diffusion couple methods.[25] For example, the same 1100 °C Ni–Mo–Fe isothermal section of Fig. 9(d) was determined by
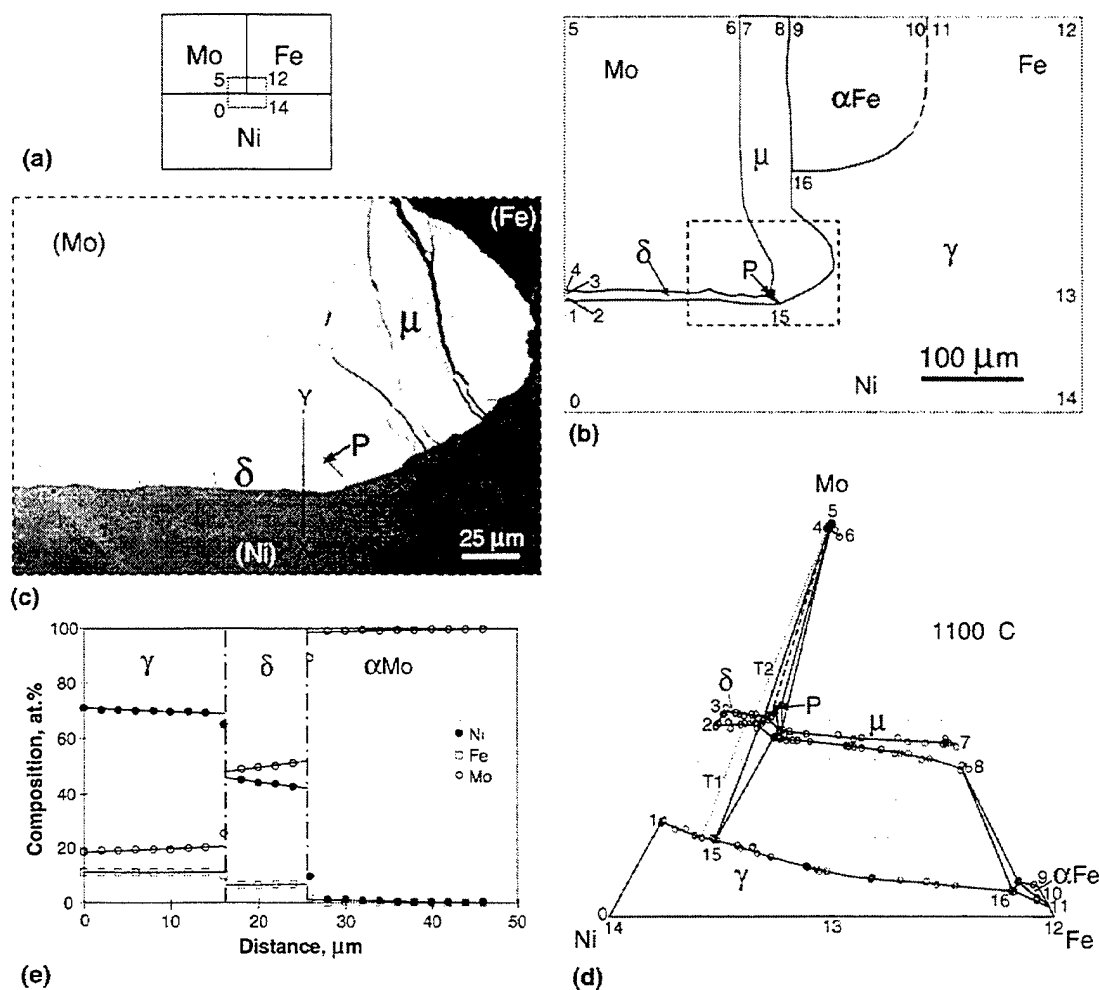
FIG. 9. Application of a diffusion triple to generate full libraries of single-phase compositions of a ternary system for a combinatorial survey of phases, crystal structures, phase equilibria, and properties: (a) diffusion triple of Ni–Mo–Fe; (b) cross-sectional view of the diffusion triple after heat treatment showing phase boundary locations and their correspondence with the phase diagram; (c) backscatter electron image of the trijunction region of the diffusion triple showing the phase distribution; (d) the whole 1100 °C isothermal section of the Ni–Mo–Fe phase diagram (composition scale in atomic percent) obtained from the diffusion triple; (e) EPMA line scan from point X to point Y in (c) showing the composition profiles that were used to evaluate the tie-lines T1 and T2 in (d).

van Loo *et al.* using 23 alloys and 7 diffusion couples.[35] The isothermal section of Fig. 9(d) measured from the single diffusion triple looks identical to that obtained by van Loo *et al.*

Since a diffusion triple can be used to map entire isothermal sections, it can be an effective screening tool for the possible appearance of new intermetallic compounds, especially when assisted with the EBSD technique. Phases that do not belong to the corresponding binary systems can be identified in the diffusion triple using EBSD crystal structure identification. For instance, a ternary compound, the P-phase,[35] was found in the Ni–Mo–Fe triple. The P-phase is orthorhombic (oP56) with a composition of approximately $Fe_{11}Ni_{36}Mo_{53}$.
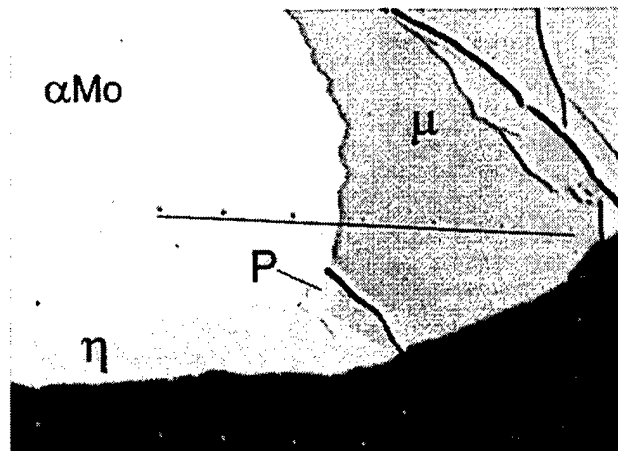
An important feature of a diffusion triple is its ability to generate full libraries of all the single-phase compositions

of a ternary system, as described earlier with reference to Fig. 2. It is clear that points 0–1–15–16–11–12–13–14–0 in Fig. 9(b) correspond to those same points in Fig. 9(d) in composition, and they envelop the entire composition region of the γ-phase. By performance of nanoindentation tests on the diffusion triple, the composition–phase–property relations were obtained for the single-phase compositions of the Ni–Mo–Fe system. Figure 10(a) shows the collected hardness and modulus data of different Fe and Mo concentrations in the entire γ-phase region (enveloped by the above mentioned points) plotted against Mo content only. The degeneration of all the hardness data into a single curve indicates that Fe has little effect on the hardness of the γ-phase, whereas Mo is a potent solution hardener. The Mo addition to the γ-phase has little effect on its modulus. The
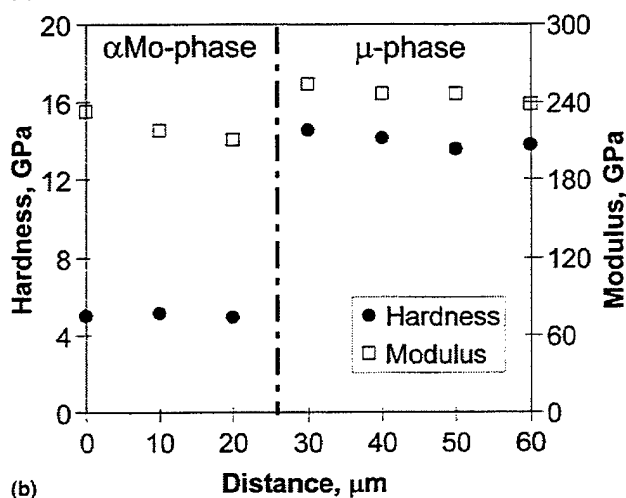
(a)
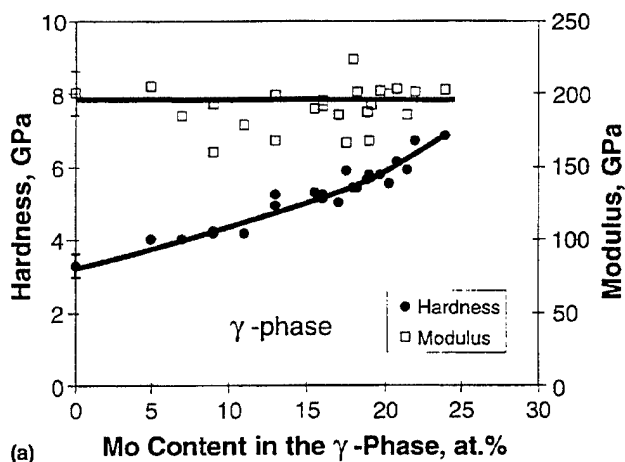
Mo Content in the γ-Phase, at.%

(b)
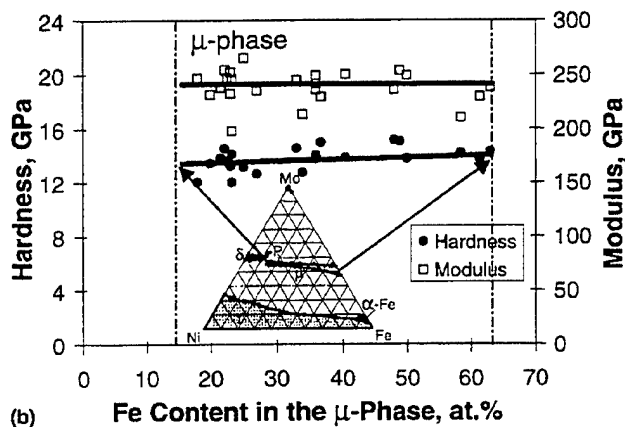
Fe Content in the μ-Phase, at.%

FIG. 10. Variation of hardness and elastic modulus with composition in the (a) γ-phase and (b) μ-phase measured by nanoindentation.

(a)

(b)

Distance, μm

FIG. 11. (a) Nanoindentation scan from α–Mo to μ and (b) the corresponding hardness and elastic modulus data for the respective phases.

average hardness values of the δ and μ phases were 15 and 14 GPa, much higher than those of γ (3.3 to 7 GPa). The elastic moduli of the δ and μ phases were 235 and 238 GPa, respectively, only slightly higher than that of γ (approximately 200 GPa). The hardness and modulus of the δ and μ phases are not strongly composition dependent, as shown in Fig. 10(b) for the μ-phase. Such composition–phase–property relations are very valuable for structural materials design.

A nanoindentation scan from the α–Mo phase to the μ-phase is shown in Fig. 11. The indents on the μ-phase were very small and difficult to see from the SEM micrograph, Fig. 11(a). Fortunately, it is not necessary to measure the size of the indents in the load- and displacement-sensing nanoindentation tests.[13–16] It is clear that the hardness of the μ-phase is much higher than that of the α–Mo phase, Fig. 11(b). The composition of each indentation point was then evaluated by correlating its position to the EPMA line scan positions. The X–Y stage positions of the EPMA scans were recorded so that the composition of each position in the diffusion triple can be estimated. The

composition–position information makes it possible to convert the property (hardness and modulus)–position information into composition–property data shown in Fig. 10 [this is similar to converting Fig. 4(d) into Fig. 4(e) using Fig. 4(b)].

A set of diffusion multiples has been designed and employed for fast and systematic surveys of a quaternary, four related ternary, and six related binary systems at the same time, as shown in Fig. 12(a) using Fe–Cr–Mo–Ni as an example. At the center of the diffusion multiples are three diffusion quadruples[17] that are used to survey the quaternary system. The elements Fe and Mo as well as Cr and Ni at the center of the left-hand side multiple in Fig. 12(a) have only line contact, thus relatively less interdiffusion. By alternation of the arrangements (there are only three combinations), three diffusion quadruples can be employed to survey wide ranges of composition in the quaternary isothermal tetrahedron, Fig. 12(b). The four related ternary systems are surveyed by the triples
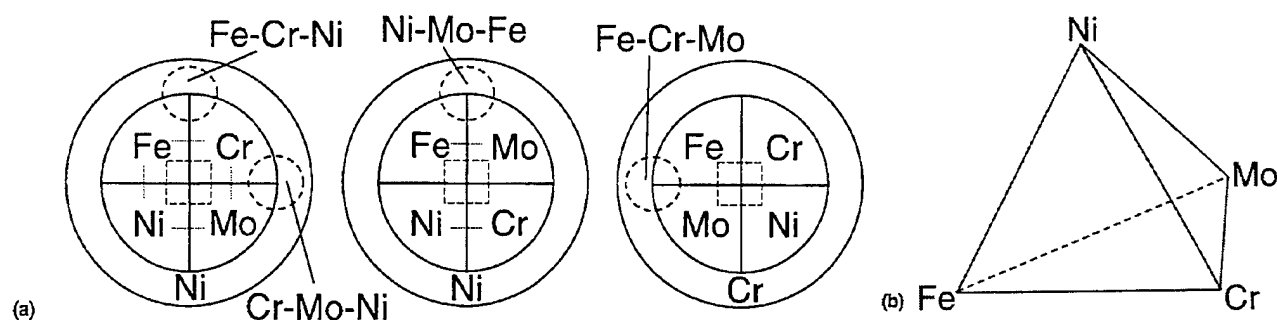
FIG. 12. New diffusion multiples for fast and systematic search of new materials in multicomponent systems. Three diffusion multiples can be used to map a quaternary phase diagram (and the related 6 binaries and 4 ternaries) and to generate large composition libraries of the binary, ternary and quaternary systems: (a) geometry of the diffusion multiples; (b) quaternary isothermal tetrahedron consisting of six binary system, four ternary isothermal sections, and the quaternary information inside the tetrahedron.

(dashed circles) at the rim of the diffusion multiples, Fig. 12(a). Thus, three diffusion multiples can create full composition libraries of all the single-phase regions of the ternaries and wide libraries of composition of the quaternary. In fact, all the results shown in Figs. 9 to 11 were obtained from a Ni–Mo–Fe triple at the rim of a diffusion multiple similar to those shown in Fig. 12(a). Three sets of diffusion multiples similar to those shown in Fig. 12(a) have been made for the Nb–Ti–Cr–Si system. Extremely large amounts of information have been obtained for this quaternary and the related ternaries and binaries. The results will be published separately.

With extension beyond the basic ternary and quaternary systems, one or more multicomponent alloys can be used as members of the diffusion multiples for combinatorial surveys of multicomponent systems, especially studying the effect of compositional modifications on properties of complex alloys. An example is shown in Fig. 13 for the Ni-based superalloy IN706. The result shown in Figs. 13(b) and 13(c) was obtained from the IN706–Fe–Mo diffusion triple [Fig. 13(a)], which was intended to evaluate the possibility of further strengthening IN706 by adding Mo. Figures 13(b) and 13(c) show a multicomponent phase diagram of the system. (The compositions of all the other elements have been obtained but not plotted for simplicity.) The lower left corner of the phase diagram represents a hypothetical composition where the 38 at.% Fe in IN706 is replaced by 38 at.% Ni (i.e., a hypothetical IN706 composition without Fe) so that the diagram can be plotted from 0 at.% Fe to 100 at.% Fe in the horizontal axis. The results showed that no Mo could be directly added to IN706 without forming the brittle μ-phase. Only when the Cr content is reduced to approximately 10 at.% and the Fe content increased to approximately 60 at.%, will 1 at.% Mo addition become possible (at 1100 °C). The maximum Mo addition is 2 at.%, and further reduction of Cr and increase in Fe do not change the Mo solubility in the γ-phase, Fig. 13(b). It is interesting to note that the Mo solubility in the γ-phase was high in the Ni–Fe–Mo

ternary system [Fig. 9(d)], but it reduced significantly in the γ-phase of IN706 due to the presence of Cr, Ti, etc. (IN706 is a Ni–Fe-based alloy). The Cr content in the phases is superimposed in Fig. 13(c) to show the high solubility of Cr in both γ and μ. This kind of multicomponent phase diagram, which has never been determined before, is very useful for alloy design by providing direct information for composition modification and selection in multicomponent alloys. It can also be used to test and improve thermodynamic modeling parameters for computational design of materials.[36–38] In addition, precipitation kinetics and composition–property correlations can be simultaneously evaluated from the composition libraries created in the diffusion multiples in a similar way as illustrated in the Ni–NiAl and Ni–Pt diffusion couples and the Ni–Mo–Fe diffusion triple.

IV. DISCUSSION

Useful tensile strength of structural materials is a combination of three properties: plastic hardness (i.e., resistance to yielding); elastic stiffness (i.e., elastic modulus); toughness (i.e., resistance to crack failure).[39] Recent advancement in nanoindentation tests enables rapid evaluation of hardness and modulus and even fracture toughness[40] of brittle phases from small areas/phases (e.g., approximately 10 μm). As more understanding is achieved on the elastoplastic behavior of nanoindentation, it is even possible to extract yield strength of materials from the load and displacement curves.[41,42] Coupled with the composition libraries generated in diffusion couples and multiples, it is now possible to evaluate these critical materials properties much more efficiently. For instance, by combination of the solution-hardening effect from the Ni–NiAl and Ni–Pt diffusion couples and the Ni–Mo–Fe diffusion triple, the solution–hardening potency of various elements in the γ-phase can be compared and assessed, as shown in Fig. 14. As more data are accumulated, a database of solution-hardening effects can be built. Such a database,

(a)

(b)

FIG. 14. Solution-hardening effect of several elements in Ni evaluated from nanoindentation tests on diffusion couples and multiples. There is a strong correlation between hardness and yield strength (more precisely flow strength). Thus, the information also represents the potency of various elements in solution strengthening.
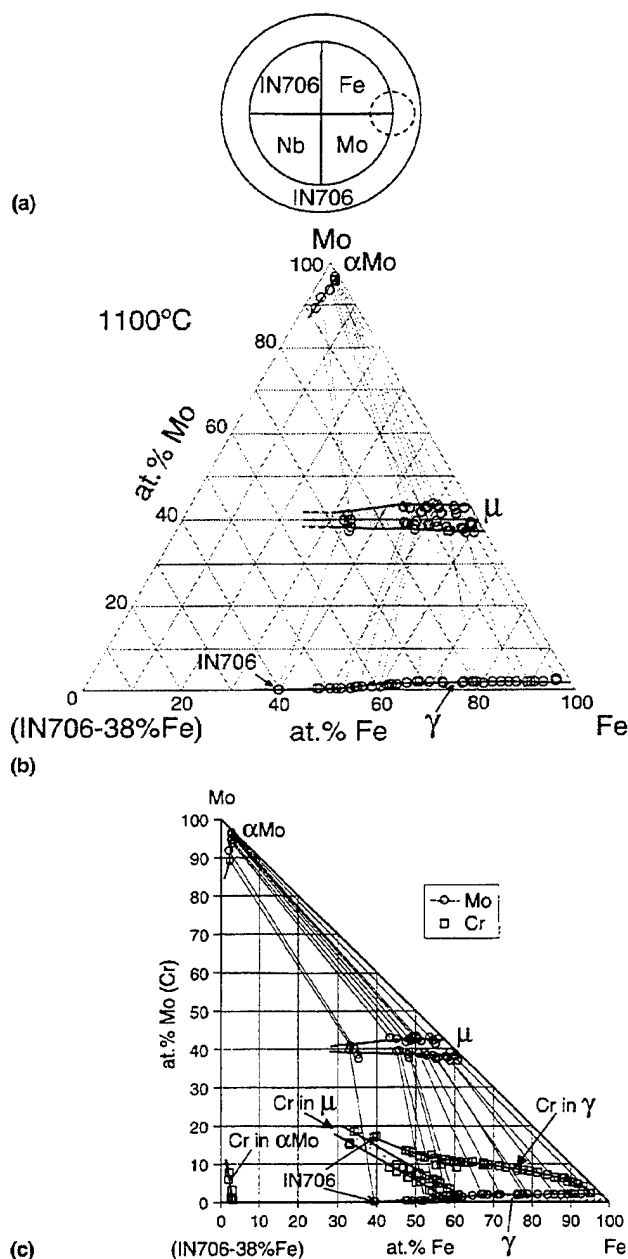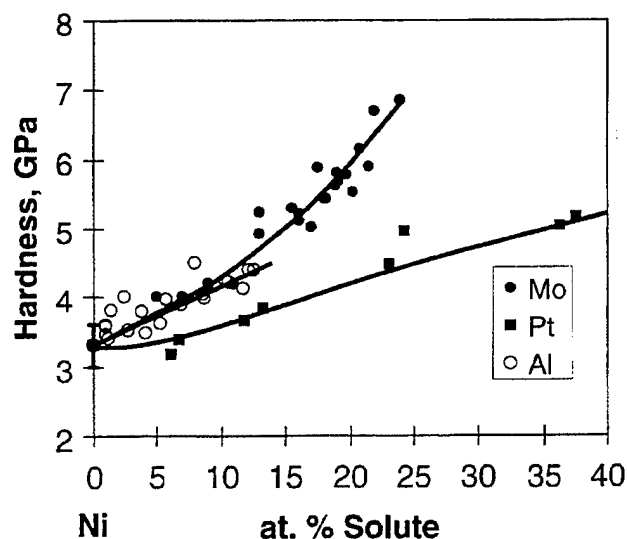
(c)

FIG. 13. Direct application of diffusion multiples to generate composition libraries in multicomponent systems by using a multicomponent alloy as members of the diffusion multiples: (a) a diffusion multiple with IN706 as a member; (b) a multicomponent phase diagram projected onto the (IN706–38% Fe)–Mo–Fe triangle; (c) the same phase diagram as (b) but with Cr concentration superimposed.

which is not readily available and would be very time-consuming and expensive to obtain using the conventional one-alloy-at-a-time approach, will be very valuable for materials design by predicting the strengthening effect from compositions and by providing guidance for elemental selection.

It may be possible to evaluate the fracture toughness of intermetallic phases formed in diffusion couples and

multiples using a cube-corner nanoindenter. Pharr et al.[40] found that the cube-corner indenter greatly reduces the load required to generate cracks in brittle phases as compared to the regular Vickers indenter. If the indentation-generated cracks are within the dimensions of the individual intermetallic phase formed in diffusion couples and multiples, then the fracture toughness can be evaluated using the simple equation developed by Lawn et al.[43,44] This kind of combinatorial survey has its advantage since sometimes it takes quite some effort to synthesize macroscale samples of these brittle intermetallic phases through casting or powder metallurgy routes. The intermetallic compounds formed relatively easily through interdiffusion in the diffusion couples and multiples. Most of the time, the intermetallic phases formed are dense and convenient for nanoscale property evaluation. Such an evaluation of fracture toughness can accelerate the exploration for structural and functional intermetallics with better properties.

As described earlier, the average elastic modulus values of Ni and Pt evaluated from nanoindentation tests agreed very well with previous literature data. The value for pure Mo phase is approximately 291 ± 13 GPa, which is quite different from the literature data, 336 GPa.[28,29] Use of a spherical indenter may help, reducing the variation.[45–47] In addition, by superimposing a small oscillation during nanoindentation loading, it is possible to extract elastic modulus data more reliably from the nanoindentation experiments.[13] Hay showed that the modulus of Mo extracted from nanoindentation using this method agreed very well with the literature data.[48] For

most materials, the hardness and modulus could be measured with an accuracy of about ±10% for materials that do not exhibit significant pile-up.[13,40,41]

The size of the indents produced by nanoindentation at a 10 mN load is <1.5 μm for all the phases tested in the present paper. The intermetallic compounds and solid solution phases formed by thermal interdiffusion in the diffusion multiples range in size from several microns to hundreds of microns in width (and several millimeters in thickness—the thickness of the bulk sample), depending on the heat treatment temperature and time, thus allowing at least several nanoindentation measurements to be made in each phase (in each scan). New nanoindentation testers allow the use of a much lighter load (e.g., 0.5 mN), thus producing significantly smaller indents on the phases. The use of a very light load will allow reliable hardness and modulus measurements for even the very narrow phases formed in diffusion multiples. Usually the spacing (step) between the indents should at least be >5 times their size to avoid any potential interaction between them.

For materials (e.g., low melting metals) exhibiting creep at ambient temperature, it is possible to extract creep resistance data from the time-dependent penetration depth.[49,50] This is usually done by loading an indenter at a constant rate to a peak load and holding for an extended period of time. Room-temperature creep data can be obtained especially when the thermal drift of the nanoindentation tester is calibrated. The use of nanoindentation in evaluating the creep resistance at elevated temperatures is challenged by the inherent difficulties in measuring small displacements at elevated temperatures.

Some limitations of the new diffusion multiple approach include the following: (i) It cannot generate the liquid–solid phase equilibrium information for solidification and casting modeling. (ii) It cannot evaluate defect formation propensity during synthesis (such as solidification and forging). (iii) To avoid melting, the highest temperature for diffusion heat treatment is limited to the lowest liquidus temperature of the multicomponent system which may not be known *a priori*. When the liquidus is low, it may take a long time to promote sufficient interdiffusion for a reliable evaluation of properties. To determine phase diagrams at relatively low temperatures, it may be advantageous to use the thin-film combinatorial approaches, since much less time is required to form a homogenous composition across the thin-film thickness, especially when the substrate is heated to the desired temperatures (care needs to be exercised to avoid possible reaction with the substrate). Kennedy *et al.*[51] demonstrated the determination of the Fe–Cr–Ni phase diagram at 760 °C using a continuous thin film composition library generated using three electron-beam physical vapor deposition (EB-PVD) pools. The substrate was

heated to 760 °C in this case, and all the phases formed were equilibrium phases. The measured phase diagram agreed well with that determined from equilibrated alloys.[51]

Very recently a melting and floating zone combinatorial approach was developed by Cohen-Adad *et al.*[52–54] This technique can be used to generate continuous composition libraries in binary and quasi-binary systems and can be used to evaluate solid–liquid equilibria. It can also be used to evaluate solidification processes due to the possible control of the solidification rate.

The diffusion multiple approach enables efficient surveys of critical materials properties such as phase diagrams, precipitation kinetics, hardness, modulus, and diffusion coefficients. Some of these properties such as precipitation kinetics and diffusion coefficients cannot be evaluated using the thin-film approaches since they are usually very different in bulk samples than in thin films due to the thickness and surface effects. Hardness and modulus can be evaluated from thin films when the substrate effect is taken into account or the thicknesses of the films are great enough to remove the substrate effect.[55] However, the usually small grain size of thin-film samples may produce additional (microstructural) hardening to confound the solution-hardening and precipitation-hardening effects. In addition, the intermetallic compounds formed in diffusion multiples are more often equilibrium phases, whereas those in thin films are quite often metastable phases, and it would take some effort to promote equilibrium phase formation by varying the deposition and heat treatment temperatures and sequences.[6] This is especially true when the substrate is not heated.

The composition libraries generated in bulk diffusion multiples also offer potential for efficient surveys of other mechanical, physical, and chemical properties. For instance, the thermal emf probe used by Westbrook *et al.*[56] may be used to evaluate emf variation with composition and phases. The emf data will provide trends for the thermal and electrical conductivity variation with composition. Some of the screening tools[1,4,6] used for thin-film approaches may also be used to survey properties from the diffusion multiples.

V. SUMMARY

The results of this work showed that large multicomponent composition libraries can be generated in bulk diffusion multiples through high-temperature thermal diffusion. The coupling of diffusion multiples and microscale composition, structure, and property measurements constitutes a powerful tool for structural materials research and development. This technique can be used to efficiently

(1) search for novel compounds in multicomponent systems using EPMA for composition evaluation and EBSD for crystal structure identifications,

(2) map composition–structure–property data (such as solution hardening effect) using EPMA and nanoindentation,

(3) evaluate diffusion coefficients from EPMA composition profiles,

(4) survey precipitation kinetics by cooling high-temperature-exposed diffusion multiples at different rates or heat-treating at lower temperatures for different periods of time, and

(5) map phase diagrams and design multicomponent (>4) alloys through compositional modifications by using one or more complex alloys as members of diffusion multiples to generate multicomponent composition libraries.

This work paves the way for efficient surveys of other materials properties by taking advantage of the composition libraries generated in diffusion multiples.

ACKNOWLEDGMENTS

REFERENCES

1. X-D. Xiang, X. Sun, G. Briceno, Y. Lou, K.A. Wang, H. Chang, W.G. Wallace-Freedman, S.W. Chen, and P.G. Schultz, Science 268, 1738 (1995).
2. G. Briceno, H. Chang, X. Sun, P.G. Schultz, and X-D. Xiang, Science 270, 273 (1995).
3. E. Danielson, M. Devenney, D.M. Giaquinta, J.H. Golden, R.C. Haushalter, E.W. McFarland, D.M. Poojary, C.M. Reaves, W.H. Weinberg, and X.D. Wu, Science 279, 837 (1997).
4. R.B. van Dover, L.F. Schneemeyer, and R.M. Fleming, Nature (London) 392, 162 (1998).
5. J.J. Hanak, J. Mater. Sci. 5, 564 (1970).
6. X-D. Xiang, Annu. Rev. Mater. Sci. 29, 149 (1999).
7. J-C. Zhao, Adv. Eng. Mater. 3, 143 (2001).
8. M. Hasebe and T. Nishizawa, in Applications of Phase Diagrams in Metallurgy and Ceramics, edited by G.C. Carter (NBS Special Publ. No. 496, Gaithersburg, MD, 1978), Vol. 2, p. 911.
9. Z. Jin, Scand. J. Metall. 10, 279 (1981).
10. J-C. Zhao and Z. Jin, Z. Metallkde. 81, 247 (1990).
11. Z. Jin and C. Qiu, Metall. Mater. Trans. 24A, 2137 (1993).
12. J.I. Goldstein, Scanning Electron Microscopy and X-Ray Microanalysis (Plenum Press, New York, 1992).
13. W.C. Oliver and G.M. Pharr, J. Mater. Res. 7, 1564 (1992).
14. M.F. Doerner and W.D. Nix, J. Mater. Res. 1, 601 (1986).
15. J.B. Pethica, R. Hutchings, and W.C. Oliver, Philos. Mag. 48A, 593 (1983).
16. G.M. Pharr, W.C. Oliver, and F.R. Brotzen, J. Mater. Res. 7, 613 (1992).
17. J-C. Zhao, Z. Jin, and P. Huang, Scr. Metall. 22, 1825 (1988).
18. C.J. Harland, P. Akhter, and A. Bewick, J. Phys. E 14, 175 (1981).
19. Electron Backscatter Diffraction in Materials Science, edited by A.J. Schwartz, M. Kumar, and B.L. Adams (Kluwer Academic/Plenum Publishers, New York, 2000).
20. J. Kim, J-C. Zhao, and M.A. Dayananda (unpublished).
21. M.M.P. Janssen, Metall. Trans. 4, 1623 (1973).
22. S. Shanker and L.L. Siegle, Metall. Trans. 9A, 1467 (1978).
23. T. Yamamoto, T. Takashima, and K. Nishida, J. Jpn. Inst. Met. 44, 294 (1980).
24. A.D. Romig, Bull. Alloy Phase Diagr. 8, 308 (1987).
25. F.J.J. van Loo, Prog. Solid State Chem. 20, 47 (1990).
26. W. Huang and Y.A. Chang, Intermetallics 6, 487 (1998).
27. Y. Ootoshi, F. Fujiwara, Z. Horita, and M. Nemoto, Mater. Trans. JIM 39, 225 (1998).
28. A. Buch, Z. Metallkde. 90, 744 (1999).
29. Metals Handbooks, 9th ed. (ASM International, Materials Park, OH, 1979), Vol. 2, p. 709.
30. S. Rosen and J.A. Goebel, Trans. TMS-AIME 242, 722 (1968).
31. R.D. Noebe, A. Misra, and R. Gibala, Iron Steel Inst. Jpn. Int. 31, 1172 (1991).
32. P. Nash and M.F. Singleton, Bull. Alloy Phase Diagr. 10, 258 (1989).
33. A.M. James and M.P. Lord, Macmillan's Chemical and Physical Data (Macmillan, London, U.K., 1992).
34. C.W. Corti, D.R. Coupland, and G.L. Selman, Platinum Met. Rev. 24, 2 (1980).
35. F.J.J. van Loo, G.F. Bastin, J.W.Q.A. Vrolijk, and J.J.M. Hendriks, J. Less-Common Met. 72, 225 (1980).
36. G.B. Olson, Science 277, 1237 (1997).
37. N. Saunders and A.P. Miodownik, CALPHAD (Elsevier Science Inc., New York, 1998), Chapter 10.
38. P.J. Spencer, G. Eriksson, and A. von Richthofen, in Thermodynamic Modeling and Materials Data Engineering, edited by J-P. Caliste, A. Truyol, and J.H. Westbrook (Springer, Berlin, Germany, 1998), p. 169.
39. A. Cottrell, MRS Bull. 25(2), 43 (2000).
40. G.M. Pharr, Mater. Sci. Eng. A 253, 51 (1998).
41. T.A. Venkatesh, K.J. van Vliet, A.E. Giannakopoulos, and S. Suresh, Scr. Mater. 42, 833 (2000).
42. A.E. Giannakopoulos and S. Suresh, Scr. Mater. 40, 1191 (1999).
43. B.R. Lawn, A.G. Evans, and D.B. Marshall, J. Am. Ceram. Soc. 63, 574 (1980).
44. G.R. Anstis, P. Chantikul, B.R. Lawn, and D.B. Marshall, J. Am. Ceram. Soc. 64, 533 (1981).
45. J.S. Field and M.V. Swain, J. Mater. Res. 8, 297 (1993).
46. J.S. Field and M.V. Swain, J. Mater. Res. 10, 101 (1995).
47. A.C. Fischer-Cripps, J. Mater. Sci. 32, 727 (1995).
48. J.L. Hay (personal communication, Oct 2001).
49. B.N. Lucas and W.C. Oliver, Metall. Mater. Trans. 30A, 601 (1999).
50. J.L. Hay and G.M. Pharr, in ASM Handbook (ASM International, Materials Park, OH, 2000), Vol. 8, p. 232.
51. K. Kennedy, T. Stefansky, G. Davy, V.F. Zackay, and E.R. Parker, J. Appl. Phys. 36, 3808 (1965).
52. M. Th. Cohen-Adad, M. Gharbi, C. Goutaudier, and R. Cohen-Adad, J. Alloys Compd. 289, 185 (1999).
53. M. Th. Cohen-Adad, L. Laversenne, M. Gharbi, C. Goutaudier, G. Boulon, and R. Cohen-Adad, J. Phase Equilib. (2001, in press).
54. L. Laversenne, Y. Guyot, C. Goutaudier, M. Th. Cohen-Adad, and G. Boulon, Opt. Mater. (2001, in press).
55. T.Y. Tsui and G.M. Pharr, J. Mater. Res. 14, 292 (1999).
56. J.H. Westbrook, A.U. Seybolt, and A.J. Peat, J. Electrochem. Soc. 111, 888 (1964).

Determination of Nb-Hf-Si Phase Equilibria

J.-C. Zhao, B.P. Bewlay, and M.R. Jackson

Determination of Nb–Hf–Si phase equilibria

J.-C. Zhao*, B.P. Bewlay, M.R. Jackson

General Electric Company, Corporate Research and Development, PO Box 8, Schenectady, NY 12301, USA

Abstract

Phase equilibria of Nb–Hf–Si at 1500 °C have been investigated for the metal-rich end of the ternary phase diagram using scanning electron microscopy, electron probe microanalysis, and electron backscatter diffraction analysis. An isothermal section at 1500 °C was constructed for this ternary system based on experimental data from 11 alloys heat treated at 1500 °C for 100 h. Phase equilibria between the following silicides, Nb(Hf)$_5$Si$_3$, Hf(Nb)$_5$Si$_3$, Nb(Hf)$_3$Si, Hf(Nb)$_2$Si, Hf(Nb)$_3$Si$_2$, Hf(Nb)$_5$Si$_4$, Hf(Nb)Si, Nb(Hf)Si$_2$, and two metal-rich solid solutions, β(Nb,Hf,Si) and α(Hf,Nb,Si) are described. © 2001 Elsevier Science Ltd. All rights reserved.

Keywords: A. Composites; B. Phase diagram; D. Microstructure; G. Aero-engine components

1. Introduction

Niobium silicide based in-situ composites are potential candidates for turbine airfoil materials in advanced aircraft engines [1–4]. Phase stability in these composites is required to define the optimum compositions and microstructures for property improvements and high temperature stability. This work defines phase equilibria in the binary and ternary systems [5–9] that are required to understand phase stability in the multicomponent composites. Hf has been added to improve oxidation resistance and strength [2,10]. However, there is presently incomplete knowledge of the Hf–Si binary system and there is little existing information on the Nb–Hf–Si ternary system. In this regard, previous work has been conducted to investigate the stability of the Hf–Si binary system [8,9] and the liquid-solid phase equilibria of the Nb–Hf–Si system using directionally solidified alloys [7]. This paper reports the isothermal section of the Nb–Hf–Si system at 1500 °C. This is required to define phase stability of the composites during service. This temperature was selected because it is below the eutectoid decomposition temperature of Nb$_3$Si, but high enough for fast decomposition kinetics. The phase

equilibria at 1500 °C are likely to be very similar to those at the potential service temperature, 1200–1400 °C.

A schematic three-dimensional (3-D) projection of the metal-rich region of the Nb–Hf–Si phase diagram (all compositions are in at.% throughout this paper) is shown in Fig. 1. The binary Nb–Hf system is based on an assessment by Fernandez-Guillermet [11]. The Nb–Si system is based on the assessments of Schlesinger et al. [12] and Liang and Chang [13] with the eutectoid temperature being adjusted to ∼1700 °C based on the result reported by Mendiratta and Dimiduk [14]. The L→ bcc(Nb) + Nb$_3$Si eutectic is adjusted to 1880 °C and 18.2 at.% Si to reflect the temperature and composition obtained by Bewlay et al. [15] on directionally solidified (DS) Nb–Si alloys. The Hf–Si binary is based on a recent assessment [9]. Experimental results supporting the Nb–Hf–Si ternary phase diagram will be presented in the present article.

A total of 10 phases are discussed in this paper. Their crystal structures are listed in Table 1 [16,17]. The Nb$_3$Si with Hf in solid solution is referred to as Nb(Hf)$_3$Si; the Nb$_5$Si$_3$ with Hf in solid solution, Nb(Hf)$_5$Si$_3$; the NbSi$_2$ with Hf in solid solution, Nb(Hf)Si$_2$; the HfSi with Nb in solid solution, Hf(Nb)Si; the Hf$_5$Si$_4$ with Nb in solid solution, Hf(Nb)$_5$Si$_4$; the Hf$_3$Si$_2$ with Nb in solid solution, Hf(Nb)$_3$Si$_2$; the Hf$_5$Si$_3$ with Nb in solid solution, Hf(Nb)$_5$Si$_3$; the Hf$_2$Si with Nb in solid solution, Hf(Nb)$_2$Si. None of these silicides is isomorphous. In addition, there were two Nb–Hf solid solutions

---

* Corresponding author. Tel.: +1-518-387-4103; fax: +1-518-387-6232.

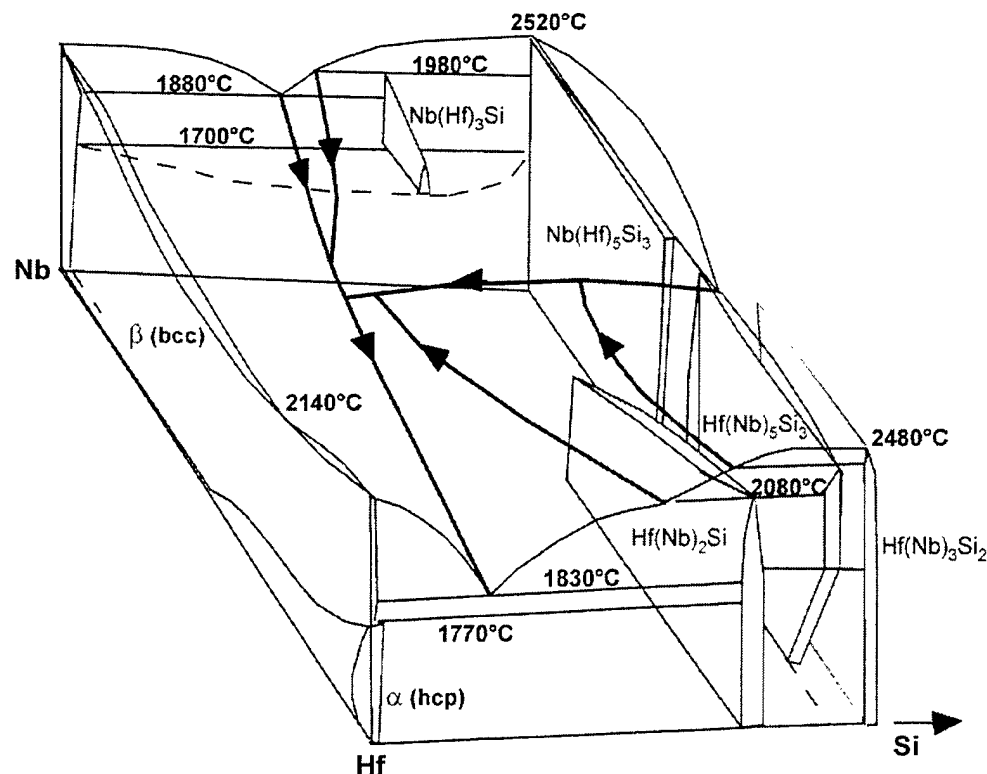*E-mail address:* zhaojc@crd.ge.com (J.-C. Zhao).

Fig. 1. Schematic 3-D projection phase diagram of the metal-rich end of the Nb–Hf–Si ternary system.

Table 1
Crystal structures of the phases observed in the Nb–Hf–Si ternary system together with the lattice parameters are for binary compounds and solid-solution phases

Phase	Prototype	Space group	Lattice parameters (nm)	Ref.
Nb(Hf)$_3$Si	PTi$_3$	P4$_2$/n	$a = 1.0224$, $c = 0.5189$	[16]
Nb(Hf)$_5$Si$_3$	Cr$_5$B$_3$	I4/mcm	$a = 0.6570$, $c = 1.1884$	[16]
Nb(Hf)Si$_2$	CrSi$_2$	P6$_4$22	$a = 0.4794$, $c = 0.6589$	[16]
Hf(Nb)Si	FeB	Pnma	$a = 0.6889$, $b = 0.3772$, $c = 0.5223$	[16,17]
Hf(Nb)$_5$Si$_4$	Zr$_5$Si$_4$	P4$_1$2$_1$2	$a = 0.7039$, $c = 1.283$	[16,17]
Hf(Nb)$_3$Si$_2$	U$_3$Si$_2$	P4/mbm	$a = 0.6988$, $c = 0.3675$	[16,17]
Hf(Nb)$_5$Si$_3$	Mn$_5$Si$_3$	P6$_3$/mcm	$a = 0.7844$, $c = 0.5492$	[16,17]
Hf(Nb)$_2$Si	Al$_2$Cu	I4/mcm	$a = 0.6553$, $c = 0.5186$	[16,17]
β(Nb,Hf,Si)	W	Im$\bar{3}$m	$a = 0.33007$ to 0.3610	[16]
α(Hf,Nb,Si)	Mg	P6$_3$/mmc	$a = 0.31946$, $c = 0.5058$	[16]

containing small amounts of Si for which the hcp phase is given the prefix α and the bcc phase is given the prefix β.

The aim of the present paper is to describe the 1500 °C isothermal section of the metal-rich end of the Nb–Hf–Si phase diagram.

2. Experimental procedures

The samples were prepared using either cold crucible directional solidification [2,18] after triple melting the starting charges from high purity elements (> 99.99%),

or induction skull melting (ISM). The DS procedure has been described in more detail previously [18]. The as-cast microstructures of the corresponding alloys have been described in detail elsewhere [7]. The sum of the concentrations of the interstitials (O, N, and C) of the starting elements was less than 80 wt. ppm. Table 2 shows the range of nominal compositions that was investigated. Samples for heat treatment were wrapped in Nb foil and heat treated at 1500 °C for 100 h in a vacuum ($< 10^{-5}$ Torr) furnace. Several samples still have not reached full equilibrium (i.e. decomposition towards equilibrium is not yet complete) after the 1500 °C/100 h heat treatment,

Table 2
Compositions and constituent phases of the alloys investigated. (The phases shown in bold are equilibrium phases for the alloys)

Composition	Phases in as-DS condition	Phases after 1500 °C/100 h heat treatment
Nb–15%Hf–16%Si Nb–10%Hf–16%Si	Primary β(Nb,Hf,Si) dendrites with Nb(Hf)$_3$Si–β(Nb,Hf,Si) eutectic	**β(Nb,Hf,Si), Nb(Hf)$_5$Si$_3$, Hf(Nb)$_2$Si**, and Hf(Nb)$_5$Si$_3$[a]
Nb–5%Hf–19%Si Nb–10%Hf–18.5%Si	Primary Nb(Hf)$_3$Si with Nb(Hf)$_3$Si–β(Nb,Hf,Si) eutectic	**β(Nb,Hf,Si) and Nb(Hf)$_5$Si$_3$**
Nb–10%Hf–25%Si	Primary Nb(Hf)$_5$Si$_3$, peritectic Nb(Hf)$_3$Si, Nb(Hf)$_3$Si–β(Nb,Hf,Si) eutectic	**β(Nb,Hf,Si), Nb(Hf)$_5$Si$_3$**, and Hf(Nb)$_5$Si$_3$[a]
Nb–30%Hf–25%Si	Primary Hf(Nb)$_5$Si$_3$, peritectic Hf(Nb)$_2$Si, Hf(Nb)$_2$Si–β(Nb,Hf,Si) eutectic	**Hf(Nb)$_2$Si and β(Nb,Hf,Si)**, and α(Nb,Hf,Si)[a]
Nb–60%Hf–25%Si Nb–40%Hf–30%Si	Primary Hf(Nb)$_2$Si with Hf(Nb)$_2$Si–β(Nb,Hf,Si) eutectic	**Hf(Nb)$_2$Si and β(Nb,Hf,Si)**, and α(Nb,Hf,Si)[a]
Nb–80%Hf–14%Si Nb–73%Hf–17%Si	Primary Hf(Nb)$_2$Si, Hf(Nb)$_2$Si–β(Nb,Hf,Si) eutectic; β→β + α	**Hf(Nb)$_2$Si and β(Nb,Hf,Si)**; β→β + α
Nb–80%Hf–5%Si	Primary β(Nb,Hf,Si) with Hf(Nb)$_2$Si–β(Nb,Hf,Si) eutectic	**Hf(Nb)$_2$Si and β(Nb,Hf,Si)**; β→β + α
Nb–90Hf–5Si	Induction skull melted	**Hf(Nb)$_2$Si, β(Nb,Hf,Si)**, and α(Nb,Hf,Si); β→β + α
Nb–50Hf–37.5Si	Primary Hf(Nb)$_5$Si$_3$, peritectic Hf(Nb)$_2$Si, and eutectic Hf(Nb)$_2$Si and β(Nb,Hf,Si)	Inhomogeneous sample. First area: **Hf(Nb)Si** + Hf(Nb)$_5$Si$_4$ + Nb(Hf)Si$_2$; the second area: **β(Nb,Hf,Si)** + **Hf(Nb)$_2$Si**
Nb–55Hf–37.5Si	Induction skull melted	Single phase **Hf(Nb)$_5$Si$_3$**. Small amounts of Hf(Nb)$_3$Si$_2$, Hf(Nb)$_2$Si and β(Nb,Hf,Si) due to inhomogeneity

[a] Formed due to inhomogeneity in the as-DS structure.

thus the phase diagram information reported in this paper is often inferred from local equilibrium at small areas and at phase interfaces.

All of the samples were examined using scanning electron microscopy (SEM) backscatter electron (BSE) imaging and energy dispersive spectrometry (EDS). Phase compositions were measured on selected samples using electron probe microanalysis (EPMA) which was performed on a JEOL 733 microprobe operating at 15 kV, 20 nA, and ~1 µm beam diameter (Japan Electron Optics Ltd., Tokyo). Pure Nb, pure Hf and stoichiometric Hf$_2$Si were used as standards for Nb, Hf and Si, respectively. There is indigenous Zr in essentially all commercially available Hf. The Zr content in the cast alloys was estimated at ≤2 at.%. Zr analysis was performed along with the other three elements and the Zr concentration in all the phases was less than ~3 at.%. In consideration of the similarity of Zr and Hf—which can be appreciated by the similarity of the Hf-Si and Zr-Si phase diagrams [9,19], Zr concentration was added to Hf concentration for each EPMA measurement. Some of the phases analyzed using EPMA were very small, effort was made to analyze phases that were larger than 3 µm. Compositions of the phases smaller than 3 µm were not used to construct the phase diagram.

Phase identification of selected compositions was also performed using the electron backscatter diffraction (EBSD) technique in SEM [20,21]. This technique allows easy selection of microstructural features using BSE imaging for rapid diffraction pattern collection and analysis. A CamScan CS44 SEM (Cam Scan Electron Optics, Ltd., Cambridge, UK) was operated using a 40 kV, ~10 nA electron beam. Positive phase identification was accomplished by direct comparison of the location and character of the diffraction bands in the experimental pattern with those calculated from simulated patterns generated using the possible structure types and lattice parameters.

3. Results and discussion

The microstructure, phase composition and crystal structure data obtained from selected samples are summarized in the isothermal section shown in Fig. 2 and in Table 2. These will be described in more detail below.

3.1. Nb–10Hf–16Si

The equilibrium microstructure was three-phase β(Nb,Hf,Si) + Nb(Hf)$_5$Si$_3$ + Hf(Nb)$_2$Si. Typical BSE micrographs are shown in Fig. 3. The bright phase was Hf(Nb)$_5$Si$_3$, the light gray phase was Hf(Nb)$_2$Si, the darker gray phase was Nb(Hf)$_5$Si$_3$, and the darkest phase was β(Nb,Hf,Si). The crystal structures of these phases were confirmed using EBSD. Most of the eutectic Nb(Hf)$_3$Si phase in the as-DS alloy [the as-DS microstructure consisted of β(Nb,Hf,Si) dendrites with interdendritic cells of Nb(Hf)$_3$Si and β(Nb,Hf,Si); see Ref. 7] underwent the eutectoid decomposition to β(Nb,Hf,Si) and Nb(Hf)$_5$Si$_3$ during the 1500 °C annealing. In addition, because of the inhomogeneous

Fig. 2. Isothermal section of the estimated equilibrium Nb–Hf–Si phase diagram at 1500 °C. The bulk alloy compositions are shown as solid squares. EPMA measurements of phase compositions are shown as open circles. The tie-triangles constructed in dashed lines were estimated.

Fig. 3. SEM BSE images of the Nb–10Hf–16Si alloy after heat treatment at 1500 °C for 100 h. The bright phase is $Hf(Nb)_5Si_3$, the light gray phase is $Hf(Nb)_2Si$, the dark gray phase is $Nb(Hf)_5Si_3$, and the dark phase is $\beta(Nb,Hf,Si)$. The area shown in a circle in (b) is non-equilibrium and is $Nb(Hf)_3Si$ that was decomposing to $Nb(Hf)_5Si_3$ and $\beta(Nb,Hf,Si)$.

nature of the as-DS alloys, there were $Hf(Nb)_2Si$ and $Hf(Nb)_5Si_3$ phases formed in Hf-rich interdendritic regions. Thus, four phases were observed in the 1500 °C sample, and this made it possible to define two three-phase regions: $\beta(Nb,Hf,Si) + Nb(Hf)_5Si_3 + Hf(Nb)_2Si$ and $Nb(Hf)_5Si_3 + Hf(Nb)_2Si + Hf(Nb)_5Si_3$. The solubility of Hf in the $Nb(Hf)_5Si_3$ phase is ∼16%. The solubility of Nb in $Hf(Nb)_5Si_3$ and $Hf(Nb)_2Si$ are ∼36 and ∼47%, respectively. After 100 h, the alloy had still not reached full equilibrium. On prolonged annealing, the $Hf(Nb)_5Si_3$ phase would be expected to transform to $Hf(Nb)_2Si$ (and/or $Nb(Hf)_5Si_3$) as more Nb diffused into the region (and Hf and Si diffused out). In addition, there were regions where the $Nb(Hf)_3Si$ was still experiencing the eutectoid decomposition process, as shown in Fig. 3(b).

3.2. Nb–10Hf–18.5Si

The annealed microstructure was similar to that of Nb–10Hf–16Si. Again the $Nb(Hf)_3Si$ phase underwent partial eutectoid decomposition into $\beta(Nb,Hf,Si)$ and $Nb(Hf)_5Si_3$ and the decomposition process was not fully complete.

3.3. Nb–10Hf–25Si

The equilibrium structure was two-phase $\beta(Nb,Hf,Si) + Nb(Hf)_5Si_3$. The $Nb(Hf)_3Si$ phase in the as-DS alloy underwent partial eutectoid decomposition to $\beta(Nb,Hf,Si)$ and $Nb(Hf)_5Si_3$ after the 1500 °C heat treatment as shown in Fig. 4. The eutectic regions in as-DS condition were richer in Hf and there was some

$Hf(Nb)_5Si_3$ formed after the 1500 °C treatment. Again the alloy had not fully equilibrated after 100 h. Some regions were still in the decomposition process, as shown in Fig. 4(b). EPMA from regions where decomposition appeared complete yielded an average composition of 95.3Nb–4.2Hf–0.5Si for the metal (bcc) phase, 55.2Nb–10.5Hf–34.3Si for the $Nb(Hf)_5Si_3$, and 36.7Nb–26.1Hf–37.2Si for $Hf(Nb)_5Si_3$.

3.4. Nb–30Hf–25Si

The microstructure consisted predominately of two-phases, $\beta(Nb,Hf,Si) + Hf(Nb)_2Si$, as shown in Fig. 5 and the equilibrium microstructure was these two phases. The primary $Hf(Nb)_5Si_3$ in as-DS alloy had transformed into the equilibrium $Hf(Nb)_2Si$ phase on annealing. The $\beta(Nb,Hf,Si)$ and $Hf(Nb)_2Si$ had compositions of 81Nb–18.5Hf–0.5Si and 33.5Nb–32.8Hf–31.7Si, respectively. In some areas, the $Hf(Nb)_2Si$ phase possessed a higher Hf concentration (24.4Nb–42.5Hf–33.1Si); this was

probably the result of compositional inhomogeneity (dendrites vs eutectic regions) in the as-DS structures. There was also some α(Nb,Hf,Si), which was probably also the result of inhomogeneity.
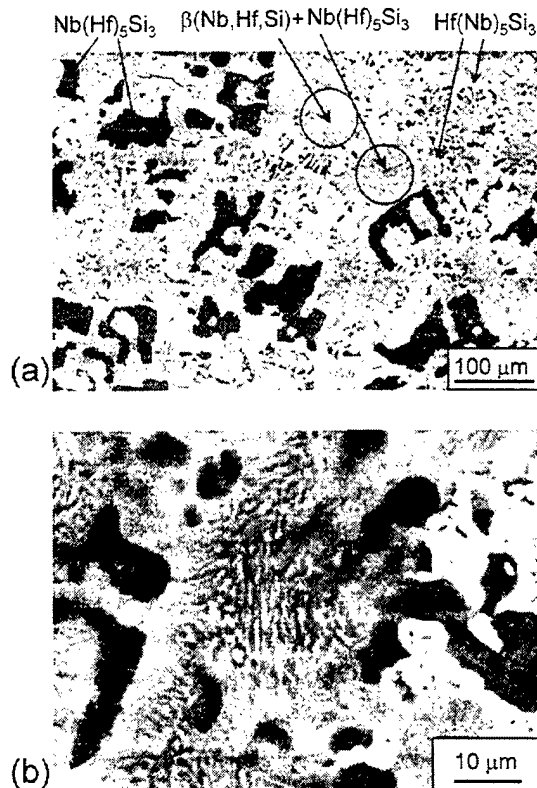

Fig. 4. SEM BSE images of the Nb–10Hf–25Si alloy after heat treatment at 1500 °C for 100 h: (a) low magnification image and (b) high magnification image. The white phase is Hf(Nb)₅Si₃ that resulted from segregation in the original as-DS structure.
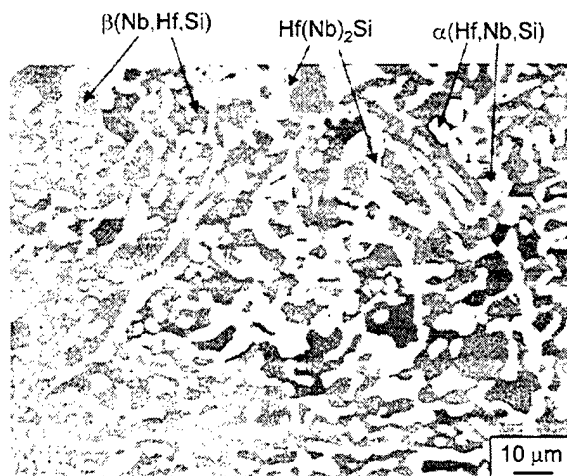

Fig. 5. SEM BSE image of the Nb–30Hf–25Si alloy after heat treatment at 1500 °C for 100 h. The white phase is α(Hf,Nb,Si) which was probably the result of inhomogeneity in the as-DS sample. The gray and dark phases are Hf(Nb)₂Si and β(Hf,Nb,Si), respectively.

3.5. Nb–40Hf–30Si

The equilibrium microstructure also consisted of two phases, β(Nb,Hf,Si) + Hf(Nb)₂Si, but the volume fraction of the Hf(Nb)₂Si phase was much higher, as shown in Fig. 6. The primary Hf(Nb)₅Si₃ in as-DS alloy had transformed into the equilibrium Hf(Nb)₂Si phase after annealing. The compositions of β(Nb,Hf,Si) and Hf(Nb)₂Si were 68.4Nb–30.7Hf–0.9Si and 23.2Nb–44.1Hf–32.7Si, respectively. The Hf concentrations of both phases are higher than those of the Nb–30Hf–25Si alloy; this is consistent with the phase diagram shown in Fig. 2. Some areas had Hf(Nb)₂Si with a higher Hf concentration (18.8Nb–48Hf–33.2Si), again this was probably the result of compositional inhomogeneity (dendrites vs eutectic regions) in the as-DS structures.

3.6. Nb–60Hf–25Si

The microstructure also consisted predominately of two phases, β(Nb,Hf,Si) + Hf(Nb)₂Si, as shown in Fig. 7, and these were the equilibrium phases. The primary Hf(Nb)₅Si₃ in the as-DS alloy had transformed into the equilibrium Hf(Nb)₂Si phase after annealing. The compositions of β(Nb,Hf,Si) and Hf(Nb)₂Si were 34.0Nb–63.9Hf–2.1Si and 9.0Nb–58.0Hf–33.0Si, respectively. There were also some small Hf-rich particles [Fig. 7(b)] that were too small to be identified using SEM, EBSD, or EMPA. These particles were either remnant of some Hf-rich regions during decomposition or precipitates that formed during cooling. There were also some larger scale (~20 μms) Hf-rich α(Hf,Nb,Si) particles with average compositions varying from 4.6Nb–92.2Hf–3.2Si to 10.9Nb–86.3Hf–2.8Si [Fig. 7(a)]. These phases were non-equilibrium and they would have been homogenized out at longer annealing times.
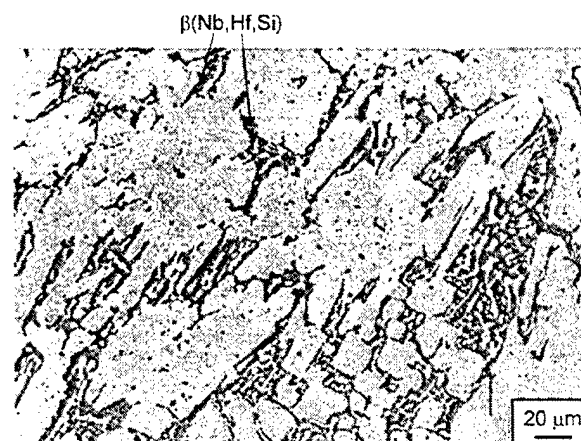

Fig. 6. SEM BSE image of the Nb–40Hf–30Si alloy after heat treatment at 1500 °C for 100 h. The gray and dark phases are Hf(Nb)₂Si and β(Hf,Nb,Si), respectively.

3.7. Nb–73Hf–17Si

Two different interpretations of the microstructure (Fig. 8) are possible. The first scenario is that the equilibrium microstructure was two-phase β(Nb,Hf, Si) + Hf(Nb)$_2$Si. The white, lath/plate-like precipitates were transformed α(Hf,Nb,Si) formed from the high temperature β(Nb,Hf,Si) phase on cooling from 1500 °C, which can be appreciated by looking at the Nb–Hf binary phase diagram [11] (see Fig. 1). There were also some α(Hf,Nb,Si) phase precipitates formed at 1500 °C in Hf-rich regions, but these had some precipitates in them, probably Hf(Nb)$_2$Si. The average composition for the Hf(Nb)$_2$Si phase was 3.8Nb–62.6Hf–33.7Si. It was difficult to measure the β(Nb, Hf,Si) phase composition at 1500 °C because of the β→α transformation. The transformed β and α compositions were 23.4Nb–74.1Hf–2.5Si and 3.3Nb–93.7Hf–3.0Si, respectively. The original β(Nb,Hf,Si) phase composition was probably

close to the average of the two, based on a near 50:50 mixture in Fig. 8. The tie-line was not drawn due to uncertainty in the β-phase composition.

The second interpretation is that the equilibrium microstructure was three-phase: α(Hf,Nb,Si) + β(Nb, Hf,Si) + Hf(Nb)$_2$Si in which the α(Nb,Hf,Si) and β(Nb, Hf,Si) phase had a composition of 3.3Nb–93.7Hf–3.0Si and 23.4Nb–74.1Hf–2.5Si, respectively. The β(Nb,Hf, Si) phase composition, however, seems inconsistent with that projected from the Nb–Hf binary phase diagram.

3.8. Nb–80Hf–5Si

The equilibrium microstructure could be two-phase β(Nb,Hf,Si) + Hf(Nb)$_2$Si, or three-phase α(Hf,Nb,Si) + β(Nb,Hf,Si) + Hf(Nb)$_2$Si. The amount of Hf(Nb)$_2$Si was very small. The β(Nb,Hf,Si) phase transformed to β(Nb, Hf,Si) and α(Hf,Nb,Si) on cooling from 1500 °C (Fig. 9). There were also precipitates, probably β(Nb,Hf,Si), formed during cooling in the original α(Hf,Nb,Si) phase [Fig. 9(b)]. No EPMA was performed on this sample. This alloy was probably in a two-phase region.

3.9. Nb–90Hf–5Si

The equilibrium microstructure probably consisted of three-phase β(Nb,Hf,Si) + α(Nb,Hf,Si) + Hf(Nb)$_2$Si (Fig. 10). The light gray phase was α(Hf,Nb,Si) with an average composition of 3.1Nb-93.1Hf-3.8Si. The dark gray phase had an average composition of 21.7Nb–75.6Hf–2.7Si and was β(Nb,Hf,Si). The original β(Nb, Hf,Si) phase further transformed to β(Nb,Hf,Si) and α(Hf,Nb,Si) on cooling from 1500 °C and appears as a two-phase structure in Fig. 10. The average composition
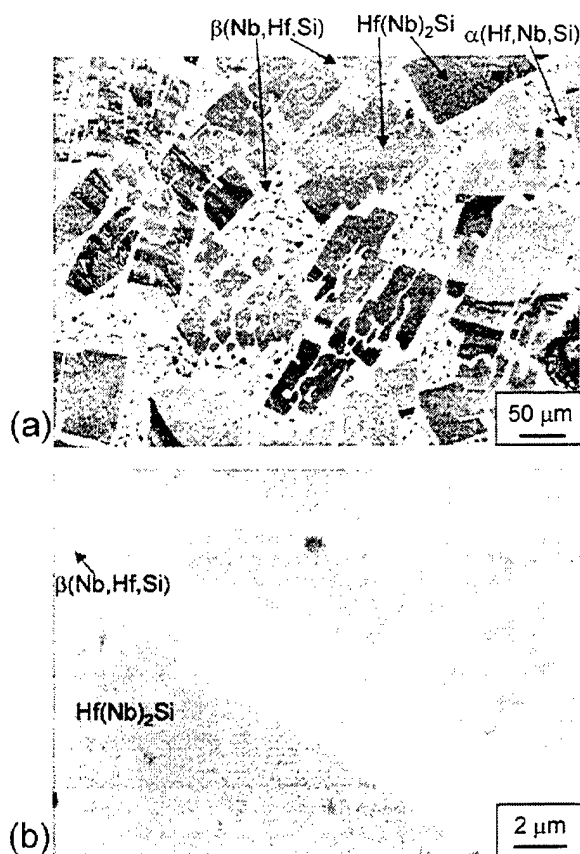

Fig. 7. SEM BSE images of the Nb–60Hf–25Si alloy after heat treatment at 1500 °C for 100 h: (a) low magnification and (b) high magnification. The dark phase is Hf(Nb)$_2$Si and the contrast in it was probably due to different grain orientations. The gray phase is β(Nb,Hf,Si). The light gray phase inside β(Nb,Hf,Si) shown in (b) is probably α(Nb,Hf,Si) formed during cooling from 1500 °C. The white phase is α(Nb,Hf,Si), very rich in Hf, which was probably the result of inhomogeneity in the as-DS structure.
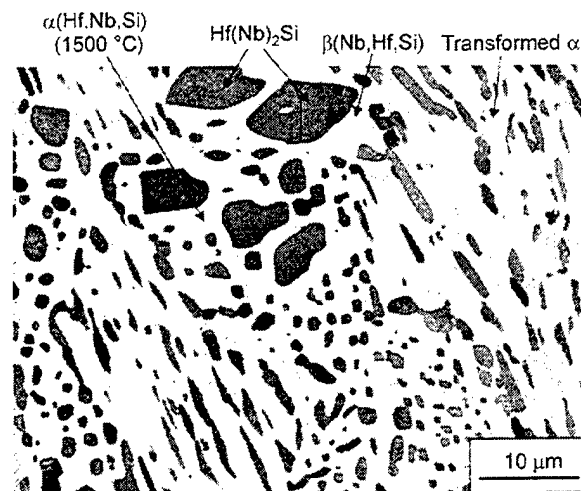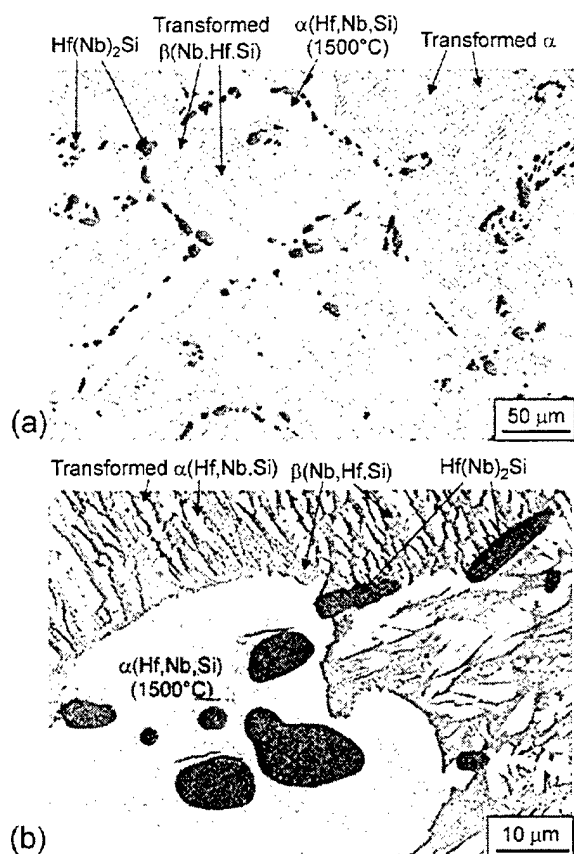

Fig. 8. SEM BSE image of the Nb–73Hf–17Si alloy after heat treatment at 1500 °C for 100 h. The dark phase is Hf(Nb)$_2$Si. The two-phase region was β(Nb,Hf,Si) at 1500 °C and it transformed into β(Nb,Hf,Si) + α(Nb,Hf,Si) during cooling. There was a very small amount of α(Nb,Hf,Si) present at 1500 °C.

of the two-phase region obtained via area-average scanning mode in EMPA was 11.3Nb–85.0Hf–3.7Si which probably represents the original β(Nb,Hf,Si) phase composition at 1500 °C. The dark phase in Fig. 10 was Hf(Nb)₂Si with a composition of 2.0Nb–64.4Hf–33.6Si.

3.10. Nb–50Hf–37.5Si

The ISM ingot was very inhomogeneous. After the 1500 °C anneal, part of the sample displayed a well-defined three-phase structure, as shown in Fig. 11(a). The three phases were identified as Hf(Nb)Si, Hf(Nb)₅Si₄, and Nb(Hf)Si₂ with compositions of 4.7Nb–45.9Hf–49.4Si, 21.6Nb–34.4Hf–44.0Si, and 26.2Nb–9.4Hf–64.4Si, respectively. In other areas, two-phase regions were observed. They were β(Nb,Hf,Si) (68.0Nb–30.9Hf–1.1Si) and Hf(Nb)₂Si (20.2Nb–46.4Hf–33.4Si), as shown in Fig. 11(b). The crystal structures of all these phases were confirmed using EBSD. The dramatic difference in
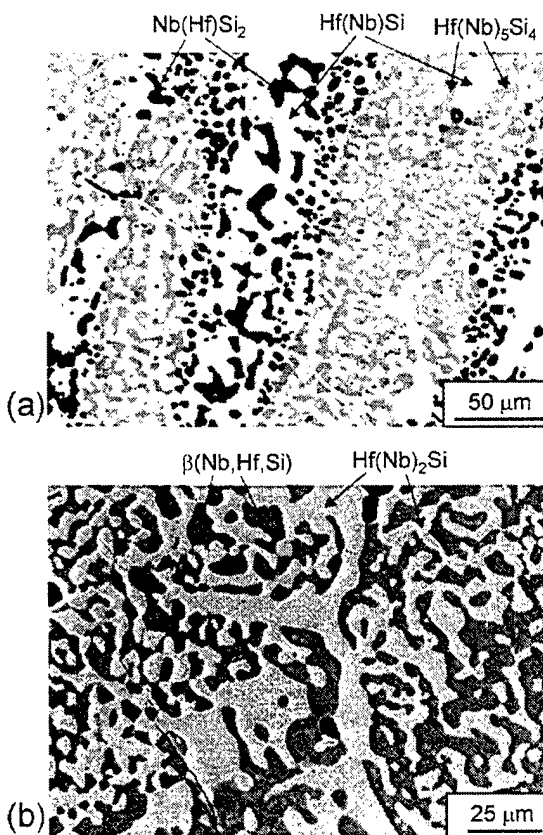

Fig. 9. SEM BSE images of the Nb–80Hf–5Si alloy after heat treatment at 1500 °C for 100 h: (a) low magnification and (b) high magnification. The dark phase is Hf(Nb)₂Si. The two-phase region was original β(Nb,Hf,Si) at 1500 °C and it transformed into β(Nb,Hf,Si)+α(Nb,Hf,Si) during cooling. The light gray phase is α(Nb,Hf,Si) which was present at 1500 °C.
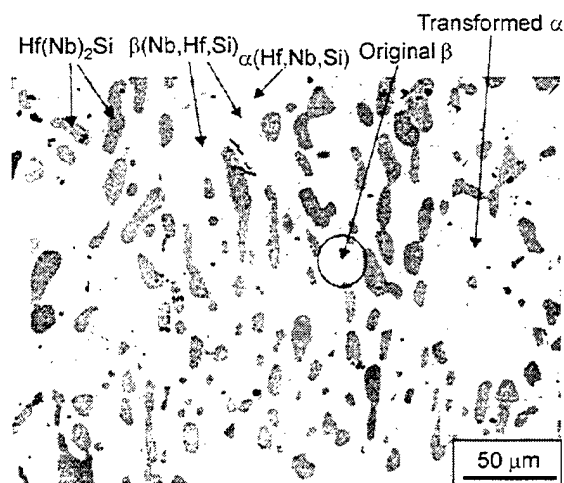
Fig. 10. SEM BSE image of the Nb–90Hf–5Si alloy after heat treatment at 1500 °C for 100 h. The darkest phase is Hf(Nb)₂Si. The white phase is α(Hf,Nb,Si). The two-phase region was original β(Nb,Hf,Si) at 1500 °C and it transformed into β(Nb,Hf,Si)+α(Nb,Hf,Si) during cooling.

Fig. 11. SEM BSE images of the Nb–50Hf–37.5Si alloy after heat treatment at 1500 °C for 100 h. These images (a) and (b) were from different regions of the sample which was inhomogeneous. The darkest phase in (a) is Nb(Hf)Si₂; the dark gray phase is Hf(Nb)₅Si₄; and the light gray phase is Hf(Nb)Si. The white lines shown in (a) were cracks in the sputtered carbon coating on the surface of the sample. The region in (b) consisted of two phases: β(Nb,Hf,Si) (darker) and Hf(Nb)₂Si (brighter).
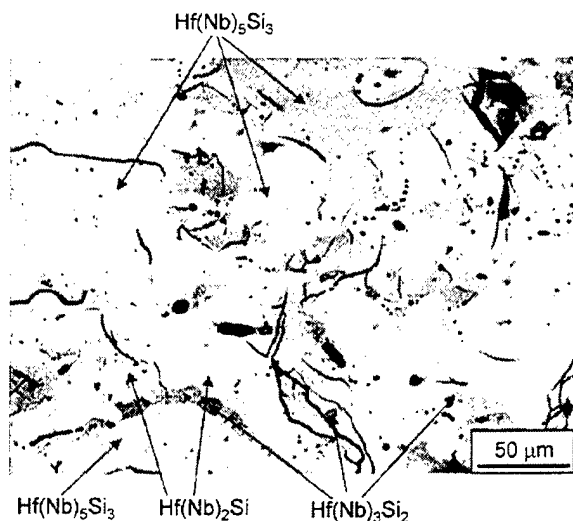
Fig. 12. SEM BSE image of the Nb–55Hf–37.5Si alloy after heat treatment at 1500 °C for 100 h. There were three phases, but there was little contrast between them. EBSD was used for phase identification. The white dots in the micrograph are imperfections in the surface carbon coating. The darkest lines and areas were cracks and pores in the sample.
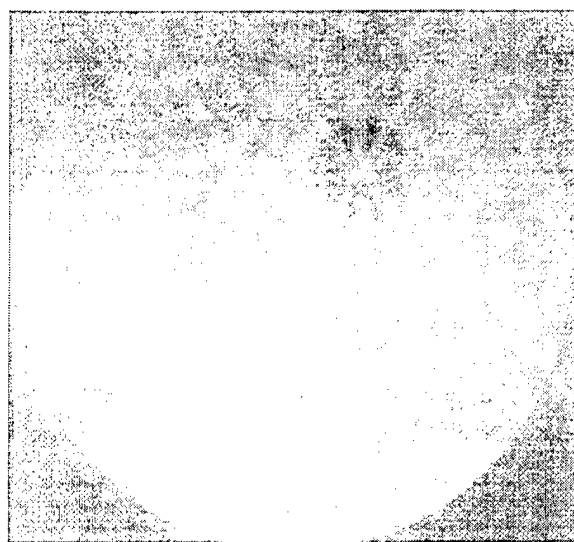

Fig. 13. EBSD pattern of the $Hf(Nb)_2Si$ phase in the Nb–55Hf–37.5Si alloy after heat treatment at 1500 °C for 100 h.

microstructure of the two areas arose becasue the ISM ingot was difficult to homogenize.

3.11. Nb–55Hf–37.5Si

The equilibrium state of this alloy was probably single-phase $Hf(Nb)_5Si_3$. The microstructure after the 1500 °C/100 h anneal consisted mostly of $Hf(Nb)_5Si_3$ with a composition of 6.9Nb–55.3Hf–37.8Si, as shown in Fig. 12. Due to the inhomogeneity of the original cast structure, there were also small amounts of $Hf(Nb)_3Si_2$

(6.5Nb–53.8Hf–39.7Si), $Hf(Nb)_2Si$ (7.9Nb–58.6Hf–33.6Si) and $\beta(Nb,Hf,Si)$ (38.7Nb–59.1Hf–2.2Si), respectively. The atomic number contrast was very low between the three silicides in this alloy, which made the contrast difference in the BSE image (Fig. 12) very low. The phases were therefore identified using EBSD. An exemplar EBSD pattern of the $Hf(Nb)_2Si$ phase is shown in Fig. 13.

4. Conclusions

The microstructures generated in the ternary Nb–Hf–Si alloys investigated contained a total of 10 phases: $\beta(Nb,Hf,Si)$, $\alpha(Hf,Nb,Si)$, $Nb(Hf)_5Si_3$, $Hf(Nb)_5Si_3$, $Nb(Hf)_3Si$, $Hf(Nb)_2Si$, $Hf(Nb)_3Si_2$, $Hf(Nb)_5Si_4$, $Hf(Nb)Si$, and $Nb(Hf)Si_2$. The isothermal section of the Nb–Hf–Si system at 1500 °C has been defined.

The Nb solubility is ~46% in $Hf(Nb)_2Si$, ~36% in $Hf(Nb)_5Si_3$, > 6.5% in $Hf(Nb)_3Si_2$, ⩾22% in $Hf(Nb)_5Si_4$, and 5% in $Hf(Nb)Si$. The Hf solubilities in $Nb(Hf)_5Si_3$ and $Nb(Hf)Si_2$ are ~16 and 9.4%, respectively. Four three-phase regions, $\beta(Nb,Hf,Si) + Nb(Hf)_5Si_3 + Hf(Nb)_2Si$, $Nb(Hf)_5Si_3 + Hf(Nb)_2Si + Hf(Nb)_5Si_3$, $\beta(Nb,Hf,Si) + \alpha(Hf,Nb,Si) + Hf(Nb)_2Si$, and $Nb(Hf)Si_2 + Hf(Nb)_5Si_3 + Hf(Nb)Si$ have been defined. The $Nb(Hf)_3Si$ phase was unstable at 1500 °C and decomposed by an eutectoid transformation to $\beta(Nb,Hf,Si)$ and $Nb(Hf)_5Si_3$.

References

[1] Mendiratta MG, Dimiduk DM. Mater Res Soc Symp Proc 1989; 133:441.
[2] Jackson MR, Bewlay BP, Rowe RG, Skelly DW, Lipsitt HA. JOM 1996;48:39.
[3] Subramanian PR, Mendiratta MG, Dimiduk DM. JOM 1996; 48:33.
[4] Bewlay BP, Lewandowski JJ, Jackson MR. JOM 1997;49:44.
[5] Bewlay BP, Jackson MR, Lipsitt HA. J Phase Equilibria 1997; 18:264.
[6] Bewlay BP, Jackson MR, Bishop RR. J Phase Equilibria 1998; 19:577.
[7] Bewlay BP, Bishop RR, Jackson MR. Z Metallkde 1999;90:413.
[8] Bewlay BP, Sutliff JA, Bishop RR. J Phase Equilibria 1999; 20:109.
[9] Zhao J-C, Bewlay BP, Jackson MR, Chen Q. J Phase Equilibria 2000;21:40.
[10] Subramanian PR, Mendiratta MG, Dimiduk DM. Mater Res Soc Symp Proc 1994;322:491.

[11] Fernandez Guillermet A. J Alloys Compounds 1996;234:111.

[12] Schlesinger ME, Okamoto H, Gokhale AB, Abbaschian R. J Phase Equilibria 1993;14:502.

[13] Liang H, Chang YA. Intermetallics 1999;7:561.

[14] Mendiratta MG, Dimiduk DM. Scripta Metall Mater 1991; 25:237.

[15] Bewlay BP, Lipsitt HA, Jackson MR, Reeder WJ, Sutliff JA. Mater Sci Eng 1995;A192/193:534.

[16] Villars P, Calvert LD, Pearsons handbook of crystallographic data for intermetallic phases, vols. 1–4, 2nd ed. Materials Park (OH): ASM International, 1991.

[17] Karpinsky OG, Evseyev BA. Russ Metall 1969;3:128.

[18] Bewlay BP, Jackson MR, Reeder WJ, Lipsitt HA. Mater Res Soc Symp Proc 1994;364:943.

[19] Okamoto H. Bull Alloy Phase Diagrams 1990;11:513.

[20] Harland CJ, Akhter P, Bewick A. J Phys 1981;E14:175.

[21] Schwartz AJ, Kumar M, Adams BL, editors, Electron backscatter diffraction in materials science. New York: Kluwer Academic/Plenum, 2000.

Alloying and Phase Stability in Niobium Silicide In-Situ Composites

J.-C. Zhao, B.P. Bewlay, M.R. Jackson, and L.A. Peluso

ALLOYING AND PHASE STABILITY IN NIOBIUM SILICIDE IN-SITU COMPOSITES

J.-C. Zhao, B.P. Bewlay, M.R. Jackson, and L.A. Peluso

General Electric Company

Corporate Research & Development

P.O. Box 8, Schenectady, NY 12301

Abstract

In-situ composites based on Nb silicides have great potential for future high-temperature applications. This paper will describe phase stability in the Nb-Ti-Si-Cr-Hf-Al system by examining the related key binary and ternary systems using new experimental data obtained from a high-efficiency diffusion multiple approach, as well as previous literature data. The Nb-Si, Nb-Ti-Si, Nb-Hf-Si, Nb-Cr-Si, Ti-Cr-Si, and Nb-Al-Si phase diagrams are discussed. The focus of this paper is placed on the phases that are major constituents in the composites, such as the liquid phase, the Nb-Ti-based bcc metal phase, Nb_5Si_3, Ti_5Si_3, Nb_3Si, and the Cr_2Nb-based Laves phases. Alloying effects of various additions of elements, such as Ti, Hf, Cr, Al to Nb-Si are discussed.

Introduction

Nb silicide-based composites show great promise for application as the next generation turbine airfoil materials with significantly higher operating temperatures than current generation advanced Ni-base superalloys [1-4]. The potential application of these composites at very high temperatures requires a balance of high creep resistance, high oxidation resistance, and low-temperature damage tolerance. The aim of the present paper is to review alloying effects and phase stability in Nb silicide based composites derived from binary, ternary and higher order alloys. The status of the development of these composites is described separately [5].

Nb-Si

The composition range and potential use temperatures of the composites are highlighted in the binary Nb-Si phase diagram, Fig. 1. The Nb silicide based composites consist of the bcc(Nb) phase and the tetragonal Nb_5Si_3 phase (tI32). The phase diagram was based on an assessment by Schlesinger et al. [6] with the eutectoid temperature being adjusted to ~ 1700°C based on the result reported by Mendiratta and Dimiduk [7]. The L → bcc(Nb) + Nb_3Si eutectic is adjusted to 1880°C and 18.2 at.% Si to reflect the temperature and composition obtained by Bewlay et al. [8] on directionally solidified (DS) Nb-Si alloys (all compositions are in at.% throughout this paper, including the phase diagrams in the figures). The products of the eutectic reaction in the binary system are bcc(Nb) + Nb_3Si. The Nb_5Si_3 phase forms after the decomposition of the Nb_3Si phase via an eutectoid reaction Nb_3Si → bcc(Nb) + Nb_5Si_3 at ~1700°C, or as the primary solidification product in hypereutectic alloys. There are two different Nb_5Si_3 phases based on the same crystal structure (tI32) but they have different lattice parameters. For the sake of simplicity, no differentiation is made throughout this paper.

Although the equilibrium phases at the potential use temperatures are bcc(Nb) + Nb_5Si_3 (Fig. 1), the composites solidify with the Nb_3Si phase during casting (including directional solidification). The decomposition kinetics of Nb_3Si were found to be very sluggish [7]. The volume fraction of silicide does change depending on whether the

silicide is Nb_5Si_3 or Nb_3Si. For instance, at 18 at.%Si, the volume fraction of the silicide is ~0.5 or ~0.7 for Nb_5Si_3 or Nb_3Si, respectively. The silicide volume fraction can have an effect on the fracture toughness of the composites.

The binary in-situ composites have excellent creep strength, but poor oxidation resistance and poor room temperature fracture toughness [1,2]. Alloying with other elements to improve the oxidation resistance and fracture toughness is required.
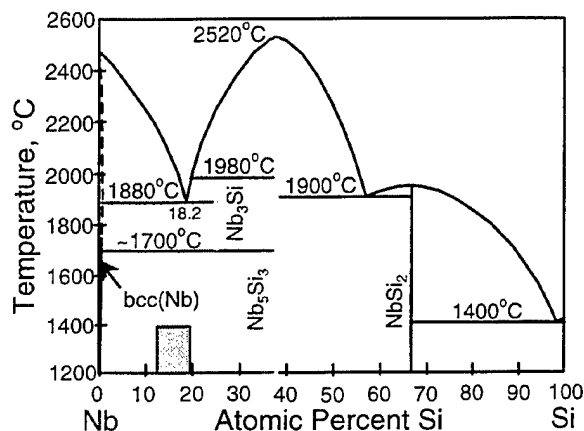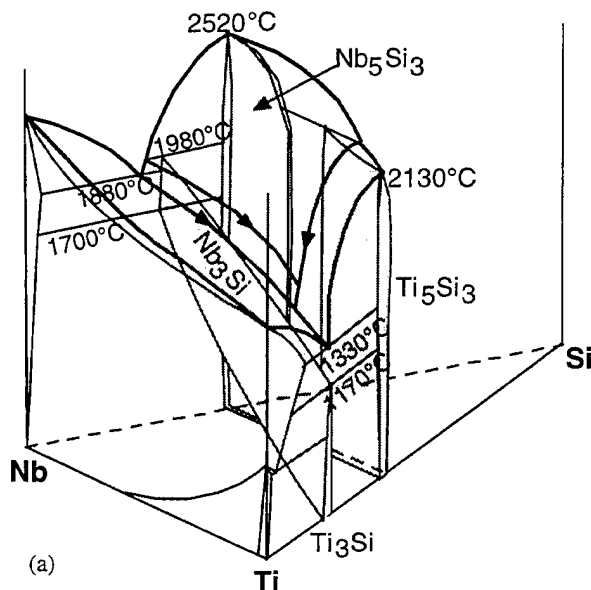

Fig. 1 Phase diagram of the Nb-Si binary system based on Schlesinger et al. [6] and results of Mendiratta and Dimiduk [7] and Bewlay et al. [8]. The shaded box shows the composition range and potential use temperatures of the composites.
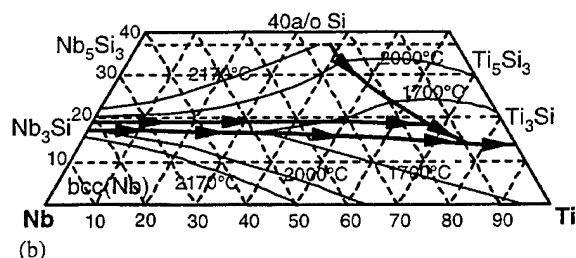
Nb-Ti-Si

Since Ti is one of the most important alloying elements in Nb silicide composites, a detailed study of the Nb-Ti-Si phase diagram was carried out by Bewlay et al. [9, 10], Subramanian et al. [11] and Zhao et al. [12]. The results are summarized in Fig. 2, in which Fig. 2(a) is a projection of a three-dimensional (3D) phase diagram. The liquidus projection was constructed by Bewlay et al. [9] by examining the microstructure of DS alloys. Isothermal sections at several different temperatures from 1000 °C to 1500°C have been measured in order to construct the whole ternary diagram [10-12]. It can been seen that Ti: 1) stabilizes Nb_3Si to lower temperatures; 2) promotes the formation of a hexagonal Ti_5Si_3 phase (hP16); and, 3) reduces the L → bcc(Nb) + Nb_3Si eutectic temperature, i.e. the melting temperature of the composites. Although additions of Ti to the composites have very beneficial effects on both oxidation resistance and room temperature fracture toughness [13], the amount of the Ti addition has to be limited to < 25 at.% in order to maintain an eutectic temperature of > 1700 °C, and to avoid the formation of the hP16 Ti_5Si_3 phase, which was found to be detrimental to the creep-rupture strength of the composites [14]. It is important to maintain the
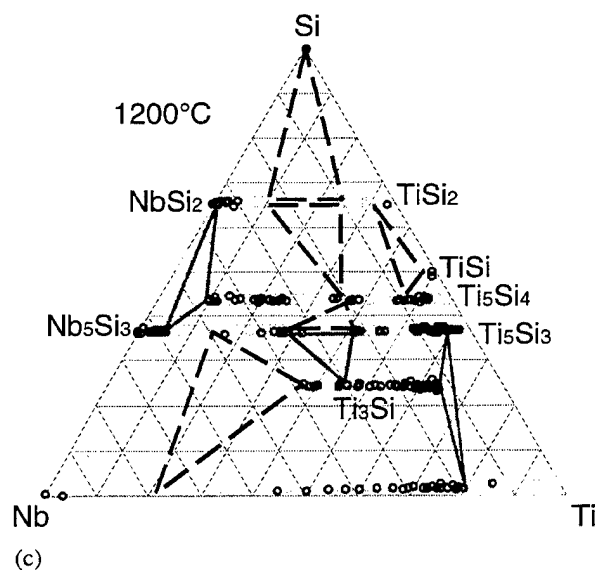
melting (eutectic) temperature of the composites above 1700°C to retain good strength to the potential use temperatures (1200 to 1400°C).

(a)

(b)

(c)

Fig. 2 Phase diagram of the Nb-Ti-Si ternary system [9,10,12]: (a) a schematic 3D phase diagram; (b) a liquidus projection; and (c) an isothermal section at 1200°C.

It can be seen from Fig. 2(c) that the solubility of Ti in the Nb$_5$Si$_3$ phase can be as high as 30 at.% and the solubility of Nb in Ti$_5$Si$_3$ is also very high, ~ 20 at.%. Surprisingly high solubility (46 at.%) of Nb in Ti$_5$Si$_4$ is also observed.

Understanding the liquid-solid and the solid-solid phase equilibria of the Nb-Ti-Si ternary system has played a significant role in the composition selection, microstructure design, selection of processing routes, and balance of properties of these composites.

Hf-Si and Nb-Hf-Si

Hf is an important alloying element for strength, toughness and oxidation resistance of the Nb silicide composites [2,4]. In order to understand the effect of Hf additions on the phase stability of the bcc(Nb), Nb$_3$Si, and Nb$_5$Si$_3$ phases, the phase diagrams of the Hf-Si binary and the Nb-Hf-Si ternary systems were investigated [15-18].

The Hf-Si phase diagram has been assessed by Gokhale and Abbaschian [19] primarily based on the experimental results of Brukl [20]. Five intermetallic compounds, Hf$_2$Si, Hf$_3$Si$_2$, Hf$_5$Si$_4$, HfSi, and HfSi$_2$, have been included in the assessed phase diagram. A Hf$_5$Si$_3$ phase with the Mn$_5$Si$_3$ crystal structure (hP16) was identified [21,22]. The Hf$_5$Si$_3$ phase was originally thought to be stabilized by interstitial impurities [19,20] and was not included in the assessed phase diagram of Gokhale and Abbaschian [19]. Recently, Bewlay et al. [15] found that the Hf$_5$Si$_3$ phase existed in a Hf-35at.%Si alloy. It was also observed that Hf$_5$Si$_3$ decomposes via an eutectoid reaction to Hf$_2$Si + Hf$_3$Si$_2$ at ~ 1925°C [16]. Therefore, Hf$_5$Si$_3$ is an equilibrium phase in the binary Hf-Si system. Based on these observations, a new version of the Hf-Si binary phase diagram was constructed as shown in Fig. 3. A peritectic reaction, L + Hf$_3$Si$_2$ ↔ Hf$_5$Si$_3$ at ~ 2360°C was proposed based on Brukl's incipient melting results. Thermodynamic modeling of the binary Hf-Si system was performed using existing phase diagram data and the reported enthalpies of formation for Hf silicides. A complete thermodynamic description of the Gibbs energies of all stable phases in the binary system was developed [16]. The Hf-Si binary system serves as a basis for understanding the Nb-Hf-Si ternary system; for example the relative stability of the Hf$_5$Si$_3$ phase with respect to the Nb$_5$Si$_3$ phase is very important.

The metal-rich region of the Nb-Hf-Si phase diagram plotted as a 3D projection is shown in Fig. 4(a) [18]. (The binary Nb-Hf system is based on an assessment by Fernandez-Guillermet [23]). This Nb-Hf-Si ternary system was based on the experimental data reported by Bewlay et al. [17] and Zhao et al. [18].

The isothermal section at 1500°C was also determined, as shown in Fig. 4(c). The phase equilibria at 1500 °C are

likely to be very similar to those at the potential service temperatures, 1200 to 1400 °C. This isothermal section was constructed based on experimental data from alloys heat treated at 1500°C for 100 hours and analyzed using scanning electron microscopy (SEM), electron probe microanalysis (EPMA), and electron backscatter diffraction (EBSD) [24] analysis [18]. Phase equilibria between the following silicides, Nb$_5$Si$_3$, Hf$_5$Si$_3$, Nb$_3$Si, Hf$_2$Si, Hf$_3$Si$_2$, Hf$_5$Si$_4$, HfSi, NbSi$_2$, and two metal-rich solid solutions, bcc(Nb,Hf) and hcp(Hf,Nb) were obtained [18], as shown in Fig. 4(c).

It can be seen from Fig. 4(c) that the Nb solubility is ~46% in Hf$_2$Si, ~36% in Hf$_5$Si$_3$, >6.5% in Hf$_3$Si$_2$, ≥22% in Hf$_5$Si$_4$, and, 5% in HfSi. The Hf solubilities in Nb$_5$Si$_3$ and NbSi$_2$ are ~16% and 9.4%, respectively. The Nb$_3$Si phase is unstable at 1500 °C and decomposes by an eutectoid transformation to bcc(Nb,Hf) and Nb$_5$Si$_3$ at temperatures > 1500°C.

Figure 4 shows that Hf additions also reduce the L → bcc(Nb) + Nb$_3$Si eutectic temperature, but the reduction is not as severe as Ti. Unlike Ti, Hf does not stabilize the Nb$_3$Si phase to lower temperatures. Although the exact Nb$_3$Si → bcc(Nb) + Nb$_5$Si$_3$ (tI32) eutectoid temperature has not been defined, it must be > 1500°C. Nb does stabilize the hexagonal (hP16) Hf$_5$Si$_3$ to lower temperatures. Similar to Ti$_5$Si$_3$, the hP16 Hf$_5$Si$_3$ phase can potentially be detrimental to the creep strength of the composites. To avoid the formation of both Hf$_2$Si and Hf$_5$Si$_3$ (at lower temperatures), Hf additions to the composites have to be < 10 at.%.
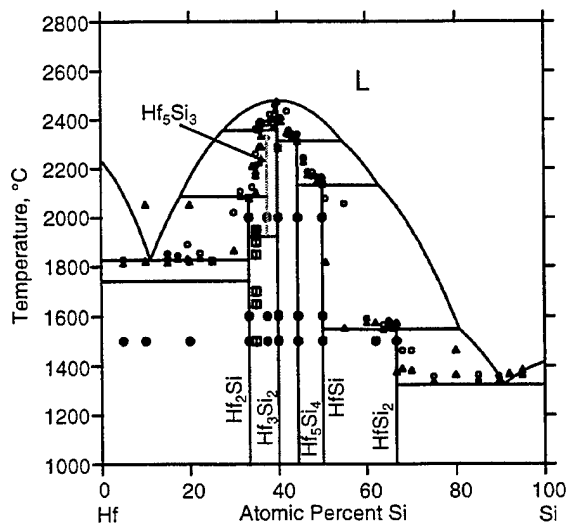

Fig. 3 Calculated phase diagram of the Hf-Si binary system [16] based on the results of Brukl [20] and Bewlay et al. [15].

485

three different Laves crystal structures (C14, C15 and C36) in the Cr₂Nb and Cr₂Ti based systems. The Cr-Nb phase diagram, Fig. 5(a) [25,26], shows two Laves phases, the high temperature hexagonal C14 (hP12) which is stable above ~1600°C and the low-temperature cubic C15 (cF24) stable at temperatures < ~1600 °C. The Cr-Ti phase diagram, Fig. 5(b) [27-29], shows one more Laves crystal structure – the hexagonal C36 (hP24) which is stable at very high temperatures > 1270 °C. The effect of Si on the stability of these Laves phases can be appreciated by studying the Nb-Cr-Si and Ti-Cr-Si systems.
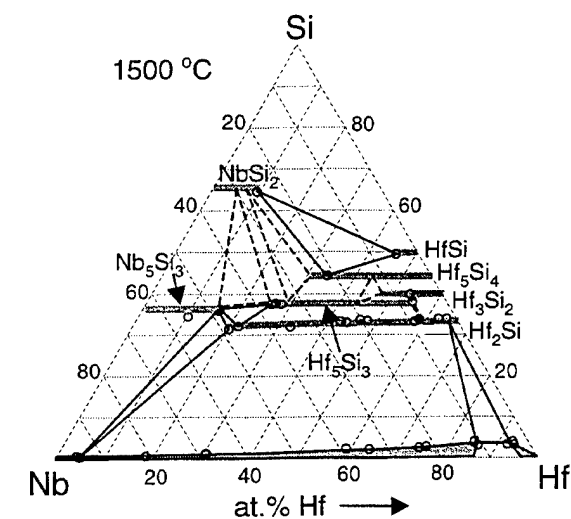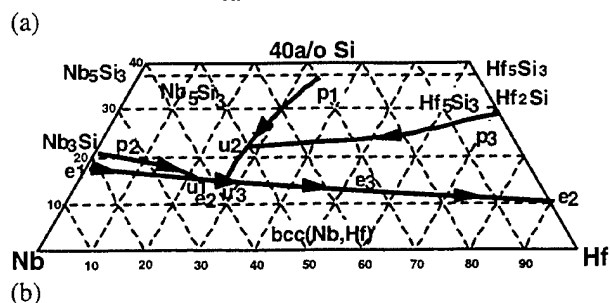

(a)

(b)

(c)

Fig. 4 Nb-Hf-Si ternary phase diagrams: (a) a schematic 3D phase diagram; (b) a liquidus projection; and (c) an isothermal section at 1500°C [17,18].

(a)

(b)
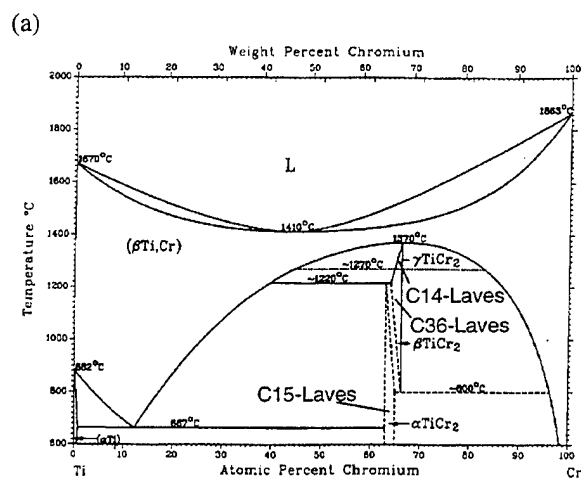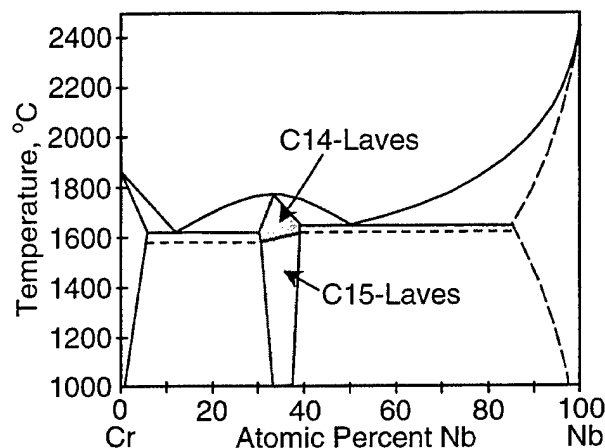
Fig. 5 Phase diagrams of the Nb-Cr (a) and Ti-Cr (b) systems showing the temperature ranges of stability for the three different Laves phases [25-29].

Nb-Cr and Ti-Cr

Additions of Cr are needed to improve the oxidation resistance of these composites. Cr stabilizes the Cr-rich Laves phases. The stability of the Laves phases is therefore critical, especially concerning the stability of

Nb-Cr-Si

An isothermal section of the Nb-Cr-Si phase diagram at 1000°C was reported by Goldschmidt and Brand [30]. It is very likely that many of the alloys used by Goldschmidt and Brand had not reached equilibrium after only a 336-

hour (2 weeks) anneal at 1000°C. Many of the Nb-base alloys, such Nb-Ti-Si alloys studied by Bewlay et al. [10,17] and Nb-Hf-Si alloys studied by Zhao et al. [18] possess very slow kinetics, and they would not be at equilibrium after a 1000 °C – 336 hour anneal.

A high-efficiency "diffusion multiple" approach [31,32] was employed to re-determine the phase diagram of the Nb-Cr-Si system. Details of the approach and experimental procedures were described separately [12]. A diffusion multiple is an assembly of four different metals arranged in a cross-sectional view shown in Fig. 6(a). The inner and outer circle diameters in Fig. 6(a) were 15.6 and 25.4 mm respectively. High purity Nb, Ti, Si and Cr pieces were assembled into the geometry. The assembled diffusion multiple was then loaded into HIP cans made of commercial purity Ti and electron beam welded. The HIP was performed at 1204 °C, 200MPa for 4 hours. The samples were then annealed at four different temperatures: 1200 °C for 1000 hours, 1150°C for 2000 hours, 1100 °C for 4000 hours, and 1000 °C for 4000 hours.

The results obtained from the Nb-Cr-Si tri-junction region (highlighted in Fig. 6(a) by a dashed circle) are shown in Fig. 7 (1150°C results only). During the long-term diffusion treatment, extensive interdiffusion among Nb, Cr and Si took place, and all the equilibrium phases, including the intermetallic phases, formed by interdiffusion among the elements in the diffusion multiple. An extremely large amount of phase equilibrium information was obtained using EPMA and EBSD. There were three intermetallic compounds, $(Cr,Nb)_6Si_5$ ($oI44$) and $(Cr,Nb)_{11}Si_8$ ($oP76$), and $NbCrSi$ ($hP9$). All of them have been observed and reported before [30,33-35]. The measured Si concentrations for all the three ternary compounds agree with their respective stoichiometries. The formation of the $NbCrSi$, $(Cr,Nb)_6Si_5$ and $(Cr,Nb)_{11}Si_8$ phases were not only identified by compositions obtained from EPMA, but also by EBSD crystal structure identification.

For such a complex system, the diffusion multiple approach is far more efficient and systematic than the equilibrated alloy approach: 1 diffusion multiple in contrast to 221 alloys used by Goldschmidt and Brand [30]. In fact the isothermal section of Nb-Ti-Si shown in Fig. 2(c) was also obtained from a Nb-Ti-Si tri-junction region of the diffusion multiple (Fig. 6(a)).

It can be seen from Fig. 7 that the Cr solubility in the bcc(Nb) and Nb_5Si_3 is ~ 3 and 10 at.% respectively (at 1150°C; the solubility of Cr in the bcc(Nb) phase varies with temperature). The bcc(Nb)–Nb_5Si_3–NbCrSi three phase equilibrium indicates that the Laves phases are not in equilibrium with bcc(Nb) and Nb_5Si_3 in the ternary

system at 1000 to 1200°C. In composites processed (cast or DS) at high temperatures, the C14 Laves phase was observed to co-exist with bcc(Nb) and Nb_5Si_3. It is likely that there is a four phase equilibrium reaction bcc(Nb)–Nb_5Si_3–C14 + C14–Nb_5Si_3–NbCrSi ↔bcc(Nb)–Nb_5Si_3–NbCrSi + bcc(Nb)–C14–NbCrSi at a temperature > 1200°C.

Although the liquidus surface for the Nb-Cr-Si system is not available, the melting temperatures of 74 alloys (out of 221 alloys) are reported by Goldschmidt and Brand
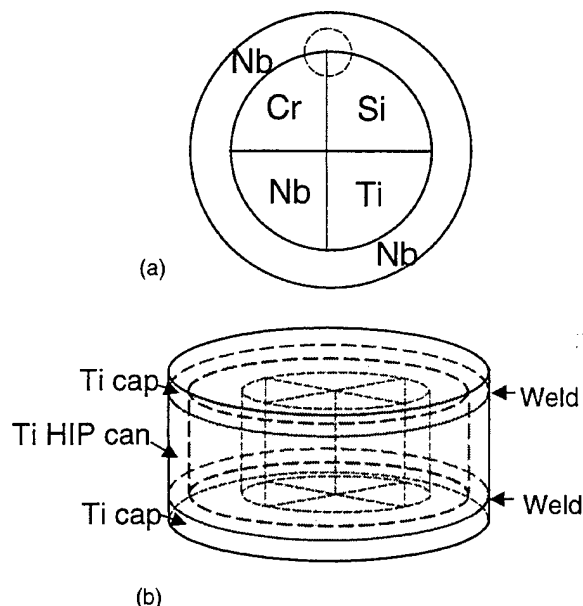

(a)

(b)

Fig. 6. A diffusion multiple for efficient mapping of Nb-Cr-Si and Nb-Ti-Si ternary phase diagrams: (a) cross-sectional view and (b) perspective view [12].
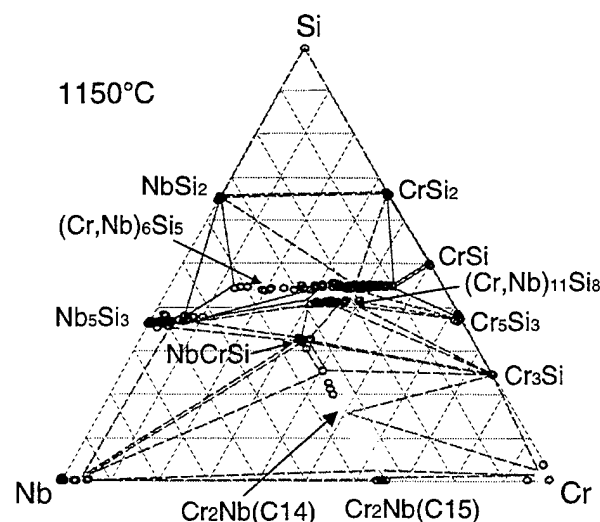

Fig. 7 The 1150°C isothermal section of the Nb-Cr-Si ternary system obtained from the diffusion multiple [12].

[30]. The data show that Cr depresses the melting temperature of the composites, probably even more strongly than Ti.

Cr additions to the composites improve the oxidation resistance, but probably degrade both fracture toughness and creep strength as well as the melting temperature. Thus Cr additions have to be tailored in order to balance the oxidation resistance, creep resistance and fracture toughness. It is currently unknown whether the NbCrSi phase is better for creep strength and whether it is possible to promote the NbCrSi phase formation during reasonable heat treatment time. If the transformation from the in-situ formed C14 Laves phase to the NbCrSi phase is very sluggish, it may not be economically feasible for real materials production.

Ti-Cr-Si

A 1000°C isothermal section of the Ti-Cr-Si system was constructed by Lysenko et al. [36] based on 135 alloys annealed at 1000°C for 650 to 1200 hours (depending on the alloys), Fig. 8. The Ti_5Si_4 phase which was an equilibrium phase for the binary Ti-Si system is missing from the phase diagram reported by Lysenko et al. due to the fact that no alloys were made around the Ti_5Si_4 composition.

It is clear from Fig. 8 that there is very little solubility of Cr in Ti_3Si, thus Cr is not a stabilizer of this phase. In other words, Cr can be added to destabilize the Ti_3Si phase if needed. The solubility of Cr in both Ti_5Si_3 and bcc(Ti) is very high, ~45 at.% and ~23 at.% respectively. The solubility of Si in the C15 Laves phase is ~ 20 at.%.

It is interesting to note that no TiCrSi (an analog to hP9 NbCrSi) phase exists in the Ti-Cr-Si system. Depending on the solubility of Ti in the NbCrSi, Ti additions to the Nb silicide based composites may de-stabilize this phase. The quaternary information obtained from the quadri-junction, the center of Fig. 6(a) where four elements meet, of the diffusion multiple may provide critical data. The work is currently in progress.

Nb-Si-Al and Nb-Cr-Al

The alloying effect of Al in Nb silicide-based composites can be appreciated by examining the Nb-Si-Al and Nb-Cr-Al phase diagrams. A partial 1500°C isothermal section of the Nb-Si-Al system was constructed by Pan et al. [37] as shown in Fig. 9. An isothermal section at 1400°C was also reported by Brukl et al. [38]. The solubility of Al in Nb_5Si_3 is ~ 12 at.%, but only ~ 5% if it is in equilibrium with the bcc phase. The solubility of Al in bcc(Nb) is ~ 8 at.%, but only ~ 3 at.% if it is in equilibrium with Nb_5Si_3. The values reported by Brukl et
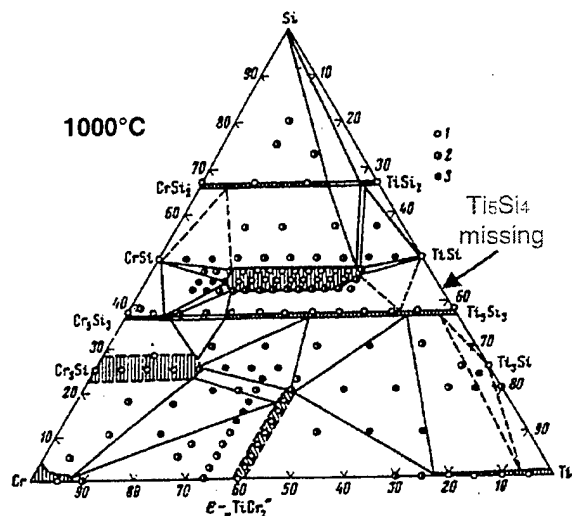
Fig. 8 Isothermal sections of the Ti-Cr-Si system at 1000°C constructed by Lysenko et al. [36] based on 135 alloys annealed at 1000°C for 650 to 1200 hours (open circles represent single phase region, half-filled circles denote 2-phase regions, and filled circles (dots) refer to 3-phase regions).
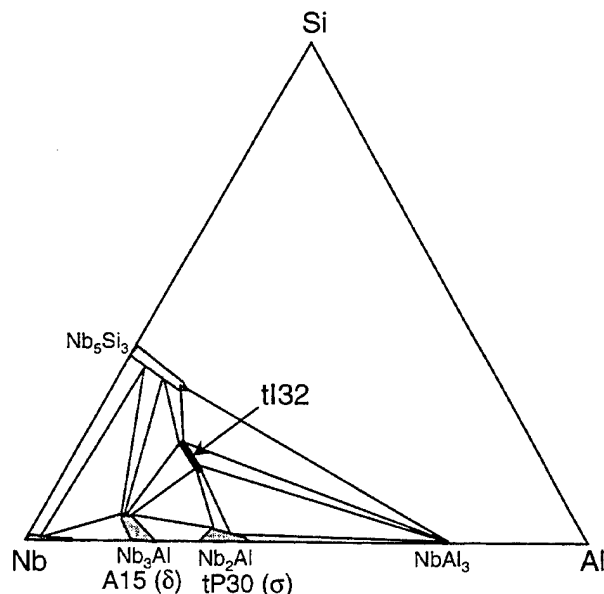
Fig. 9 A partial 1500°C isothermal section of the Nb-Si-Al system by Pan et al. [37]

al. are slightly different. Thus, when the Al additions to the Nb-Si alloys are beyond 5at.%, an A15-type Nb_3Al phase will appear in the ternary system. The solubility of Al in the phases will be strongly dependent on the Ti concentration in the composites. It is unknown whether the A15 Nb_3Al phase will be beneficial or detrimental to creep-rupture properties.

488
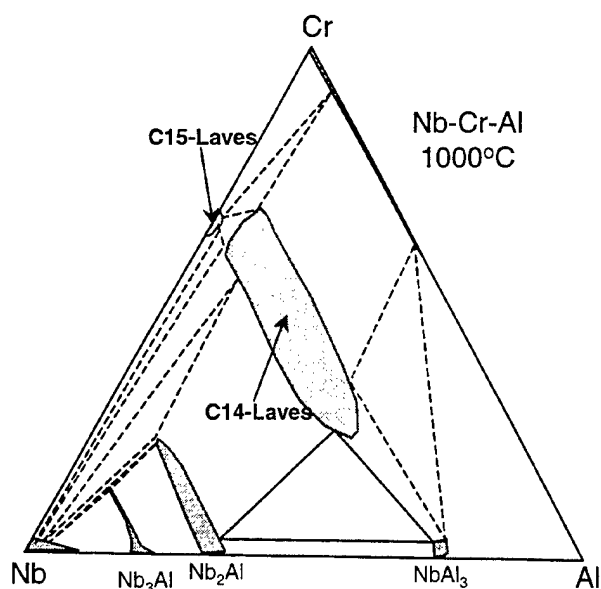
Fig. 10 Isothermal section at 1000°C of the Nb-Cr-Al system obtained by Hunt and Raman [39].

In composites with Cr additions, the Al additions may help promote the C14 Laves phase instead of the A15 Nb₃Al phase. This can be appreciated by examining the Nb-Cr-Al phase diagram. An isothermal section at 1000°C was reported by Hunt and Raman [39], as shown in Fig. 10. The C14 Laves phase may be a simple line compound instead of having a significant variation of Nb composition as shown in Fig. 10. Some of the off-stoichiometric (different from 33.3 at.% Nb) compositions might have formed the C14 Laves phase during solidification (primary liquidus surface of C14 Laves). The Laves phase had not fully decomposed after only a 168-hour (1-week) anneal at 1000°C due to its sluggish decomposition kinetics. In general, Al additions to the composites are likely to be incorporated into the bcc(Nb), Nb₅Si₃ and C14 Laves.

Thermodynamic Modeling

The basic binary and ternary phase diagrams shown in Figs. 1 to 6 and Figs. 8 to 10 describe the effect of alloying on phase equilibria in these composites. However, these basic diagrams cannot accurately predict the phases and their compositions in the multicomponent composites. For instance, it is difficult to predict if the NbCrSi phase is more stable than the C14 Laves phase when several elements such as Ti, Hf, and Al are added at the same time. The solubility of theses elements in bcc(Nb) and Nb₅Si₃ is difficult to predict in multicomponent solid solutions.

Thermodynamic modeling via the CALPHAD approach [41] provides an easy way to extrapolate the binary and

ternary phase equilibria into the multicomponent system. The following key systems need to be modeled to construct a thermodynamic database for the Nb-Ti-Si-Hf-Cr-Al system [42].

Binary systems: **Nb-Ti, Nb-Si, Nb-Hf, Nb-Cr, Nb-Al, Ti-Si, Ti-Hf, Ti-Cr, Ti-Al, Hf-Si, Cr-Si, Al-Si, Hf-Cr, Hf-Al, and Cr-Al.**

Ternary systems: **Nb-Ti-Si, Nb-Ti-Hf, Nb-Ti-Cr, Nb-Ti-Al, Nb-Si-Hf, Nb-Si-Cr, Ti-Si-Cr,** Nb-Si-Al, Nb-Cr-Al, Ti-Si-Al, and Ti-Cr-Al.

The systems shown in **bold** above have either been modeled or are in the process of being modeled. The rest of the systems need to be assessed in the future.

Concluding Remarks

In order to achieve an optimum balance of properties, the Nb-Ti-Si-Cr-Hf-Al composites will contain bcc(Nb), Nb₅Si₃ and possibly C14 Laves, as predicted from the phase equilibria presented in this paper. This is schematically shown in Fig. 11. To balance the properties, the desired volume percents of the phases typically are: 40-45% bcc(Nb), 45-55% Nb₅Si₃ (silicide), and 0-15% C14 Laves. This multicomponent phase diagram is constructed based on the assumption that: 1) the Ti additions are < 25 at.% to prevent the formation of the hP16 Ti₅Si₃ phase, but Ti is high enough to destabilize the NbCrSi phase; 2) the Hf additions are < 10 at.% to prevent the formation of both Hf₅Si₃ and Hf₂Si; and, 3) the Al additions are low enough so that no Nb₃Al or other phases are formed. In composites formed by casting or directional solidification, there will probably be some Nb₃Si phase, but it will be very likely that Nb₃Si will decompose into bcc(Nb) and Nb₅Si₃.
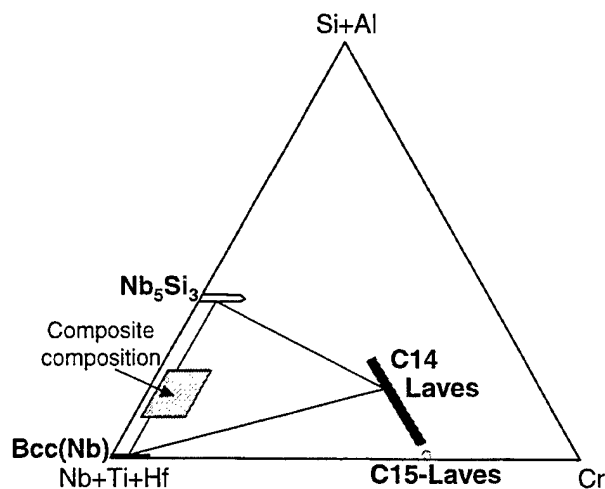

Fig. 11. Schematic diagram showing the major phases in the Nb silicide-based composites.

Ni-base superalloys have been used for half a century, but only in recent years has a multicomponent thermodynamic database been constructed. The thermodynamic data can now predict phase stability of multicomponent superalloys with good accuracy [42]. The present review describes the present understanding of phase stability in the Nb silicide composites (as it has been developed in parallel with the alloy development efforts). The accompanying understanding of the basic binary and ternary systems reviewed in this paper has contributed significantly to the development of the Nb silicide-based composites that show a promising balance of properties. With the high-efficiency diffusion multiple approach [31,32] and the state-of-the-art thermodynamic modeling software, it may be possible to both determine the phase diagrams of the basic ternary systems and perform thermodynamic modeling ahead of the alloy development. This methodology provides a tool that allows predictive design of multicomponent composites.

References

1. M.G. Mendiratta and D.M. Dimiduk, Mat. Res. Soc. Symp. Proc., 133 (1989), 441- 446.
2. M.R. Jackson, B.P. Bewlay, R.G. Rowe, D.W. Skelly, and H.A. Lipsitt, JOM, 48 (1996), 39-44.
3. P.R. Subramanian, M.G. Mendiratta, and D.M. Dimiduk, JOM, 48 (1996), 33-38.
4. B.P. Bewlay, J.J. Lewandowski, and M.R. Jackson, JOM, 49 (1997), 44-45.
5. S.J. Balsone, B.P. Bewlay, M.R. Jackson, P.R. Subramanian, J.-C. Zhao, A. Chatterjee, and T. Heffernan, in this Proceedings.
6. M.E.Schlesinger, H. Okamoto, A.B. Gokhale, and R. Abbaschian, J. Phase Equilibria, 14 (1993), 502.
7. M.G. Mendiratta and D.M. Dimiduk, Scripta Metall. Mater., 25 (1991), 237-242.
8. B.P. Bewlay, H.A. Lipsitt, M.R. Jackson, W.J. Reeder, and J.A. Sutliff, Mater. Sci. Eng., A192/193 (1995), 534-543.
9. B.P. Bewlay, M.R. Jackson, and H.A. Lipsitt, J. Phase Equilibria, 18 (1997), 264-278.
10. B.P. Bewlay, M.R. Jackson, and R.R. Bishop, J. Phase Equilibria, 19 (1998), 577-586.
11. P.R. Subramanian, M.G. Mendiratta, and D.M. Dimiduk, Mat. Res. Soc. Symp. Proc., 322 (1994), 491- 502.
12. J.-C. Zhao, B.P. Bewlay, M.R. Jackson, and L.A. Peluso, to be published.
13. M.R. Jackson, R. G. Rowe, and D. W. Skelly, Mat. Res. Soc. Symp. Proc., 364 (1995), 1339-1344.
14. B.P. Bewlay, M.R. Jackson, and M.F.X. Gigliotti, in Intermetallic Compounds - Principles and Practice, Vol. 3, Eds. R.L. Fleischer and J.H. Westbrook, John Wiley, New York, 2001, In print.
15. B.P. Bewlay, J.A. Sutliff, and R.R. Bishop, J. Phase Equilibria, 20 (1999), 109-112.
16. J.-C. Zhao, B.P. Bewlay, M.R. Jackson, and Q. Chen, J. Phase Equilibria, 21 (2000), 40-45.
17. B.P. Bewlay, R.R. Bishop, and M.R. Jackson, Z. Metallkd., 90 (1999), 413-422.
18. J.-C. Zhao, B.P. Bewlay, and M.R. Jackson, to be published.
19. A.B. Gokhale and G.J. Abbaschian, Bull. Alloy Phase Diagrams, 10 (1989), 390-393.
20. C.E. Brukl, "Ternary Phase Equilibria in Transition Metal-B-C-Si Systems. Part I. Binary System, Vol. 13. The Zr-Si and Hf-Si Systems", Tech. Rep. AFML-TR-65-2, Air Force Materials Lab., WPAFB, OH, 72 p. (1968).
21. H. Nowotny, E. Laube, R. Kieffer, and F. Benesovsky, Monatsh. Chem., 89 (1958), 701-707.
22. O.G. Karpinsky and B.A. Evseyev, Russ. Metall., 3 (1969), 128-130.
23. A. Fernandez Guillermet, J. Alloys Compounds 234 (1996), 111.
24. A.J. Schwartz, M. Kumar, and B.L. Adams, Electron Backscatter Diffraction in Materials Scicence, Kluwer Academic / Plenum Publishers, New York, 2000.
25. M. Venkatraman and J.P. Neumann, Bull. Alloy Phase Diagrams, 7 (1986).
26. J.G. Costa Neto, S.G. Fries, and H.L. Lukas, CALPHAD, 17 (1993), 219-228.
27. J.L. Murray, Phase Diagrams of Binary Titanium Alloys, ASM International, Materials Park, OH,1987, 68-78 (Cr-Ti)
28. W. Zhuang, J. Shen, Y. Liu, L. Ling, S. Shang, Y. Du, and J.C. Schuster, Z. Metallkd., 91 (2000), 121-127.
29. K.C. Chen, S.M. Allen, and J.D. Livingston, Mat. Res. Soc. Symp. Proc., 364 (1995), 1401.
30. H. J. Goldschmidt and J. A. Brand, J. Less-Common Met., 3 (1961), 34-43.
31. J.-C. Zhao, Adv. Eng. Mater., 3 (2001), 143-147.
32. J.-C. Zhao, J. Mater. Res., 16 (6) (2001), in print.
33. J. Steinmetz, B. Malaman, and B. Roques, J. Less-Commnon Met., 57 (1978), 133-146.
34. P.I. Kripyakevich, Ya.P. Yarmolyuk, and E.I. Gladyshevskii, Sov. Phys. Crystall., 13(5) (1968), 677-681.

35. J. Steinmetz, B. Malaman, J.M. Albrecht, and B. Roques, Mater. Res. Bull., 10 (1975), 571-576.

36. L. A. Lysenko, V. Ya. Markiv, O. V. Tsybukh, and E. I. Gladyshevskii, Inorganic Mater., 7(1) (1971), 157-159.

37. V.M. Pan, V.L. Latysheva, O.G. Kulik, A.G. Popov, and E.N. Litvinenko, Russ. Metall., (4) (1984), 233-235.

38. C.E. Brukl, H. Nowotny, and F. Benesovsky, Monatsh. Chem., 92 (1961), 967-980.

39. C.R. Hunt and A. Raman, Z. Metallkd., 59 (1968), 701-707.

40. N. Saunders and A.P. Miodownik, CALPHAD, Elsevier Science Inc., New York, 1998, Chapter 10.

41. H. Liang and Y.A. Chang, Intermetallics, 7 (1990), 561-570.

42. N. Saunders, in Superalloys 1996, Eds. R.D. Kissinger, D.J. Deye, D.L. Anton, A.D. Cetel, M.V. Nathal, T.M. Pollock, D.A. Woodford, TMS, Warrendale, PA, 101-110.

Materials Beyond Superalloys - Exploiting High-Temperature Composites

S.J. Balsone, B.P. Bewlay, M.R. Jackson, P.R. Subramanian, J.-C. Zhao, A. Chatterjee, and T. Heffernan

MATERIALS BEYOND SUPERALLOYS - EXPLOITING HIGH-TEMPERATURE COMPOSITES

S.J. Balsone*, B.P. Bewlay*, M.R. Jackson*, P.R. Subramanian*, J.-C. Zhao*, A. Chatterjee[+], T.M. Heffernan[#]

*General Electric Company, Schenectady, NY 12301
[+] Materials & Processes, Speed Code W-05, Rolls-Royce Corporation, 2001 S. Tibbs Ave., Indianapolis, IN 46268
[#] Allison Advanced Development Company, Indianapolis, IN 46241

Abstract

Temperatures of blade surfaces in advanced aircraft engines are approaching superalloy limits. Innovations in refractory metal-intermetallic composites (RMIC's) are being pursued in systems based on Nb-Ti-Si and Mo-Si-B. These systems have the potential for service at surface temperatures > 1350°C. If either system is to be employed, a balance of properties is required for many different behaviors that must be integrated into a workable design, and affordable fabrication of the composite components must be possible. Progress in the development of tough high-temperature composites for aircraft engine applications will be compared to performance needed to make these materials competitive choices for future turbine designs.

Introduction

Land-based gas turbines and aircraft engines have several different gages of system performance. Fuel efficiency in producing power or thrust is an important gage, and increasing the combustion temperature generally leads to efficiency improvements. Reducing the cooling air demand also improves efficiency, since less of the work done in compressing the air for combustion is lost to supplying a portion of that compressed air to cool the hot metallic components. For both of these gages, an increase in metal temperature capability can improve performance. Another measure of system performance relates to service reliability – the time between outages for turbines, or the time-on-wing for engines. An increase in metal temperature capability can generally be exploited by life extension, by higher firing temperature, or by a combination of higher firing temperature and life extension. Generally, if increased capability is taken in part as life extension, the component made from the new material will have less damage in service, and will show a greater repair yield than would a less-capable alloy.

For rotating components, performance improvements can also be achieved without an increase in firing temperature or metal temperature. Stronger materials and lighter materials can provide increased specific strength (strength/density). For materials that are stronger at the critical stress-temperature points of turbine blades (or buckets) than are the currently used materials, airfoil mass can be reduced, provided a thinner airfoil wall can be manufactured. For materials with similar strength to current alloys but with a lower density, a reduction in airfoil mass can be achieved at the same wall thickness. If the airfoil mass can be reduced significantly, the centrifugal stress on the rotor is reduced, and a smaller, lighter rotor can be achieved (as will be discussed subsequently). This can have a major impact on thrust-to-weight performance of the turbine.

Hot-section materials development has made a critical contribution to performance gains of both gas turbines and jet engines. Advances in processing of Ni-base superalloys have allowed evolution of microstructure from equiaxed structures three and four decades ago, to directionally solidified (DS) multi-grain and single crystal (SC)

components today. With added capability from compositional flexibility coupled to processing [1] over that time period, high pressure turbine blade temperatures have increased by 125°C. Metal surface temperatures at the hottest locations on state-of-the-art jet engine airfoils now approach 1150°C, not only in a "hot streak" condition (hotter than the design intention, due to combustor or vane performance anomalies), but also at the thermal condition intended by the design. Thermal barrier coatings (TBC's) provide insulation from the hot gas, so that TBC surface temperatures are appreciably higher. The most severe combination of stress and temperature in present engine designs corresponds to bulk average metal temperatures approaching 1000°C, using the first- and second-generation single crystal alloys. These materials (alloys developed in the 1970's and 1980's) rely on the use of substantial additions of W, Ta, Mo and Re to strengthen the γ and γ' phases. The concentration of the sum of these elements has been further increased in the third- and fourth-generation single crystals, to >20w/o levels. These newest superalloys may allow metal surface temperatures of 1200°C and bulk average temperatures of 1050°C.

Substantial improvement beyond the fourth-generation single crystal alloys will be very difficult to implement for Ni-base systems. Most advanced superalloys melt at approximately 1350°C. Depending on processing and heat treatment, chemical segregation in the superalloy can lead to incipient melting at ~1270°C. The interaction zone created between the bond coating (such as NiAl or Pt-modified NiAl) and the single crystal airfoil can also lead to melting point reductions, to <1250°C. In service, the TBC can be lost due to foreign object damage or excessive growth of the protective alumina scale. Should the TBC be lost, the nominal maximum local metal surface temperature may rise above 1200°C, and coating interaction zone melting, or incipient melting of the alloy may occur. Single crystal superalloy strength levels may be improved to allow bulk average temperatures in excess of 1050°C, but any increase toward a 1200°C metal surface temperature may require substantial gains in TBC damage tolerance and reliability, as well as the melting point of the complex coating interaction zone.

High-temperature materials are needed which can survive well beyond the 1200°C limit to metal surface temperature that appears to be a major barrier for Ni-base superalloy single crystals. Ideally, a new family of materials will have high melting point, low density, good oxidation resistance to 1300-1400°C, and exceptional high-temperature strength (Figure 1). The Nb-Si based intermetallic composite system is being developed toward these goals. However, in even meeting these awesome requirements, there will be many other barriers to surpass, ranging from ballistic impact resistance to fracture toughness, to component cost.
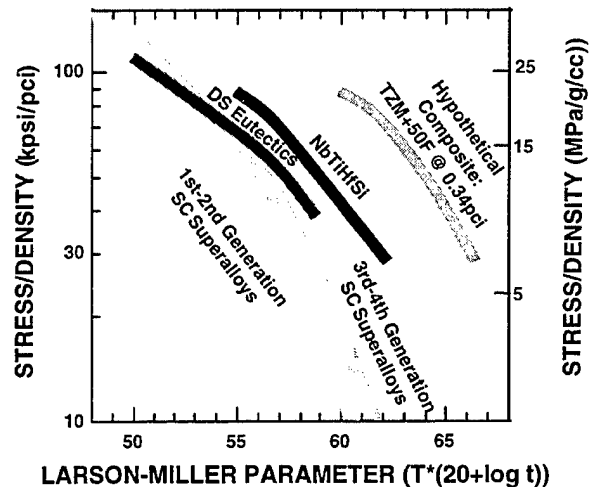
Figure 1: Specific strength of Nb-25Ti-8Hf-16-18Si is compared to single crystal superalloys and directionally solidified eutectics using the Larson-Miller parameter (°R, hours). Included is a curve for a hypothetical material 50°F better than TZM Mo, with a density of 9.4g/cc (.34pci), as an estimate of possible properties for a Mo-Si-B based RMIC [2]. (pci refers to pounds / cubic inch).

Experiences In New Materials Implementation

One of the major challenges facing the materials community during the development of any new high temperature material is finding a balance of mechanical properties that satisfies all of the engineering requirements. The alloy developer must make such engineering trade-offs, for example, between high temperature strength and creep resistance with low temperature ductility, toughness, and damage tolerance. In such cases, successful alloy development must be guided by the design requirements of the particular application under consideration. Without these design requirements, the alloy development occurs in a vacuum, and the probability of successful new material introduction into product is very low. This is particularly true when we look at the introduction of new, high temperature material systems that are only useful when the component is designed to take full advantage of the material's unique properties while at the same time, minimizing the impact of the less desirable characteristics. A good example of this is component design using materials with highly anisotropic material properties. Therefore, it is imperative that for cost-effective new materials development and implementation, a strong coupling of the design community and design requirements with materials development must occur as early as possible in the development cycle. In cases where this was done too late or not at all, critical materials properties, processing requirements, and other factors, such as cost, were not adequately addressed with the end result being the new material never made it into production hardware. There is a tendency to wait to address the most difficult and critical roadblocks because we don't want to give a new material a "black eye" too early in the development cycle. Too often

once this happens, the risks are viewed as too high, and continued development is stopped. In today's environment, new materials development must be done with full knowledge of the specific design requirements so that major issues are identified early in the development cycle. The following are several examples of large new materials development activities that resulted in limited application of these materials in high payoff applications because we waited too late or missed entirely one (or more) of the critical design requirements, including cost.

Directionally Solidified Eutectics: The anticipated improved performance over single crystal superalloys for directionally solidified *in situ* composites was achieved with Ni matrices strengthened with phases such as monocarbide fibers or Ni_3Nb lamellae [3-5]. These composites were developed in the 1980's and had stress rupture resistance matching or exceeding that of today's third- and fourth-generation single crystal superalloys at the temperatures of the critical blade design points. Aligned eutectics were produced in alloys that incorporated strong, ductile composite matrices that were full-complexity multi-element compositions derived from a rich knowledge of Ni-base superalloys. These eutectics possessed very-high-temperature strength (>120 MPa for 1000 hours at 1100°C). However, a number of potential obstacles were uncovered during development. Through alloy iterations, these obstacles were overcome: oxidation and fatigue behaviors were improved, transverse ductility was improved with boron additions, carbide stability during thermal cycling was excellent for a broad range of composite compositions, and matrix stability during cyclic thermal exposure was improved, providing excellent property retention [3]. Engine tests were successful [5-6], both for solid and hollow eutectic blades. However at that time, low processing rates ultimately prevented implementation of these materials. The low solidification rates required for aligned microstructural growth (typically $< 3 \times 10^{-2}$ cm/min) and the small numbers of parts that could be manufactured in a single furnace cycle resulted in large numbers of furnaces being required for the anticipated production volumes. The financial investment proved very high, and the return on investment too low to make this technology economically attractive. As a result, DS Ni-base eutectics never made it into production.

NiAl Intermetallics: During the late 1980's, there was a significant investment in the development of nickel aluminide, NiAl, based materials for high temperature applications [7]. Because of NiAl's lower density as compared to state-of-the-art Ni-base superalloys, NiAl appeared very attractive on a specific strength basis for such applications as high temperature gas turbine airfoils. Oxidation resistance of these alloys was very good. The focus of the early alloy development efforts was on improving the poor room temperature ductility and high-temperature strength of these alloys. A large research effort

resulted in some improvement in room temperature ductility values and significant improvement in high-temperature strength, and the design community began to look at design concepts for turbine blades and vanes to accommodate the low ductility and poor fracture behavior at low temperatures. Prototype NiAl turbine blades and vanes were manufactured, and plans were put in place to engine test these NiAl parts in demonstrator engines. Impact tests were run early in the development phase of the program, and testing continued with the promising alloys. The results demonstrated that the ballistic impact resistance was inadequate for blade engine conditions, but could be adequate for vane applications. For this reason the program emphasized vane applications. Innovative attachment concepts to prevent cracking due to thermal expansion mismatch between the NiAl airfoils and surrounding Ni-base superalloy structures were successfully tested in a small turboshaft engine without cracking of the NiAl vanes. However, a business case for introducing NiAl just for vane applications could not be made, and further work on NiAl implementation for gas turbine applications ceased.

TiAl Intermetallics: Another intermetallic material of particular interest to the gas turbine engine community is the titanium aluminide TiAl [8]. TiAl alloys promise to extend the temperature capability of titanium-base materials and to replace much heavier Ni-base superalloys in some applications with a material one-half the density. TiAl alloys appear to have attractive mechanical properties, such as high specific strength, specific modulus, specific creep resistance, and good oxidation/hot corrosion resistance. Research on TiAl alloys started in the early 1970's, and there has been a tremendous investment in alloy and process development for TiAl over the past decade. Development of TiAl intermetallic materials still continues today across the materials community. TiAl alloys appear to be close to application and to have great potential for widespread implementation. However, with the exception of a few non-aerospace related applications, for example turbocharger rotors and auto engine valves, and several gas turbine engine components that have been engine tested (e.g. bearing support seal, low pressure turbine blades, compressor blades), TiAl has yet to break into large-scale production. Gas turbine engine applications envisioned for TiAl include compressor blades, vanes, shrouds, turbine disk cover plates, blade outer air seals, and low pressure turbine blades. Also under consideration are large static structures, such as diffusers, ducts, and cases. For many of these applications, TiAl alloys can be produced as a casting or in wrought form. Slight chemistry variations and changes in processing can result in dramatic changes in the microstructural condition of TiAl alloys. As a result, there is quite a large window for manipulating microstructure and tailoring the balance of mechanical properties for a given application. Significant interaction between designers and materials developers will be required to take maximum advantage of TiAl's high temperature properties for any

one of the wide variety of potential applications. Some applications have been limited because of scale-up difficulties and final part cost. Other applications demand greater high temperature strength/creep resistance, or improved damage tolerance, to make TiAl a viable candidate material. Selection of an alloy chemistry, processing route, product form, and final manufacturing process will rely heavily on the specific component design requirements.

Candidate Innovative Materials

For the high temperature applications envisioned for the next advances in jet engines, Nb- and Mo-based RMIC's are considered to be the most likely candidates [9-17]. These are metal-toughened, intermetallic-strengthened composites with volume fraction of metallic phase of between 0.35 and 0.6. The Nb-RMIC's consist of a bcc Nb solid solution, with Nb_3Si and/or Nb_5Si_3 silicide phases; a small volume fraction (<0.15) of a $NbCr_2$-based Laves phase, can also be added for improved oxidation resistance. A typical composition is Nb, 22a/oTi, 4a/oHf, 4a/oCr, 2a/oAl, 16a/oSi. The Mo-RMIC's consist of a bcc Mo solid solution, with Mo_5SiB_2 T2 phase, and in some cases a small amount of Mo_3Si [2, 16-17]. A typical composition might be Mo, 8a/oSi, 16a/oB.

The refractory metals Nb and Mo have been previously identified as being most suited to the engine environment [18]. Both Nb and Mo have wide solubility for a number of strengthening additions; Nb is inherently ductile at room temperature, and has a relatively low density (lower than Ni) of $8.56g/cm^3$; Mo has a higher density ($10.2g/cm^3$), and relatively low ductility at room temperature. The room temperature ductility of Mo-based metals can be improved by thermo-mechanical processing, but on subsequent high-temperature exposure, the ductility generally reverts to the levels inherent to Mo. Both metals have substantial oxidation limitations, and their RMIC's depend on an intermetallic phase to provide the high-temperature oxidation resistance. For an appreciable range of chemistries, oxidation resistance better than fourth-generation superalloys has been achieved. Both composite systems also have been alloyed to exceed the rupture strength of fourth-generation superalloys at stresses <175 MPa. To date, very few compositions have been evaluated for both oxidation resistance and rupture strength, and results for compositions surpassing fourth-generation superalloys in both oxidation and rupture have not been published. Melting points of these composites are in excess of 1750°C. Densities of the Nb-RMIC's are in the range of 6.6-7.2 g/cc, while for the Mo-RMIC's, the values are 8.6-9.4 g/cc. Fracture toughness of the Nb-based RMIC system
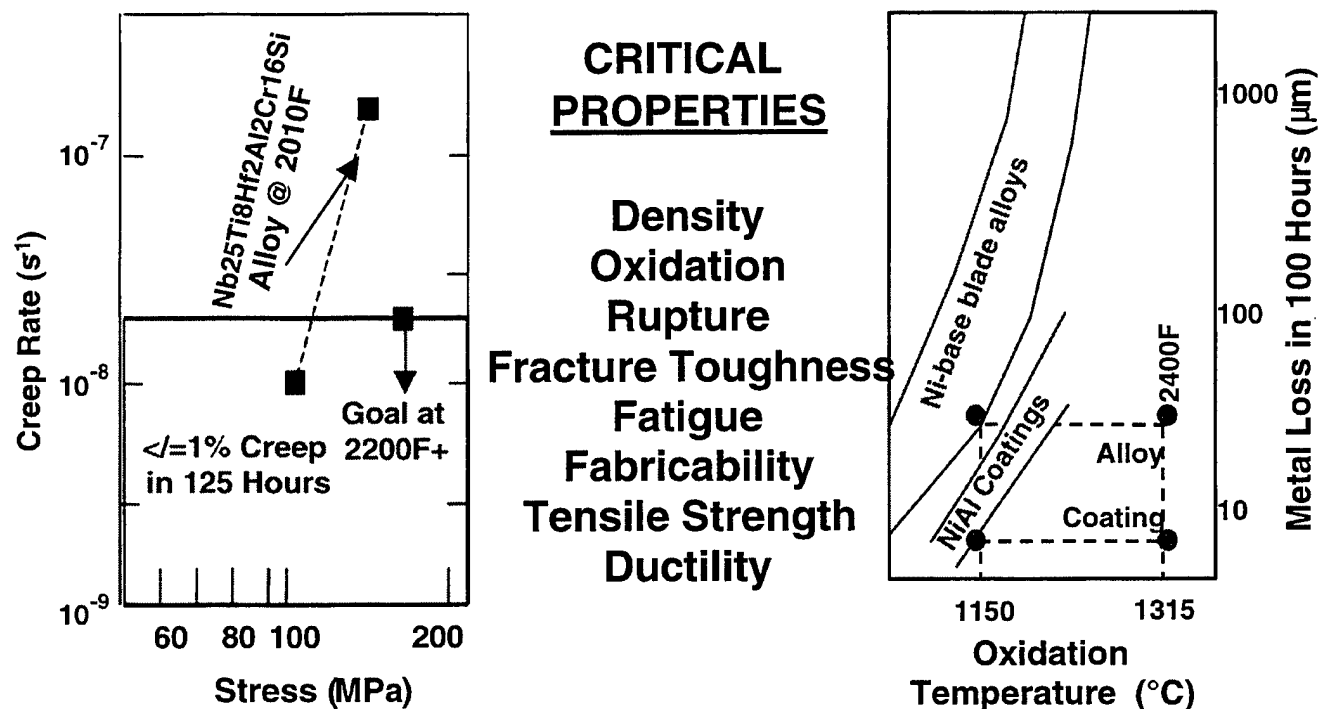

Figure 2: Many properties must be balanced for new materials to be useful. In particular, <1% creep is desired in 125h at >1200°C (2200°F) for tensile stresses of at least 175 MPa (25 Kpsi); oxidation losses for the RMIC and its coatings at 2400°F (1315°C) should be no more than the losses that superalloys and their coatings exhibit at 2100°F (1150°C).

has reached >20 MPa m$^{0.5}$ [10], while values for the Mo-based RMIC are generally <15 MPa m$^{0.5}$. The differences in fracture toughness are reflected in the fatigue behavior of the RMIC's, with the Nb-RMIC showing metallic da/dN – ΔK response, and the Mo-RMIC displaying ceramic-like response [10, 19-20].

For either RMIC system to be exploited, a balance of properties must be achieved for many different behaviors, these behaviors must be integrated into a workable design, and an affordable method of fabrication of the composites must be possible. Both systems represent innovations aimed at surpassing fourth generation single crystal Ni-superalloys, but current funding restraints for advanced systems dictate that only one system is likely to be exploited. The following discussions will concentrate on the Nb-RMIC's, whose density, fracture toughness, fatigue behavior, and fabricability show an advantage compared to Mo-RMIC's. The preliminary creep and oxidation properties indicate that (in the opinions of the authors) these Nb-RMIC alloys may be capable of being integrated into blade designs with substantial weight and cooling savings payoffs relative to fourth-generation superalloy blade designs.

Design-Materials Integration

In November 1998, the Air Force awarded the team of General Electric and Allison Advanced Development Company a contract to develop the materials, processes, and fabrication techniques for the demonstration of Nb-Si intermetallic airfoils for aero-engine turbine applications. The team recognized early in the contract the need for clear property goals for the development of Nb-Si alloys. During the structuring of the technical program, a task was included to conduct design trade studies. This task was to provide the alloy developers with detailed material property requirements for specific airfoil applications. These material property requirements allowed the alloy developers to identify shortfalls in material property capability during the alloy screening process. It also allowed them to track progress toward attaining the required properties for candidate Nb-Si alloys. Material property requirements were ranked in priority of importance to the airfoil design, and sensitivity trade studies were conducted to understand the design payoff/benefit for making changes in any given material property.

The design trade study was structured so that results were continually updated and refined as additional physical and mechanical property data were generated. In this way the fidelity of the design and the resulting material property requirements increased throughout the execution of the contract. A preliminary set of mechanical properties for a "generic" Nb-Si alloy was provided as initial input, and simple, preliminary design tools were used to size the

airfoil and establish temperature profiles. This set the material creep requirements and oxidation requirements. Oxidation and creep resistance became two of the primary screening criteria during the alloy development in the program (see results in next section). The design studies also considered the requirements for bondcoat and thermal barrier coating application to Nb-Si alloy substrates. The effect of coating thickness and the impact of changes in TBC conductivity with time were investigated. These studies helped to establish the preliminary coating requirements for airfoil design and application. As additional mechanical property data on Nb-Si alloys are generated, especially fatigue, fatigue crack growth, and impact resistance, the design trade studies will employ more sophisticated design tools, and produce more robust life calculations for a given airfoil design concept.

Inherent in conducting these design trade studies to determine material property requirements is the selection of an airfoil configuration. In the Air Force contract, several airfoil design concepts were investigated to determine the airfoil configuration that best took advantage of the unique balance of material properties offered by Nb-Si alloys. Included in the analysis of an airfoil design concept were the issues of fabrication, including any required machining of Nb-Si material and bonding/joining to other materials. Selection of leading airfoil configurations included system payoff/benefits to the component efficiency and the overall aero-engine performance. Table I shows the calculated turbine rotor weight for Nb-Si and Mo-Si (using density and rupture properties used in constructing Figure 1) alloy airfoils relative to a current Ni-base superalloy blade and disk configuration. This type of design trade study helped to establish the system performance enhancement resulting from the introduction of new materials, such as these high temperature intermetallic alloys. The interaction between the design community and the materials community has been an important aspect of the current Air Force contract. These interactions help to assure successful materials development and implementation into product.

Table I – Design trade study showing the impact of two intermetallic airfoil concepts on turbine rotor weight.

Rotor Weight Relative to Ni Alloy Baseline	Nb-Ti-Si-X	Mo-Si-B-X
Advanced HPT	Saves 20%	Adds 24%
Current HPT	Saves 22%	Adds 9%
Current LPT	Saves 21%	Saves 13%

State-of-the-Art for Nb-Si RIMC's

Our ongoing research program [21-23] has been evaluating the feasibility of the Nb-RMIC's for aircraft engine blade applications at temperatures where superalloys will be weak or will melt. There is intrinsic thermodynamic stability of the phases in these composites, which is a critical requirement for long term applications at elevated temperatures. Efforts have centered on developing fundamental understanding of the behavior of the Nb-RMIC system, and on improving the oxidation and rupture resistance. Using these results, preliminary studies of how to integrate these materials into advanced designs have been performed. Currently, evaluations are being made of process and fabrication methods best suited to exploit these alloys. Defining the required balance of properties was described in the previous section, and achieving that balance is the focus of on-going work [23]. The status of the material development and design evaluation is reviewed below.

Oxidation: The long-term goal for oxidation behavior is to achieve at 1315°C the 1150°C oxidation life of today's fourth-generation superalloys [23]. The current best Nb-RMIC's miss that target by ~90°C, and closing that gap while achieving rupture strength, fatigue and fracture toughness goals will be difficult. These materials may require more dependence on coatings because of the high surface temperatures. Of course, there may be great value in exploiting these materials at less than the target surface temperatures, since they still offer substantial reductions in airfoil weight and cooling air.

The near-term goal is to achieve sufficient oxidation resistance in the uncoated condition to survive a proposed demanding engine test. The uncoated Nb-RMIC will be expected to lose <200 microns in ten hours of test stand demonstration exposure at 1370°C, if it is to survive the proposed engine test.

In current alloy developments, several design-of-experiment iterations have been performed to characterize oxidation behavior as a function of composition. The main-element effects of Ti, Hf, Si, Cr, and Al, have been determined in terms of weight change or diameter change at temperatures from 760°C to 1370°C. As would be expected, the composition-oxidation relationship varies with varying temperature, so that optimization of chemistry for oxidation resistance will need to consider the length of service in each temperature regime. However, good oxidation resistance can be achieved for chemistries with Nb:[Ti+Hf] ratios of 1.8-2.1 and Si levels of 17-19a/o, which are desired for excellent creep behavior. Both Cr and Al have a strong beneficial role on oxidation behavior.

Elements such as Mo, W, V, Zr and Ta are expected to have a positive influence on creep behavior of the bcc metallic matrix, but all have a negative effect on oxidation behavior, particularly at higher temperatures. Although V, Zr and Mo appear to be most damaging to oxidation behavior, alloys with 1a/o Mo have been shown to suffer little reduction in oxidation resistance compared to Mo-free alloys. Levels of Ta and W (2a/o of each) have demonstrated minimal reduction in oxidation resistance, compared to (Ta, W)-free alloys, and these addition elements are probably the best candidates for achieving a good balance of oxidation and creep rupture behavior.

A number of studies [22,23] have evaluated substitutional elements for some of the main alloying elements, including Ge and B partially substituting for Si, and Fe partially substituting for Cr. The greatest positive effects have been observed for Ge, at levels up to ~6a/o. Small additions of B (2-6a/o) may be helpful, but higher levels are damaging to oxidation resistance. Additions of Fe appear to be equally as effective as Cr at levels up to 5a/o, but combinations of Cr+Fe are no more effective than Cr alone, for the same total concentrations.

Refractory metals are prone to pesting (preferential oxidation at microstructural features such as grain boundaries, coupled with oxygen embrittlement, which can lead to self-pulverization in samples cycled from room temperature to relatively low temperatures, generally <950°C). Additions of Al and Hf are known to reduce the pesting susceptibility of Nb,Ti-based metals, but Nb-RMIC's can still be attacked in this manner. By alloying with ~1.5a/o Sn, the pesting problem has been essentially eliminated in the 750-950°C regime. The addition of Sn has minimal effect on oxidation at >1200°C.

Figure 3 illustrates the state-of-the-art oxidation resistance for the uncoated Nb-RMIC's. The short-term goal has been achieved (losses of <200 microns in ten hours of test stand demonstration exposure at 1370°C). Meeting the long-term goal (<75 microns in 100 hours of oxidation exposure at 1315°C) while also achieving the required balance of properties will be more difficult.

Creep Behavior: Tension and compression creep behavior of Nb silicide-based *in-situ* composites at temperatures in the range 1000 to 1200°C have been investigated in detail [23]. The density-normalized creep rupture behavior of a typical Nb-silicide RMIC (Nb-25Ti-8Hf-16Si-2Al-2Cr) is compared with the creep rupture behaviors of DS and SC Ni-based superalloys in the Larson-Miller plot in Figure 4. These data indicate that the creep rupture behavior of the Nb-silicide RMIC is similar to that of the SC superalloy. Figure 4 illustrates the increase in specific rupture performance that results from the substantial reduction in density of the Nb-silicide
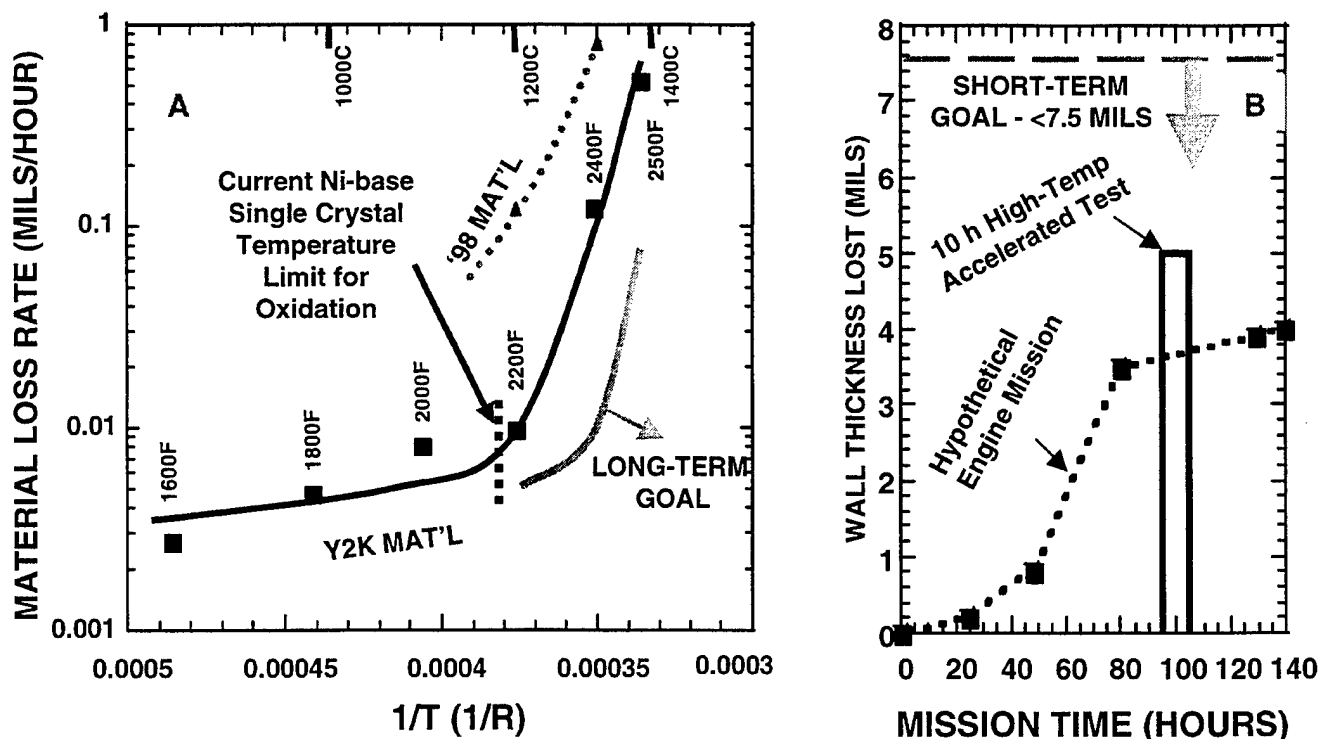
Figure 3: Oxidation behavior of the Nb-RMIC's has been improved ten-fold recently. This satisfies the short-term goal of a hypothetical engine mission (B) (with calculated losses of 100-125 μm, compared to an allowable 190μm). However, the long-term goal (A) requires another ten-fold reduction in oxidation losses.

RMIC. Detailed fundamental investigations of the effects of alloying additions, such as Hf, Ti, Cr, Al and Mo, on the creep behavior have also been performed during the composite development [23]. Creep of composites is controlled by a combined function of creep in the silicide and metallic phases. Creep studies of monolithic Nb_5Si_3 generated from binary and higher order alloys suggests that creep deformation in Nb_5Si_3 is controlled by diffusion of Nb in the Nb_5Si_3 phase [23].

The rupture strength that will be required for future applications will be well beyond performance that has been measured to date. Current estimates are that a

Figure 4: Creep resistance progress. The Nb-Si RIMC has a composition of Nb-25Ti-8Hf-2Al-2Cr-16Si.

further factor of ten increase over present rupture lives may be required for application of the silicide-based composites [23]. The goal for creep performance is that there must be no more than 1% creep in 125 hours at high temperatures and stresses, such as 1200°C and >170 MPa. If there is minimal primary creep (typically, less than 0.1% primary creep in these systems), this corresponds to a secondary creep rate of 2.2×10^{-8} s^{-1}. This has been demonstrated in binary Nb-Si, ternary Nb-Ti-Si, and quaternary Nb-Ti-Hf-Si composites, but not in higher order systems [23].

Coatings: Excellent coatings have been developed for the Nb-RMIC's that can withstand 1370°C for > 100 hours. We have evaluated 12 different potential coating compositions. One of the coatings is shown in Figure 5 in both the as-deposited condition and after 1370°C 100 hours (cycles) exposure. There are cracks formed in the coating probably due to the brittle nature of the coating phases and the difference in coefficients of thermal expansion (CTE) between them. These cracks are self-healing, i.e., they do not propagate with further high temperature exposure or thermal cycling, Figure 5(b). A TBC of yttria-stabilized zirconia (YSZ) was applied on the coating by the air plasma spray (APS) process. The test buttons were made of Nb silicide composites of 2.5 cm diameter and 0.3 cm thick. The specimens with the bond coat and the APS TBC were subjected to furnace cycle tests (FCT) to 870, 1200, and 1370°C. During FCT
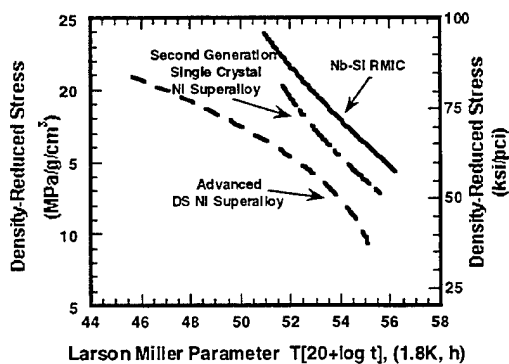
tests, the specimens were heated to the test temperature for 1 hour in air and then taken out of the furnace and cooled for 10 minutes with blowing air from a fan. The specimens were then re-loaded into the high temperature furnace. These tests were repeated for 100 cycles for each temperature. No internal oxidation of the substrate was observed and no pesting was observed at any of the temperatures. In addition, the TBC still adhered to the bond coat after the FCT for 100 cycles at 1370 °C. Very little interaction between the coating and the substrate occurred, i.e., the bond coat was very stable, as shown in Figure 5(b). The coating has also been tested at 1430°C for 50 hours (cycles). There was substantial growth of the interaction zone, but the coating was still protective and there was no internal oxidation. Thus, the coating has the capability up to at least 1400 °C. The performance of the coating was very encouraging and it serves as a base for further coating development.
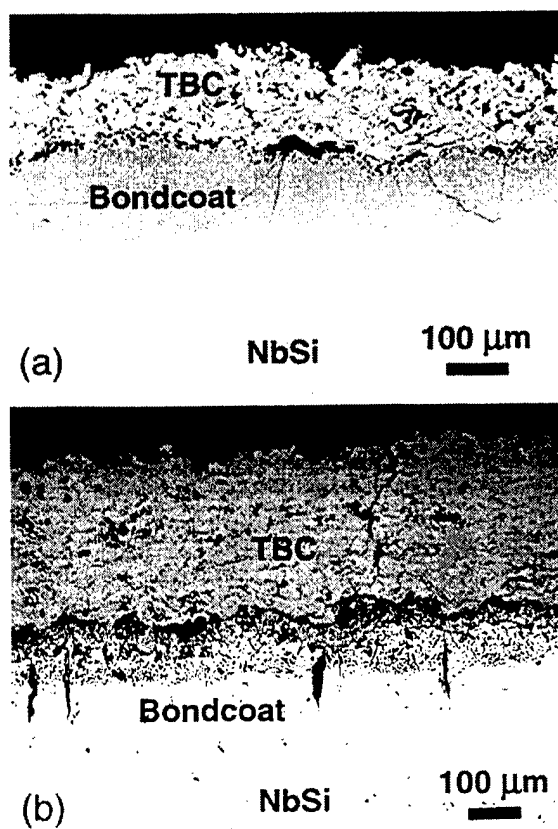

(a) NbSi 100 μm

(b) NbSi 100 μm

Figure 5: Micrographs of a coating developed for Nb silicide composites showing the microstructure in as-deposited condition (a) and after 1370 °C 100 hours (cycles) exposure (b). Cracks in the as-deposited coating did not propagate during cyclic exposure.

Investment Casting: The Nb-Si RMIC's have been fabricated using a range of processes, including arc-melting, ingot casting plus thermo-mechanical processing, directional solidification, vapor deposition, and powder-

metallurgy processing [11]. However, from a practical point of view, investment casting of near-net shape structures of these advanced alloys has received the least attention, partly because of the difficulty of finding ceramic mold materials capable of withstanding the high melting temperatures of the RMIC's. Initial efforts to evaluate the castability of this class of alloys showed some promise [24]. In the present work, the feasibility of investment casting thin sheets of selected Nb-Si RMIC's was explored using a hybrid arc-melting and drop-casting technique that was developed. In this process, the alloys were arc-melted using conventional techniques, and drop-cast into heated ceramic molds. The molds were prepared using conventional slurry techniques. Appropriate face-coats were applied to the ceramic molds to prevent mold-metal interaction. Investment-cast plates with dimensions of 76mm length, 25mm width, and thickness from 3-8mm were obtained with this process. Prototype airfoil shapes were also successfully cast using this technique. Alloys ranging from ternary Nb-Ti-Si to multicomponent Nb-Ti-Hf-Cr-Al-Si-base compositions were investigated. Figure 6 shows backscattered electron (BSE) images of the microstructure of two selected compositions. The phase distribution and compositions in the cast microstructures were similar to those obtained by the other casting processes, and there was no evidence of any gross segregation. Oxygen content was found to be 670 to 1020 wppm; the average is similar to arc-cast materials. Detailed analysis near the mold has not been performed.

Challenges / Issues For Exploiting Nb-Si RMIC's

The trends to date indicate that a promising balance of low-temperature and high-temperature properties can be obtained through appropriate alloying, processing, and microstructural control. However, there is still a limited database of engineering properties on a reduced set of alloys. For further development of the Nb-Si RMICs, fracture toughness no longer appears to be a major barrier, provided that further alloying additions do not reduce the present toughness levels. The levels of toughness measured, the crack growth characteristics, and the ability to perform common cutting, grinding and machining tasks with standard practices, suggest that further improvements in toughness are not critical to the implementation of these RMIC's. However, dynamic impact properties of these alloys have not been investigated, and could be a barrier to their implementation.

Initial fatigue data [10] have been obtained at room temperature; additional fatigue data are required as a function of temperature. Threshold stress intensities (ΔK_{th}) of >10 MPa m$^{0.5}$ will be required with Paris law slopes not greater than 5 for component applications. A systematic effort therefore is required toward generating
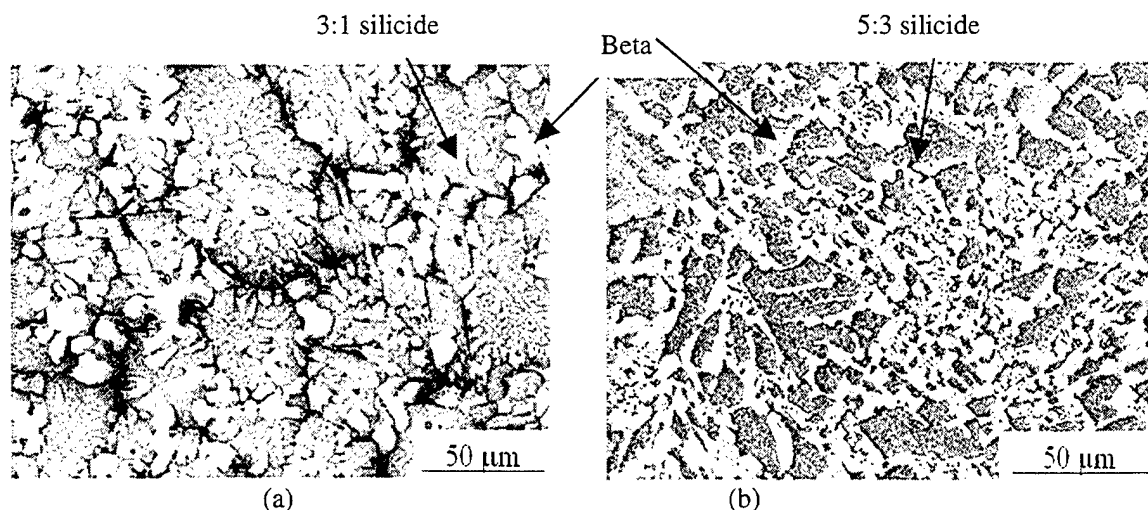
Figure 6. Backscattered SEM microstructures of transverse sections of investment-cast (a) Nb-34Ti-16Si alloy, and (b) Nb-23Ti-2Hf-4Cr-3Al-16Si alloy with 2.5 at.% of additional elements.

properties, such as fracture toughness, fatigue-crack growth, tensile strength, and creep performance, as well as stress rupture, before these alloy systems can be considered for service.

There is a clear need for further research on the effect of composition on both processing and microstructural control. In general, processing methods for these advanced alloy systems have not been sufficiently explored. Traditional processing of the multicomponent, multiphase alloys poses serious technical challenges. Process developments are required to enhance RMIC properties and to establish the capability to manufacture complex articles of these composites. Process developments, such as investment casting and vapor deposition, are relatively unexplored. Investment casting of RMIC's offers a relatively low-cost processing approach for fabricating near net-shape components, such as blades and vanes. However, the casting methods are still at their infancy, and extensive efforts are required to identify high-temperature mold materials and face-coats that are compatible with the RMIC compositions. Vapor deposition of RMIC's offers the potential for designing composite microstructures and complex component articles. However, a sufficient combination of chemistry and microstructure control has to be developed to provide the required balance of high- and low-temperature mechanical properties.

While substantial recent improvements in oxidation resistance have been realized through alloying efforts, a further improvement in the base composite performance of a factor of 10 is required in order to achieve the goal of <25 µm loss per 100 hours for component surface temperatures of 1315°C (2400°F). Even with these improvements, the RMIC's will require oxidation-protective coatings and TBC's for any long-term use in the temperature range of proposed service. The role and performance of coatings for RMIC's are still in their infancy. Although coatings developed to date have shown significant promise in terms of oxidation protection, coating development for the advanced alloys will require additional research on new compositions, as well as coating deposition technologies. The influence of coatings on the mechanical properties of the base RMICs needs to be systematically evaluated. In essence, the challenge in developing these alloys is to extend the oxidation performance and guarantee stability under cyclic conditions, while ensuring the microstructures and mechanical properties achieved to date.

Summary

Very high temperature Nb-Si RMIC systems are attractive candidates for future jet engine turbine components. While superalloy airfoils operate with surfaces at 1150°C, advanced designs will need the Nb-based RMIC's to operate equally successfully at temperatures up to 1315°C; this requires further improvement in rupture and oxidation resistance. Rupture capability has been demonstrated surpassing fourth-generation single crystal Ni-base alloys, and specific rupture is improved because RMIC's possess 20% lower density than superalloys. Coating chemistries and processes for these RMIC's have demonstrated oxidation resistance and retention of TBC's for 100 hours of cycling to 1370°C. Extrusion, directional solidification, and investment casting all have been used successfully to produce RMIC's.

The greatest barrier today to the insertion and exploitation of new materials is the disparity between traditional material/process development cycles and shrinking engine development cycles. Using disciplined, computer-aided practices and accurate performance simulation models, designers have reduced the engine development cycle to

less than four years. Prevailing materials development cycles are twice as long. This disparity too often results in premature material insertion or decisions rejecting any new material insertion. Thus, interest is lost in the potential benefits of new materials and in investing in new materials technology

The differences in behavior between RMIC's and superalloys (ductility, toughness, oxidation, etc) may represent an obstacle. The engine design practice built upon experience with superalloys needs to be modified to account for these differences. It is critical that, very early on, the engine designers become comfortable with the differences in materials behavior. In this way, the designers can develop new tools and practices to take advantage of better materials properties, while designing around weaker properties. The development of new RMIC's is, thus, not simply an alloy/process effort. Instead, strong ties need to be developed between the materials development and engine design communities.

The development of RMIC's can benefit greatly from the approach being developed in the DARPA Accelerated Insertion of Materials (AIM) initiative (the participants include GE, Pratt and Whitney, and Boeing). The principal goal of AIM is to create a process that accelerates the insertion of new materials and processes to achieve parity with the engine development cycle. When it is completed, the process will drive valuable cultural and technical changes for materials development. Design engineers will be early partners in materials development, developers will exploit new tools and information technology to design and analyze new materials, and will learn from and build on previous developments, shortening the development cycle. The development of RMIC's will use these tools when they are available.

References

1. G.L. Erickson, *JOM*, 47, 1995, pp. 36-39.
2. D.M. Berczik, United Technologies Corporation, 1997, US Patent 05693156.
3. D.A. Woodford, *JOM*, 42, 1990, pp. 50-55.
4. T. Khan, *Conf on In Situ Composites-III*, J.L. Walter, M.F. Gigliotti, B.F. Oliver and H. Bibring, eds., Ginn Cust Publ, Lexington MA, 1979, pp. 378-388.
5. C.A. Bruch, R.W. Harrison, M.F.X. Gigliotti, M.F. Henry, R.C. Haubert, and C.H. Gay, *Conf on In Situ Composites-III*, J.L. Walter, M.F. Gigliotti, B.F. Oliver and H. Bibring, eds., Ginn Cust Publ, Lexington MA, 1979, pp. 258-267.
6. R.G. Menzies, C.A. Bruch, M.F.X. Gigliotti, J.A.Smith and R.C. Haubert, *Superalloys 1988*, TMS, 1988, pp. 355-364.
7. R.D. Noebe and W.S. Walston, "Prospects for the Development of Structural NiAl Alloys," *Structural Intermetallics 1997*, eds. M.V. Nathal et al, TMS, 1997, 573.
8. Young-Won Kim and Dennis M. Dimiduk, "Designing Gamma TiAl Alloys: Fundamentals, Strategy, and Production," *Structural Intermetallics 1997*, op cit, 531.
9. M.R. Jackson, B.P. Bewlay, R.G. Rowe, D.W. Skelly and H.A. Lipsitt, *JOM* 48, 1996, pp. 39-45.
10. B.P. Bewlay, J.J. Lewandowski and M.R. Jackson, *JOM*, 49, 1997, pp. 46-48.
11. B.P. Bewlay, M.R. Jackson, and P.R Subramanian, *JOM*, 51, 1999, pp. 32-36.
12. B.P. Bewlay, M.R. Jackson, and H.A. Lipsitt, *Metall. Mater. Trans.*, 27A, 1996, pp. 3801-3808.
13. B.P. Bewlay, R.R. Bishop and M.R. Jackson, *Z. Metallkunde*, 90 (60), 1999, pp. 413-422.
14. P.R. Subramanian, M.G. Mendiratta and D.M.Dimiduk, *JOM*, 48, 1996, pp. 33-38.
15. P.R. Subramanian, M.G. Mendiratta, D.M.Dimiduk, and M.A. Stucke, *Mater. Sci. Eng.*, A239-240, 1997, pp. 1-13.
16. D.M. Berczik, United Technologies Corporation, 1997, US Patent 05595616.
17. H.A. Lipsitt, M. Blackburn and D.M. Dimiduk, in *Intermetallic Compounds – Principles and Practice – Vol. 3*, Eds. R.L. Fleischer and J.H. Westbrook, John Wiley, 2001.
18. R.W. Buckman, Jr. *Alloying*, ASM, 1988, pp. 419-445.
19. D.M. Berczik, United Technologies Corporation, AF Contract F33615-98-C-2874.
20. H. Choe, D. Chen, J.H. Schneibel and R.O. Ritchie, <http://www.lbl.gov/Ritchie/Library/PDF/Mo-TMS.pdf> TMS Fall conference, 2000.
21. M.R. Jackson, R. G. Rowe and D. W. Skelly, *Mat Res Soc Symp Proc. 364*, 1995, pp. 1339-1344.
22. M.R. Jackson and B.P. Bewlay, USAF Delivery order report, AFML, 1998.
23. B.P. Bewlay, M.R. Jackson, and M.F.X. Gigliotti, in *Intermetallic Compounds – Principles and Practice – Vol. 3*, Eds. R.L. Fleischer and J.H. Westbrook, John Wiley, 2001.
24. D.M. Dimiduk, Air Force Research Laboratory, WPAFB, OH, private communication, 1999.

A Diffusion Multiple Approach for Accelerated Design of Structural Materials

J.-C. Zhao, M.R. Jackson, L.A. Peluso, and L. Brewer
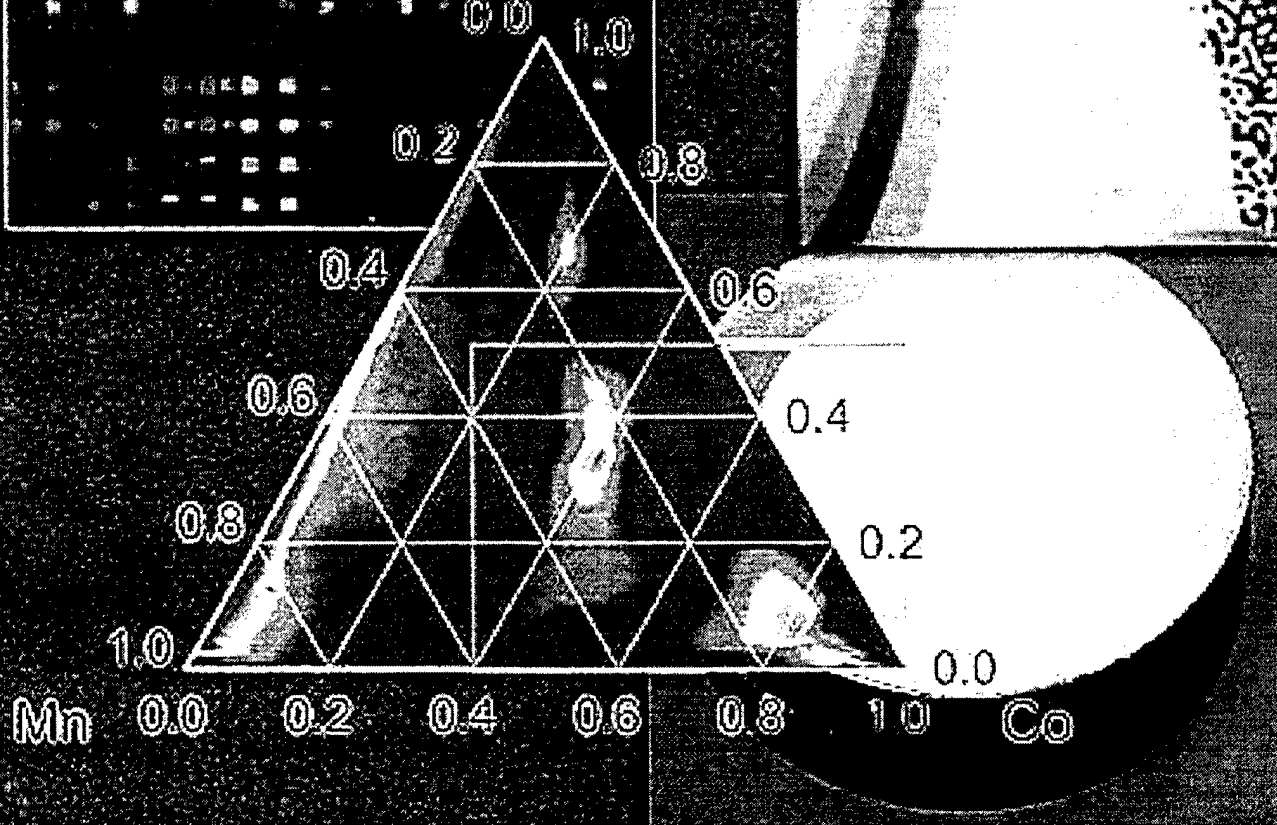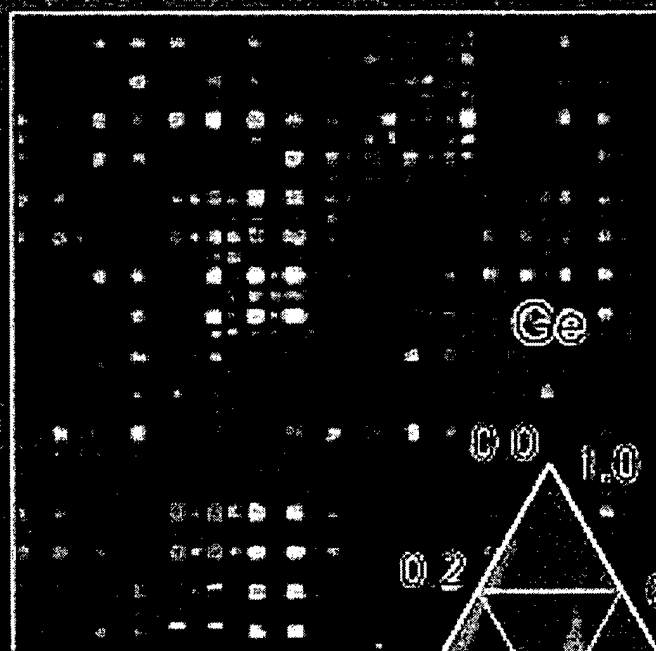
MRS Bulletin, April 2002

Combinatorial Materials Science

Ge

Co

1.0

0.2

0.8

0.4

0.6

0.6

0.4

0.8

0.2

1.0

0.0

Mn   0.0   0.2   0.4   0.6   0.8   1.0   Co

A Diffusion Multiple Approach for the Accelerated Design of Structural Materials

Ji-Cheng Zhao, Melvin R. Jackson, Louis A. Peluso, and Luke N. Brewer

Abstract

A diffusion multiple is an assembly of three or more different metal blocks, in intimate interfacial contact, that is subjected to a high temperature to allow thermal interdiffusion. The power of using a diffusion multiple approach in the efficient mapping of phase diagrams and materials properties for multicomponent alloy systems is illustrated in this article using several examples. It is now possible to map phase diagrams and materials properties at an efficiency some 3 orders of magnitude higher than the conventional one-alloy-at-a-time approach. With this high efficiency, many critical materials data that otherwise would be too time-consuming and expensive to acquire can be obtained and employed to accelerate our understanding of a system's materials physics and chemistry. It is postulated that coupling the diffusion multiple approach with the CALPHAD (calculation of phase diagrams) method will have a significant impact on the computational design of materials.

Keywords: *combinatorial methods, diffusion, elastic properties, mechanical properties, nanoindentation, phase equilibria, structural materials.*

Introduction

Structural alloys usually consist of several alloying elements and multiple phases in order to simultaneously achieve and balance several properties such as strength, ductility, modulus, fatigue resistance, and environmental resistance. The fundamental questions facing alloy designers are (1) which elements will be most effective for strengthening, (2) how can the precipitation of desirable phases be induced to strengthen the alloy while avoiding the formation of detrimental phases, and (3) how stable will the precipitates and microstructure be against coarsening and long-term exposure? Addressing these questions requires information such as phase diagrams, solution-hardening effects, and kinetic data. As more advanced alloys are required for more de-

manding applications, alloy developers are resorting to the addition of more alloying elements to achieve the required properties. For instance, advanced Ni-based superalloys have 8–11 elements. As the number of elements increases, the amount of information required to predict the phases and properties of a multicomponent alloy also rapidly increases. The traditional one-alloy-at-a-time approach for measuring phase diagrams and composition–property relationships is too slow for the alloy development process.

The desire for rapid mapping of phase diagrams and materials properties dates back a long way. A brief history can be found in the introductory article in this issue of *MRS Bulletin*. Metallurgists have

been using diffusion couples for more than a century to evaluate diffusion coefficients and phase diagrams by taking advantage of the local equilibrium at the phase interfaces. However, the composition variations generated in the diffusion couples were generally not exploited. Part of the reason is that few microscale probes were then available to measure useful properties. Recent advances in instrumented nanoindentation[1,2] allow the effective measurement of both elastic modulus and hardness from very small areas (4–25 μm^2), thus allowing, for the first time, critical composition–property (hardness and modulus) relationships to be mapped from diffusion couples.[3,4] The elastic modulus can be evaluated either from the slope of the unloading curve when the elastic part of the deformation pushes the indenter out, or from the loading curve when an oscillation is superimposed.[1,2]

To extend the idea into multicomponent systems, a diffusion multiple approach was developed to generate composition variations in order to map the phase diagrams and properties of the systems.[3,4] A diffusion multiple is an assembly of three or more different metal blocks, in intimate interfacial contact, that is subjected to a high temperature to allow thermal interdiffusion. The concept is an extension of a diffusion triple method introduced by Hasebe and Nishizawa[5] and Jin et al.[6,7] A new method of making diffusion multiples using hot isostatic pressing (HIP) and the new idea of using multicomponent alloys as one of the members, coupled with advanced microanalytical techniques such as electron probe microanalysis (EPMA), electron backscatter diffraction (EBSD), and nanoindentation, make diffusion multiples a powerful approach for structural materials research and development. Using multicomponent alloys as one of the members of a diffusion multiple permits facile assessment of the effects of intentional or adventitious composition variations on the alloys' properties.[3,4]

We will show examples to illustrate how diffusion multiples are used to map critical data for structural materials design such as phase diagrams, the solution-hardening effect, and the compositional dependency of the elastic modulus. The impact of this approach to structural materials design will also be discussed. We will then complete the article by describing and commenting on other approaches on the horizon that have potential application to structural materials design.

The Diffusion Multiple Approach

In order to explore the phase relations and properties of the Ni-Fe-Mo system

and the effects of these elements on modifying the properties of a commercial alloy, a diffusion multiple of Ni, Fe, Mo, and the Ni-based superalloy Inconel 706 (IN706) was made by placing quarter-pie-shaped components into a pure Ni tube, as shown in Figure 1.[3,4] Two Ni caps were placed on the top and bottom of the Ni tube and welded in a vacuum using an electron beam. The welded assembly was treated by HIP for 4 h at 1100°C under 200-MPa pressure to provide good contacts among the elements and the alloy. The assembly was then annealed for 1500 h at 1100°C to cause extensive interdiffusion. At the Ni-Mo-Fe tri-junction, where these three elements meet, extensive interdiffusion took place. All of the binary and ternary intermetallic compounds (δ, μ, and P) formed in situ due to diffusion reactions (Figure 1d). The local equilibrium at the phase interfaces allows mapping of the

entire phase diagram from the tri-junction area (Figure 1c), and the phase diagram obtained from this diffusion multiple agrees extremely well with the one in the literature determined from equilibrated bulk alloys.[3,4]

In addition, the diffusion process created composition variations of all of the single-phase regions (including all of the intermetallic compounds),[3,4] which allowed rapid mapping of hardness and elastic modulus as a function of composition for each phase (Figure 1b). For instance, we can quickly find out whether the Ni substitution of Fe in the μ phase changes its modulus and hardness. In this case, no significant change was observed. The hardness and elastic modulus properties of intermetallic compounds can now be evaluated effectively without going through the time-consuming synthesis processes of individual compounds. Because of the

brittle nature of most intermetallics, synthesis can be very challenging, especially for those with very high melting points. The diffusion multiple approach can be used to quickly screen structural intermetallics, especially now that it is possible to extract fracture-toughness data from nanoindentation using a cube-corner indenter.[8] In this application, the EBSD technique[9] is also extremely useful for identifying the crystal structures of the intermetallics without going through the time-consuming sample-making process for transmission electron microscopy. The intermetallic compounds formed in diffusion multiples can be identified by combining the compositional information from EPMA and crystal structure information from EBSD.

A more recent diffusion multiple example[10] is shown in Figure 2. In this case, rectangular foils of pure Pd, Pt, and Rh, 254 μm (10 mils) thick, were stacked on a notched rectangular piece of Ru (1 mm on one side and 0.5 mm on the other) in a bricklaying pattern. The whole stack was placed inside a slot measuring 13 mm × 1.8 mm cut from a 25-mm-diameter pure Cr disk 3 mm thick. Intimate interfacial contact among all of these pieces was achieved through a HIP process. We mapped 10 ternary phase diagrams from this single sample;[10] it would probably take more than a thousand alloys to map these diagrams. Thus, efficiency can be increased by about 3 orders of magnitude with this approach. The Cr-Rh-Ru phase diagram is shown in Figure 2 as an example.

At the Pd-Pt-Rh tri-junction, the composition variation of the entire ternary system was generated by interdiffusion. By performing nanoindentation across the ternary and binary areas, the compositional dependency of hardness and elastic modulus was mapped, as shown in Figure 2. To our knowledge, this is the first time an entire ternary system has been surveyed with respect to its mechanical properties. Nonlinear behaviors can be evaluated very effectively. A positive deviation from linear hardening was observed for all three binary systems, Pd-Pt, Pd-Rh, and Pt-Rh; the three-dimensional (3D) surface representing hardness in the Pd-Rh-Pt system also shows a positive deviation from a simple rule-of-mixtures linear hardening everywhere in the alloy space. This has been determined efficiently both for alloying elements with very different hardnesses (i.e., adding relatively hard Rh to relatively soft Pd-Pt mixes) as well as for alloying elements with very similar hardnesses (i.e., adding relatively soft Pt to variable-hardness mixes of Pd-Rh with near-constant Rh content).
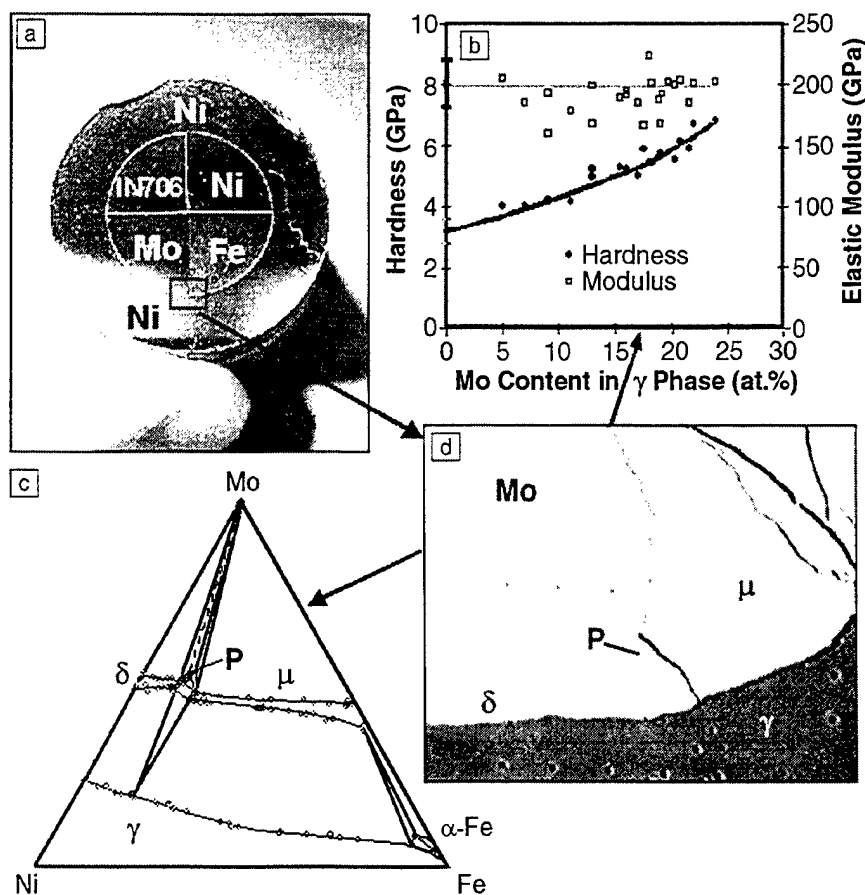

Figure 1. (a) A diffusion multiple of Ni, Fe, Mo, and the Ni-based superalloy Inconel 706 (IN706) and (b)–(d) part of the results obtained from the Fe-Mo-Ni tri-junction region. (b) Hardness variation with Mo content in the γ phase. (c) The 1100°C isothermal section of Fe-Mo-Ni.[10] (d) Backscattered electron image showing the formation of the intermetallic phases.
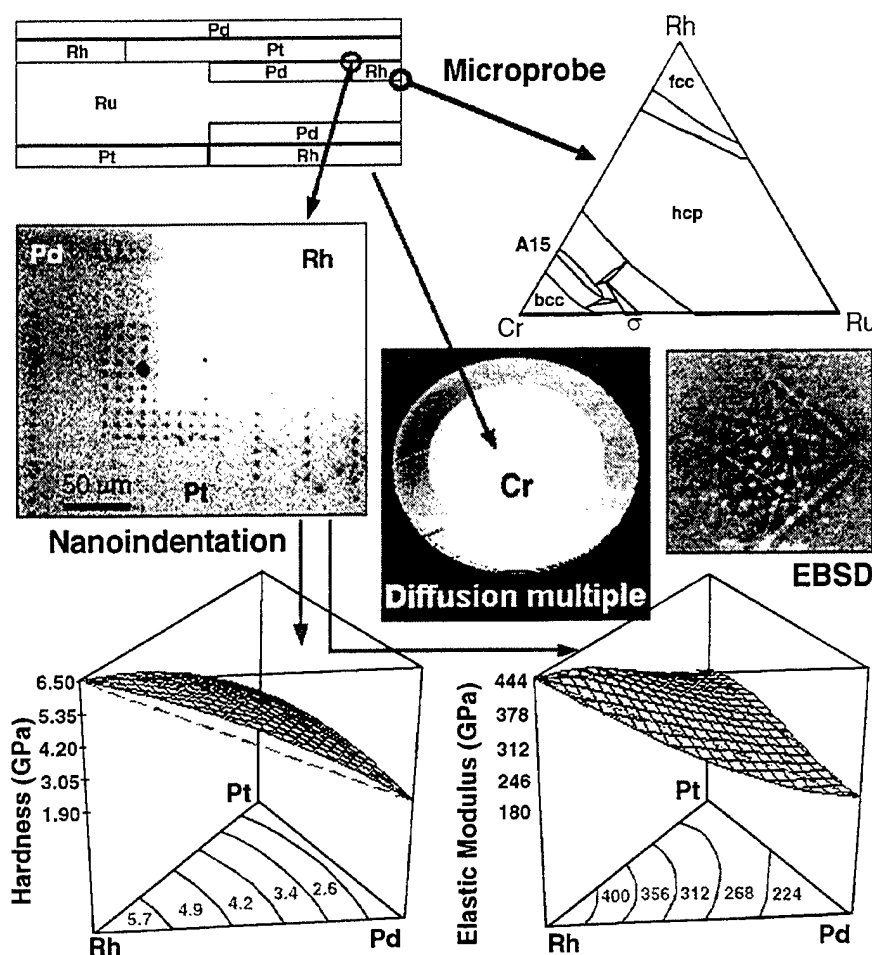
Figure 2. A diffusion multiple made up of Pd, Pt, Rh, Ru, and Cr. Some of the results shown are the 1200°C isothermal section of the Cr-Rh-Ru phase diagram and the hardness and modulus variation with composition for the Pd-Pt-Rh ternary system.[16] The image marked EBSD was obtained by electron backscatter diffraction of the A15 phase.

Ni-based superalloys diffuses into super-alloy substrates during high-temperature service, thus consuming the substrate and reducing the Al content in the coating, which degrades the coating's oxidation resistance. It is highly desirable to have a diffusion barrier to retain high Al in the coating while saving the substrate. There are several potential attributes that may be critical for effective diffusion barriers: (1) thermodynamic stability against both superalloy substrates and the coatings, which usually contain NiAl (β) phase; (2) low Al solubility; (3) low diffusion co-efficients; and (4) high elemental partitioning among the coating, the substrate, and the diffusion barrier. It was not known which of these attributes were the most critical ones, and the available thermodynamic and kinetic databases were insufficient for designing the diffusion barriers.

To quickly screen these attributes and find effective diffusion barriers, three diffusion multiples were made,[11] each containing as many as 12 different coating/substrate/barrier combinations. Their geometry and arrangement are schematically shown in Figure 3. Slabs of single-phase NiAl were used as a proxy for the coating. Many diffusion-barrier compositions were selected to test the desired attributes, and alloys were made. Wedges of diffusion-barrier alloys were sandwiched between superalloys and NiAl pieces 3 mm thick. Several different superalloy compositions and many diffusion barriers were tested at the same time. The diffusion barriers were annealed at high temperatures for a prolonged time period (100–1000 h). The wedge-shaped design was intended to test several effects at the same time. At location 1 (Figure 3), where there was no diffusion barrier, the interdiffusion between the superalloy substrate and NiAl was severe, and it served as a baseline for comparing the effectiveness of various diffusion barriers. At location 2, where a thin diffusion barrier was present, the effectiveness of the diffusion barrier could be assessed, and the stability of a thin diffusion barrier against the interdiffusion of the NiAl and the superalloy could be evaluated. We could also estimate the required thickness of the particular diffusion barrier. At location 3, the stability/interaction between the diffusion barrier and the superalloy could be evaluated without the presence of NiAl. Similarly, at location 4, the stability/interaction between the diffusion barrier and NiAl could be evaluated without the presence of the superalloy. Some barrier compositions tested had little interaction with the superalloys but had intensive interaction with NiAl, while others behaved the opposite.

Results for the elastic modulus survey across the entire Pd-Rh-Pt ternary system are also shown in Figure 2. The negative deviation from a linear rule-of-mixtures modulus was observed for the Pd-Rh binary system. However, the Pd-Pt and Pt-Rh systems show different deviations from a linear modulus, unlike the case for hardness. For Pt-Rh, the modulus deviates slightly positively from linearity, while for Pd-Pt, the modulus essentially follows the linearity for Pd-rich compositions, and deviates oppositely for Pt-rich compositions. Thus, the 3D surface representing the elastic modulus of the Pd-Rh-Pt system shows more complex deviation from a simple rule of mixtures than was the case for hardness. Again, this complex behavior has been determined efficiently for both alloying elements with very different moduli (i.e., adding Rh to Pd-Pt mixes) as well as for alloying elements with very similar moduli (i.e., adding Pt to Pd-Rh mixes of near-constant Rh content).

The solution hardening and softening effects, as well as the modulus behavior, contain a great amount of information about the elemental interaction: bonding, nonlinear solid-state interaction, and so on. The data shown in Figure 2 can serve as experimental inputs to test and improve ab initio calculation algorithms. The diffusion multiple approach offers a fast way to generate critical experimental data to test theoretical predictions.

Diffusion multiples can be designed with different shapes and forms to achieve different purposes. For instance, diffusion multiples were designed and made to screen for effective diffusion barriers for high-temperature coating applications.[11] In this case, Al from Al-rich coatings on

A Diffusion Multiple Approach for the Accelerated Design of Structural Materials
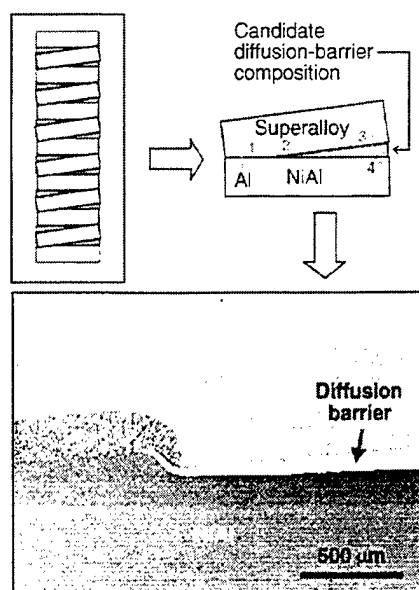

Figure 3. Application of diffusion multiples in the development of diffusion barriers to reduce the interdiffusion between the Al-rich coating and the superalloy substrate.[17] See the text for details.

We quickly identified the critical attributes for effective diffusion barriers, and a couple of diffusion barriers identified from the diffusion multiples are currently under testing for an advanced jet-engine application. In this case, we tested many ideas, compositions, and thickness variations, as well as chemical (thermodynamic) stability/compatibility and kinetics at the same time. The three diffusion multiples served as a comprehensive design of experiment with a very high efficiency. They allowed us to quickly find the "chemistry" behind an effective barrier, and thus develop a strategy for designing it.

Impact on Structural Materials Design

While the use of diffusion multiples for screening diffusion barriers is one example of their various potential applications, some of the areas where this approach will have the most impact will probably be in the rapid mapping of phase diagrams, solution-hardening effects, binary diffusivity matrices, and modulus dependency on composition and phases, to provide critical data for the computational design of materials.

The CALPHAD (calculation of phase diagrams) approach[12,13] is a major part of the computational design of mate-

rials. It provides multicomponent phase-equilibrium data, the driving force for precipitation modeling, the segregation and latent heat data for solidification modeling, and thermodynamic factors for constructing the diffusion-coefficient matrices for multicomponent alloys.[14] Thermodynamic calculations using the CALPHAD approach are presently performed on a daily basis in industrial laboratories such as the GE Corporate Research Center.[15]

In the CALPHAD approach, the Gibbs energy of each phase is fitted to a polynomial as a function of composition and temperature. The fitting parameters (so-called thermodynamic parameters) are optimized from the pure element (unary) data (melting point, specific heat, allotropic transition temperature, Curie temperature if any, heat of fusion), binary and ternary phase-diagram data (tie-lines, tie-triangles, invariant reaction temperatures, and compositions), and thermodynamic data (heat of formation for the compounds, activity, heat of mixing). The Gibbs energy functions of the binary and ternary systems are then extrapolated into multicomponent systems. The approach has proven to be very successful over the last three decades.

Since most unary and binary phase-diagram data already exist, the critical data required for building a reliable multicomponent thermodynamic database are experimental ternary phase diagrams. The number of ternaries required is very large, but the available ones are far fewer, especially for new alloy systems such as Mg alloys. The diffusion multiple approach for the rapid mapping of phase diagrams will have a high impact on the establishment of reliable thermodynamic databases for the computational design of materials. As R.W. Cahn put it, "I expect to see this approach developed in the near future; then the years involved in determining a ternary phase diagram will be drastically shortened, especially if the combinatorial approach is linked with CALPHAD calculations."[16] The efficiency of diffusion multiples in mapping phase diagrams is now so high that the time-limiting step in building thermodynamic databases will no longer be the experimental determination of phase diagrams, but rather the thermodynamic assessments (optimization).

Some particular advantages might also accrue from studies of ternary systems, especially if ternary compounds can be identified that equilibrate with a desired solid-solution matrix. Other factors being equal (melting point, crystal structure, etc.), ternary compounds are more attractive as second phases than binary compounds because (1) the dispersions are likely to be

more stable due to slowed diffusion rates (two components must diffuse for growth to occur), (2) slowed diffusion rates should contribute to strength maintenance in high-temperature regimes of diffusion-controlled deformation, and (3) ternary compounds are known to be more resistant than binaries to strength degradation with increasing temperature, probably because of (2).[17,18]

With the support of the Air Force Office of Scientific Research (AFOSR), we are currently using diffusion multiples to map phase diagrams for the Nb-Ti-Si-Cr-Al system[19] to provide experimental data for building a thermodynamic database for the design of Nb silicide composites. These composites showed high promise for use in advanced jet-engine turbine airfoils with higher operating temperatures than Ni-based superalloys can withstand.[20,21] With the support of the Accelerated Insertion of Materials (AIM) program of the Defense Advanced Research Projects Agency (DARPA), we are using diffusion multiples to map critical ternary phase diagrams to improve the current thermodynamic database of Ni-based superalloys.[15]

Mapping phase diagrams for thermodynamic modeling (left-hand side of Figure 4) is only one of the contributions of the diffusion multiple approach to materials design. The binary diffusion profiles from diffusion multiples can also be used to evaluate binary diffusion coefficients. These coefficients, along with the thermodynamic factors calculated from thermodynamic databases, can be used to predict the diffusion coefficients of higher-order systems. The diffusion databases are critical for simulating kinetic processes of materials such as precipitation kinetics and coarsening kinetics. This is schematically shown in the middle column of Figure 4.

Because of the link between diffusion coefficients and thermodynamic factors, the diffusion coefficients themselves show ordering or clustering in a solid solution. In simple terms, the sign of the heat of mixing, whether positive (clustering) or negative (ordering), relates to the pair interactions of the atoms. For instance, the diffusion coefficients[22] evaluated from the Pd-Pt, Pt-Rh diffusion profiles measured from the diffusion multiple in Figure 2 showed complex behaviors that can be used to test the first-principles prediction.[23] Thus, the diffusion coefficients also add to our understanding of the bonding and physics in the alloy system. Phase-diagram and modulus–composition profiles also contain such information.

The right-hand side of Figure 4 illustrates the importance of hardness and modulus mapping for structural materials

A Diffusion Multiple Approach for the Accelerated Design of Structural Materials
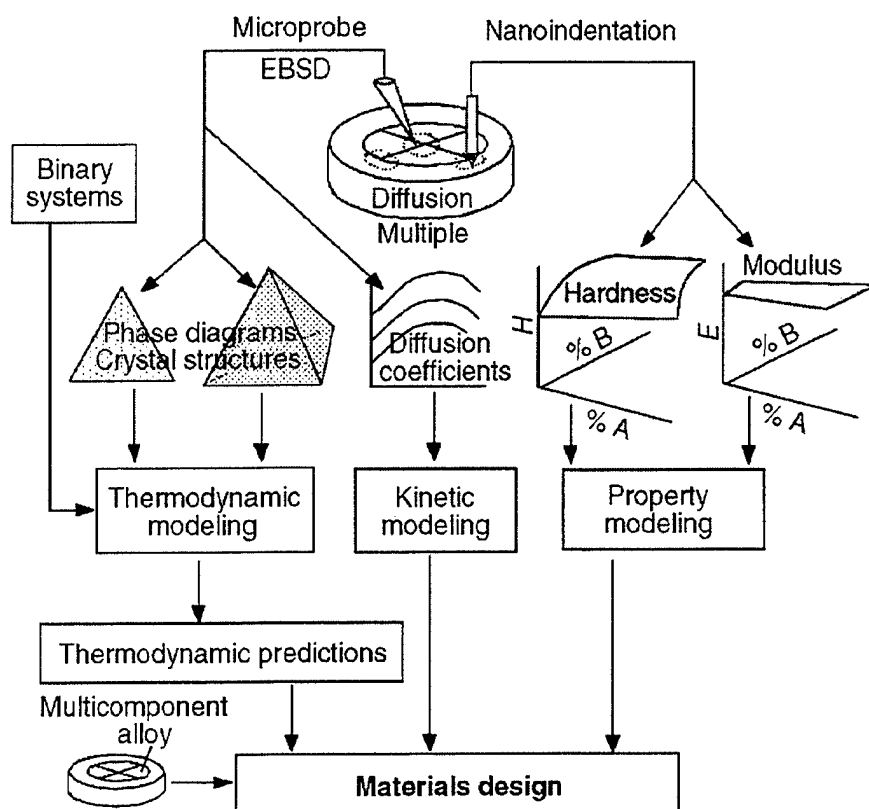

Figure 4. Schematic diagram summarizing the outputs from the diffusion multiples that are important inputs for materials design. See the text for details.

design. Solution strengthening involves complex interactions: atomic size effects, energy-band interactions, and so on; it is not easy to make accurate predictions from first principles. Rapid mapping of hardness and modulus will provide critical data for materials design and for testing the first-principles predictions. In this case, any ternary interactions can be discerned from the mapped property surfaces. Moreover, a solution-hardening database can be rapidly built to allow alloy developers to pick effective elements for strengthening the alloys.

While not described in this article, the composition variations generated in diffusion multiples can be used to study precipitation kinetics. Precipitation hardening is the most important strengthening mechanism for most structural materials. Diffusion multiples allow the rapid assessment of precipitation kinetics simultaneously for a range of compositions,[3,4] in contrast to the traditional approach, where a single alloy (composition) is studied. Precipitation kinetics is extremely critical for controlling the microstructure, and thus the properties, of structural materials.

Moreover, the different microstructures generated in the different composition regions of the diffusion multiples during kinetic-study experiments can be directly screened using nanoindentation for desired mechanical properties. The results can be very useful for materials designs that are not based on the CALPHAD approach.[24,25]

Figure 4 summarizes the major outputs from diffusion multiples that will be important for structural materials design. Again, the left-hand column shows the construction of a thermodynamic database to predict phase equilibria in multicomponent alloys. This is like building a "global map" for a particular multicomponent system. Since the thermodynamic data are extrapolated mostly from binary and ternary systems, the global map may not be very accurate, but it will guide us to the proximity of desired locations (phases) in the multicomponent space. By using one or more multicomponent alloys as members of diffusion multiples, we can then generate a detailed "local map" to optimize the alloy and specify the composition windows. This is schematically shown at the bottom left of Figure 4.

Other Approaches

One of the limitations of diffusion multiples is that they cannot be used to evaluate liquid–solid phase equilibria, which are important for modeling solidification processing. Recently, a melting and floating zone approach was used by Cohen-Adad et al.[26-28] to generate continuous composition variations in binary and quasi-binary systems, and it can be used to evaluate liquid–solid equilibria. It complements the diffusion multiple approach very well by defining the liquid–solid part of the phase diagrams. It can also be used to evaluate solidification processes due to the possible control of the solidification rate.

Very recently, Ikeda et al.[29] employed a diffusion couple made of pure Al and an Fe-15at.%Al alloy to study the ordering phase diagram of the Fe-Al binary system. They made the diffusion couple by melting pure Al in an Fe-15at.%Al alloy cup. The diffusion couple was first annealed at 1300°C for 4 h to generate the composition variation and then was sliced into disks for annealing at lower temperatures to evaluate the ordering equilibria. The results obtained from the diffusion couple agreed well with those obtained from individual alloys.

Thin-film approaches,[30-35] especially the continuous phase-diagram mapping approach,[33,35] may find application in structural materials. To determine phase diagrams at relatively low temperatures, it may be advantageous to use thin-film approaches, since much less time is required to form a homogeneous composition across the thin-film thickness. In contrast, it may take a long time to promote sufficient interdiffusion in diffusion multiples to map phase diagrams and properties at low temperatures. In addition, occasionally equilibrium intermetallic compounds do not form in diffusion couples at low temperatures, probably due to nucleation difficulties. This phenomenon has been observed in a few alloy systems and usually occurred at temperatures below half of the homologous melting point. At such low temperatures, the compounds may be easier to form in thin films, especially when the substrate is heated to the desired temperatures. Care needs to be exercised to avoid possible reaction of the film with the substrate and the environment (oxygen, carbon, hydrogen, etc.). In addition, there are kinetic barriers to the formation of equilibrium phases, even in thin films at low temperatures. The situation improves if the thin films started as an amorphous structure. More work needs to be carried out in this area.

To evaluate properties such as hardness and modulus, thick films are highly desir-

able since the thickness has to be larger than the typical microstructural scale of structural materials. Large grain size is also necessary for evaluating solution- and precipitation hardening while minimizing the complication of structural (e.g., grain size) hardening. In this regard, the high efficiency of electron-beam physical vapor deposition (EB-PVD) becomes very attractive. Continuous composition variations can be generated by EB-PVD using different evaporation pools, as demonstrated by Kennedy et al.[30] The deposition efficiency and flexibility of generating composition variations become even better with the EB-DVD process recently developed by Groves et al.[36] This process is especially attractive for generating composition variations for ceramic materials.

Very recently, the thin-film approach using reactive magnetron sputtering and plasma-enhanced chemical vapor deposition was employed to develop hard coatings and rewritable optical data-storage materials.[37] Similar approaches would accelerate the coating development for structural materials, especially when nanoindentation is also employed.[38]

As more microscale property probes become available, we anticipate even more applications of the diffusion multiple approach in the mapping and design of structural and functional materials.

Acknowledgments

References

1. W.C. Oliver and G.M. Pharr, *J. Mater. Res.* 7 (1992) p. 1564.
2. M.F. Doerner and W.D. Nix, *J. Mater. Res.* 1 (1986) p. 601.
3. J.-C. Zhao, *Adv. Eng. Mater.* 3 (2001) p. 143.
4. J.-C. Zhao, *J. Mater. Res.* 16 (2001) p. 1565.
5. M. Hasebe and T. Nishizawa, in *Application of Phase Diagrams in Metallurgy and Ceramics*, Vol. 2, NBS Special Publication 496, edited by G.C. Carter (National Bureau of Standards, Gaithersburg, MD, 1978) p. 911.
6. Z. Jin, *Scand. J. Metall.* 10 (1981) p. 279.
7. J.-C. Zhao and Z. Jin, *Z. Metallkd.* 81 (1990) p. 247.
8. G.M. Pharr, *Mater. Sci. Eng., A* 253 (1998) p. 151.
9. A.J. Schwartz, M. Kumar, and B.L. Adams, eds., *Electron Backscatter Diffraction in Materials Science* (Kluwer Academic/Plenum Publishers, New York, 2000).
10. J.-C. Zhao, M.R. Jackson, L.A. Peluso, and L. Brewer, *JOM* 54 (10) (2002) in press.
11. J.-C. Zhao, M.R. Jackson, and R. Darolia (unpublished).
12. L. Kaufman and H. Bernstein, *Computer Calculation of Phase Diagrams with Special Reference to Refractory Materials* (Academic Press, New York, 1970).
13. N. Saunders and A.P. Miodownik, CALPHAD (Elsevier Science, New York, 1998).
14. C.E. Campbell, W.J. Boettinger, and U.R. Kattner, *Acta Mater.* 50 (2002) p. 775.
15. J.-C. Zhao and M.F. Henry, *JOM* 54 (1) (2002) p. 37.
16. R.W. Cahn, *MRS Bull.* 25 (9) (2000) p. 59.
17. J.H. Westbrook, in *Deformation in Solids*, Vol. 10, edited by F.R.N. Nabarro and M.S. Duesbery (North-Holland, Amsterdam, 1996) p. 1.
18. J.H. Westbrook (private communication).
19. J.-C. Zhao, M.R. Jackson, B.P. Bewlay, and L. Peluso (unpublished).
20. B.P. Bewlay, M.R. Jackson, and M.F.X. Gigliotti, in *Intermetallic Compounds Principles and Practice: Progress*, Vol. 3, edited by J.H. Westbrook and R.L. Fleischer (John Wiley & Sons, New York, 2002) p. 541.
21. S.J. Balsone, B.P. Bewlay, M.R. Jackson, P.R. Subramanian, J.-C. Zhao, A. Chatterjee, and T. Heffernan, in *Structural Intermetallics 2001*, edited by K. Hemker, D.M. Dimiduk, H. Clemens, R. Darolia, H. Inui, J.M. Larsen, V.K. Sikka, M.

Thomas, and J.D. Whittenberger (The Minerals, Metals and Materials Society, Warrendale, PA, 2001) p. 99.
22. Y.H. Sohn and J.-C. Zhao (unpublished).
23. Z.W. Lu, B.M. Klein, and A. Zunger, *J. Phase Equilib.* 16 (1995) p. 36.
24. N.N. Kiselyova, in *Intermetallic Compounds Principles and Practice: Progress*, Vol. 3, edited by J.H. Westbrook and R.L. Fleischer (John Wiley & Sons, New York, 2002) p. 811.
25. S. Naka and T. Khan, in *Intermetallic Compounds Principles and Practice: Progress*, Vol. 3, edited by J.H. Westbrook and R.L. Fleischer (John Wiley & Sons, New York, 2002) p. 841.
26. M.Th. Cohen-Adad, M. Gharbi, C. Goutaudier, and R. Cohen-Adad, *J. Alloys Compd.* 289 (1999) p. 185.
27. M.Th. Cohen-Adad, L. Laversenne, M. Gharbi, C. Goutaudier, G. Boulon, and R. Cohen-Adad, *J. Phase Equilib.* 22 (2001) p. 379.
28. L. Laversenne, Y. Guyot, C. Goutaudier, M.Th. Cohen-Adad, and G. Boulon, *Opt. Mater.* 16 (2001) p. 475.
29. O. Ikeda, I. Ohnuma, R. Kainuma, and K. Ishida, *Intermetallics* 9 (2001) p. 755.
30. K. Kennedy, T. Stefansky, G. Davy, V.F. Zackay, and E.R. Parker, *J. Appl. Phys.* 36 (1965) p. 3808.
31. X.-D. Xiang, X.-D. Sun, G. Briceño, Y. Lou, K.-A. Wang, H. Chang, W.G. Wallace-Freedman, S.W. Chen, and P.G. Schultz, *Science* 268 (1995) p. 1738.
32. R.B. van Dover, L.F. Schneemeyer, and R.M. Fleming, *Nature* 392 (1998) p. 162.
33. X.-D. Xiang, *Annu. Rev. Mater. Sci.* 29 (1999) p. 149.
34. Y.K. Yoo, F.W. Duewer, H. Yang, D. Yi, J.-W. Li, and X.-D. Xiang, *Nature* 406 (2000) p. 704.
35. Y.K. Yoo, T. Ohnishi, G. Wang, F.W. Duewer, X.-D. Xiang, Y.-S. Chu, D.C. Mancini, Y.-Q. Li, and R.C. O'Handley, *Intermetallics* 9 (2001) p. 541.
36. J.F. Groves, G. Mattausch, H. Morgner, D.D. Hass, and H.N.G. Wadley, *Surf. Eng.* 16 (2000) p. 461.
37. R. Cremer, S. Dondorf, M. Hauck, D. Horbach, M. Kaiser, S. Kyrsta, O. Kyrylov, E. Munstermann, M. Philipps, K. Reichert, and G. Strauch, *Z. Metallkd.* 92 (2001) p. 1120.
38. B. Roebuck, M. Stewart, R. Morrell, and M. Gee, *Mater. World* 9 (11) (2001) p. 16. □

Diffusion Multiples for High Efficiency Alloy Design

J.-C. Zhao, L.A. Peluso, L. Brewer, and M.R. Jackson

Diffusion Multiples for High Efficiency Alloy Design

J.-C. Zhao, L.A. Peluso, L.N. Brewer, and M.R. Jackson

General Electric Company, GE Global Research Center
P.O. Box 8, Schenectady, NY 12301.

Abstract

Application of the diffusion multiple approach in efficient mapping of alloy phase diagrams and critical materials properties such as hardness, modulus, solution-hardening effects, etc. is illustrated in this chapter. The approach can achieve about three orders of magnitude increase in efficiency over the traditional one-alloy-at-a-time method. The emphasis of this presentation is on describing the various analytical (mapping) techniques for efficient survey of materials structure and properties from diffusion multiples, and the state-of-the art capabilities and limitations of these techniques. Examples are given to for systems containing Cr and precious metals, Pd, Pt, Rh and Ru.

1.   Introduction

Unlike functional materials which most often are used for one specific physical or chemical property, structural materials often need to satisfy simultaneously several different properties such as strength, ductility, modulus, fracture toughness, environmental resistance, etc. In addition, many structural materials undergo several different processes such as casting, forging, rolling and the like before they are used in the final product. Thus, it is not very practical to "screen" for structural materials directly. Instead, high-efficiency approaches can be used to map critical properties and data to accelerate the design of structural materials.

The strength of structural alloys is controlled by dislocation mobility and it comes predominately from three sources: solution strengthening, precipitation/dispersion strengthening, and microstructural strengthening. The first case involves atoms of different sizes distorting a crystal lattice, thus making dislocations more difficult to move. Alloy designers would like to know which elements are more effective than others in solution-strengthening and by what amount. Currently, predictions from first principles are still not up to the challenge. Experimental mapping of the solution-strengthening effects would be very useful for alloy design, especially for new alloy systems. The second case involves in-situ formation (precipitation) or intentional addition (dispersion) of second phase particles in a crystalline matrix to slow/block dislocation movements. In this case, it is critical to know the stability and the nucleation and growth kinetics of the particles. To predict these properties requires phase diagrams and diffusion coefficients. Phase diagrams are also very useful to guide alloy designers to promote phases which have been identified as beneficial precipitates and to avoid detrimental ones. The third

1

case involves microstructural imperfections such as dislocation tangles/pile-ups induced by alloy processing (such as cold rolling). The grain size effect (the Hall-Petch effect) is an example of this type of strengthening. Microstructural strengthening is accomplished by processing and is not a necessary part of the alloy composition design. Therefore, phase diagrams, solution-strengthening effects and diffusion coefficients are among the very basic information required for alloy design.

This paper describes the diffusion multiple approach for efficient mapping of phase diagrams, solution-hardening effect, diffusion coefficients, and modulus variation with composition and phases. The emphasis is placed on explaining the detailed microanalytical probes that make efficient mapping possible and the detailed process of obtaining data from the diffusion multiples. The authors hope to show colleagues in other fields how to use tools such as electron probe microanalysis (EPMA), electron backscatter diffraction (EBSD) and nanoindentation to screen composition, crystal structure, and elastic modulus in other materials.

2.   Diffusion Multiple Fabrication

The diffusion multiple shown in Fig. 1 was made by cutting a slot of 1.8 mm width and 12.7 mm length from a 25 mm diameter pure Cr disk of 3 mm thickness. Pure Pd, Pt, and Rh foils of 0.25 mm thickness are arranged in a bricklaying geometry shown in Fig. 1 and put into the slot in the Cr disk along with a pure Ru piece with 2 steps on it. The Ru piece had a thickness of 1 mm on one side and 0.5 mm on the other. Two pure Cr disks (without the slot) of 25.4 mm diameter and 3.2 mm thickness were placed on top and bottom of the slotted Cr disk containing all the precious metals. The assembly was then placed in a pure Ti tube of 25.5 mm inner diameter and 32 mm outer diameter and 9.6 mm height. Two Ti disks of 32 mm diameter and 3.2 mm thickness were placed on the top and the bottom of the Ti tube filled with the three Cr disks. The assembly was welded using an electron beam in vacuum along the top and bottom outer circular edges of the Ti tube. The welded outer Ti tubes and caps served as a hot isostatic pressing (HIP) can. The whole assembly then underwent a HIP run of 1200°C, 200 MPa for 4 hours. The diffusion multiple was further annealed at 1200°C for 36 hours in a vacuum furnace – making the total diffusion exposure time as 40 hours at 1200°C. The Cr disks and the Ti HIP can serve as protection for the precious metals from any interstitial contamination during heat treatment. The diffusion time was chosen to develop diffusion profiles measurable over lengths of ~100 microns, so that neighboring diffusion sources would not interfere with the couple or triple being evaluated.

The annealed diffusion multiple was then cut into halves parallel to two Ti caps and at the mid-point of the thickness direction. The sample was then ground and polished for EPMA, EBSD, and nanoindentation tests. Nanoindentation was performed using a Hysitron (Minnesota, USA) instrumented indenter. All results reported in this paper were obtained from this single sample.

The bricklaying pattern allows the formation of ten different diffusion triples in this diffusion multiple, as shown in Fig. 1 highlighted with circles. The Cr-Pt-Ru tri-junction is shown in Fig. 2. Based on the binary phase diagrams, there should be one intermetallic compound (Cr_3Pt with an A15 crystal structure) formed between Cr and Pt, and also one compound (σ with a tetragonal crystal structure) between Cr and Ru. There should be no compound between Pt and Ru, just the fcc / hcp equilibrium. The scanning electron microscopy (SEM) backscatter electron (BSE) image clearly shows the A15 (Cr_3Pt) and the σ phase and a clear fcc / hcp phase boundary. But, it is difficult to locate the phase boundary between the A15 and the σ phase using SEM BSE image alone. We will show how we can combine the EPMA and EBSD techniques to identify the phase boundaries and to obtain the tie-line information to construct the ternary phase diagram. In addition to the formation of all the intermetallics compounds, the diffusion multiple also creates a complete variation of all the single phase compositions [1,2]. These compositions will allow us to map solution-hardening effects and modulus-phase-composition relationships. A brief introduction of various microanalytical techniques will be presented first to give the reader a sense of their spatial resolution, accuracy, and analytical procedures.

3.   Microanalysis

In choosing analytical techniques for high throughput materials characterization, several factors are especially important: spatial resolution, automation, and spatial registry between techniques. The granularity of a compositional variation will be controlled either by the spatial resolution of the processing technique or by the spatial resolution of the analytical technique. A high degree of analytical automation is required to efficiently characterize the hundreds of compositional points and phase boundaries present in a single diffusion multiple. Spatial registry between techniques is equally important. To characterize a sample and connect it with physical properties, different analytical techniques must be able to accurately and reliably address the same compositional (X-Y) point on a diffusion multiple or any other compositional library. Below we will discuss the use of EPMA, EBSD and imaging, and nanoindentation as characterization techniques capable of meeting these demands as high throughput characterization tools. Each of these techniques is already highly developed and commercially available. While we will review the basic principles of each technique, the emphasis will be on the use of the technique for the diffusion multiple studies with the precious metal diffusion multiple as a guiding example.

3.1 Microprobe

The electron probe microanalyzer (EPMA) is a powerful instrument for the micro-chemical analysis of inorganic materials. EPMA is a technique capable of chemically analyzing solid, vacuum-compatible materials with high spatial resolution and sensitivity. The volume excited under typical electron microprobe conditions is on the order of a cubic micron, which is equivalent to a sample size of a few picograms. EPMA can detect elements spanning most of the periodic table, from Be to U, with typical detection limits of 0.1% atomic and down to a few ppm in select cases. It can provide accuracy of less

than 1% relative for most major sample components, and 3-5% relative for minor components, depending upon matrix effects. Most electron microprobe instruments operate in the 10^{-7} to 10^{-6} torr range, which allows more rapid sample throughput than ultra-high vacuum (UHV) instruments. Sample preparation requirements for EPMA are less stringent than many other instruments. EPMA can be performed on all conductive materials and most non-conductive materials with the application of a thin, conductive coating (e.g., carbon) which can be done with resistive evaporation or by common sputter coaters, to provide a pathway for electrons away from the electron beam-sample interaction area.

EPMA utilizes a finely focused, high-energy electron beam, which bombards a pre-selected location on a solid specimen. The resulting emission includes back-scattered primary electrons, secondary electrons, low-energy photoelectrons, Auger electrons, x-ray and optical photoemission (Fig. 3). In EPMA, the radiation of interest is the characteristic x-ray emission. The specific X-ray energies (or wavelengths) are characteristic of the particular element which was initially excited. This phenomenon allows correlation of the measurement of characteristic x-rays to the composition of a probed region on a specimen.

Detection of x-rays and subsequent identification of elements present in a specimen can be carried out by solid-state energy-dispersive spectrometry (EDS) or wavelength-dispersive spectrometry (WDS). WDS is preferred for data acquisition over EDS in EPMA for several reasons, including a much better energy resolution and higher peak x-ray count rates and peak-to-background ratios, which allow much lower minimum detection limits.

The basis for modern electron microprobe analysis was established in 1951 by Castaing in his Ph.D. thesis in which he set out its fundamental principles and its realization as a metallurgical tool [3]. He outlined a method for obtaining a quantitative x-ray analysis from a micrometer-sized region of a solid specimen. This was achieved by measuring the ratio ("K") of characteristic x-ray emission intensity ("I") of element "A" from the specimen to that of a pure elemental standard. This ratio was shown to be proportional to the composition ("C") of element "A" in the analyzed area, to a first approximation.

$$K_A = \frac{I_{A,specimen}}{I_{A,s\tan dard}} = f(C_A) \qquad (1)$$

Castaing's second-order approximations employed an empirical coefficient "ZAF" to account for certain matrix-dependent effects [4]. These physical phenomena which significantly attenuate or amplify the characteristic x-rays generated within a specimen include the electron scattering/atomic number effect "Z", absorption within the sample "A", and the fluorescence effect "F".

Improvements in computer hardware and continued development of algorithms which model these effects have greatly increased the accuracy in quantitative EPMA. We can now simulate the electron trajectories in a single or multi-element sample to calculate the

range of electrons along multiple scattering events as a function of many variables such as incident beam energy and average atomic number. These Monte Carlo calculations [5] enable us to predict the energy distribution of the incident beam within the specimen, and the transfer of energy on the atomic level. From these range simulations, we can model continuum and characteristic x-ray production as well. This ability is very helpful to the analyst in the preparation of an analysis traversing multiple varying composition regimes.

The resultant X-ray excitation volume exceeds that of the electron scattering volume. We can see from Fig. 4 that significant opportunity for X-ray production occurs for chromium kα well below the surface, less so for platinum. However, since only emitted X-ray signal is measured, we must correct for the absorption of X-ray signal by the matrix (effectively reducing the volume sampled), as well as "secondary" X-ray signal created by primary X-ray fluorescence (increasing the volume sampled). These and other factors result in an X-ray production density which is not constant with interaction volume [6].

Correction procedures for these phenomena have evolved for decades, and are still undergoing refinement [7]. Some of the most useful ones today are based upon $\phi\rho z$ distributions from various samples which carefully define the distribution of characteristic x-ray productions with depth.

The depth beneath the sample surface is often expressed as "ρZ", represents mass thickness. From the simple depiction shown in Fig. 5, we can see that the largest proportion of X-rays generated come from a fairly shallow region relative to the entire x-ray excitation volume. "$\phi(\rho Z)$ curves" are widely used models which have been important in the calculation of X-ray intensities for multi-element systems, Fig. 5.

The fundamentals of this analytical technique devised over a half-century ago remain intact. Great improvements in mechanical hardware have allowed precise, multi-element compositional profiling. The ability to move a specimen accurately in very exact and uniform increments while measuring characteristic X-ray intensities of many elements at each interval has advanced its value as a tool for materials science. The development of optically-encoded WDS spectrometers allows multiple element analysis of both peak and background X-ray signals on a single spectrometer with excellent reproducibility of positioning. The invention of synthetic, multi-layer "pseudo-crystals" and anti-contamination systems have improved light element detection by orders of magnitude. The latest large-area crystals such as LiF (lithium fluoride), PET (pentaerythritol) and TAP (thallium acid phthalate) crystals offer microprobe operators huge count rate advantages, thus allowing productivity gains when applied to multi-element composition profiling. These large count rates can indirectly help improve spatial resolution in some cases, by allowing the use of lower beam current to achieve optimized x-ray counting statistics.

EPMA is naturally well-suited to achieving efficient and accurate composition profiles with high spatial resolution. The marriage of high speed computer automation and very precise sample stage and X-ray spectrometer hardware has provided a powerful analytical

tool for high-throughput approaches to materials research. The microprobe work done in mapping of phase diagrams and in phase equilibria determination in the present study was performed on a Cameca SX50 with four vertical wavelength-dispersive spectrometers and fully integrated PGT EDS system automated by a Sun Ultra1 Unix workstation, Fig. 6. Modern EPMA systems are usually equipped with a motorized stage that has a positional precision of 0.5 μm in X-, Y- and Z-directions, and can move over a range of several centimeters. Such a system allows automated data collection by logging the EPMA line scan positions ahead of time into a executable file and allows the instrument to collect data without the presence of the operator.

Data reduction (from X-ray intensity ratios to composition in weight percent) was typically performed using "PAP", developed by F. Pichoir and J.L. Pouchou [8], a modified $\phi(\rho Z)$ program and good general model for a wide range of X-ray energies (100eV to over 10keV) and accelerating voltages (1 to 40keV), and better accounts for the depth distribution of energies than common matrix correction procedures (ZAF).

It is very important to achieve very high throughput EPMA while maintaining acceptable accuracy and precision in the resultant compositions measured. In measuring large numbers of phases and intermetallic compounds throughout this work with compositions varying only slightly among some of them, we need to carefully select the analysis parameters that would give the most productive results. A large effort is placed in both qualitative and quantitative examination of these diffusion multiples in advance of more thorough quantitative profiling in order to balance the accuracy needed with the total acquisition time during analyses of on the order of 10^3 to 10^4 data points. Usually the EPMA analysis was performed on the order of one minute per point.

The main procedures of automating the electron microprobe effort can be broken down into four activities: identify, screening, analysis design, and acquisition. The "identify" activity involves a combination of light optical and backscatter electron imaging coupled with some form of qualitative analysis to distinguish meaningful regions from artifact (topographic or crystallographic differences). Typically the multiple is given light optical inspection after the metallographic preparation. Next, secondary electron or back-scattered electron micrographs are taken to identify the best sections within a given diffusion multiple for further evaluation from average atomic number contrast. In many cases, more than one section of a specific multiple needs to be analyzed due to porosity, cracking of intermetallic compounds during sample preparation, or other deleterious effects along a particular binary or ternary region in a given metallographic section.

The phases identified by backscatter electron contrast would be compared to adjacent regions using semi-quantitative surveys to determine presence of unique phases or diffused regions - a critical step to avoid spending hours performing unnecessary quantitative analysis. This was often done using X-ray counting integration for specific elements present over a pre-set time, or by performing an EDS spectral acquisition on the areas for comparison. In some cases a quick WDS count rate meter comparison was used. The choice of comparison method and attention to detail of these inspections was also influenced by knowledge of the expected phases generated from the literature, especially

the binary phase diagrams. This could help predict and identify compositions generated as a function of the annealing parameters of the various diffusion multiples. This "identify" activity of analysis allows the locations of all significant phases in the multiple section to be logged into the computer.

The "screening" activity includes using either EDS, WDS or both for semi-quantitative and quantitative analysis. Here we tried to obtain a matrix of count rates from identified phases for the elements present. Typically the screening was performed in automated mode and analysis was done over a very small sub-set of the actual analysis matrix to approximate the composition ranges to be measured. This gave vital information to allow selection of all analysis parameters.

In the "analysis design" activity, the goal is to optimize all the conditions for the impending analyses. The primary electron beam energy, beam current, choice of standard, spectrometer crystal, detector bias and pulse height discrimination must be selected as results of the abbreviated "screening" trials. It is made certain the statistical accuracy required in crucial regions is met and pre-determined number of composition profiles are tested to "map" the multiple most efficiently. Also important here are X-ray counting times, dead time error, detection limits and the accuracy required. We also determine the "step-size" (distance between points along a profile) as a result of the screening. Since the acquisitions are performed in automated fashion, we can alter specific sections of the acquisition to accommodate needs of greater sensitivity, varying step size, counting time on peak and background positions, etc. as a function of the composition ranges we have found.

The Monte Carlo simulations such as those shown in Fig. 4 provide us critical information regarding necessary thickness of the intermetallic compounds in the diffusion multiples and the "step size" for EPMA analysis. For instance, the X-ray excitation volume would be less than 1 μm^3 for the Cr_3Pt phase (Fig. 4), thus theoretically the thickness of this phase only needs to be a few microns to allow reliable analysis of its composition. The thickness of the Cr_3Pt phase in the precious metal diffusion multiple is only about 10 μm (Fig. 2), but it is more than enough to allow reliable EPMA analysis. In addition, since the thickness is small and the interaction volume is also small, it makes sense to use 1 μm step size for the analysis of the Cr-Pt-Ru region of the diffusion multiple.

The "acquisition" activity includes intermittent analyses of the standards as a measure of "drift" of beam current, stage, spectrometer position and other instrument stability issues. This can help salvage data by restoring acquired values relative to known variation from the standard. It also helps identify long-term stability limits.

Due to the enormous number of data points collected for a given EPMA acquisition, our ultimate challenge is to minimize the x-ray counting times at each data point. A few unnecessary seconds spent counting at each data point represent nearly 24 hours of acquisition time for typical EPMA runs.

We can utilize established statistical relationships to help decide on the level of accuracy necessary in measured intensity data commensurate with our needs:

The level of homogeneity, in +/- weight% is described by

$$\pm\frac{W_{1-\alpha}}{C} = \frac{\pm\left(t_{n-1}^{1-\alpha}\right)S_C(100)}{n^{1/2}\overline{N}} \tag{2}$$

The analytical sensitivity in weight percent and its relationship to counting statistics is shown in

$$\Delta C = C - C' \geq \frac{2^{1/2}C\left(t_{n-1}^{1-\alpha}\right)S_C}{n^{1/2}\left(\overline{N} - \overline{N}_B\right)} \tag{3}$$

Here "C" is the actual concentration in weight percent of the sample. S_C is the standard deviation of measured values, n is the number of repetitions, $\overline{N}$ and $\overline{N}_B$ are the average number of X-ray counts for the sample and continuum of the sample respectively, and $t_{n-1}^{1-\alpha}$ (known as "student t value") represents a confidence level of 1-α for n-1 degrees of freedom.

In EPMA, the confidence level is usually chosen between 0.95 and 0.99; that is, only between 5% and 1% of the repeated measurements of a composition will be outside of homogeneity. It is statistically more difficult to measure a given level of homogeneity as C decreases. To do so, an analyst must increase counting time per point.

Having some knowledge of the approximate levels of elemental concentration within a phase and along a gradient to be measured is extremely important in making decisions about the counting statistics and dwell times needed at each measurement for all elements and for both peak and background X-ray integrations. Having a *priori* knowledge also allows us to make predictions using the above equations to better reduce the total number of steps along a composition gradient to avoid acquiring data below ΔC, thus reducing acquisition time and increasing efficiency.

Another important consideration is the amount of time spent measuring the background signal, and whether to measure it at all. It is common practice in EPMA to select only a "baseline" measurement for background counts associated with a given characteristic X-ray peak. In many cases this is acceptable, but as peak counts approach background counts, it becomes imperative to measure the background accurately in order to obtain the composition. In multi-element systems, background measurements must be taken on both sides of a measured peak if there are interference peaks from the presence of elements which are variable in magnitude, or if the compositional variations present differences in effective absorption of the measured element.

In order to measure the peak and the continuum X-ray signals efficiently and minimize counting statistical uncertainties, we can try to appropriate the time spent according to the optimization equation below, which shows the ratio of time (T) spent on the X-ray peak (p) relative to background (b) equal to the square root of ratios of their respective count rates:

$$\frac{T_p}{T_b} = \sqrt{\frac{R_p}{R_b}} \qquad\qquad (4)$$

Of course, every multiple-element system offers unique challenges for characterization. One example outlined in detail in this chapter is the Ru-Pd-Rh-Pt-Cr diffusion multiple. The $L\alpha$ X-rays for periodic table "neighbors" Pd, Rh and Ru presented serious overlap issues. Using the PET crystal, a nearly direct peak overlap exists for the first-order $PdL\alpha1$ with first-order $RuL\beta2$, and first-order $RhL\beta1$. Subsequent overlaps of second-order $CrK\alpha1$ and $RuL\,\beta1$ with first-order $RhL\alpha1$. In addition, a number of problem overlap peaks interfered with regions "off-peak", normally used to measure and fit background intensities.

In these severe conditions of overlapping peaks, we use interpolations from the standards in which we measure artifacts from overlapped peaks and extrapolate to the unknowns (specimens). This can introduce greater error into the analysis, due to non-linearity of the model, dead-time errors, absorption edges causing non-linear background effects and others.

There are other approaches to de-convoluting overlapped peaks, such as the use of principle component analysis, which may generate better results for specific X-ray overlap cases. Other areas for possible improvement include X-ray collection using hybrid EDS/WDS methods. EDS can bring much higher X-ray collection efficiencies due to geometric advantage over WDS, and might be applied for simultaneous analysis of major elements or where the degree of accuracy required is less of a concern.

3.2 EBSD

Electron backscatter diffraction (EBSD) and backscatter electron (BSE) imaging add crystallographic and compositional information to the quantitative compositional information obtained by electron microprobe. Backscattered electrons are high energy (10-40 keV) electrons, which interact with the top layer (<0.5 μm) of the sample through high angle, virtually elastic scattering events. EBSD uses the diffraction of these high energy electrons to identify the crystalline phase and its three-dimensional orientation at a given point on the surface. Backscatter imaging provides semi-quantitative compositional information due to the dependence of the BSE scattering cross section on the average atomic number of the sample at a given point. A great deal of work has been done in this field and good reviews can be found in texts by Randle [9], Schwartz et al. [10], and Goldstein et al. [11].

EBSD is performed by collecting diffracted BSE's from the surface of a tilted SEM sample (Fig. 7). The sample is tilted to maximize the collection of diffracted BSE's. The diffracted BSE's strike a phosphor screen, generating light. This light is normally captured by either a CCD camera or by a silicon intensified target (SIT) camera. The output of this detector is then run through a digital signal processor and into computer-

based acquisition software. The collected EBSD pattern resembles the Kikuchi electron diffraction patterns observed in TEM. The bands of intensity in the EBSD pattern are actually the intersection of diffraction cones with the phosphor screen. Each band corresponds to one type of {hkl} crystallographic planar spacing. Most automated EBSD analysis packages use the Hough transformation to detect the diffracted {hkl} bands. The angles between detected bands and their widths are compared to lists of calculated reflections for crystals input by the user. A solution criterion is used to identify the best-fit between the experimental EBSD pattern and a given crystalline phase at a specific three-dimensional orientation. The final output of this calculation is the crystalline phase and a set of three Euler angles describing its orientation (Fig. 7(b)).

Both EBSD and BSE imaging are currently available as commercial techniques. Most commercial SEM's come equipped with some sort of BSE detector. An EBSD system is comprised of a special detector, acquisition hardware and software, and analysis software and is available from a number of commercial vendors. The EBSD camera fits onto most standard SEM's. Commercial software can automatically index EBSD patterns of any crystal system at a rate of greater than 20 patterns per second at the fastest, although 10 patterns per second is more reasonable for a total experimental cycle time when scanning the beam. The measurements described in this section were performed on a CamScan CS44 SEM with a tungsten filament at a beam energy of 20 keV. The HKL Channel 5 EBSD acquisition and analysis system was used for collecting the EBSD data. This particular system used a Hammamatsu silicon intensified target (SIT) camera for the detector.

Standard metallographic mounts can be used for EBSD samples with a few qualifications. Most metallographic procedures finish polishing with a 1 µm diamond medium. This finishing step leaves a damage layer on the surface on the order of 0.5-1 µm, particularly for metallic samples. This level of surface damage can severely degrade the quality of EBSD patterns due to the shallow depths (~100 nm) of beam interaction. To relieve this surface damage, vibratory polishing with a 0.05 µm silica suspension for many hours (usually more than 12) is suggested. Mounting of samples in a conductive medium is also beneficial, when possible. The use of standard mounting epoxies will cause sample charging, which will stigmate the optics of the SEM and cause sample drift, particularly at the 70° tilt used in EBSD experiments. Removing metallic samples from the mounting material or using conductive epoxies will help to alleviate sample charging. For insulating samples, such as ceramics, carbon coating may be necessary to alleviate charging even with a conductive mount.

The spatial resolution of EBSD is well suited to the compositional libraries created by diffusion multiples and is somewhat better than electron microprobe. The physics governing the spatial resolution of EBSD are quite similar to that of electron microprobe because both techniques are performed with focused electron beams. The principal difference between the two techniques is the signal collected. Diffracted BSE's emanate from a sub-micron volume around the probe's intersection with the sample. A minimum theoretical probe size of ~50 nm in the X direction and ~150 nm in Y direction (sample is tilted 70° about the X direction) has been suggested for tungsten filament instruments

[12]. These estimates will vary strongly as a function of beam energy (larger energy gives a larger interaction volume) and as a function of sample atomic number (heavier elements have greater electron stopping power and consequently a smaller interaction volume). We have observed a practical resolution limit of 250-500nm for standard metallurgical alloys.

The automation of EBSD is driven by the automated collection and analysis procedure and by the automation of the sample stage. The automation of pattern collection and analysis is the key point in the commercialization of the technique. As mentioned above, automated analysis routines are available from a number of vendors, which allow for rapid discrimination between a number of input phases (greater than 20 patterns per second). The automation of the sample stage is also important for rapid EBSD measurements. Most SEM's can collect grid patterns on the samples surface by deflecting the beam with the scan raster coils. Beam scanning can be done very rapidly with extremely fine step sizes (<0.1 μm). However, beam scanning cannot be done over large areas (>400 μm) without distorting the diffraction geometry. SEM's with motorized stages are increasingly the norm. A standard motorized stage has a positional precision of 0.5-1 μm and can move over a range of several centimeters. Using a motorized stage allows the point of interest to always be in the appropriate position for imaging and diffraction, but is much slower than beam scanning (300 ms per point), more expensive, and can suffer from mechanical hysteresis in the stage.

Microcrystallography is the primary use of EBSD. From a phase diagram mapping standpoint, EBSD's importance lies in its ability to detect phase boundaries and identify phases, and is critical to efficient experimental planning in the "identify" and "screening" activities. If a list of expected phases in the sample can be generated, then EBSD can be used to rapidly detect the spatial positions of the phase boundaries on the diffusion multiple. The spatial positions of these phase boundaries can be directly related to the quantitative compositions measured by electron microprobe, resulting in phase boundary positions on the phase diagram. BSE imaging can also be helpful in determining the position of phase boundaries on the sample. In addition to phase boundary detection, EBSD could be used to sample microtexture in samples with gradients in crystallographic texture or even gradients in plastic strain.

Another important use of EBSD is phase identification. Complete structure determination (point symmetry, point group, space group) for a crystallographic unknown is difficult for EBSD and requires detailed and relatively slow analysis of individual EBSD patterns [13]. The determination of lattice parameters with automated EBSD is quite limited but is an active area of research using individually analyzed EBSD patterns [14]. Phase matching is a much more rapid and readily available form of phase identification in EBSD. Phase matching describes the process of comparing an experimental EBSD pattern from an unknown phase with a list of possible crystallographic phases from either the literature or a crystallographic database. Commercial vendors now provide an automatic search procedure with standard crystallographic databases. The use of compositional information from either EDS (qualitative) or WDS (quantitative) is extremely valuable to phase identification or

matching. Even a qualitative picture of the elements present in a given phase can reduce the number of possible phases significantly. BSE imaging is also helpful in identifying the phases in question due to its sensitivity to changes in composition. These procedures are not completely automated but can be performed on the order of minutes by a trained operator.

As an example of the utility of EBSD in the diffusion multiple approach, we will examine the Cr-Pt-Ru intersection. A BSE image of this region clearly shows five different phases as well as a region of diffusion of Ru and Pt into Cr (Fig. 2). Indexing of individual EBSD patterns taken from these regions identifies the phases as Cr (bcc), Pt (fcc), Ru (hcp), Cr_3Pt (A15), and CrRu (σ phase) (Fig. 8). An EBSD phase map of this same area locates the positions of the phase boundaries (especially the A15 / σ phase boundary) which are used for intelligent placement of EPMA scan locations.

In brief, EBSD and BSE imaging are characterization tools capable of adding crystallographic and compositional information to the mapping of diffusion multiples. For diffusion multiple studies, these techniques provide the position of phase boundaries for comparison with microprobe compositional data and assist in the identification of phases.

3.3. *Example Analysis of the Precious Metal Diffusion Multiple*

The novel diffusion multiple approach has challenged the field of quantitative microanalysis to provide higher levels of efficiency, throughput and mechanical and electron beam stability while maintaining a high level of accuracy. Here we present the details of such a study.

The interdiffusion of elements at the tri-junction regions of the diffusion multiple allows the formation of all the intermetallic compounds and the generation of composition variations for all the single-phase regions. Detailed explanation of this can be found elsewhere [1,2]. An example of the analysis procedure for EPMA mapping of the Cr-Pt-Ru ternary system (tri-junction) is provided here (Figs. 2 and 8). The interdiffusion of Cr and Pt formed the A15 phase, and that of Cr and Ru formed the σ phase. Close to the tri-junction region, ternary interdiffusion took place. In order to determine the tie-line compositions of the ternary system, EPMA analysis was performed using automatic stepping along the lines shown in Fig. 8. These lines were chosen to: 1) cover all the composition regions, 2) provide enough tie-line and tie-triangle data to construct the phase diagram, 3) produce more data in regions near the three-phase triangles (intersections) and less data elsewhere, 4) reduce the number of EPMA points for the reduction of cost and data-collection time. Longer scans were made to collect diffusion profiles for the three binary systems for diffusivity evaluation. Since the intermetallic compounds were very thin (≤ 10 μm), 2 μm steps were used in most EPMA scans shown in Fig. 8. This decision was based on the very small electron beam - sample interaction volume, thus very small X-ray excitation volume (<1 μm), for this particular ternary system (Fig. 4). The 2 μm steps made it possible that we were not over-sampling the

region (not producing many unnecessary points while still producing enough data points in the thin intermetallic phases to allow the extrapolation to the interfaces to obtain reliable tie-line data. The entire Cr-Pt-Ru system was mapped with 558 EPMA points which were done in about 9 hours.

An example scan is shown in Fig. 9(a) showing a 40 μm scan from bcc(Cr) to A15 to fcc(Cr,Pt) phases. Six data points were collected in the thin A15 phase, which were enough to make reliable extrapolation to the interface to obtain the tie-line data. There was a data point (at the 24 μm location) at the very interface of the A15 – fcc(Cr,Pt) interface. Since it has sampled both phases, its composition was in the middle of the two-phase region. All the tie-line information obtained from the Cr-Pt-Ru tri-junction was collected in Fig. 9(b) to construct the phase diagram. The tie-lines from Fig. 9(a) are highlighted in Fig. 9(b).

The local equilibrium at the phase interfaces was the basis for using diffusion multiples to map phase diagrams. The existence of such local equilibrium and its reliability in establishing equilibrium tie-line information has been demonstrated for many years in diffusion couples.

By performing EPMA and EBSD analysis of all the tri-junction regions in the diffusion multiple, we were able to map isothermal section phase diagrams of 10 ternary systems, as shown in Fig. 10. The efficiency gain is tremendous - it would probably take approximately a thousand individual alloys to map these phase diagrams that we obtained from a single sample.

As we discussed earlier, the key balance in EPMA analyses is to obtain enough reliable data while reducing the total number of points and mapping time. This all relates back to our discussion about the counting time on peak and background, counting statistics, stepping size, scan length, scan locations, selection of beam voltage and current. Based on our experience, the two key factors in achieving high efficiency mapping are scan locations and stepping size. The EBSD phase identification is extremely helpful in locating the phase boundaries, and thus facilitates greatly our decision of placing the scans at the proper locations (Fig. 8) to get the most critical data. For instance, EBSD identification of the A15 – σ phase boundary and the hcp – fcc boundary in the Cr-Pt-Ru system help us placing the line scan positions to minimize the number of scans required for this system. The stepping size is very critical since it will reduce the analysis time to half just by increasing the step size from 1 μm to 2 μms. The stepping size decision needs to be made based on the size of the phases and the interaction volume. Again using the Cr-Pt-Ru system as an example, both the thickness of both the A15 and σ phase was around 10 μm (Fig. 8) and the beam interaction volumes were less than 1 μm. Thus it is reasonable to use 2 μm steps in EPMA analysis. On the other hand, it is important to generate enough data points to allow reliable extrapolation to the local equilibrium tie-line compositions. This has been demonstrated in Fig. 9(a).

In addition to mapping phase diagrams, EPMA analysis was also required to evaluate the composition of the nanoindentation positions so that the hardness and modulus – location

information such as the one shown in Fig. 11(a) can be converted to the hardness and modulus – composition information (Fig. 11(b)). This is usually done after the nanoindentation experiment.

Since large amounts of EPMA data are generated during the analysis of the diffusion multiple, we have developed automatic plotting procedures based on Microsoft Excel Spreadsheet. During data reduction, we usually plot two figures for each scan to help judging the tie-line compositions. The first one plots compositions of individual points against location (distance in X- or Y- direction). This helps to extrapolate to the local equilibrium compositions at the phase interface (Fig. 9(a)). The second one plots one element (e.g., Pt) against another (e.g., Ru in the Cr-Pt-Ru case). This plot basically shows the "diffusion path" of the scan location in the corresponding phase diagram format. The two plots define the tie-line compositions. The tie-triangles are usually obtained by extrapolating the three two-phase tie-lines.

For each tie-line, we can only obtain one set of data in one polished cross section of the diffusion multiple. This is different from analysis of individual alloy samples from which several repeats can be made for a single tie-line. Fortunately, the consistency of the tie-line trends in the diffusion multiple results (e.g. Fig. 9(b)) give us as much confidence as that from repeated results from individual alloys.

The massive increase in efficiency and reduction in analysis time of diffusion multiples as compared to individual alloys is not just a mere reduction of the number of samples. It takes a long time for the EPMA to reach a good vacuum (~ 10^{-6} torr) and for the electron beam to stabilize. In the case of individual alloys, the time to wait for vacuum and beam stabilization is a significant part of the analysis time - whereas in the diffusion-multiple case, it is negligible.

4. Physical and Mechanical Behavior

The mapping of phase chemistry and behavior is the critical step for the alloy designer. Here we describe measurement techniques and the application of these techniques to complex phase systems. The mechanical behavior, represented by hardness, instructs us regarding solid solution effects, while the physical behavior, represented by elastic modulus, instructs us regarding atomic interactions and bonding.

4.1 Nanoindentation

Nanoindentation provides the connection between the compositional and crystallographic information discussed above and the mechanical properties that are of ultimate interest in structural alloy development. In fact, it is the ability to obtain mechanical property information at the same length scale and locations as the microstructural information that transforms the diffusion multiple into a high throughput approach for alloy development.

14

Nanoindentation, or instrumented indentation, is a fairly general technique for measuring the mechanical properties of solid materials at small length scales. Instrumented indentation at a basic level consists of inserting a shaft with a diamond tip into the surface of a sample and then withdrawing the tip. During this process, the load and the displacement of the shaft are continuously measured. The result is a load-displacement curve associated with an indentation ranging from 20 nm to 100 μm in depth and 100 nm to 700 μm in width, depending upon the load and the material (Fig. 12).

From the load-displacement curves, a number of important mechanical properties can be calculated. Most indenters use sharp tips with geometries that are self-similar (Vickers and Berkovich). Hardness, elastic modulus, and work of indentation can all be readily calculated from the load displacement curve. Good reviews of the calculation of these mechanical properties can be found in Pharr [15,16] and Cheng and Cheng [17]. The self-similar nature of these tips prevents the direct measurement of yield strength from the indentation measurement using standard analysis techniques. The measurement of indentation yield strength is a topic of active research using both spherical indenters and advanced analysis techniques [18,19].

The spatial resolution of nanoindentation in the X-Y plane is dictated completely by the depth of indentation (Z-direction). Traditionally, nanoindentation has been focused on the depth or spatial resolution in the Z (or sample thickness) direction. For work on coatings and thin films, the position on the X-Y plane was typically of less importance. For characterizing compositional libraries, however, the X-Y plane and Z direction resolution are equally important. For a Berkovich indentation of 1 μm in width in the X-Y plane, the depth of the indent is approximately 140 nm, which is certainly measurable by nanoindentation but is noisier than an indent, which is 500 nm or 1 μm deep. In general, as the indentation depth increases, the quality of the data increases because of decreasing sensitivity to surface roughness, geometric aberrations of the indenter tip, and noise in the displacement measurement. However, a deeper indent increases the lateral size of the indentation rapidly (approximate seven to one width to depth ratio). Indentation experimental practice suggests that indentations be spaced at a minimum of twice the width of the indentation in order to negate overlapping stress fields associated with each indent [20]. For the measurements on the Pd-Pt-Rh-Ru-Cr diffusion multiple, a spacing of 10 μm between indentations was used with indentation depths of up to 225 nm.

Nanoindentation is now a commercial, highly automated technique. Standard instruments have sample stages with automated motion in the X, Y, and Z directions. These stages have an accuracy and precision of around 0.5-1 μm. Automated imaging using optical or topographic signals is also available, depending upon the manufacturer. The registry between the optic axis and the indentation axis is approximately 1 μm. The automation of the indentation experiment is somewhat complicated by concerns over mechanical drift and thermal drift. Mechanical drift can be of concern both in actual placement of the indentation (hysteresis of motors) and in vibrational noise during the indentation experiment (affecting the accuracy of the displacement measurement). Both of these sources of mechanical drift are largely accounted for in commercial instruments.

Thermal drift is caused by temperature fluctuations inside the indentation chamber during a single indentation experiment. Thermal drift between indentations is less of a concern because the load-displacement curve for each indent is analyzed separately. Most commercial systems use enclosures to reduce both mechanical and thermal drift and use back correction algorithms to account for thermal drift. Analysis of the indentation curves can be performed by an automated batch analysis.

Measurable quantities on the load displacement (P-h) curve, such as h_{max}, h_{final}, P_{max}, and $\left.\dfrac{dP}{dh}\right|_{h_{max}}$, can be related to useful mechanical quantities such as the stiffness, hardness, and reduced modulus of the material (Fig. 13) [16,21]. The elastic modulus is calculated from the initial slope of the unloading curve. The loading portion of the indentation curve, or P-h curve, contains both elastic and plastic information while the initial portion of the unloading curve contains elastic information only. The unloading portion of the P-h curve is fit to the following power law relation

$$P = B(h - h_{final})^m \tag{5}$$

The stiffness, S, is taken to be the initial derivative of the unloading curve, $\left.\dfrac{dP}{dh}\right|_{h_{max}}$. The contact depth, h_C, is then calculated by

$$h_C = h_{max} - 0.75\frac{P_{max}}{S} \tag{6}$$

The hardness is given by

$$H = \frac{P_{max}}{A(h_C)} \tag{7}$$

where P_{max} is the maximum applied load, $A(h_C)$ is the projected contact area of the indenter at the contact depth. The area function, $A(h)$, is calculated from a polynomial fit to a calibration curve on an isotropic material of well-established modulus and hardness, such as a fused silica or a single crystal Al standard [16]. The reduced modulus, E_r, is given by

$$E_r = \frac{\sqrt{\pi}}{2\sqrt{A(h_C)}} S \tag{8}$$

and can be related to the actual modulus of the material by

$$E = (1 - v^2)\left(\frac{1}{E_r} + \frac{1 - v_o^2}{E_o}\right)^{-1} \tag{9}$$

where v for the material is the Poisson's ratio, v_o is the Poisson's ratio for the diamond indenter (0.07), and E_o is the modulus for the diamond indenter (1141 GPa) [16].

Another quantity for characterizing the plasticity of a material is the calculation of the irreversible work of indentation, which is the area inside the indentation curves (Equation 6) [17].

$$W_{irreversible} = \int_{0}^{h_{max}} P(h)_{loading}\, dh - \int_{h_{max}}^{h_{final}} P(h)_{unloading}\, dh \qquad \textbf{10}$$

The first term in this expression calculates both elastic and plastic work of indentation, while the second term calculates only the elastic work upon unloading. This quantity is often expressed as the plasticity index, P_i, which is given by

$$P_i = \frac{W_{total} - W_{elastic}}{W_{total}} \qquad 11$$

From this, it is expected that materials which exhibit limited plastic deformation with a large elastic recovery should have a plasticity index approaching zero, while materials which exhibit large plasticity will have a plasticity index approaching one.

4.2 Example of Analysis of Mapping Behavior With Chemistry

As an example of these methods on diffusion multiples, we will again consider the precious metal diffusion multiple. All of these measurements were performed on the Hysitron Triboindenter system using a Berkovich diamond indenter tip. Optical microscopy was used to position the sample at the Pd-Pt-Rh ternary intersection (The Pd-Pt-Rh system has completely mutual solubility during high temperature heat treatment, thus it formed a complete fcc solid solution for the entire ternary system compositions). A grid of 10 by 10 indentations with 10 μm spacing was made using a maximum load of 2500 μN (Fig. 14). Indentation line scans were also made across the binary interfaces under the same conditions. Multiple line scans were made across the Pt-Rh interface to investigate the reproducibility of the data. The Oliver-Pharr equations [16] were used to calculate the elastic modulus and hardness at each indentation point.

A clear transition in both elastic modulus and hardness can be seen for the line scans across the Pt-Rh interface (Fig. 15(a)). The reproducibility between the three lines scans was quite high. Electron microprobe was performed along these same lines allowing the replacement of the spatial position with a compositional axis (Fig. 15(b)). This result demonstrates the importance of spatial registry between techniques (nanoindentation and electron microprobe) and the efficiency of the diffusion multiple approach for alloy development (in contrast to creating several binary alloy compositions for modulus measurement).

The elastic modulus data from the ternary section also shows expected trends as a function of position and composition. A dramatic increase in modulus is observed in the upper right hand portion of the grid, corresponding to increased Rh content (Fig. 11(a)). The moduli of Pd and Pt are similar and this fact is demonstrated by the small measured differences in modulus from top left to bottom left. A much more useful representation of the mechanical property data comes from its combination with the compositional data

from electron microprobe. The mechanical property information (100+ modulus measurements) can be plotted as a three dimensional surface overlying the isothermal section of the Pd-Pt-Rh ternary phase diagram (Fig. 11(b)). This representation serves as an extremely efficient library for accessing the modulus or hardness at a given (Pd, Pt, Rh) composition.

5.   Concluding Remarks

From a single diffusion multiple assembly, ten ternary isothermal phase diagrams have been determined in on the order of 100 hours of microprobe measurements, an extremely efficient generation of ternary equilibria. With a similar investment of time, information on hardness and modulus across this very extensive chemistry space can be mapped. For the alloy designer, this highly efficient diffusion multiple approach can have a tremendous impact on the time required to define the most favored chemistry space.

This mapping of phase diagrams, resulting in material properties– composition relationships, is about one thousand times more efficient than using individual alloys. With such a high efficiency, many critical materials data which otherwise would be too time-consuming and expensive to acquire can be obtained and employed to accelerate our understanding of the materials physics and chemistry. This chapter explains the approach, the mapping techniques and examples. Readers are encouraged to read an earlier paper by the same authors on the potential impact of this diffusion multiple approach for accelerated design of structural materials [22]. The authors hope this chapter provides the details concerning the various analytical probes such that researchers in other fields may be able to take advantage of these probes for efficient screening of high-throughput samples.

References:

1. J.-C. Zhao, Adv. Eng. Mater., 3 (2001), p. 143.
2. J.-C. Zhao, J. Mater. Res., 16 (2001), p. 1565.
3. R. Castaing, PhD Thesis, University of Paris (1951).
4. V.D. Scot and G. Love, (1983) in *Quantitative Electron-Probe Microanalysis*, ed. V.D. Scot and G. Love, Ellis Horwood Ltd., Great Britain, p. 32.
5. E. Lifshin, Private communication.
6. J. I. Goldstein,D.E. Newbury, P. Echlin, D.C. Joy, A.D. Romig, C.E. Lyman, C. Fiori, and E. Lifshin, eds. (1981). In *Scanning Electron Microscopy and X-ray Microanalysis*, Plenum Press, N.Y., p. 111.
7. J.T. Armstrong, Proceedings of the Annual MSA/MAS meeting, (1999) p. 561.
8. F. Pichoir and JL Pouchou, Rech. Aerosp., **5** (1984). p. 349
9. V. Randle, *Microtexture Determination and Its Applications* (The Institute of Materials, London, 1992).
10. A.J. Schwartz, M. Kumar, and B.L. Adams, *Electron Backscatter Diffraction in Materials Science* (Kluwer Academic/ Plenum Publishers, New York, 2000).
11. J.I. Goldstein, D.B. Williams, and G. Cliff, *Quantitative X-ray Analysis* (Plenum Press, New York, 1986).
12. D.J. Dingley, "The Development of Automated Diffraction," in *Electron Backscatter Diffraction in Materials Science*, edited by A.J. Schwartz, M. Kumar, and B.L. Adams (Kluwer Academic/ Plenum Publishers, New York, 2000), pp. 1-18.
13. J.R. Michael, "Phase Identification Using Electron Backscatter Diffraction in the Scanning Electron Microscope," in *Electron Backscatter Diffraction in Materials Science*, edited by A.J. Schwartz, M. Kumar, and B.L. Adams (Kluwer Academic/ Plenum Publishers, New York, 2000), pp. 75-89.
14. J.R. Michael and J.A. Eades, Ultramicroscopy **81**, 67-81 (2000).
15. G.M. Pharr and W.C. Oliver, MRS Bulletin **July**, 28-33 (1992).
16. G.M. Pharr, Mater. Sci. Eng., **A253**, 151-159 (1998).
17. Y.T. Cheng and C.M. Cheng, Appl. Phys. Lett., **73** (5), 614-616 (1998).
18. E.G. Herbert, G.M. Pharr, W.C. Oliver, B.N. Lucas, and J.L. Hay, MRS Symp. Proc. vol **649**, pp. Q3.4.1-3.4.6 (2000).
19. N. Dao, N. Chollacoop, K.J. VanVliet, T.A. Venkatesh, and S. Suresh, Acta Materialia **49**, 3899-3918 (2001)).
20. T. Altan, S. Oh, and H.L. Gegel, *Metal Forming-Fundamentals and Applications* (ASM, Metals Park, OH, 1983).
21. M.F. Doerner and W.D. Nix, J. Mater. Res., **1**, 601-610 (1986).
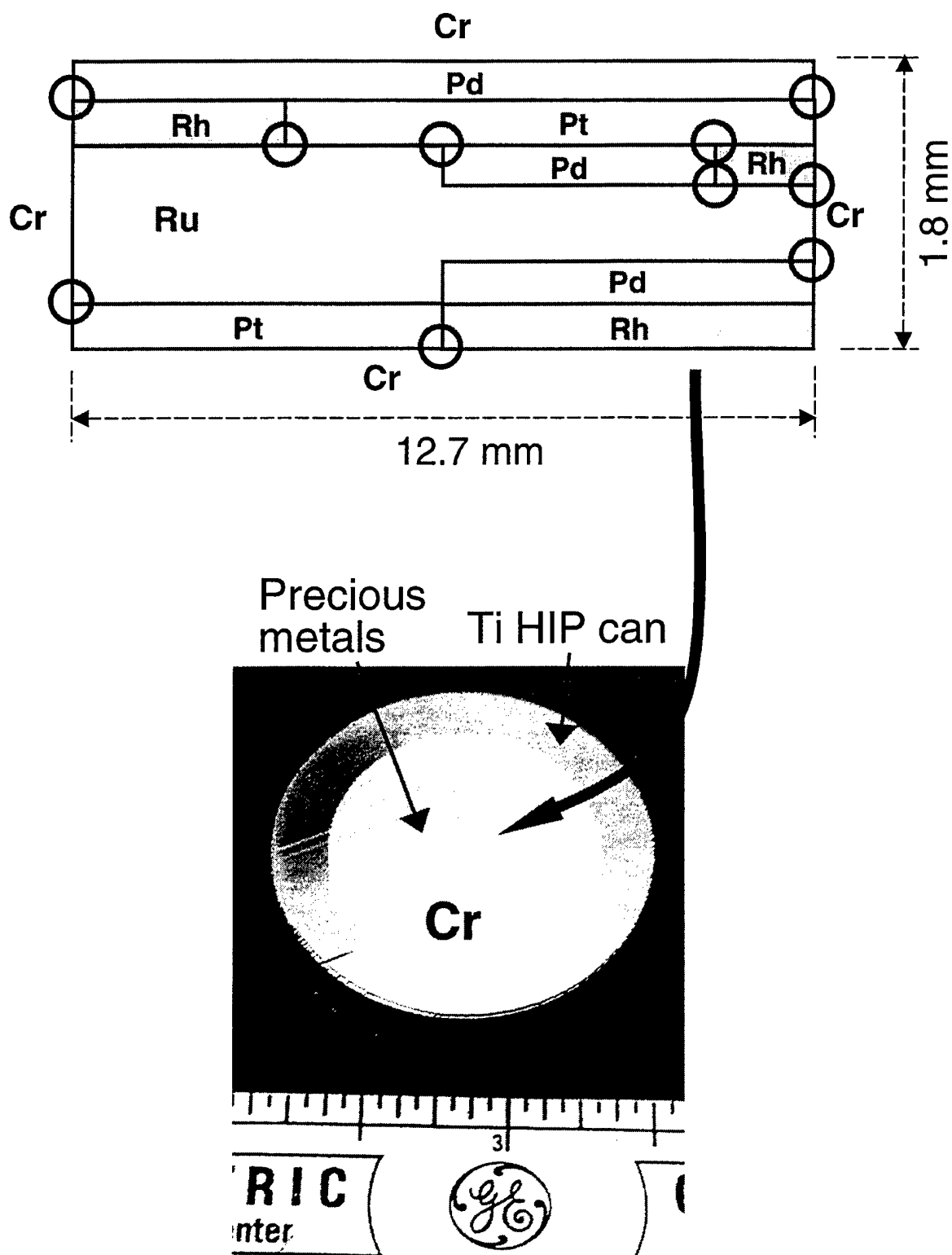22. J.-C. Zhao, M.R. Jackson, L.A. Peluso, and L. Brewer, MRS Bulletin, **27**, 324-329 (2002).

Fig. 1. The size and geometry of the diffusion multiple. The thickness of the Pd, Pt and Rh layers is 0.25 mm. The thickness of the Ru layer is 1 mm on one side and 0.5 mm on the other.
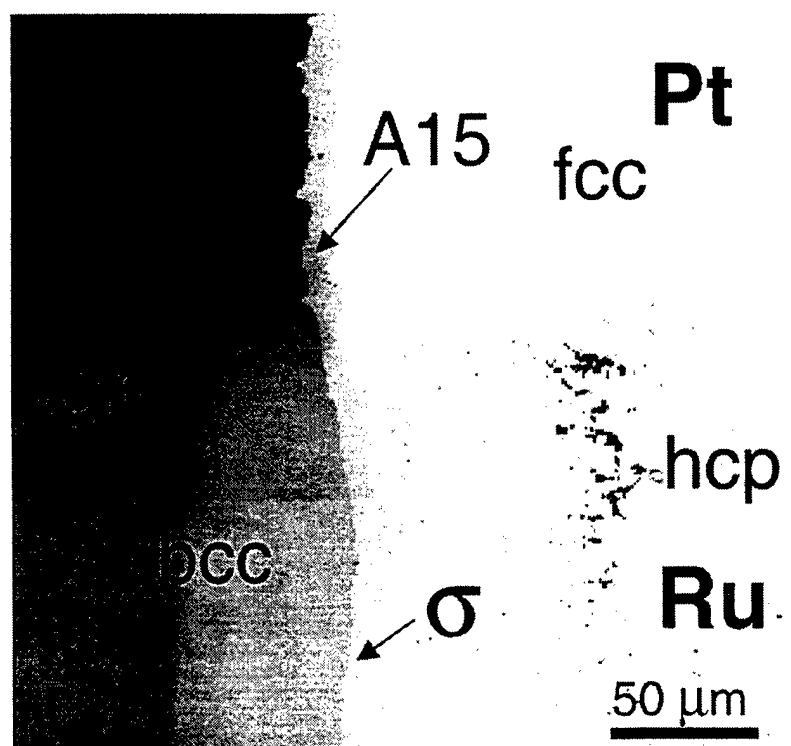
Fig. 2. Backscatter electron image of the Cr-Pt-Ru tri-junction of the diffusion multiple showing the formation of the A15 and σ phases due to interdiffusion of Pt, Ru and Cr.
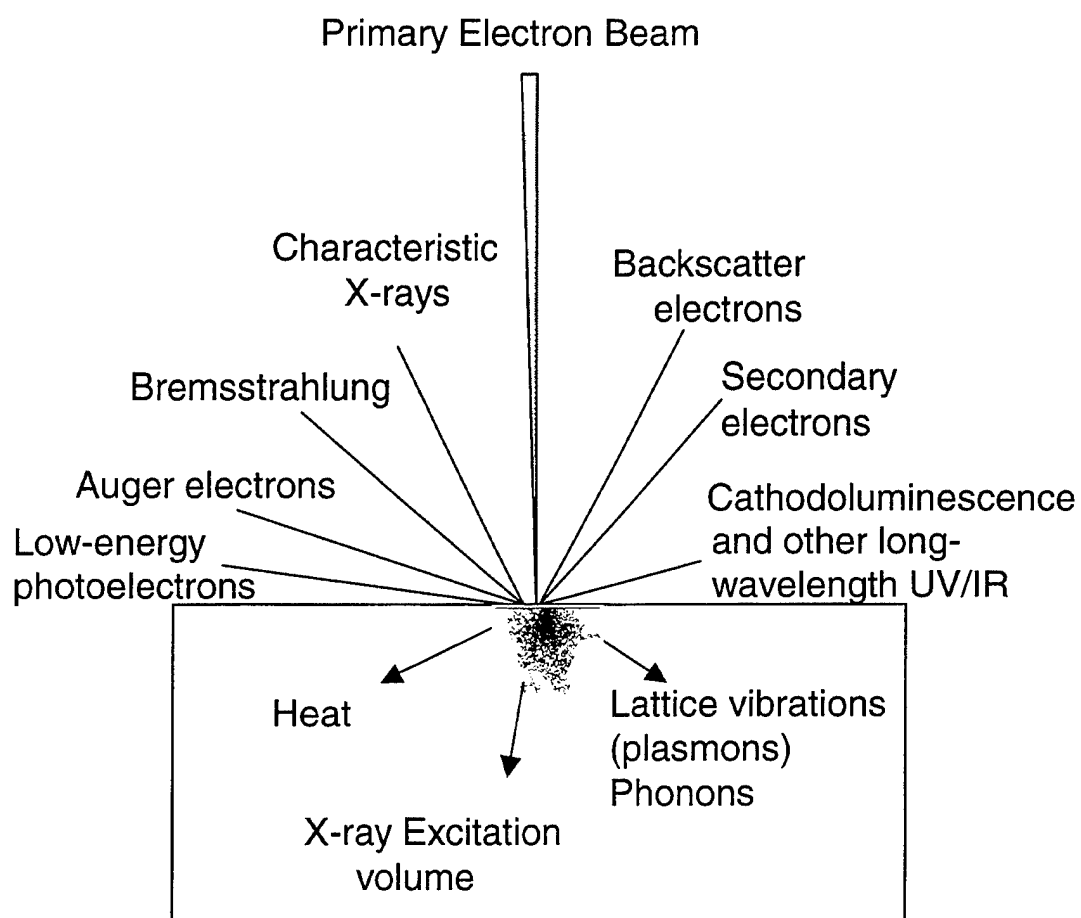
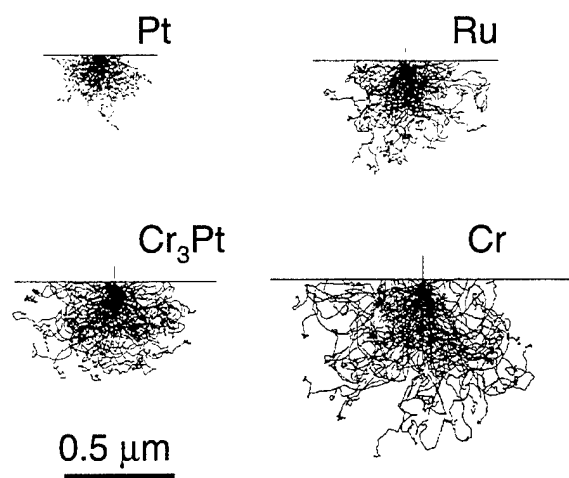**Fig. 3** Schematic diagram showing the primary electron beam - sample interaction and generation of various signals from the sample.

Fig. 4 Monte Carlo simulation results of 15keV electron trajectories at an 90° incident angle.
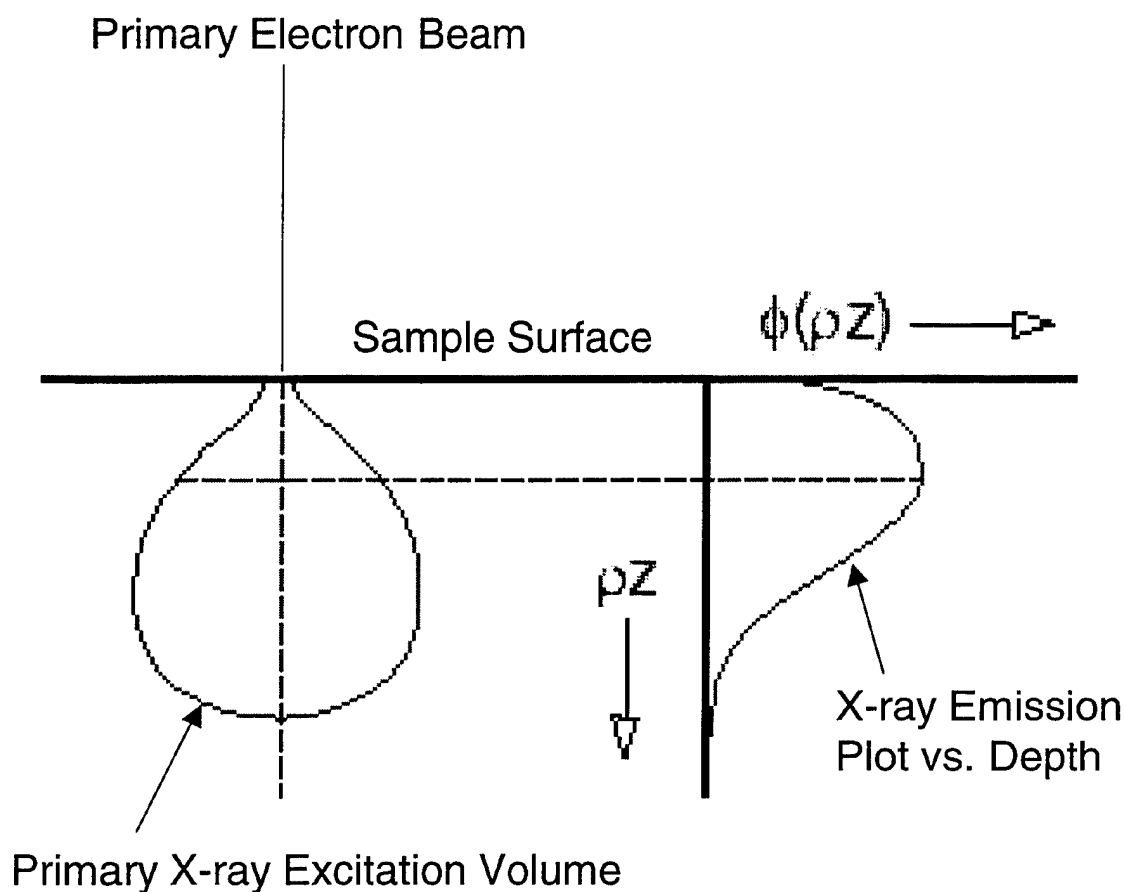
Primary Electron Beam

Sample Surface $\phi(\rho Z)$ ⟶

ρZ

X-ray Emission
Plot vs. Depth

Primary X-ray Excitation Volume

Fig. 5. The "$\phi(\rho Z)$" curves. Near the surface of the sample, X-ray emission is enhanced by scattered electrons from below. X-ray intensity continues to increase with depth due to scattering of the incident electrons which increases the mean path length per unit depth. As electron paths become random, the X-ray intensity per unit depth begins to decrease due to electron scattering and energy loss.
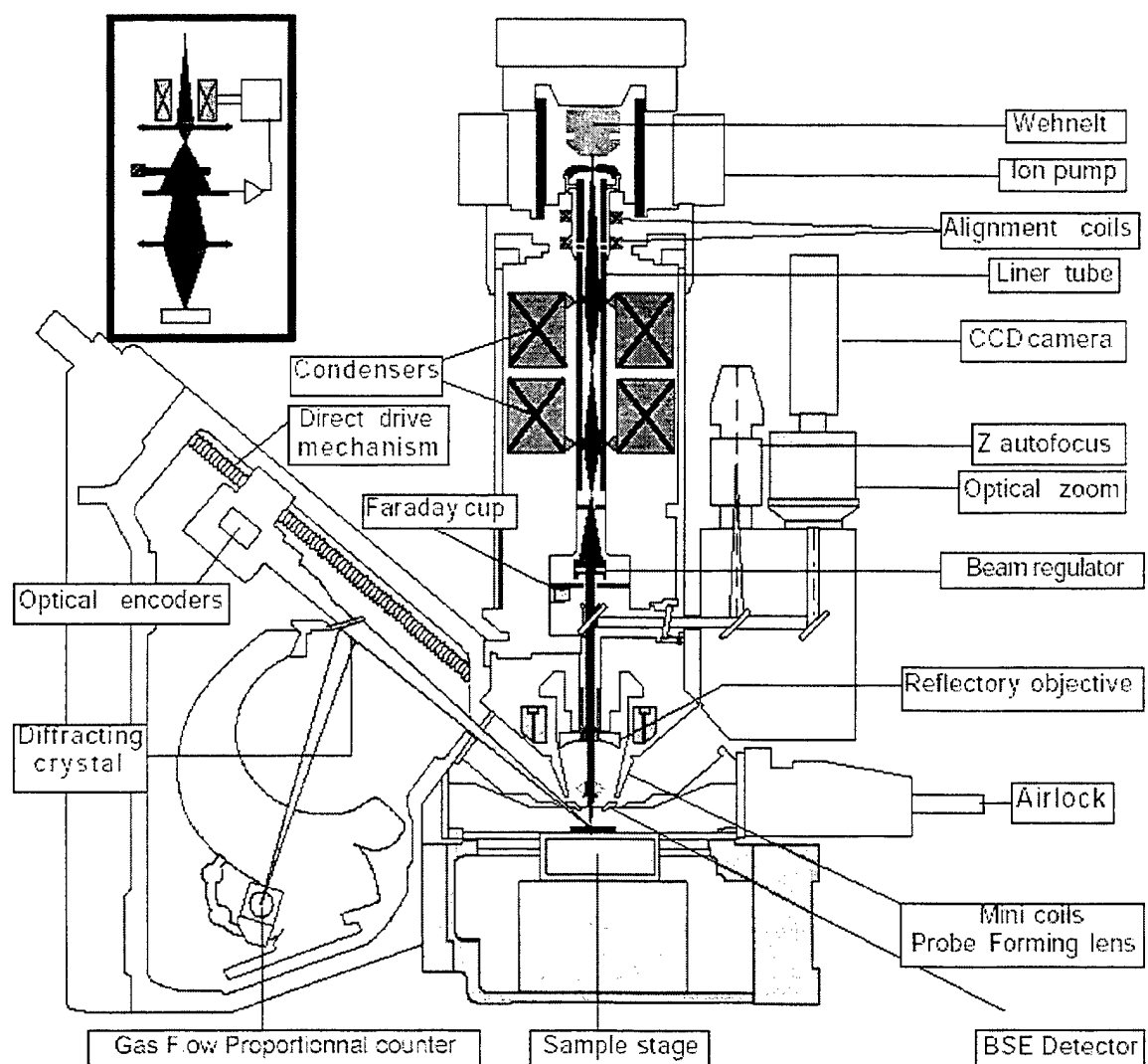
24

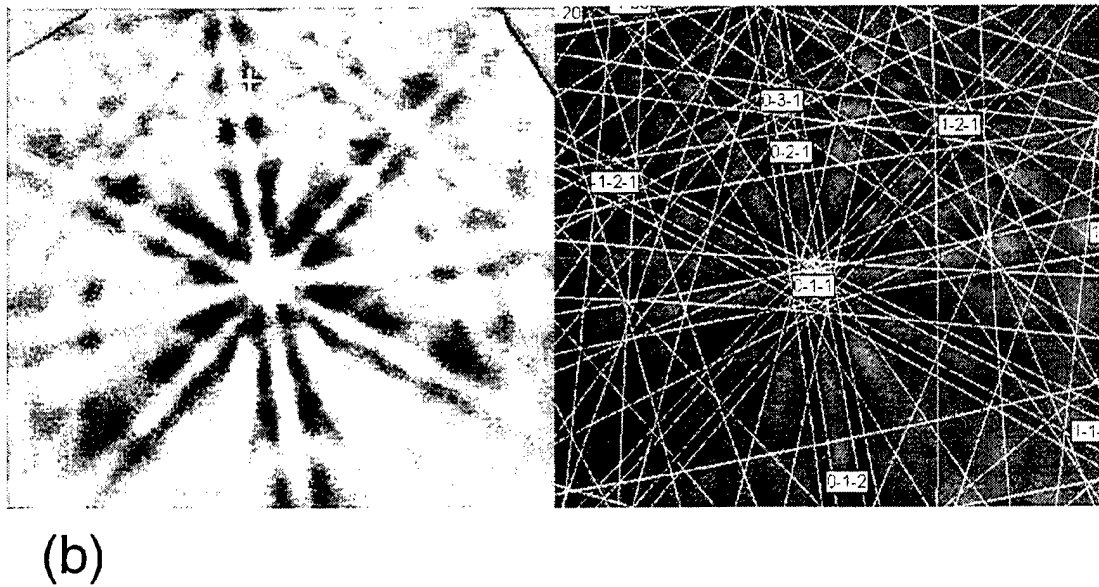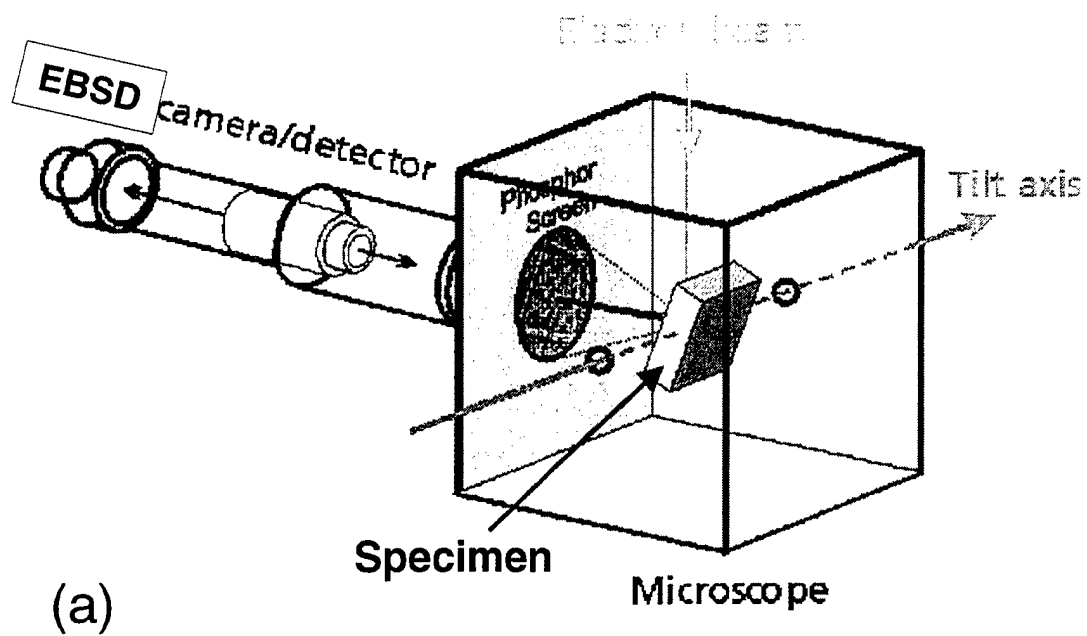**Fig. 6.** Schematic diagram of the Cameca SX50 electron microprobe (Courtesy Cameca Inc., France).

Labels in figure:
- Wehnelt
- Ion pump
- Alignment coils
- Liner tube
- CCD camera
- Z autofocus
- Optical zoom
- Beam regulator
- Reflectory objective
- Airlock
- Mini coils Probe Forming lens
- BSE Detector
- Condensers
- Direct drive mechanism
- Faraday cup
- Optical encoders
- Diffracting crystal
- Gas Flow Proportionnal counter
- Sample stage

Fig. 7. A.EBSD technique for crystal structure identification: (a) Schematic of EBSD equipment and experiment; (b) EBSD pattern of Pt (fcc) and its indexed solution (1° mean angular deviation).
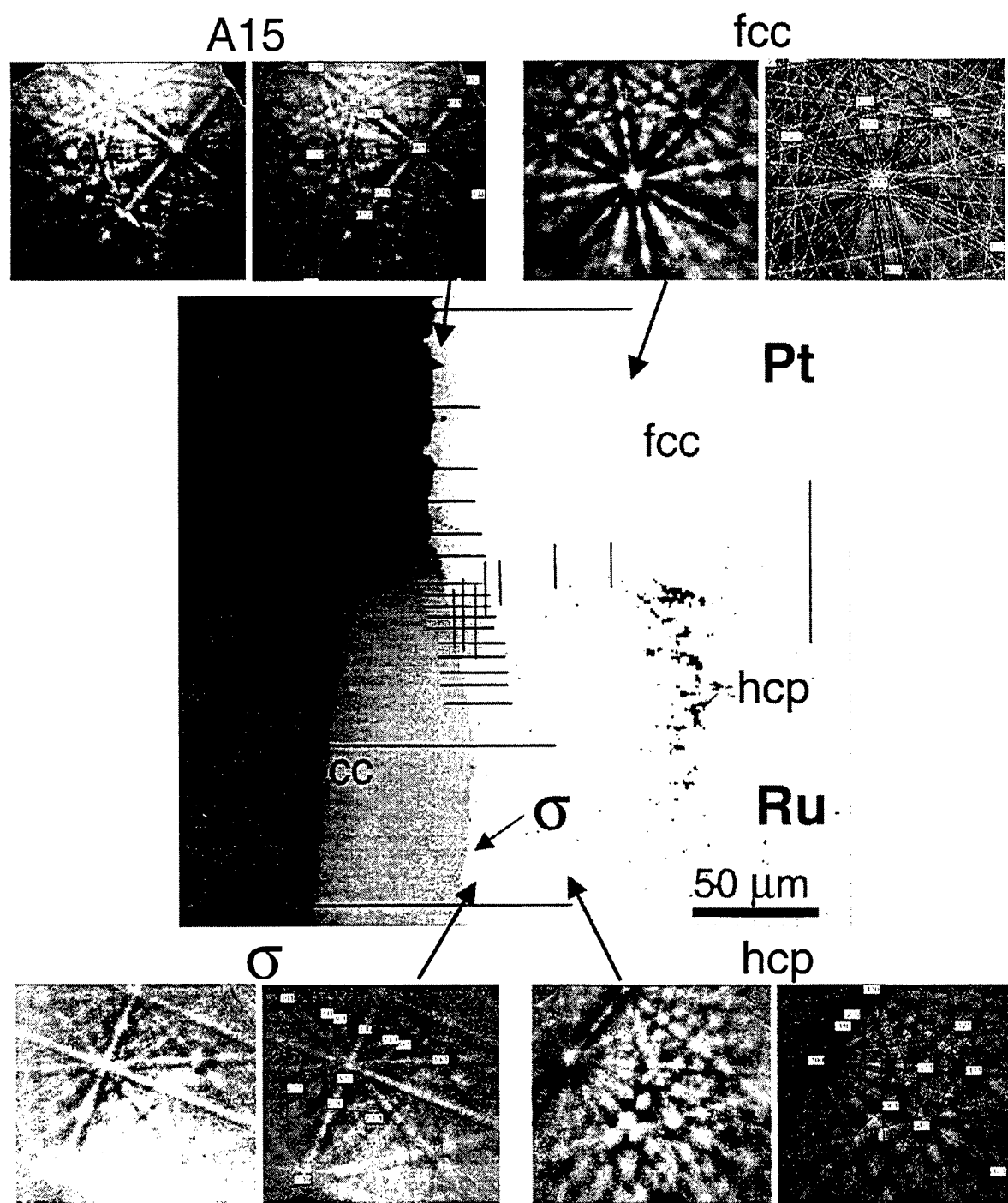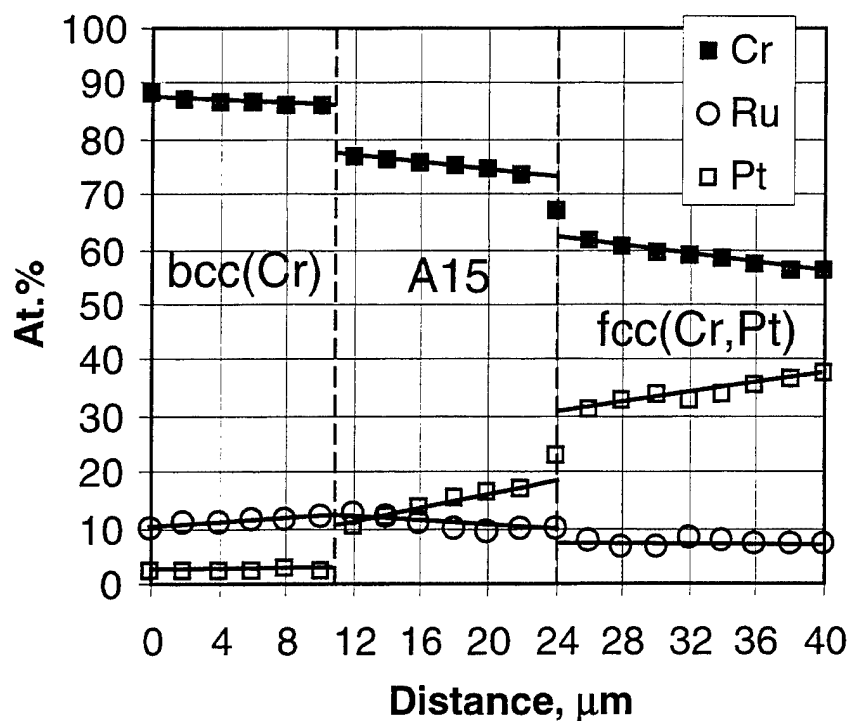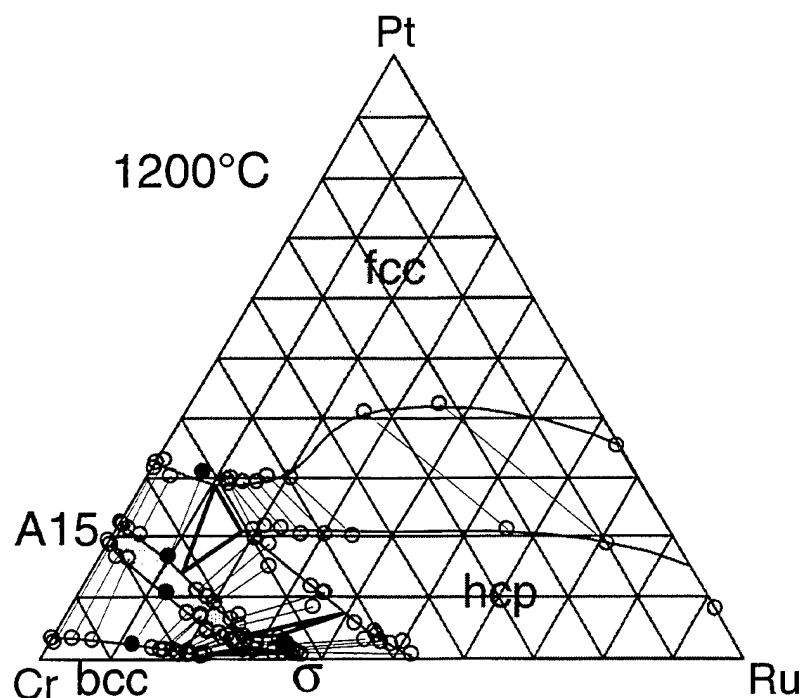
Fig. 8. EBSD identification of phases in the Cr-Pt-Ru ternary system in the diffusion multiple. The lines on the SEM backscatter electron image (in the middle) represent the locations of the EPMA scans.

Fig. 9. EPMA analysis of the Cr-Pt-Ru ternary system with line scans shown in Fig. 8. (a) a line scan showing a typical composition profile produced by EPMA. (b) all the tie-line information based on the EPMA scans for the construction of the Cr-Pt-Ru ternary phase diagram. Filled points represent tie-lines determined in (a).
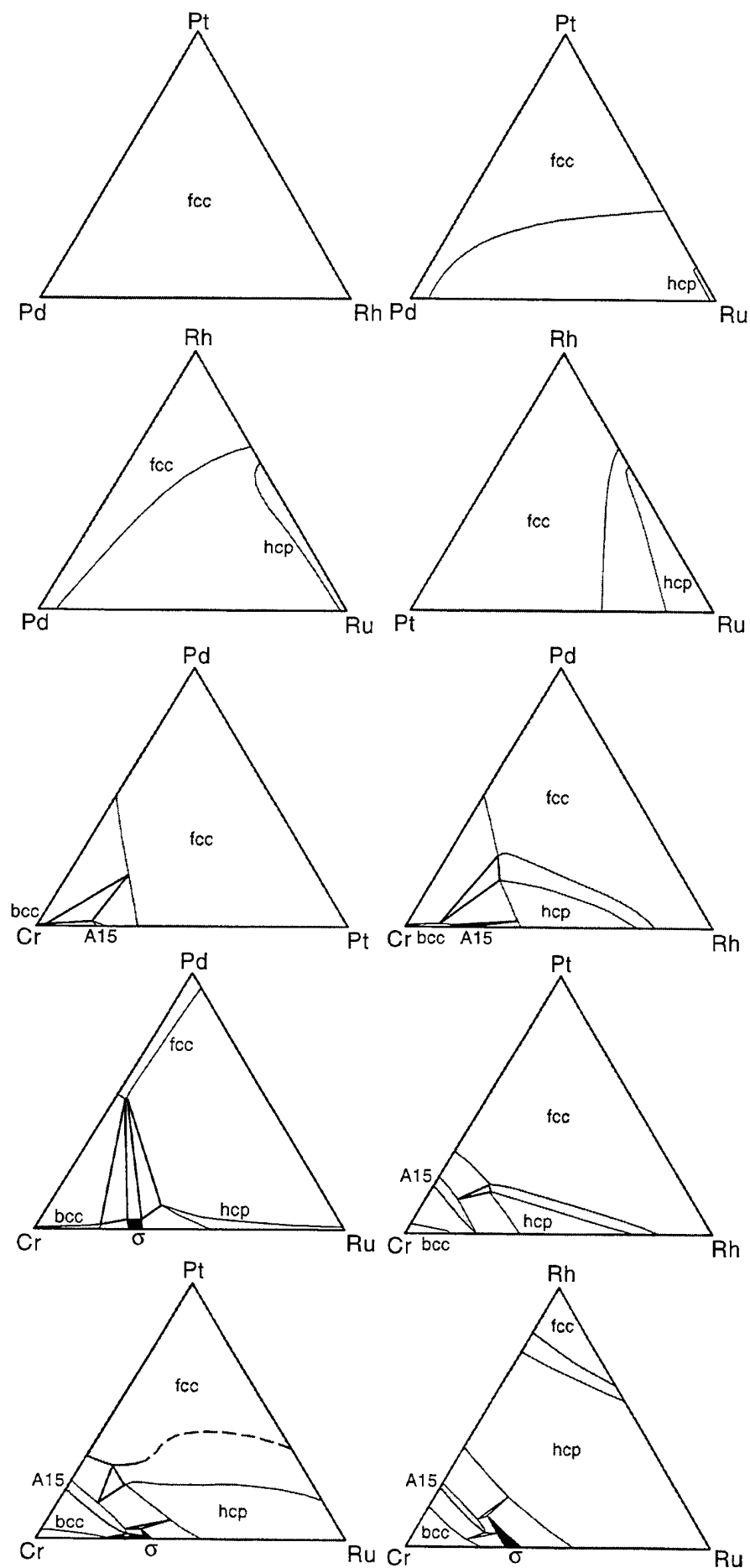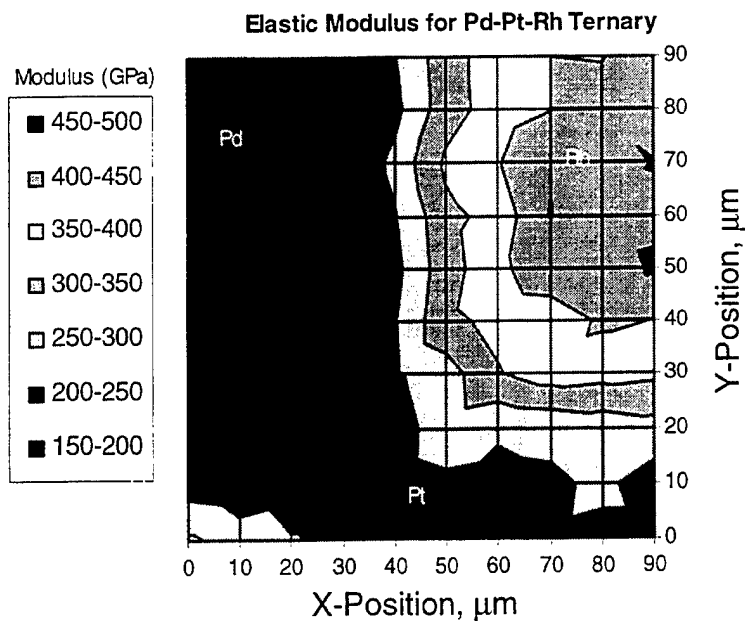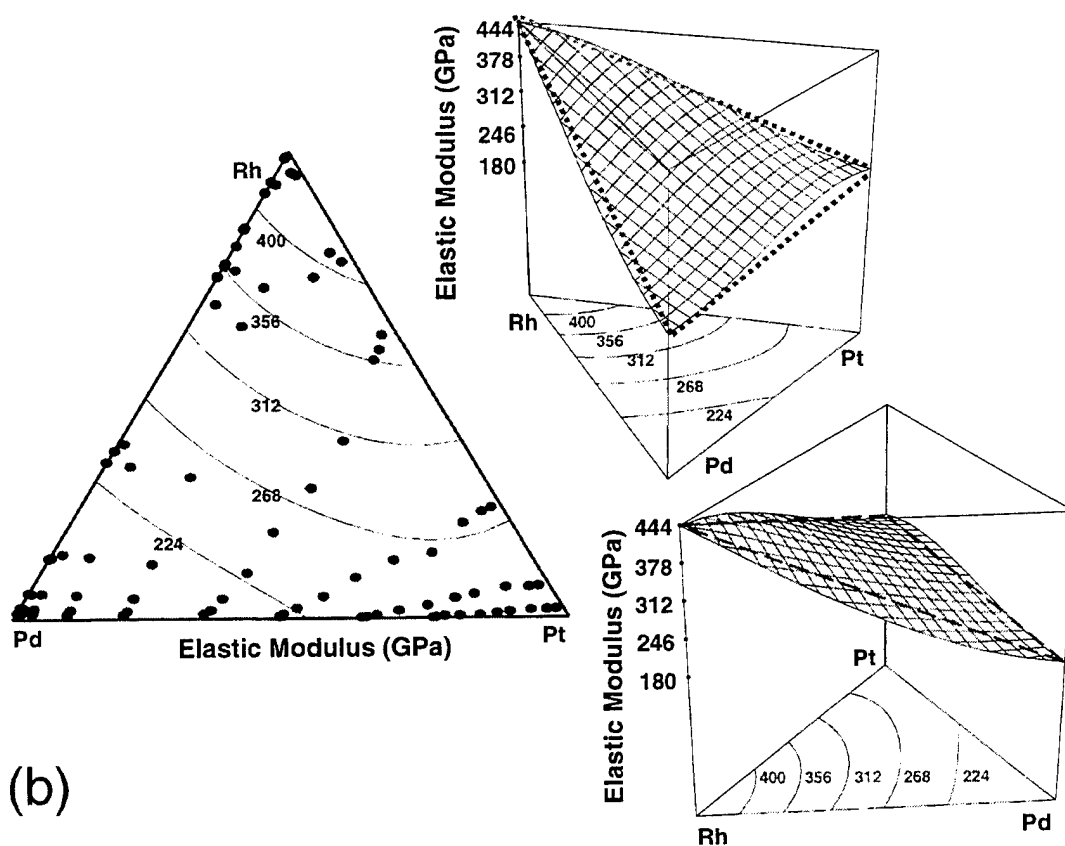
Fig.10. Ten ternary phase diagrams (isothermal sections at 1200°C) obtained from the single diffusion multiple shown in Fig. 1. They are plotted in atomic percent axis with the scale removed for simplicity.

29

Fig. 11. Nanoindentation grid from the Pd-Pt-Rh ternary intersection. (a) Elastic modulus versus position across the Pd-Pt-Rh intersection. (b) Elastic modulus mapped onto the Pd-Pt-Rh ternary phase diagram.

Applied electromagnetic
or electrostatic force

Capacitive or interferometry
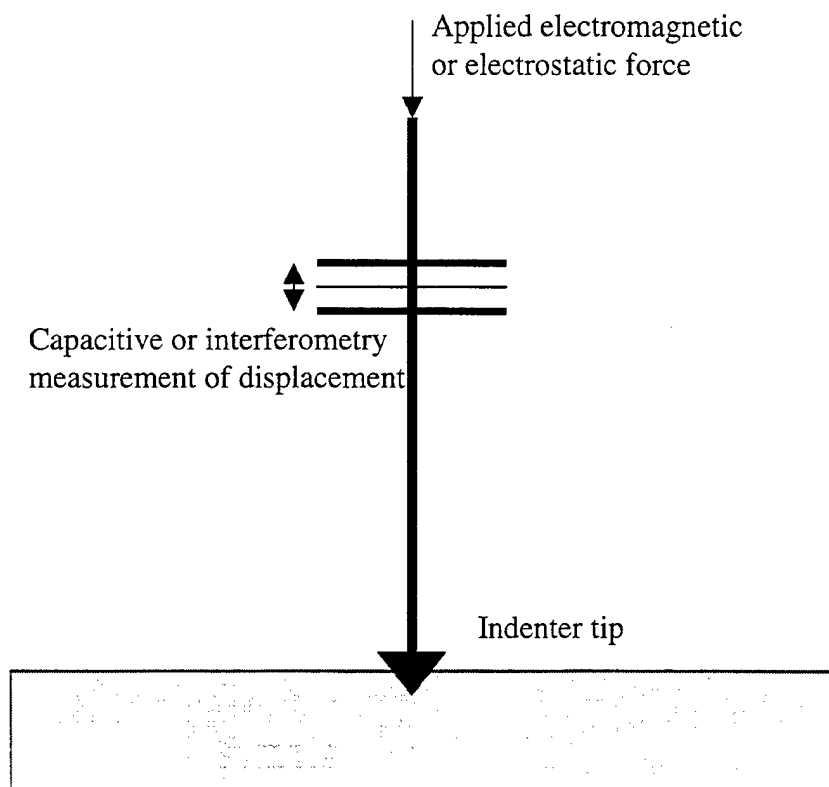measurement of displacement

Indenter tip

Fig. 12. Schematic of instrumented indenter.

Nanoindentation Load-Depth Curve
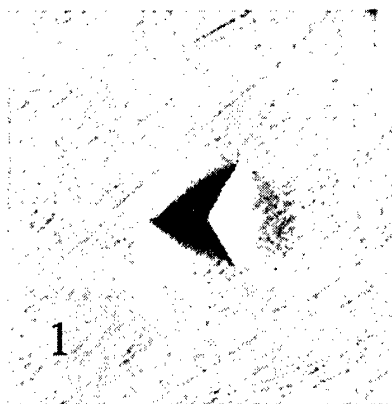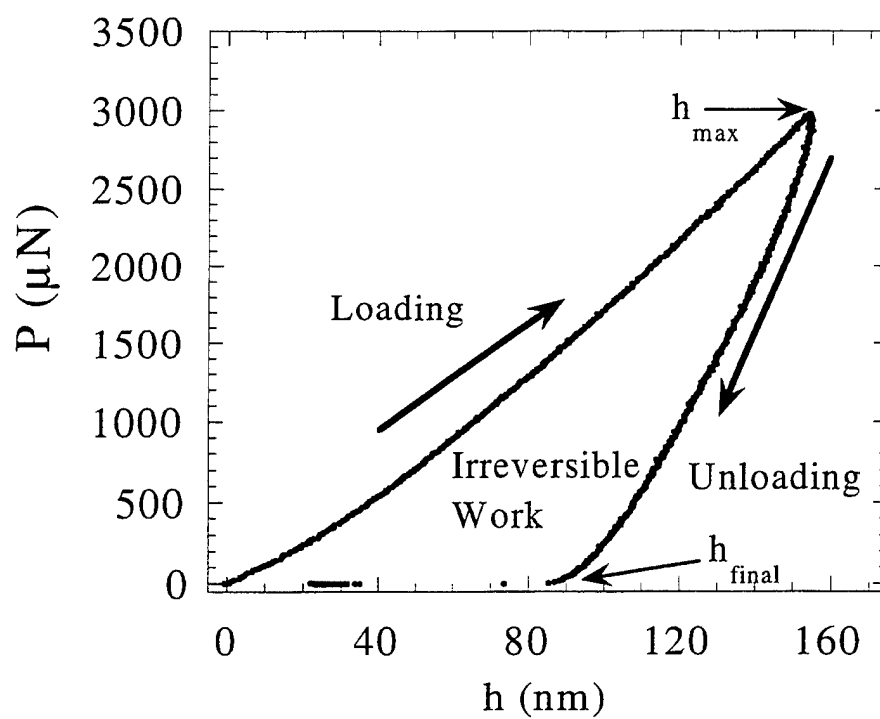
Fig. 13. Load-displacement curve taken from indentation in Pt and an image of the indent.
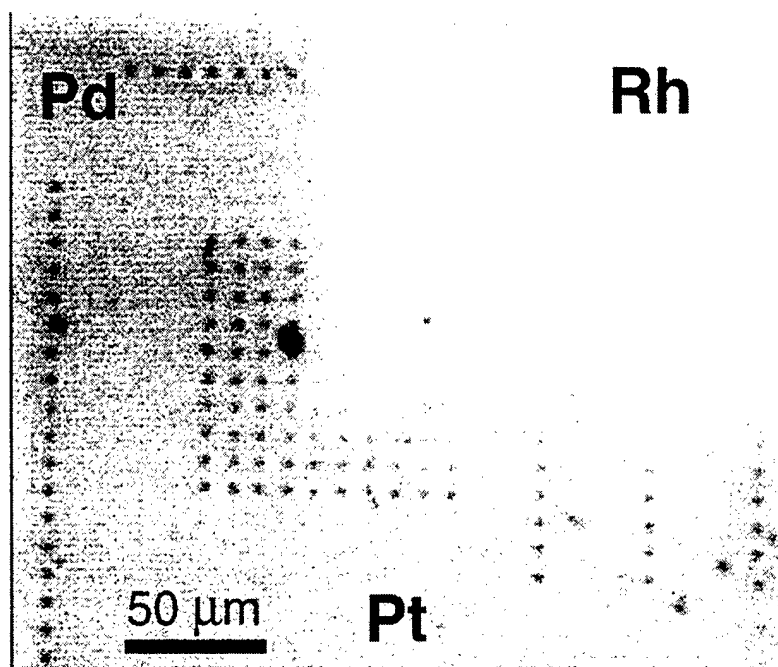
Fig. 14. Optical image of indentation grid made at the Pd-Pt-Rh ternary intersection.

Fig. 15. Nanoindentation line scans across the Pt-Rh interface. (a) Elastic modulus versus position across the Pt-Rh interface. (b) Elastic modulus as a function of Rh content.

Mapping of the Nb-Cr-Si Phase Diagram Using Diffusion Multiples

J.-C. Zhao, M.R. Jackson, and L.A. Peluso

Mapping of the Nb-Cr-Si Phase Diagram Using Diffusion Multiples

J.-C. Zhao, M.R. Jackson, and L.A. Peluso
General Electric Company
GE Global Research Center, P.O. Box 8, Schenectady, NY 12301, USA
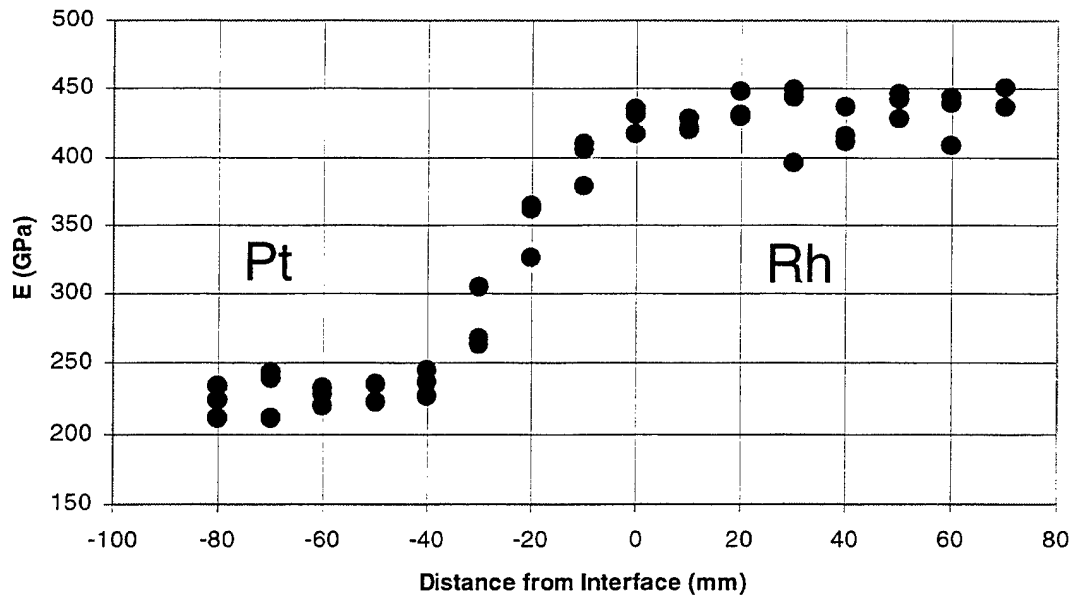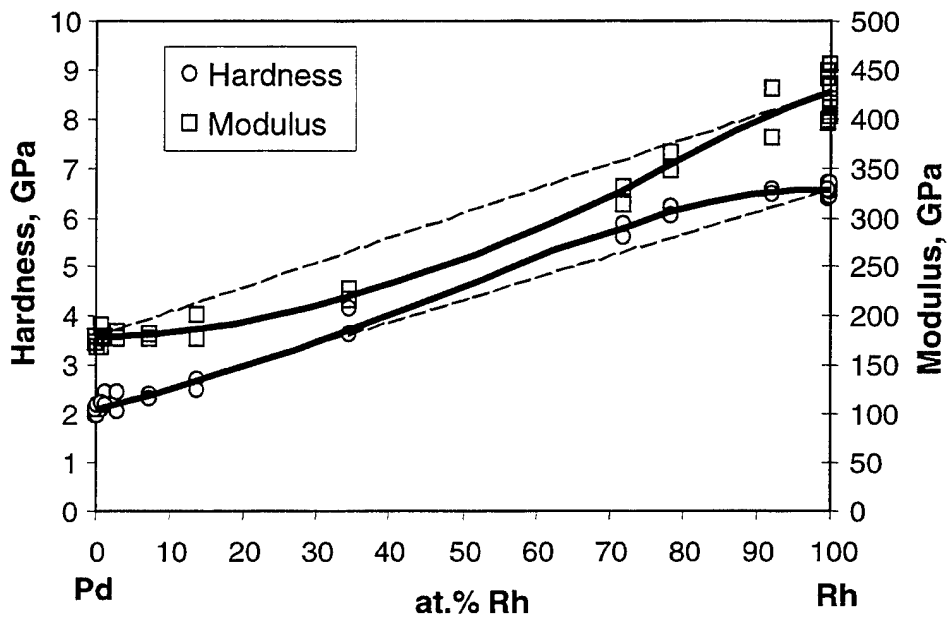
ABSTRACT

A high-efficiency diffusion-multiple approach was employed to map the phase diagram of the Nb-Cr-Si ternary system which is critical for the design of niobium silicide-based in-situ composites. These composites have high potential as a replacement for Ni-base superalloys for jet engine applications. The formation of the $Nb(Cr,Si)_2$ Laves phase is essential for the high oxidation resistance of the composites and the Nb-Cr-Si system serves as the base for understanding the Laves phase formation. The Nb-Cr-Si ternary system which contains 14 phases also serves as an excellent model system to test the applicability of the diffusion-multiple approach to such complex systems. The results clearly demonstrate the high efficiency of the diffusion-multiple approach in mapping complex phase diagrams. Two isothermal sections at 1000 and 1150 °C were constructed from the results obtained from diffusion multiples using scanning electron microscopy (SEM), electron probe microanalysis (EPMA), and electron backscatter diffraction (EBSD). Three ternary compounds, $CrNbSi$, $(Cr,Nb)_6Si_5$ and $(Cr,Nb)_{11}Si_8$, were observed at both temperatures, and the $C14$-Laves phase of the Cr-Nb binary system was stabilized by Si to lower temperatures.

Keywords: Nb-Cr-Si, diffusion multiple, Laves phase, silicide, phase diagram, composites.

1. INTRODUCTION

Niobium silicide-based in-situ composites show great promise for applications as the next generation turbine airfoil materials with significantly higher operating temperatures than current generation advanced Ni-base superalloys [1-6]. The Nb-Si binary composites have excellent creep strength, but poor oxidation resistance and poor room temperature fracture toughness [1-2]. Alloying with Cr can significantly improve the oxidation resistance by stabilizing the Cr-rich Laves phase $NbCr_2$. The potential application of these composites at very high temperatures requires a balance of high creep resistance, high oxidation resistance, and good low-temperature damage tolerance (fracture toughness). To achieve such a property balance, elements such as Cr, Ti, Hf and Al are added to the composites and significant progress has been made in improving the properties of the composites. Some of the alloying concepts were discussed by Zhao *et al.* [7]. The advanced design of the composites requires a fair understanding of the phase equilibria in the Nb-Si-Ti-Cr-Hf-Al system. Since a reasonable definition of the Nb-Hf-Si system has been achieved [8-10], our effort has been focused on the ternary systems Nb-Cr-Si, Nb-Si-Al, Nb-Cr-Al, Ti-Si-Cr, Ti-Si-Al, Ti-Cr-Al, Nb-Ti-Si, Nb-Ti-Cr, and Nb-Ti-Al. Other ternary systems related to the six-element system such as Nb-Ti-Hf, Nb-Cr-Hf, Nb-Hf-Al, Ti-Si-Hf, Ti-Cr-Hf, and Cr-Hf-Al have either good phase equilibria data or are less critical for the design of the Nb silicide composites. We will report the results of the Nb-Cr-Si system in the present paper and the results of other systems will be communicated separately.

1

The high-efficiency diffusion-multiple approach [11-14] is ideally suited for mapping phase diagrams of these ternary systems. It would take thousands of alloys to determine these systems using the traditional one-alloy-at-a-time (equilibrated alloy) approach. For instance, it took Goldschmidt and Brand [15] about 220 alloys to map just the Nb-Cr-Si ternary system and similarly about 135 alloys were employed by Lysenko et al. [16] to determine the Ti-Cr-Si system. These alloys have very high melting temperatures and are difficult to make and to homogenize. Extra effort also needs to be taken to avoid interstitial (oxygen, nitrogen, carbon, etc.) contamination during alloy casting and heat treatment. Apart from possible deleterious effects, interstitial elements are well known to stabilize binary and ternary intermetallic phases that would otherwise not form. In contrast, the diffusion-multiple approach needs no or only a few cast alloys; the samples are easy to make; and safe-guarding against the interstitial contamination can be very easily implemented as will be discussed later. The general diffusion-multiple approach has been discussed in detail previously [11-14] and has been successfully applied to many alloy systems. It would be interesting to see its applicability in a very complex system such as Nb-Cr-Si with more than 10 different phases.

For the ease of understanding the complex phase equilibria in the Nb-Cr-Si system, the constitutive binary phase diagrams of Cr-Nb [17], Cr-Si [18] and Nb-Si [19] are briefly discussed here. The crystal structures of the phases in the binary and the ternary system are listed in Table 1 [20].

Table 1. Crystal structure of phases in the Nb-Cr-Si ternary system [20].

System	Conditions	Pearson Symbol	Space Group	Lattice Parameters, nm				Comments
				a	b	c	γ	
Cr		cI2	Im$\underline{3}$m	0.28847				
Nb		cI2	Im$\underline{3}$m	0.33067				
Si		cF8	Fd$\underline{3}$m	0.54309				
Cr_3Si	$\leq$ 1770°C	cP8	Pm$\underline{3}$n	0.4555				
βCr_5Si_3	1505-1680°C	hP16	P6$_3$/mcm	0.6993		0.4726	120°	
αCr_5Si_3	$\leq$ 1505°C	tI38	I4/mcm	0.9150		0.4639		
CrSi	$\leq$ 1413°C	cP8	P2$_1$3	0.4622				
$CrSi_2$	$\leq$ 1490°C	hP9	P6$_2$22	0.4430		0.6365	120°	
Nb_3Si	1700-1980°C	tP32	P4$_2$/n	1.0224		0.5189		
βNb_5Si_3	$\geq$ 1940°C	tI32	I4/mcm	1.0040		0.5081		
αNb_5Si_3	$\leq$ 1940°C	tI32	I4/mcm	0.6571		1.1889		
$NbSi_2$	$\leq$ 1940°C	hP9	P6$_2$22	0.481		0.661	120°	
Cr_2Nb	$\geq$ ~1600°C	hP12	P6$_3$/mmc	0.4931		0.8123	120°	C14 Laves
Cr_2Nb	$\leq$ ~1600°C	cF24	Fd$\underline{3}$m	0.695				C15 Laves
CrNbSi		hP9	P$\underline{6}$2m	0.6598		0.3359	120°	
$(Cr,Nb)_6Si_5$		oI44	Ibam	1.585	0.753	0.491		
$(Cr,Nb)_{11}Si_8$		oP76	Pnma	1.327	0.4892	1.590		

The Cr-Nb phase diagram [17,21] shows two NbCr$_2$-based Laves phases with the high-temperature hexagonal C14 (hP12) and low-temperature cubic C15 (cF24) structures. The

transformation takes place at ~ 1585 to 1625 °C. The effect of Si on the stability of the two Laves phases can be appreciated by studying the Nb-Cr-Si system as we have done here.

The Cr-Si phase diagram was well assessed by Gokhale, *et al.* [18] and it has four intermetallic compounds: Cr_3Si, Cr_5Si_3, $CrSi$, and $CrSi_2$. The Cr_5Si_3 phase undergoes a polymorphic transformation at 1505 °C with tetragonal structure at low temperature. Although the high-temperature crystal structure of βCr_5Si_3 has not been determined, it was assumed to be the same crystal structure as Ti_5Si_3 [22].

The Nb-Si phase diagram was assessed by Schlesinger *et al.* [19]. A slight revision was made [7] with the eutectoid temperature being adjusted to ~1700°C based on the result reported by Mendiratta and Dimiduk [23] and the L $\leftrightarrow$ bcc(Nb) + Nb_3Si eutectic reaction being adjusted to 1880°C and 18.2 at.%Si to reflect the temperature and composition obtained by Bewlay *et al.* [24] on directionally solidified (DS) Nb-Si alloys. The Nb_5Si_3 phase forms after the decomposition of the Nb_3Si phase via an eutectoid reaction Nb_3Si $\leftrightarrow$ bcc(Nb) + Nb_5Si_3 at ~1700°C, or as the primary solidification product in hypereutectic alloys. Two different tetragonal Nb_5Si_3 phases based on the same crystal structure (*tI*32) with different lattice parameters were reported. The high-temperature and low-temperature phases are designated βNb_5Si_3 and αNb_5Si_3 respectively.

The phase diagram information from the literature for the Nb-Cr-Si system is very limited. An isothermal section of this system at 1000 °C was reported by Goldschmidt and Brand [15] as shown in Fig. 1. There is confusion on the phases and equilibria of this complex system which will be discussed in detail later.
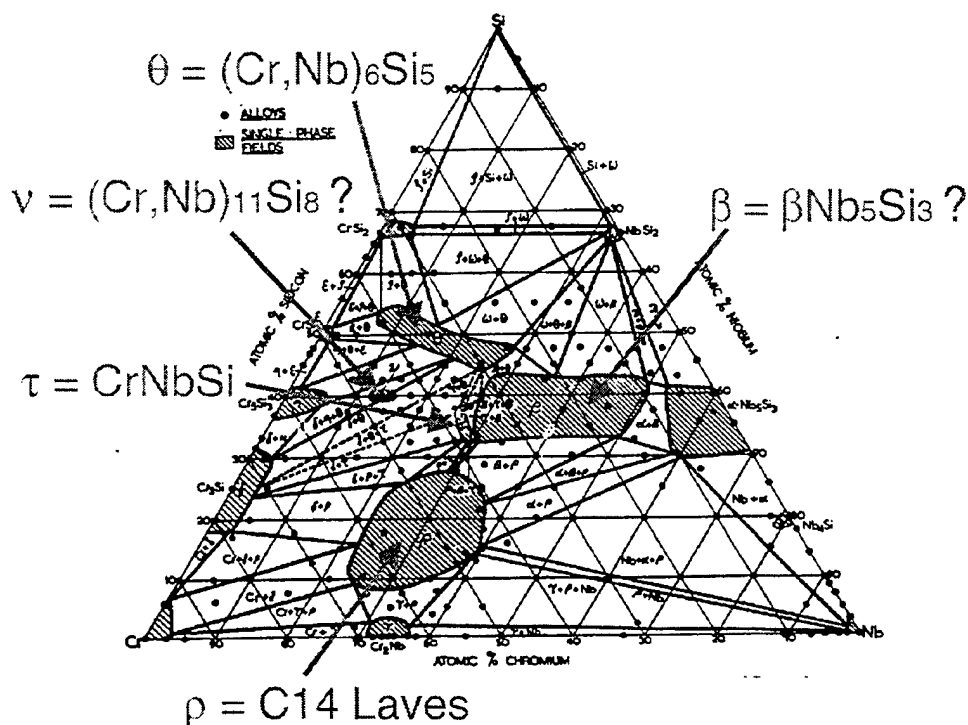

Figure 1. The 1000 °C isothermal section of the Nb-Cr-Si ternary system as reported by Goldschmidt and Brand [15] based on 220 alloys. It is very likely this is not an equilibrium phase diagram because many alloys might not have reached equilibrium.

3

2. EXPERIMENTAL METHOD

A diffusion multiple with the cross-section view shown schematically in the Fig. 2(a) was made. The inner and outer circle diameters were 15.6 and 25.4 mm respectively to guarantee that the dimensions of the pure element pieces are much larger than the diffusion distance, thus there will be pure elements left after the long term diffusion anneal. High purity Nb, Cr, Si and Ti were machined into the proper shapes (quarter pies and round shells, Fig. 2(a)) by electro-discharge machining (EDM). The re-cast layer on the EDM'ed surfaces was removed by mechanical grinding to make clean surfaces. The pieces were ultrasonically cleaned in methanol and then assembled into the geometry shown in Fig. 2(a). The height of all pieces was 25 mm. The assembled diffusion multiples were then loaded into cans made of commercial purity Ti (schematically shown in Fig. 2(b)), and subjected to hot isostatic pressing (HIP) 1204 °C, 200 MPa for 4 hous. A 25-μm thick layer of Ta foil was placed between the diffusion multiples and the HIP cans to isolate any interstitial contaminants that may diffuse into the HIP can from the quartz capsule during long term annealing. The top and bottom caps of the HIP can were electron beam welded. The HIP cans containing the diffusion multiples were then encapsulated in evacuated quartz tubes backfilled with pure argon. Since both Nb and Ti are susceptible to oxygen and nitrogen contamination, it is critical to keep the diffusion multiples from interstitial elements. To further absorb any oxygen that might diffuse into the quartz tube, a packet of pure yttrium was wrapped in Ta foils and was then placed inside each quartz tube. Thus, the diffusion multiples were protected from the interstitials (O, N, C, etc.) by the quartz tube, the pure yttrium absorber, the Ti HIP can, and the Ta diffusion barrier. The encapsulated samples were then annealed in argon at two different temperatures (1150°C for 2000 hrs and 1000 °C for 4000 hrs). Two identical diffusion multiples were made and each was annealed at one temperature. After the heat treatment, the diffusion multiples were taken from the furnace and cooled down to ambient temperature by breaking the quartz tube and quenching the diffusion multiples into water. The diffusion multiples were then cut into halves parallel to the ends using wire EDM, ground and polished.
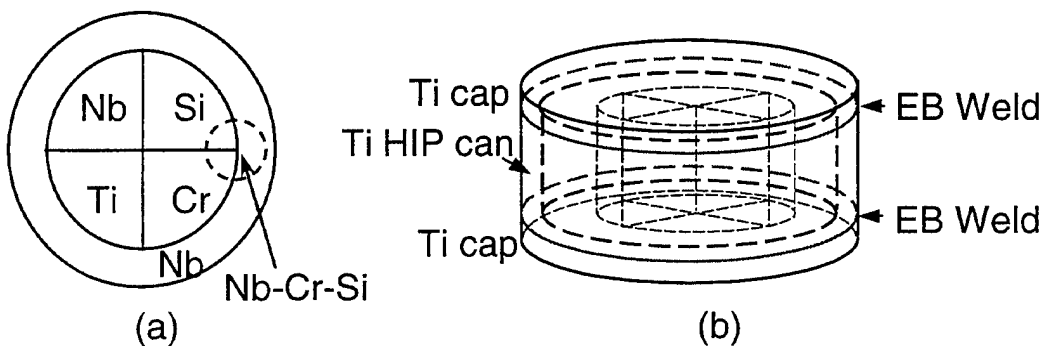

Figure 2. A diffusion multiple for efficient mapping of the Nb-Cr-Si ternary phase diagrams: (a) cross-sectional view; and (b) perspective view. See text for the size of the sample.

The samples were first examined using scanning electron microscopy (SEM), especially the backscatter electron (BSE) imaging. Most phases could be seen (although not identified explicitly) in the BSE images due to the differences in their average atomic weight. Quantitative EPMA analysis was performed on a CAMECA (Paris, France) microprobe using 15 kV voltage, 40 nA current and a 40° take-off angle. Electron backscatter diffraction (EBSD) analysis was performed to obtain crystal structure information of the phases formed in the diffusion multiple. Phase identification was accomplished by a direct match of the diffraction bands in the experimental backscatter pattern with simulated patterns generated using known structure types and lattice parameters. A detailed discussion on this powerful EBSD technique can be found in Schwartz *et al.* [25].

3. RESULTS AND DISCUSSION

A backscatter electron image taken from the Nb-Cr-Si tri-junction (schematically circled area in Fig. 2(a)) of the diffusion multiple annealed at 1000 °C for 4000 hours is shown in Fig. 3. During the long-term diffusion treatment, extensive interdiffusion among Nb, Cr and Si took place, and all the equilibrium phases, including the intermetallic phases, formed by interdiffusion reactions. By performing EPMA analysis in this tri-junction area, an extremely large amount of phase equilibrium information was obtained. Based on the compositional information from EPMA, EBSD analysis was performed to identify the crystal structure of the phases. Three ternary intermetallic compounds, $(Cr,Nb)_6Si_5$ ($oI44$), $(Cr,Nb)_{11}Si_8$ ($oP76$), and NbCrSi ($hP9$) as well as stabilization of the Laves phase $Nb(Cr,Si)_2$ in a C14 crystal structure were confirmed from both compositional data from EPMA and crystal structure identification from EBSD. EBSD is extremely useful for this system since several phases have compositions very close to one another and EPMA data alone would not be enough to differentiate them. For instance, the compositions of the phases $(Cr,Nb)_6Si_5$ and $(Cr,Nb)_{11}Si_8$ are very similar, without EBSD it would require time-consuming transmission electron microscopy (TEM) and electron diffraction analysis to tell them apart. Also, the ternary NbCrSi phase sits right on the same Nb concentration as the C14 Laves phase, it would have been very easy to mistakenly plot the C14 $Nb(Cr,Si)_2$ Laves phase region (line) all the way to the NbCrSi composition. The EBSD results helped us correctly interpret the data. The EBSD patterns of $(Cr,Nb)_6Si_5$ and $(Cr,Nb)_{11}Si_8$ are shown in Fig. 4.

The 1000°C isothermal section constructed, based on both EPMA and EBSD data, is shown in Fig. 5. We have defined eleven tie-triangles (three-phase equilibria) and four additional three-phase equilibria are estimated. We did not obtain these four tie-triangles due to cracking of brittle phases during sample cutting, grinding and polishing. The tie-lines are defined from the EPMA line profiles by taking advantage of the local equilibrium at interfaces formed among the phases.

The isothermal section obtained from the Nb-Cr-Si tri-junction region of the diffusion multiple heat treated at 1150 °C for 2000 hours is shown in Figure 6. It can be seen from Figs. 5 and 6 that the Cr solubility in the bcc(Nb) and Nb_5Si_3 is similar at 1000 and 1150 °C with 3 and 10 at.% Cr, respectively (the solubility of Cr in the bcc(Nb) phase varies slightly with temperature). The C14-Laves phase, which is only stable at temperatures > ~1585°C in the binary Cr-Nb system, was stabilized by Si to lower temperatures. Its stability range extends from ~6 to ~26 at.% Si and the Si solubility in C14-Laves phase does not change much with temperature varying from 1150 to 1000°C. The stable range for $(Cr,Nb)_6Si_5$ and $(Cr,Nb)_{11}Si_8$ increased significantly with temperature from 1000 to 1150 °C. These two ternary compounds are essentially line compounds with variable Cr/Nb ratio but stoichiometric concentration of Si. The CrNbSi ternary compound is a stoichiometric compound with very little variation of composition.

The C14 Laves phase also appears as a line compound with variable Cr/Si ratio and very little variation in Nb concentration.

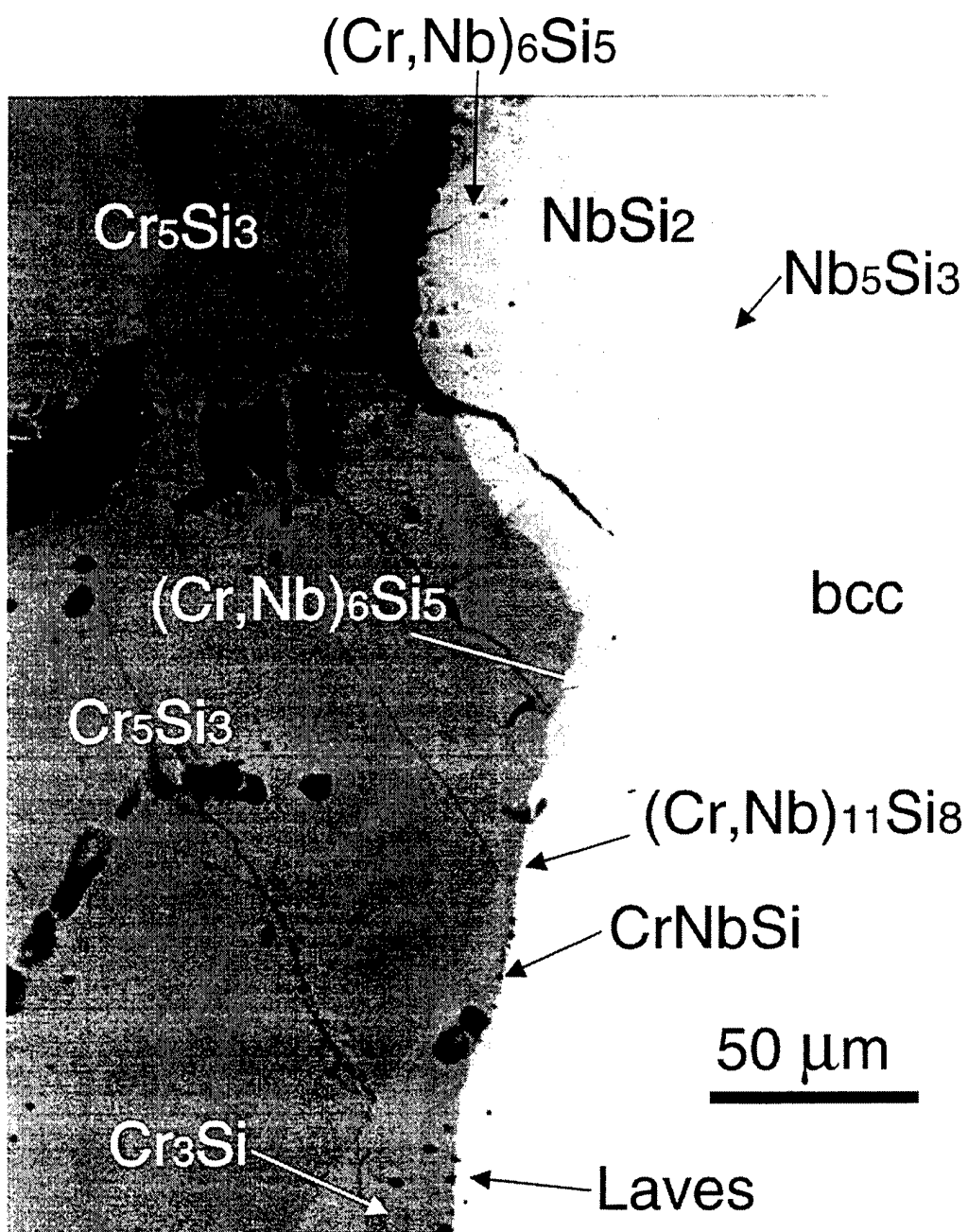Figure 3. Backscatter electron SEM image of the Nb-Cr-Si tri-junction area of the diffusion multiple annealed at 1000°C for 4000 hrs showing the formation of many different intermetallic compounds, including the three ternary compounds, $(Cr,Nb)_6Si_5$ ($oI44$), $(Cr,Nb)_{11}Si_8$ ($oP76$), and NbCrSi ($hP9$) as well as stabilization of the C14 Laves phase from the Cr-Nb binary system to the ternary system by Si.

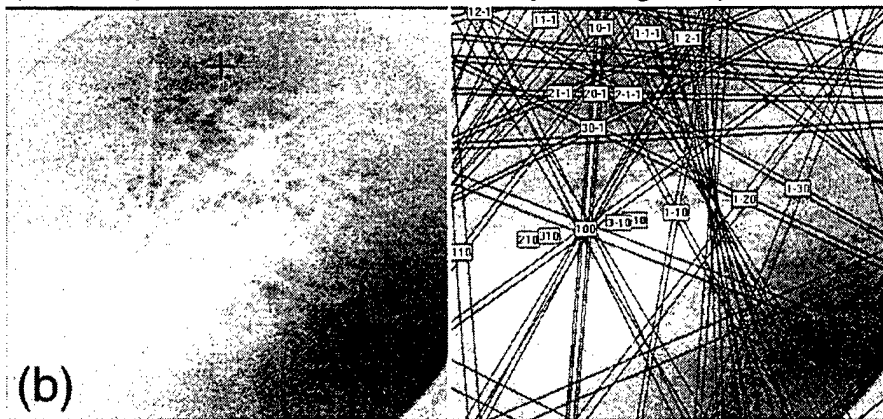# (Cr,Nb)₆Si₅: *ol*44, Ibam, space group # 72
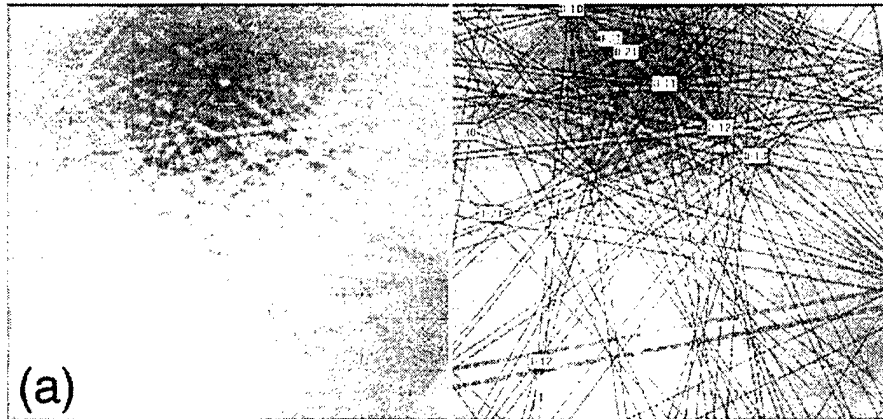
(Cr,Nb)₁₁Si₈: *oP*76, Pnma, space group # 62

Figure 4. EBSD patterns of the ternary compounds $(Cr,Nb)_6Si_5$ (a), $(Cr,Nb)_{11}Si_8$ (b) with the un-indexed pattern on the left and the indexed pattern on the right.

It is very likely that many of the alloys used by Goldschmidt and Brand had not reached equilibrium after only 336 hours (2 weeks) anneal at 1000°C. Many Nb-base alloys, such as Nb-Ti-Si alloys studied by Bewlay *et al.* [8, 26] and Nb-Hf-Si alloys studied by Zhao *et al.* [9] possess very slow kinetics, and they would not be at equilibrium after being annealed at 1000 °C for only 336 hours. For instance, even after annealing at 1500°C for 100 hours, several Nb-Hf-Si alloys still had not reached full equilibrium [9]. It is very likely that the Nb-Cr-Si alloys would possess similar slow kinetics as well, thus the data reported in the phase diagram of Goldschmidt and Brand may not represent equilibrium conditions. This argument is supported by the fact the Nb_5Si_3 and Cr_3Si phases have very narrow composition range in the equilibrium binary phase diagrams, whereas in the phase diagram presented by Goldschmidt and Brand, these phases show extensive composition ranges. This indicates that the decomposition process of the primary solidification phase (surface) was incomplete and equilibrium at 1000 °C might have not been reached for many of their alloys. Goldschmidt and Brand reported a very large single-phase field for the β phase which they claimed to be the βNb_5Si_3 (high temperature form). This must be the primary solidification βNb_5Si_3 that has not yet been decomposed to the equilibrium phases at

7

1000°C. They also reported a Nb$_4$Si phase which is certainly not an equilibrium phase, since this phase does not appear in the Nb-Si equilibrium binary phase diagram.
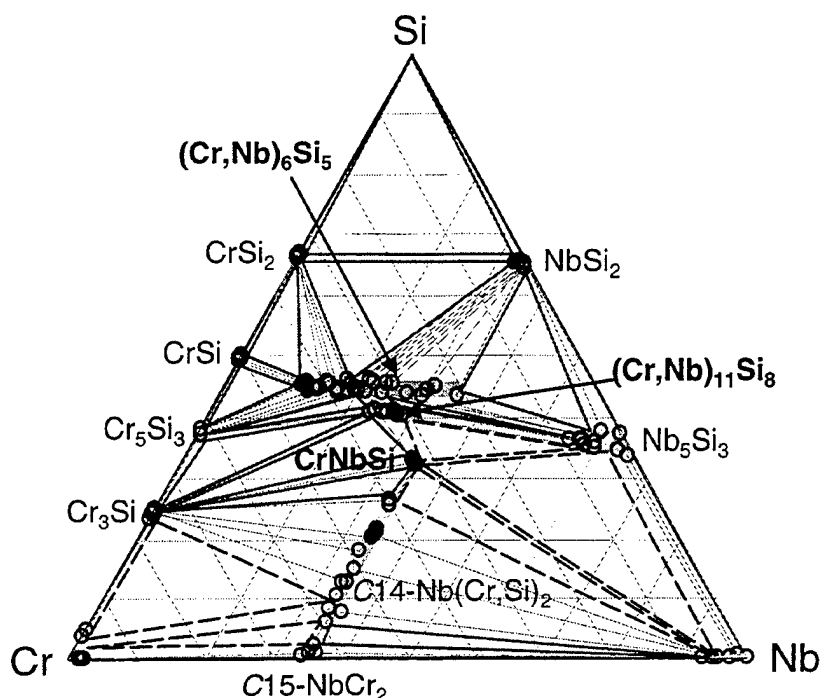

Figure 5. The 1000°C isothermal section of the Nb-Cr-Si system obtained from the tri-junction area of the diffusion multiple annealed at 1000°C for 4000 hrs. The phase diagram is plotted in atomic percent axes with the numbers removed for simplicity. The solid triangles indicate well-defined three-phase equilibria and the open circles show the tie-line compositions. The tie-lines are shown with dotted lines. The dashed triangles are hypothesized three-phase equilibria.

The crystal structure of the θ-phase (Fig. 1) reported by Goldschmidt and Brand is the same as that of (Cr,Nb)$_6$Si$_5$ and the θ-phase is in equilibrium with CrSi$_2$, NbSi$_2$, CrSi, and Cr$_5$Si$_3$ phases which was also observed in the present study for (Cr,Nb)$_6$Si$_5$ (Figs. 5 and 6). Thus it is safe to conclude that their θ-phase is (Cr,Nb)$_6$Si$_5$. The composition of the θ-phase is off the stoichiometric composition of (Cr,Nb)$_6$Si$_5$, which may be due to the primary solidification process. The ν-phase (Fig. 1) is very likely (Cr,Nb)$_{11}$Si$_8$. The crystal structure of the τ-phase is the same as CrNbSi, thus they are the same phase. Again the composition of the τ-phase is off the stoichiometry of CrNbSi probably due to the solidification process. The ρ-phase is certainly the C14 Nb(Cr,Si)$_2$ Laves which Goldschmidt and Brand already reported.

The existence of (Cr,Nb)$_6$Si$_5$ was reported by Steinmetz et al. [27]. Steinmetz et al. [28,29] also found the CrNbSi and (Cr,Nb)$_{11}$Si$_8$ ternary phases with hexagonal and orthorhombic structure, respectively. A "ternary" phase "Cr$_3$Nb$_2$Si$_3$" was reported by Vilasi et al. [30] at 1250°C. Since its crystal structure and lattice parameters are essentially the same as the C14 Laves and its composition is also very close to the C14 Laves, it should be the same phase.

Our equilibrium phase diagrams (Figs. 5 and 6) greatly help to clarify the confusion in the phases of this ternary system and put the phases at the right stoichiometric positions in the phase diagram. Without the present study it would have been much harder to correlate the θ, ν and τ

8

phases since their reported compositions did not correspond to the crystal structure stoichiometries. Our work from diffusion multiples provides, for the first time, a much clearer picture of the phase equilibria in this very complex Nb-Cr-Si ternary system.
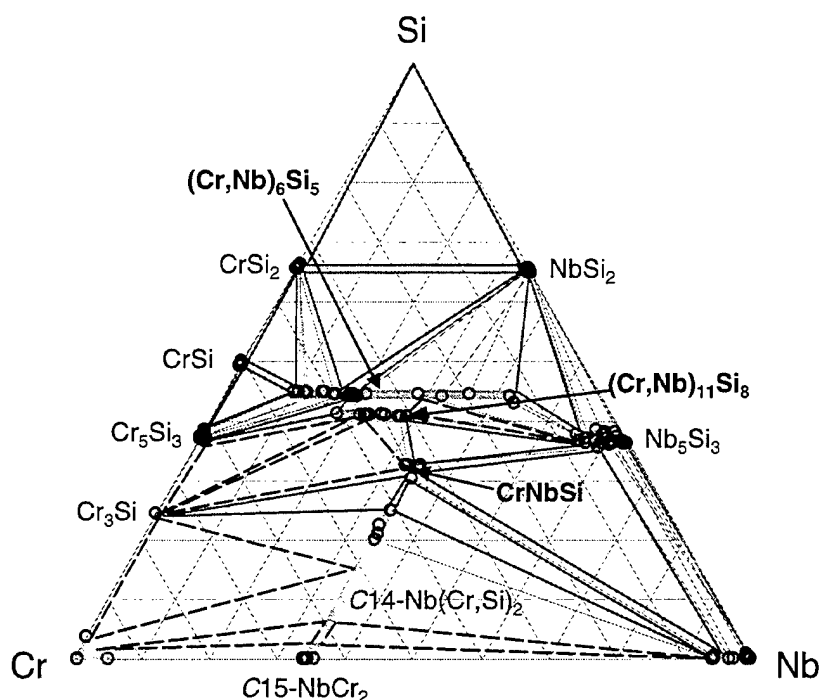

Figure 6. The 1150°C isothermal section of the Nb-Cr-Si system obtained from the tri-junction area of the diffusion multiple annealed at 1150°C for 2000 hrs. The phase diagram is plotted in atomic percent axes with the numbers removed for simplicity. The solid triangles indicate well-defined three-phase equilibria and the open circles show the tie-line compositions. The tie-lines are shown with dotted lines. The dashed triangles are hypothesized three-phase equilibria.

The diffusion multiples make it easier to form equilibrium phases especially for alloys with very sluggish decomposition kinetics. This is somewhat counter-intuitive: one would think that the equilibrated alloy method (melting, casting and heat treatment of individual alloys) is the ultimate "gold-standard" for equilibrium. However, since it involves the process of solidification and heat treatment, true equilibrium can be difficult to reach if the solid-state decomposition process is sluggish for some of the phases (as in the case of several Nb-base systems). For instance, the βNb_5Si_3 which was formed directly from solidification (from its primary liquidus surface) and which is not an equilibrium phase for the Nb-Cr-Si ternary system at 1000°C, did not decompose to the equilibrium phases after annealing at 1000°C for 336 hours, Fig. 1. Alternatively, to avoid the solidification phase formation / segregation, to shorten diffusion distances, and to equilibrate more quickly, a powder metallurgy (solid state reaction of elemental powders) approach would be preferred. We found an excellent example to illustrate this case during our study of the Nb-Cr-Al system [31]. Hunt and Raman [32] used the melting and annealing method whereas Mahdouk and Gachon [33] employed solid-state reaction of fine powders (without melting) to determine the same ternary phase diagram. Both groups annealed the samples at 1000°C for 168 hours (1 week). The alloys of Mahdouk and Gachon reached equilibrium near the C14 Laves phase, whereas the off-stoichiometric alloys near the C14 Laves phase melted by Hunt and Raman did not decompose into the equilibrium phases. This clearly

shows the advantage of the power metallurgy route in reaching equilibrium for very high temperature alloys. The powder metallurgy route also has its drawbacks. It is very easy to introduce oxides or nitrides or moisture at fine particle surfaces, thus contaminating the samples and potentially causing interstitial stabilization of non-equilibrium phases. Here again the diffusion-multiple method can be superior.

In the diffusion multiples, there are no problems associated with melting or powder contamination since all the phases form by diffusion reactions of bulk constituents at the temperature of interest (heat treatment). The phases formed should all be equilibrium phases and local equilibrium at the phase interface would give the equilibrium phase diagram. However, the diffusion-multiple approach is not fool-proof either: in rare occasions one of the phases does not form by interdiffusion reactions. The exact reason for this is still not well understood. However, for phases with narrow stoichiometry surrounded by phases with broad stoichiometry and higher diffusivity, the phases with narrow stoichiometry may be reduced to interfacial phases (near zero thickness) for lower temperatures. Fortunately, all these instances occurred at temperatures below half of the homologous melting points. Even though the occurrence was very rare, when using diffusion couples and diffusion multiples in mapping phase diagrams one should always be watchful for the possibility of missing phases (especially at low temperatures). In the case of Nb-Cr-Si, we are very confident that the phase diagrams (Figs. 5 and 6) we obtained are equilibrium ones since all the binary phases appeared and all the confirmed ternary compounds were observed. It is always a good check to see whether all the binary phases and reported ternary phases appear.

The bcc(Nb)–Nb_5Si_3–CrNbSi three-phase equilibrium indicates that the Laves phases are not in equilibrium with bcc(Nb) and Nb_5Si_3 in the ternary system at 1000 to 1150°C. In composites processed (cast or DS) at high temperatures, the $C14$ $Nb(Cr,Si)_2$ Laves phase was observed to co-exist with bcc(Nb) and Nb_5Si_3. It is likely that there is a four phase equilibrium reaction bcc(Nb)–Nb_5Si_3–$C14$ + $C14$–Nb_5Si_3–CrNbSi → bcc(Nb)–Nb_5Si_3–CrNbSi + bcc(Nb)–$C14$–CrNbSi at a temperature > 1150°C.

Cr additions to the composites improve the oxidation resistance, but probably degrade both fracture toughness and creep strength as well as the melting temperature. Although the liquidus surface for the Nb-Cr-Si system is not available, the melting temperatures of 74 alloys (out of 220 alloys) were reported by Goldschmidt and Brand [15]. The data show that Cr depresses the melting temperature of the composites, probably even more strongly than Ti. Thus Cr additions have to be tailored in order to balance the oxidation resistance, creep resistance and fracture toughness. It is currently unknown whether the CrNbSi phase is better for creep strength and whether it is possible to promote the CrNbSi phase formation during reasonable heat treatment time. If the transformation from the in-situ formed $C14$ Laves phase to the CrNbSi phase is very sluggish, it may not be economically feasible for real materials production.

The phase equilibrium information of the Nb-Cr-Si system is very useful for the design of both Nb silicide composites and coatings for these composites. This is one of the key systems for which we would like to perform CALPHAD modeling and add the data into the developing thermodynamic database for Nb silicide based systems [10,34-35].

4. CONCLUSIONS

The results of this work clearly demonstrate the power and the high-efficiency of the diffusion-multiple approach to map phase diagrams of systems as complex as the Nb-Cr-Si ternary which contains 14 phases, including three ternary compounds. Two isothermal sections at 1000 and 1150 °C were constructed from the results obtained from two diffusion multiples using scanning electron microscopy (SEM), electron probe microanalysis (EPMA), and electron backscatter diffraction (EBSD). Three ternary compounds, CrNbSi, $(Cr,Nb)_6Si_5$ and $(Cr,Nb)_{11}Si_8$, as well as stabilization of the C14 Laves phase were observed at both temperatures. Our equilibrium phase diagrams (Figs. 5 and 6) greatly help to clarify the confusion of the phases in this ternary system and provides, for the first time, a much clearer picture of the phase equilibria in this very complex ternary system.

REFERENCES

1. M.G. Mendiratta and D.M. Dimiduk, *Mat. Res. Soc. Symp. Proc.*, 133 (1989), 441-446.
2. M.R. Jackson, B.P. Bewlay, R.G. Rowe, D.W. Skelly, and H.A. Lipsitt, *JOM*, 48 (1996), 39-44.
3. P.R. Subramanian, M.G. Mendiratta, and D.M. Dimiduk, *JOM*, 48 (1996), 33-38.
4. B.P. Bewlay, J.J. Lewandowski, and M.R. Jackson, *JOM*, 49 (1997), 44-45.
5. S.J. Balsone, B.P. Bewlay, M.R. Jackson, P.R. Subramanian, J.-C. Zhao, A. Chatterjee, and T. Heffernan, in *Structural Intermetallics 2001* (K. Hemker, D.M. Dimiduk, H. Clemens, R. Darolia, H. Inui, J.M. Larsen, V.K. Sikka, M. Thomas, and J.D. Whittenberger, eds.), TMS, Warrendale, PA, 2001, 99-108
6. B.P. Bewlay, M.R. Jackson, J.-C. Zhao, and P.R. Subramanian, *Metallurgical and Materials Transactions,* Accepted November 2002.
7. J.-C. Zhao, B.P. Bewlay, M.R. Jackson, and L.A. Peluso, in *Structural Intermetallics 2001* (K. Hemker, D.M. Dimiduk, H. Clemens, R. Darolia, H. Inui, J.M. Larsen, V.K. Sikka, M. Thomas, and J.D. Whittenberger, eds.), TMS, Warrendale, PA, 2001, 483-491.
8. B.P. Bewlay, R.R. Bishop, and M.R. Jackson, *Z. Metallkde.*, 90 (1999), 413-422.
9. J.-C. Zhao, B.P. Bewlay, and M.R. Jackson, *Intermetallics,* 9 (2001) 681-689.
10. Y. Yang, Y.A. Chang, J.-C. Zhao, and B.P. Bewlay, *Intermetallics,* Accepted November 2002.
11. J.-C. Zhao, *Adv. Eng. Mater.*, 3 (2001), 143-147.
12. J.-C. Zhao, *J. Mater. Res.*, 16 (2001), 1565-1578.
13. J.-C. Zhao, M.R. Jackson, L.A. Peluso, and L. Brewer, *MRS Bulletin*, 27 (2002) 324-329.
14. J.-C. Zhao, M.R. Jackson, L.A. Peluso, and L. Brewer, *JOM*, 54 (7) (2002) 42-45.
15. H.J. Goldschmidt and J.A. Brand, *J. Less-Common Met.*, 3 (1961), 34-43.
16. L.A. Lysenko, V.Ya. Markiv, O.V. Tsybukh, and E.I. Gladyshevskii, *Inorganic Mater.*, 7(1) (1971), 157-159.

17. M. Venkatraman and J.P. Neumann: in *Binary Alloy Phase Diagrams*, 2nd ed., T.B. Massalski, ed., ASM International, Materials Park, OH, 1990.

18. A.B. Gokhale and G.J. Abbaschian: in *Binary Alloy Phase Diagrams*, 2nd ed., T.B. Massalski, ed., ASM International, Materials Park, OH, 1990.

19. M.E. Schlesinger, H. Okamoto, A.B. Gokhale, and R. Abbaschian, *J. Phase Equilibria*, 14 (1993), 502.

20. P. Villars, L.D. Calvert, *Pearson's Handbook of Crystallographic Data for Intermetallic Phases*, 2nd ed., ASM International, Materials Park, OH, 1991.

21. J.G.C. Neto, S.G. Fries, and H.L. Lukas, *CALPHAD*, 17 (1993), 219-228.

22. Y. Du, J.C. Schuster, L. Perring, *J. Am. Ceram. Soc.*, 83(8) (2000) 2067-2073.

23. M.G. Mendiratta and D.M. Dimiduk, *Scripta Metall. Mater.*, 25 (1991), 237-242.

24. B.P. Bewlay, H.A. Lipsitt, M.R. Jackson, W.J. Reeder, and J.A. Sutliff, *Mater. Sci. Eng.*, A192/193 (1995), 534-543.

25. *Electron Backscatter Diffraction in Materials Science*, edited by A.J. Schwartz, M. Kumar, and B.L. Adams (Kluwer Academic / Plenum Publishers, New York, 2000).

26. B.P. Bewlay, M.R. Jackson, and R.R. Bishop, *J. Phase Equilibria*, 19 (1998), 577-586.

27. J. Steinmetz and B. Roques, *J. Less-Common Metals*, 52 (1977) 247-258.

28. J. Steinmetz, B. Malaman, J.M. Albrecht, and B. Roques, *Mater. Res. Bull.*, 10 (1975) 571-576.

29. J. Steinmetz, B. Malaman, and B. Roques, *J. Less-Common Metals*, 57 (1978) 133-146.

30. M. Vilasi, M. Francois, H. Brequel, R. Podor, G. Venturini, and J. Steinmetz, *J. Alloys Compounds*, 269 (1998) 187-192.

31. J.-C. Zhao, M.R. Jackson, and L.A. Peluso, to be published.

32. C.R. Hunt and A. Raman, *Z. Metallkd.*, 59 (1968), 701-707.

33. K. Mahdouk and J.C. Gachon, *J. Alloys Compounds*, 321 (2001), 232-236.

34. H. Liang and Y.A.Chang, *Intermetallics*, 7 (1999) 561.

35. Y. Yang and Y.A. Chang (University of Wisconsin – Madison), private communication, 2002.

Phase Diagram of the Nb-Cr-Al Ternary System

J.-C. Zhao, M.R. Jackson, and L.A. Peluso

Phase Diagram of the Nb-Cr-Al Ternary System

J.-C. Zhao, M.R. Jackson, and L.A. Peluso
General Electric Company
GE Global Research Center, P.O. Box 8, Schenectady, NY 12301, USA

ABSTRACT

A high-efficiency diffusion-multiple approach was employed to map the phase diagram of the Nb-Cr-Al ternary system which is very valuable for the design of niobium silicide-based composites. These composites have high potential as a replacement for Ni-base superalloys for jet engine applications. Both Cr and Al are alloying elements for these composites, thus the Nb-Cr-Al phase diagram, especially the stability of the oxidation-resistant Laves phase, is important information for the composite design. A 1000°C isothermal section was constructed from the results obtained using electron probe microanalysis (EPMA) from a diffusion multiple made up of Nb, Cr, NbAl$_3$ and NbSi$_2$. The stabilization of the C14 Laves phase by Al dominates the 1000°C isothermal section, and the solubility of Al in the C14 Laves phase is as high as ~45 at.%.

Keywords: Nb-Cr-Al, diffusion multiple, silicide, phase diagram.

1. INTRODUCTION

Niobium silicide-based composites show great promise for applications as the next generation turbine airfoil materials with significantly higher operating temperatures than current generation advanced Ni-base superalloys [1-6]. The Nb-Si binary composites have excellent creep strength, but poor oxidation resistance and poor room temperature fracture toughness [1-2]. Alloying with Al can improve the oxidation resistance. The potential application of these composites at very high temperatures requires a balance of high creep resistance, high oxidation resistance, and good low-temperature damage tolerance (fracture toughness). To achieve such a property balance, elements such as Cr, Ti, Hf and Al are added to the composites and significant progress has been made in improving the properties of the composites. Some of the alloying concepts were discussed by Zhao *et al.* [7]. The advanced design of the composites requires a fair understanding of the phase equilibria in the Nb-Si-Ti-Cr-Hf-Al system. Since a reasonable definition of the Nb-Hf-Si system has been achieved [8-10], our effort has been focused on the ternary systems Nb-Cr-Si, Nb-Si-Al, Nb-Cr-Al, Ti-Si-Cr, Ti-Si-Al, Ti-Cr-Al, Nb-Ti-Si, Nb-Ti-Cr, and Nb-Ti-Al. Other ternary systems related to the six-element system such as Nb-Ti-Hf, Nb-Cr-Hf, Nb-Hf-Al, Ti-Si-Hf, Ti-Cr-Hf, and Cr-Hf-Al have either good data or are less critical for the design of the Nb silicide composites. We will report the results of the Nb-Cr-Al system in the present paper and the results of other systems will be communicated separately.

In addition to being valuable for the design of the Nb silicide composites, the Nb-Cr-Al ternary phase diagram is also very useful for the design of other high temperature alloys and coatings [11-14]. For instance, the Nb-rich aluminides, Nb$_3$Al and Nb$_2$Al, have demonstrated good strength and creep resistance at high temperatures [11,12]. The Al-rich intermetallic phase,

$NbAl_3$, is also a candidate material for advanced aeropropulsion systems because of its high melting point and low density. Cr addition is very important for the oxidation resistance of these aluminides and coatings.

The high-efficiency "diffusion multiple" approach [15-18] is ideally suited for mapping phase diagrams of the six-element related systems mentioned earlier. It would take thousands of alloys to determine the nine ternary systems using the traditional one-alloy-at-a-time (equilibrated alloy) approach. For instance, it took Goldschmidt and Brand [19] about 220 alloys to map just the Nb-Cr-Si ternary system and similarly about 135 alloys were employed by Lysenko et al. [20] to determine the Ti-Cr-Si system. These alloys have very high melting temperatures and are difficult to make and to homogenize. Extra effort also needs to be taken to avoid interstitial (oxygen, nitrogen, carbon, etc.) contamination during alloy casting and heat treatment. In contrast, the diffusion multiple approach needs only a few cast alloys and the samples were easy to make, and safe-guarding against the interstitial contamination can be very easily implemented as will be discussed later. The general diffusion multiple approach was discussed in detail previously [15-18] and has been successfully applied to many alloy systems.

The constitutive binary phase diagrams of the Nb-Cr-Al system, i.e., Nb-Al [21], Nb-Cr [22,23] and Al-Cr [24-29] are already available in the literature. There is still active research on the phase diagram of the Al-Cr binary system [26,27]. The crystal structures of the phases in the binary and the ternary system are listed in Table 1 [30].

Table 1. Crystal structure of phases in the Nb-Cr-Al ternary system. The data were taken from Villars and Calvert [30] for most phases, from Knapp [31] for Al_9Cr_4, and from Audier, et al. [27] for Al_4Cr and $Al_{11}Cr_2$.

System	Conditions	Pearson Symbol	Space Group	Lattice Parameters					Comments
				a	b	c	β	γ	
Al		$cF4$	Fm$\bar{3}$m	0.40497					
Cr		$cI2$	Im$\bar{3}$m	0.28847					
Nb		$cI2$	Im$\bar{3}$m	0.33067					
$AlCr_2$	≤ 910°C	$tI6$	I4/mmm	0.3005		0.8649			
Al_8Cr_5	≤ ~1130°C		R3m	1.2813		0.7951		120°	
Al_9Cr_4			Cubic	0.9123					
Al_4Cr	≤ 1030°C	$hP574$	P6$_3$/mmc	1.998		2.467	119.33°		
$Al_{11}Cr_2$	≤ 940°C		Cmcm	1.24	3.46	2.02	122.20°		
Al_7Cr	≤ 790°C		C2/m	2.5256	0.7582	1.0955	128.68°		
Nb_2Al	≤ 1940°C	$tP30$	P4$_2$/mnm	0.9945		0.5171			
Nb_3Al	≤ 2060°C	$cP8$	Pm$\bar{3}$n	0.5186					
$NbAl_3$	≤ 1680°C	$tI8$	I4/mmm	0.3844		0.8605			
Cr_2Nb	≥ ~1600°C	$hP12$	P6$_3$/mmc	0.4931		0.8123		120°	C14 Laves
Cr_2Nb	≤ ~1600°C	$cF24$	Fd$\bar{3}$m	0.695					C15 Laves

The first isothermal section of the Nb-Cr-Al systems was reported by Hunt and Raman [32] for 1000°C, as shown in Fig. 1(a) [20]. It provided a rough overview of this system, but most of the phase boundaries and the tie-triangles were un-defined. Mahdouk and Gachon [33] recently reported an isothermal section at 1000°C (Fig. 1(b)) based on EPMA analysis of small-charge samples produced in a direct reaction calorimeter and then annealed at 1000°C for 168 hours (1 week). There are large discrepancies of Cr solubility in Nb aluminides ($NbAl_3$, Nb_2Al, and

Nb₃Al) and bcc (Nb) between the results of Mahdouk and Gachon [33] and Hunt and Raman [32]. In addition, the phase equilibria between the two $(Cr,Al)_2Nb$ Laves phases, $C15$ and $C14$, are not determined. Our work will help comparing and judging the reliability of the literature data and generating new data for the phase equilibria of the Nb-Cr-Al ternary system.

2. EXPERIMENTAL METHOD

A diffusion multiple with the cross-section view shown schematically in Fig. 2(a) was made. The dimensions were designed so that the pieces of pure elements and compounds are much larger than the diffusion distance, thus there will be pure elements and compounds left after the long-term diffusion annealing. To avoid the low melting point of Al, we used both $NbAl_3$ and $NbSi_2$ compounds as members of the diffusion multiple. Both these compounds were made using arc-melting. They were then cut into square bars of 7 x 7 x 25 mm using electro-discharge machining (EDM). A 14 x 14 mm square opening was cut from a 25.4 mm diameter by 25.4 mm height cylindrical piece of pure Nb. The square open was cut across the whole height of the Nb piece. Pieces of high purity Nb and Cr in the dimension of 7 x 7 x 25 mm were also machined using EDM. The re-cast layer on the EDM'ed surfaces was removed by mechanical grinding to make clean surfaces. The pieces were ultrasonically cleaned in methanol and then assembled into the geometry shown in Fig. 2(a). The height of all pieces was 25.4 mm. The assembled diffusion multiple was then loaded into hot isostatic press (HIP) cans made of commercial purity Ti, which is schematically shown in Fig. 2(b). A 25 µm layer of Ta was placed between the diffusion multiple and the HIP cans to isolate any interstitial contaminants that may diffuse into the HIP can from the quartz capsule during long-term annealing. The top and bottom caps of the HIP can were electron beam welded. HIPing was performed at 1204 °C, 200MPa for 4 hrs. The HIP can containing the diffusion multiple was then encapsulated in an evacuated quartz tube backfilled with pure argon. Since Nb is susceptible to oxygen and nitrogen contamination, it is critical to keep the diffusion multiple from interstitial elements. To further absorb any oxygen that may diffuse into the quartz tube, a packet of pure yttrium was wrapped in Ta foils and was then placed inside the quartz tube. Thus, the diffusion multiple was protected from the intersitials (O, N, C, etc.) by the quartz tube, the pure yttrium absorber, the Ti HIP can, and the Ta diffusion barrier. The encapsulated sample was then annealed at 1000°C for 2000 hours. After the heat treatment, the diffusion multiple was taken from the argon furnace and cooled down to ambient temperature by breaking the quartz tube and quenching the diffusion multiple into water. The diffusion multiple was then cut into halves parallel to the ends using wire EDM, ground and polished.

The samples were first examined using scanning electron microscopy (SEM), especially the backscatter electron (BSE) imaging. Most phases could be seen (although not identified explicitly) in the BSE images due to the differences in their average atomic weight. Quantitative EPMA analysis was performed on a CAMECA (Paris, France) microprobe using 15 kV voltage, 40 nA current and a 40° take-off angle.

3. RESULTS AND DISCUSSION

Backscatter electron images taken from the Nb-Cr-NbAl₃ tri-junction (schematically circled area in Fig. 2(a)) of the diffusion multiple annealed at 1000 °C for 2000 hrs are shown in Fig. 3. During the long-term diffusion treatment, extensive interdiffusion among Nb, Cr and Al took place, and all the equilibrium phases, including the intermetallic phases, formed by interdiffusion reactions. The black area on top of Fig. 3(a) was a crack probably formed during specimen

3

preparation (EDM cutting, grinding and polishing). The Nb_2Al and Nb_3Al phases which are difficult to see in Fig. 3(a) can be seen in Fig. 3(b) and (c). Even in Fig. 3(b), the Nb_3Al is still difficult to see since the atomic number contrast among Nb_2Al, Nb_3Al and bcc(Nb) is very low. At the location of Fig. 3(b), Nb_2Al started to disappear (thus it is very thin in this area), i.e., it was de-stabilized by Cr on the right-hand side of the image where higher Cr concentration was present Figure 3(c) is at the location where Nb_2Al started to disappear, i.e., this phase was also de-stabilized by Cr on the right-hand side of the image where higher Cr concentration was present. Note that at the locations of Fig. 3 (b) and (c), as the Nb_3Al and Nb_2Al phases were extremely thin, we took account of overlapping and over-sampling effects when analyzing the EPMA data.

By performing EPMA analysis in this tri-junction area, a large amount of phase equilibrium information was obtained. Based on the compositional information from EPMA and by taking advantage of the local equilibrium at phase interfaces, an isothermal section of the Nb-Cr-Al system for 1000 °C was constructed as shown in Fig. 4. Detailed procedures of phase diagram mapping using diffusion multiples can be found elsewhere [15-18].

The new 1000°C isothermal section of the Nb-Al-Cr ternary system shows the same phase relationships as those reported by Hunt and Raman [32] as well as Mahdouk and Gachon [33]. Due to the fact that we used $NbAl_3$ instead of pure Al as a member of the diffusion multiple, we did not obtain any phase equilibrium information at the Al-rich end of the phase diagram. This is also partly due to the very stable nature of the C14 Laves phase which dominates the center of the phase diagram. Nevertheless, we still obtained a large amount of information for seven single-phase regions and five three-phase regions. Identical to the observations of Hunt and Raman [32] as well as Mahdouk and Gachon [33], we observed the stabilization of the high-temperature hexagonal C14-Laves phase of the binary Cr-Nb system (Cr_2Nb) by Al addition, and the solubility of Al in C14 was as high as ~45. at.%, which is consistent with previous observations [32,33]. The composition of the C14 Laves phase was almost a line-compound in the form of $(Cr,Al)_2Nb$. Our result is consistent that of Mahdouk and Gachon [33], and the results together suggest that the very wide (Nb variation) phase region of the C14 Laves reported by Hunt and Raman [32] is un-reliable. The widening of the C14 Laves phase region in the case of Hunt and Raman [32] was probably due to the primary solidification process (primary liquidus surface of C14-Laves). The C14 Laves with composition away from $(Cr,Al)_2Nb$ formed during solidification did not have sufficient time to decompose due to its sluggish kinetics. In our diffusion multiple, the C14 Laves formed at 1000°C by diffusion reactions and it did not go through the solidification process, thus it is much easier to reach local equilibrium at the phase interfaces. In the case of Mahdouk and Gachon [33], the direct reaction calorimetry process involves fine powders that react together in the solid state, thus it also avoids the problem associated with melting and solidification. The work of both Hunt and Raman [32] and Mahdouk and Gachon [33] is a great example to show that it is much easier to reach equilibrium by solid-state reactions than to go through a solidification and decomposition process when involving high-melting compounds and when the decomposition kinetics is sluggish. Both Hunt and Raman [32] and Mahdouk and Gachon [33] annealed their samples at 1000°C for 168 hours (1 week); Mahdouk and Gachon [33] reached equilibrium through solid-state reaction, whereas Hunt and Raman [32] did not reach equilibrium for the C14 Laves using melting/solidification and decomposition annealing.

Most of the results obtained from the diffusion multiples agreed well with those reported by Mahdouk and Gachon [33] except the bcc(Nb) + C14 Laves + $Nb_2(Al,Cr)$ three-phase equilibrium. Our result showed much higher Al concentration in the C14 Laves phase in equilibrium with both bcc(Nb) and $Nb_2(Al,Cr)$. In addition, we observed very low solubility of

4

Cr in the Nb$_3$Al, which is slightly different from the result of Mahdouk and Gachon [33], Fig. 1(b). We clearly defined, for the first time, the $C14 + C15 + bcc(Nb)$ and $C14 + C15 + bcc(Cr)$ three-phase regions.

In Nb silicide composites with both Cr and Al additions, both elements help promote the $C14$-Laves phase (instead of the $A15$ Nb$_3$Al phase for the Al case). The alloying effect of Cr and Al in Nb silicide-based composites can be appreciated by examining the Nb-Cr-Si, Nb-Al-Si and Nb-Cr-Al phase diagrams. Our work on the Nb-Cr-Si and Nb-Al-Si ternary systems will be reported separately [34].

The phase equilibrium information of the Nb-Cr-Al system is very useful for the design of both Nb silicide composites and coatings for these composites. This is one of the key systems we would like to perform CALPHAD modeling and add the data into the developing thermodynamic database for Nb silicide based systems [10, 35-36].

4. CONCLUSIONS

Using the high-efficiency diffusion-multiple approach, we mapped the 1000°C isothermal section of the Nb-Cr-Al ternary system. There was no ternary compound for this ternary system. The high-temperature C14 Laves of the Cr-Nb binary system was stabilized to 1000°C by Al addition and the Al solubility in the C14 Laves is as high as ~45 at.%. We reported results on seven single-phase regions and five three-phase regions. We results are in good agreement with the data reported by Mahdouk and Gachon [33].

ACKNOWLEDGMENTS

REFERENCES

1. M.G. Mendiratta and D.M. Dimiduk, *Mat. Res. Soc. Symp. Proc.*, 133 (1989), 441- 446.
2. M.R. Jackson, B.P. Bewlay, R.G. Rowe, D.W. Skelly, and H.A. Lipsitt, *JOM*, 48 (1996), 39-44.
3. P.R. Subramanian, M.G. Mendiratta, and D.M. Dimiduk, *JOM*, 48 (1996), 33-38.
4. B.P. Bewlay, J.J. Lewandowski, and M.R. Jackson, *JOM*, 49 (1997), 44-45.
5. S.J. Balsone, B.P. Bewlay, M.R. Jackson, P.R. Subramanian, J.-C. Zhao, A. Chatterjee, and T. Heffernan, in *Structural Intermetallics 2001* (K. Hemker, D.M. Dimiduk, H. Clemens, R. Darolia, H. Inui, J.M. Larsen, V.K. Sikka, M. Thomas, and J.D. Whittenberger, eds.), TMS, Warrendale, PA, 2001, 99-108

6. B.P. Bewlay, M.R. Jackson, J.-C. Zhao, and P.R. Subramanian, *Metall. Mater. Trans.,* Accepted November 2002.
7. J.-C. Zhao, B.P. Bewlay, M.R. Jackson, and L.A. Peluso, in *Structural Intermetallics 2001* (K. Hemker, D.M. Dimiduk, H. Clemens, R. Darolia, H. Inui, J.M. Larsen, V.K. Sikka, M. Thomas, and J.D. Whittenberger, eds.), TMS, Warrendale, PA, 2001, 483-491.
8. B.P. Bewlay, R.R. Bishop, and M.R. Jackson, *Z. Metallkde.,* 90 (1999), 413-422.
9. J.-C. Zhao, B.P. Bewlay, and M.R. Jackson, *Intermetallics,* 9 (2001), 681-689.
10. Y. Yang, Y.A. Chang, J.-C. Zhao, and B.P. Bewlay, *Intermetallics,* Accepted November 2002.
11. D.L. Anton and D.M. Shah, *Mater. Res. Soc. Symp. Proc.,* 288 (1993), 141-150.
12. D.M. Dimiduk, P.R. Subramanian, and M.G. Mendiratta, *Acta Metall. Mater.,* 8 (1995), 519-530.
13. M.G. Hebsur, J.R. Stephens, J.L. Smialek, C.A. Barrett, and D.S. Fox, Influence of Alloying Elements on the Oxidation Behavior of NbAl₃, *Sci. Tech. Aerosp. Rep.,* 27(4) (1989) Abstr. No. N89-12717.
14. J. Doychak and M.G. Hebsur, *Oxid. Met.,* 36 (1991), 113.
15. J.-C. Zhao, *Adv. Eng. Mater.,* 3 (2001), 143-147.
16. J.-C. Zhao, *J. Mater. Res.,* 16 (2001), 1565-1578.
17. J.-C. Zhao, M.R. Jackson, L.A. Peluso, and L. Brewer, *MRS Bulletin,* 27 (2002) 324-329.
18. J.-C. Zhao, M.R. Jackson, L.A. Peluso, and L. Brewer, *JOM,* 54 (7) (2002) 42-45.
19. H.J. Goldschmidt and J.A. Brand, *J. Less-Common Met.,* 3 (1961), 34-43.
20. L.A. Lysenko, V.Ya. Markiv, O.V. Tsybukh, and E.I. Gladyshevskii, *Inorganic Mater.,* 7(1) (1971), 157-159.
21. U.R. Kattner: in *Binary Alloy Phase Diagrams,* 2nd ed., T.B. Massalski, ed., ASM International, Materials Park, OH, 1990.
22. M. Venkatraman and J.P. Neumann: in *Binary Alloy Phase Diagrams,* 2nd ed., T.B. Massalski, ed., ASM International, Materials Park, OH, 1990.
23. J.G.C. Neto, S.G. Fries, and H.L. Lukas, *CALPHAD,* 17 (1993), 219-228.
24. J.L. Murray, in *Binary Alloy Phase Diagrams,* 2nd ed., T.B. Massalski, ed., ASM International, Materials Park, OH, 1990.
25. J.G.C. Neto, S. Gama, and C.A. Ribeiro, *J. Alloys Compounds,* 182 (1992), 271-280.
26. K. Mahdouk and J.C. Gachon, *J. Phase Equili.,* 21(2000), 157-166.
27. K. Mahdouk, J.C. Gachon, *Arch. Metal.,* 46 (2001), 233-238.
28. M. Audier, M. Durandcharre, E. Laclau, H. Klein, Phase-Equilibria in the Al-Cr System, *J. Alloys Compound,* 220 (1995) 225-230.
29. X.Z. Li, K. Sugiyama, K. Hiraga, A. Sato, A. Yamamoto, H.X. Sui, K.H. Kuo, *Z. Kristallographie,* 212 (1997), 628-633.
30. P. Villars and L.D. Calvert, *Pearson's Handbook of Crystallographic Data for Intermetallic Phases,* 2nd ed., ASM International, Materials Park, OH, 1991.
31. A. Knapp, *Z. Metallkde.,* 33 (1941) 153.
32. C.R. Hunt and A. Raman, *Z. Metallkd.,* 59 (1968), 701-707.
33. K. Mahdouk and J.C. Gachon, *J. Alloys Compounds,* 321 (2001), 232-236.
34. J.-C. Zhao, M.R. Jackson, and L.A. Peluso, to be published.
35. H. Liang and Y.A.Chang, *Intermetallics,* 7 (1999) 561.
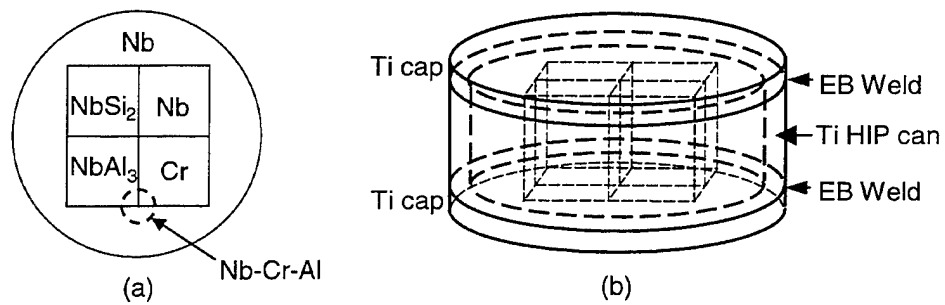36. Y. Yang and Y.A. Chang (University of Wisconsin – Madison), private communication, 2002.

Figure 1. The 1000°C isothermal sections of the Nb-Cr-Al ternary system from the literature: (a) an approximate phase diagram reported by Hunt and Raman [32] showing that phase boundaries and tie-triangles were not well defined; and (b) an isothermal section recently reported by Mahdouk and Gachon [33]. Tie-lines are indicated by dashed lines. The question mark indicates that the limits of the two forms of $(Cr,Al)_2Nb$ Laves phases are not determined accurately.

7

Figure 2. A diffusion multiple for efficient mapping of the Nb-Cr-Al ternary phase diagram: (a) cross-sectional view; and (b) perspective view. See text for the size of the sample. The results reported in this work were all obtained from the tri-junction corner of $Nb - Cr - NbAl_3$ circled in (a).
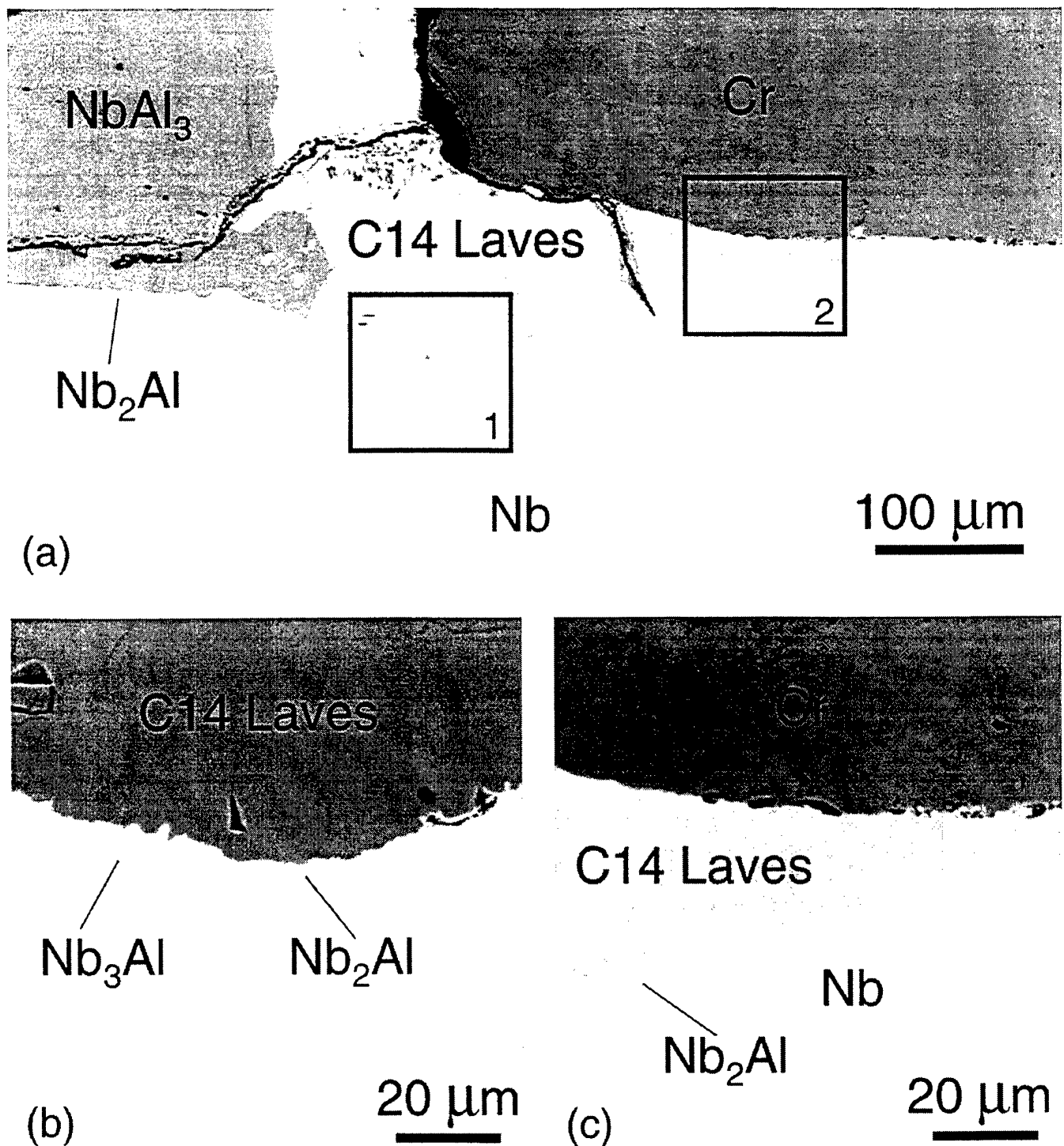
Figure 3. Backscatter electron SEM images of the Nb-Cr-NbAl$_3$ tri-junction area of the diffusion multiple (Fig. 2) annealed at 1000°C for 2000 hrs showing the formation of many different intermetallic compounds: (a) a low-magnification image showing the overall tri-junction; (b) a high-magnification image of location 1 in (a) showing the very thin layers of Nb$_2$Al and Nb$_3$Al; and (c) a high-magnification image of location 2 in (a) showing the location of the Nb$_2$Al phase.
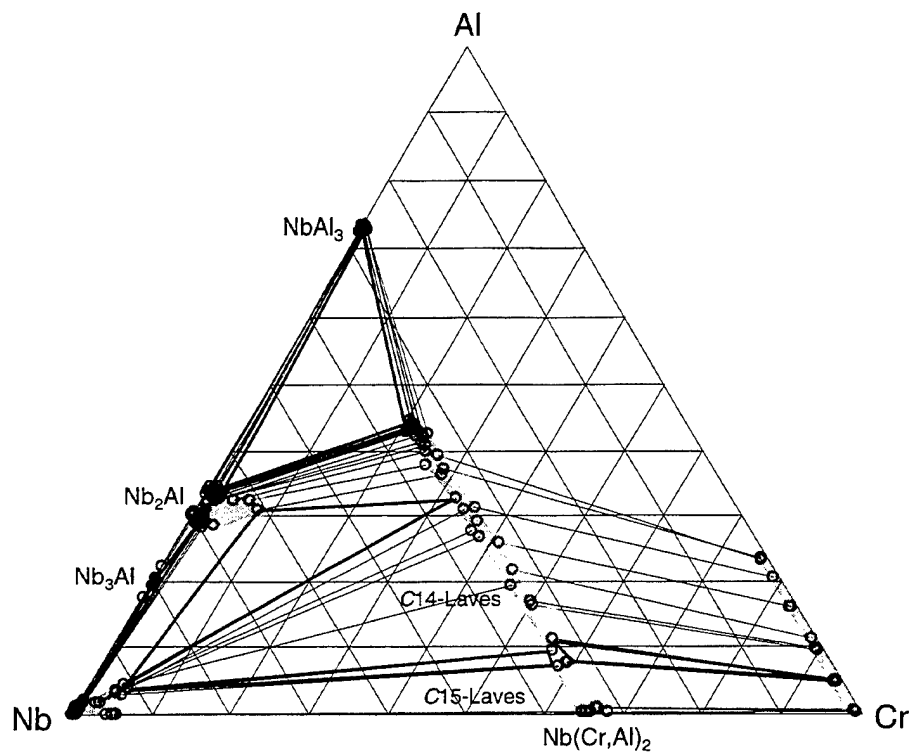
Figure 4. The 1000°C isothermal section of the Nb-Cr-Al system obtained from the Nb-Cr-NbAl₃ tri-junction area of the diffusion multiple annealed at 1000°C for 2000 hrs. The phase diagram is plotted in atomic percent axes with the numbers removed for simplicity. The solid triangle indicates well-defined three-phase triangles and the open circles show the tie-line compositions. The tie-lines are shown with light dotted lines.

Phase Diagram of the Nb-Al-Si Ternary System

J.-C. Zhao, M.R. Jackson, L.A. Peluso, and L. Tan

Phase Diagram of the Nb-Al-Si Ternary System

J.-C. Zhao, L.A. Peluso, and M.R. Jackson
General Electric Company
GE Global Research Center, P.O. Box 8, Schenectady, NY 12301, USA

and

Lizhen Tan
Department of Materials Science and Engineering
University of Wisconsin – Madison, Madison, WI 53705, USA

ABSTRACT

A high-efficiency diffusion-multiple approach was employed to map the phase diagram of the Nb-Al-Si ternary system which is very valuable for the design of niobium silicide-based composites. These composites have high potential as a replacement for Ni-base superalloys for jet engine applications. Aluminum is an alloying element for these composites, thus the Nb-Al-Si phase diagram, especially solubility of Al in Nb_5Si_3, is important information for the composite design. An isothermal section at 1000°C was constructed from the results obtained from a diffusion multiple using scanning electron microscopy (SEM) and electron probe microanalysis (EPMA). A ternary phase $Nb_3Si_5Al_2$ was observed. The solubility data of Al in αNb_5Si_3 and $NbSi_2$ as well as Si solubility in Nb_3Al, Nb_2Al and $NbAl_3$ were obtained. The new isothermal section helps to judge the reliability of the existing literature results and to add new data to the Nb-Al-Si phase equilibria.

Keywords: Nb-Al-Si, diffusion multiple, silicide, phase diagram.

1. INTRODUCTION

Niobium silicide-based composites show great promise for applications as the next generation turbine airfoil materials with significantly higher operating temperatures than current generation advanced Ni-base superalloys [1-6]. The Nb-Si binary composites have excellent creep strength, but poor oxidation resistance and poor room temperature fracture toughness [1-2]. Alloying with Al can improve the oxidation resistance. The potential application of these composites at very high temperatures requires a balance of high creep resistance, high oxidation resistance, and good low-temperature damage tolerance (fracture toughness). To achieve such a property balance, elements such as Cr, Ti, Hf and Al are added to the composites and significant progress has been made in improving the properties of the composites. Some of the alloying concepts were discussed by Zhao *et al.* [7]. The advanced design of the composites requires a fair understanding of the phase equilibria in the Nb-Si-Ti-Cr-Hf-Al system. Since a reasonable definition of the Nb-Hf-Si system has been achieved [8-10], our effort has been focused on the ternary systems Nb-Cr-Si, Nb-Si-Al, Nb-Cr-Al, Ti-Si-Cr, Ti-Si-Al, Ti-Cr-Al, Nb-Ti-Si, Nb-Ti-Cr, and Nb-Ti-Al. Other ternary systems related to the six-element system such as Nb-Ti-Hf, Nb-Cr-Hf, Nb-Hf-Al, Ti-Si-Hf, Ti-Cr-Hf, and Cr-Hf-Al have either good data or are less critical for the design of the Nb

1

silicide composites. We will report the results of the Nb-Al-Si system in the present paper and the results of other systems will be communicated separately.

In addition to being valuable for the design of the Nb silicide composites, the Nb-Al-Si ternary phase diagram is also very useful for the design of other high temperature alloys and coatings [11-19]. For instance, the Nb-rich aluminides, Nb_3Al and Nb_2Al, have demonstrated good strength and creep resistance at high temperatures [11,12]. The Al-rich intermetallic phase, $NbAl_3$, is also a candidate material for advanced aeropropulsion systems because of its high melting point and low density. The $Nb_3Si_5Al_2$ phase showed good strength and excellent oxidation resistance at 1300 °C with a thin adherent Al_2O_3 layer, but it showed poor oxidation resistance at 750 °C [13]. Nb-Al-Si coatings are also pursued for high temperature sulfidation and oxidation applications [14,15].

The high-efficiency "diffusion multiple" approach [20-23] is ideally suited for mapping phase diagrams of the six-element related ternary systems mentioned earlier. It would take thousands of alloys to determine these ternary systems using the traditional one-alloy-at-a-time (equilibrated alloy) approach. For instance, it took Goldschmidt and Brand [24] about 220 alloys to map just the Nb-Cr-Si ternary system and similarly about 135 alloys were employed by Lysenko et al. [25] to determine the Ti-Cr-Si system. These alloys have very high melting temperatures and are difficult to make and to homogenize. Extra effort also needs to be taken to avoid interstitial (oxygen, nitrogen, carbon, etc.) contamination during alloy casting and heat treatment. In contrast, the diffusion multiple approach needs only a few cast alloys and the samples were easy to make, and safe-guarding against the interstitial contamination can be very easily implemented as will be discussed later. The general diffusion multiple approach was discussed in detail previously [20-23] and has been successfully applied to many alloy systems.

The constitutive binary phase diagrams of the Nb-Al-Si system, i.e., Nb-Al [26], Al-Si [27] and Nb-Si [7,28-30] are already well assessed in the literature. The crystal structures of the phases in the binary and the ternary system are listed in Table 1 [31].

Table 1. Crystal structure of phases in the Nb-Al-Si ternary system [31].

System	Pearson Symbol	Space Group	Lattice Parameters			
			a	b	c	γ
Al		Fm3m	0.40497			
Nb		Im3m	0.33067			
Si		Fd3m	0.54309			
Nb_3Si		$P4_2/n$	1.0224		0.5189	
βNb_5Si_3	tI32	I4/mcm	1.0040		0.5081	
αNb_5Si_3	tI32	I4/mcm	0.6571		1.1889	
$NbSi_2$		$P6_222$	0.481		0.661	120°
Nb_2Al		$P4_2/mnm$	0.9945		0.5171	
Nb_3Al		Pm3n	0.5186			
$NbAl_3$		I4/mmm	0.3844		0.8605	
$Nb_3Si_5Al_2$	oF24	Fddd	0.8403	0.4901	0.8794	

An isothermal section of the Nb-Al-Si ternary system was first reported by Brukl et al. [32], as shown in Fig. 1(a). Strangely, the same isothermal section was said to be for both 500 and

2

1400°C, which is very unlikely true – It is hard to believe that the phases have identical solubilities at both 500 and 1400°C! Brukl $et\ al.$ identified two ternary compounds $Nb_3Si_5Al_2$ and $Nb_{10}Si_3Al_3$ and found them in equilibrium with each other. A contradictory result was reported by Pan $et\ al.$ [33] who found that these two compounds were not in equilibrium; instead αNb_5Si_3 was in equilibrium with $NbAl_3$. Pan $et\ al.$ constructed a partial isothermal section at 1500°C, as shown in Fig. 1(b). Using 11 different alloy compacts prepared by spark plasma sintering, Murakami $et\ al.$ [13] recently confirmed the equilibrium between αNb_5Si_3 and $NbAl_3$, and presented a tentative isothermal section for the temperatures of 1200 to 1600°C, as shown in Fig. 1(c). All the phase boundaries were un-defined, and only three-phase equilibria were tentatively defined. Note that the Al solubility in αNb_5Si_3 was reported very differently by different groups, near zero by Brukl $et\ al.$ [32], ~ 10 at.% by Pan $et\ al.$ [33], and near zero by Murakami $et\ al.$ [13]. Our experimental result will help to judge which data were reliable.

Allibert $et\ al.$ [34] studied the phase equilibria in the Al and Si rich alloys (with Nb < 40 at.%) and reported partial isothermal sections at both 1300 and 1500°C. They found two three-phase equilibria, Liquid + $NbAl_3$ + $Nb_3Si_5Al_2$ and Liquid + $Nb_3Si_5Al_2$ + $NbSi_2$. Our work will be complementary to theirs in defining the Nb-rich part of the phase diagram.

2. EXPERIMENTAL METHOD

A diffusion multiple with the cross-section view shown schematically in Fig. 2(a) was made. The dimensions were designed so that the pieces of pure elements and compounds are much larger than the diffusion distance, thus there will be pure elements and compounds left after the long-term diffusion annealing. To avoid the low melting point of Al, we used both $NbSi_2$ and $NbAl_3$ compounds as members of the diffusion multiple. Both these compounds were made by arc-melting. They were then cut into square bars of 7 x 7 x 25 mm using electro-discharge machining (EDM). A 14 x 14 mm square opening was cut from a 25.4 mm diameter by 25.4 mm height cylindrical piece of pure Nb. The square open was cut across the whole height of the Nb piece. Pieces of high purity Nb and Cr in the dimension of 7 x 7 x 25 mm were also machined using EDM. The re-cast layer on the EDM'ed surfaces was removed by mechanical grinding to make clean surfaces. The pieces were ultrasonically cleaned in methanol and then assembled into the geometry shown in Fig. 2(a). The height of all pieces was 25.4 mm. The assembled diffusion multiple was then loaded into hot isostatic press (HIP) cans made of commercial purity Ti, which is schematically shown in Fig. 2(b). A 25 μm layer of Ta was placed between the diffusion multiple and the HIP cans to isolate any interstitial contaminants that may diffuse into the HIP can from the quartz capsule during long-term annealing. The top and bottom caps of the HIP can were electron beam welded. HIPing was performed at 1204 °C, 200MPa for 4 hrs. The HIP can containing the diffusion multiple was then encapsulated in an evacuated quartz tube backfilled with pure argon. Since Nb is susceptible to oxygen and nitrogen contamination, it is critical to keep the diffusion multiple from interstitial elements. To further absorb any oxygen that may diffuse into the quartz tube, a packet of pure yttrium was wrapped in Ta foils and was then placed inside the quartz tube. Thus, the diffusion multiple was protected from the intersitials (O, N, C, etc.) by the quartz tube, the pure yttrium absorber, the Ti HIP can, and the Ta diffusion barrier. The encapsulated sample was then annealed at 1000°C for 2000 hours. After the heat treatment, the diffusion multiple was taken from the argon furnace and cooled down to ambient temperature by breaking the quartz tube and quenching the diffusion multiple into water. The diffusion multiple was then cut into halves parallel to the ends using wire EDM, ground and polished.

The sample was first examined using scanning electron microscopy (SEM), especially the backscatter electron (BSE) imaging. Most phases could be seen (although not identified explicitly) in the BSE images due to the differences in their average atomic weight. Quantitative EPMA analysis was performed on a CAMECA (Paris, France) microprobe using 15 kV voltage, 40 nA current and a 40° take-off angle.

3. RESULTS AND DISCUSSION

Backscatter electron images taken from the $Nb-NbSi_2-NbAl_3$ tri-junction (schematically circled area in Fig. 2(a)) of the diffusion multiple annealed at 1000 °C for 2000 hrs are shown in Fig. 3. During the long-term diffusion treatment, extensive interdiffusion among Nb, Al and Si took place, and all the equilibrium phases, including the intermetallic phases, formed by interdiffusion reactions. The black area on top of Fig. 3(a) was a crack probably formed during specimen preparation (EDM cutting, grinding and polishing). Some of the porosity shown in Fig. 3 may be due to Kirkendall voiding. The Nb_2Al and Nb_3Al phases which are difficult to see in Fig. 3(a) can be seen in Fig. 3(b) to 3(d). Figure 3(c) shows a very thin layer of Nb_3Al on the right-hand size of the image, but on the left-hand side, it almost became an interfacial phase. The Nb_3Al phase remained very thin in almost all areas except at location X in Fig. 3(b). Both Nb_2Al and Nb_3Al became extremely thin at the location in Fig. 3(d). The Nb_2Al phase completely disappeared at location Y and to the left, whereas the Nb_3Al phase completely disappeared at location Z and left on Fig. 3(d). Since the Nb_3Al phase is extremely thin, we took account of overlapping and over-sampling effects when analyzing the EPMA data.

By performing EPMA analysis in this tri-junction area, a large amount of phase equilibrium information was obtained. Based on the compositional information from EPMA and by taking advantage of the local equilibrium at phase interfaces, an isothermal section of the Nb-Al-Si system was constructed as shown in Fig. 4. Detailed procedures of phase diagram mapping using diffusion multiples can be found elsewhere [20-23].

We observed only one ternary compound $Nb_3Si_5Al_2$ instead of two ($Nb_3Si_5Al_2$ and $Nb_{10}Si_3Al_3$) as suggested by previous investigations [13,32,33]. When our result was first obtained, we thought we might have a missing phase situation for this ternary system. However, after careful examination of the crystal structure and lattice parameters of the $Nb_{10}Si_3Al_3$ phase, we realized that this "ternary" compound actually is the binary βNb_5Si_3 phase stabilized to lower temperatures by Al addition. For instance, the crystal structure and lattice parameters of the $Nb_{10}Si_3Al_3$ reported by Brukl et al. were tI32 (I4/mcm) and a=1.0160 nm and c=0.5081 nm which are the identical crystal structure and very close lattice parameters of βNb_5Si_3 (Table 1). We conclude that $Nb_{10}Si_3Al_3$ is $\beta Nb_5(Si,Al)_3$. With this understanding, our result is not in contradiction with the literature results. Our result and these of the literature suggest that Al addition stabilizes $\beta Nb_5(Si,Al)_3$ to 1400°C, but not to 1000°C. The fact that all the binary compounds, Nb_3Al, Nb_2Al, $NbAl_3$, Nb_5Si_3 and $NbSi_2$, have formed in the diffusion multiple suggest that the likelihood of one phase missing is very low. It should be mentioned that although Brukl et al. [32] claimed the same isothermal section (Fig. 1(a)) for two very different temperatures (500 and 1400°C), the likelihood of this isothermal section being an equilibrium one for 500°C is very slim. We suggest regarding it as only for 1400°C.

The phase diagram of Brukl et al. [32] (Fig. 1(a)) suggested very low solubility of Al in αNb_5Si_3 at 1400°C, but that of Pan et al. [33] suggested ~ 12 at.% at 1500°C. Our result showed ~ 8 at.% at 1000°C, supporting the result of Pan et al. Pan et al. drew the single-phase field of

4

αNb_5Si_3 to point to the direction of $NbAl_3$, which suggests that Al substitutes for both Nb and Si sites in αNb_5Si_3. Our results (Fig. 4) clearly show that Al substitutes for Si only in αNb_5Si_3. Thus, the direction of substitution of Al in αNb_5Si_3 in Pan et al. is questionable. At 1000°C, we observed very little solubility of Si in both Nb_3Al and Nb_2Al, and only ~ 2at.% in $NbAl_3$. Si only substitutes for Al in $NbAl_3$, and Al only substitutes for Si in $NbSi_2$ (Fig.4).

Our observation of a direct equilibrium between Nb_5Si_3 and $NbAl_3$ is consistent with that of both Pan et al. [33] and Murakami et al. [13], and the results together suggest that the two three-phase equilibria $Nb_3Si_5Al_2 + \beta Nb_5(Si,Al)_3$ [$Nb_{10}Si_3Al_3$] + αNb_5Si_3 and $Nb_3Si_5Al_2 + \beta Nb_5(Si,Al)_3$ [$Nb_{10}Si_3Al_3$] + $NbAl_3$ shown by Brukl et al. (Fig. 1(a)) are very likely incorrect.

The alloying effect of Al in Nb silicide-based composites can be appreciated by examining the Nb-Al-Si phase diagram (Figs. 4 and 1). Although the solubility of Al in αNb_5Si_3 is ~ 8 to 12 at.% depending on the temperature, but it is only ~ 3 to 5 at.% when in equilibrium with the bcc(Nb) phase (the two major phases in Nb silicide composites). Thus, when the Al additions to the Nb-Si alloys are beyond ~3 at.%, an A15-type Nb_3Al phase will appear in the ternary system. The solubility of Al in the phases will be strongly dependent on the Ti concentration in the composites. It is unknown whether the A15 Nb_3Al phase will be beneficial or detrimental to creep-rupture properties. In composites with Cr additions, the Al additions may help promote the C14 Laves phase instead of the A15 Nb_3Al phase. This can be appreciated by examining the Nb-Cr-Al phase diagram. Our work on the Nb-Cr-Al ternary system will be reported separately [35].

The phase equilibrium information of the Nb-Al-Si system is very useful for the design of both Nb silicide composites and coatings for these composites. This is one of the key systems we would like to perform CALPHAD modeling and add the data into the developing thermodynamic database for Nb silicide based systems [10,36-37].

4. CONCLUSIONS

Using the high-efficiency diffusion-multiple approach, we mapped the 1000°C isothermal section of the Nb-Al-Si ternary system. We observed one ternary compound, $Nb_3Si_5Al_2$ which was reported in the literature before. Based on the crystal structure and lattice parameter information, we concluded that the so-called ternary $Nb_{10}Si_3Al_3$ compound is actually the βNb_5Si_3 stabilized to lower temperature by Al addition. Al stabilizes this phase to 1400°C, but not to 1000°C. The Al solubility in αNb_5Si_3 was measured ~ 8 at.% at 1000°C, and Al only substitutes on the Si sites in the compound. Our observation of a direct equilibrium between αNb_5Si_3 and $NbAl_3$ is consistent with that of both Pan et al. [33] and Murakami et al. [13], and the results together suggest that the phase diagram shown by Brukl et al. (Fig. 1(a)) is very likely incorrect. Our equilibrium phase diagram (Fig. 4) helps to clarify the confusion in the phases and equilibria of this ternary system.

representing the official policies or endorsement, either expressed or implied, of the AFOSR or the U.S. Government.

REFERENCES

1. M.G. Mendiratta and D.M. Dimiduk, *Mat. Res. Soc. Symp. Proc.*, 133 (1989), 441- 446.
2. M.R. Jackson, B.P. Bewlay, R.G. Rowe, D.W. Skelly, and H.A. Lipsitt, *JOM*, 48 (1996), 39-44.
3. P.R. Subramanian, M.G. Mendiratta, and D.M. Dimiduk, *JOM*, 48 (1996), 33-38.
4. B.P. Bewlay, J.J. Lewandowski, and M.R. Jackson, *JOM*, 49 (1997), 44-45.
5. S.J. Balsone, B.P. Bewlay, M.R. Jackson, P.R. Subramanian, J.-C. Zhao, A. Chatterjee, and T. Heffernan, in *Structural Intermetallics 2001* (K. Hemker, D.M. Dimiduk, H. Clemens, R. Darolia, H. Inui, J.M. Larsen, V.K. Sikka, M. Thomas, and J.D. Whittenberger, eds.), TMS, Warrendale, PA, 2001, 99-108
6. B.P. Bewlay, M.R. Jackson, J.-C. Zhao, and P.R. Subramanian, *Metall. Mater. Trans.*, Accepted November 2002.
7. J.-C. Zhao, B.P. Bewlay, M.R. Jackson, and L.A. Peluso, in *Structural Intermetallics 2001* (K. Hemker, D.M. Dimiduk, H. Clemens, R. Darolia, H. Inui, J.M. Larsen, V.K. Sikka, M. Thomas, and J.D. Whittenberger, eds.), TMS, Warrendale, PA, 2001, 483-491.
8. B.P. Bewlay, R.R. Bishop, and M.R. Jackson, *Z. Metallkde.*, 90 (1999), 413-422.
9. J.-C. Zhao, B.P. Bewlay, and M.R. Jackson, *Intermetallics*, 9 (2001), 681-689.
10. Y. Yang, Y.A. Chang, J.-C. Zhao, and B.P. Bewlay, *Intermetallics*, Accepted November 2002.
11. D.L. Anton and D.M. Shah, *Mater. Res. Soc. Symp. Proc.*, 288 (1993), 141-150.
12. D.M. Dimiduk, P.R. Subramanian, and M.G. Mendiratta, *Acta Metall. Mater.*, 8 (1995), 519-530.
13. T. Murakami, S. Sasaki, K. Ichikawa, and A. Kitahara, *Intermetallics*, 9 (2001), 621-627 & 629-635.
14. D.-B. Lee, *Metals and Materials*, 7 (2001), 461-466.
15. H. Habazaki, D.B. Lee, A. Kawashima, and K. Hashimoto, *Corrosion Sci.*, 42 (2000), 721-729.
16. K.S. Chan and D.L. Davidson, *Metall. Mater. Trans.*, 32A (2001), 2717-2727.
17. Y. Murayama and S. Hanada, *J. Japan Inst. Met.*, 63 (1999), 1519-1526.
18. R. Gerling, A. Bartels, H. Clemens, M. Oehring, F.-P. Schimansky, *Acta Mater.*, 45 (1997), 4057-4066.
19. M. Es-Souni, R. Wagner, P.A. Beaven, and A. Bartels, *Mater. Sci. Eng.*, A153 (1992), 444-450.
20. J.-C. Zhao, *Adv. Eng. Mater.*, 3 (2001), 143-147.
21. J.-C. Zhao, *J. Mater. Res.*, 16 (2001), 1565-1578.
22. J.-C. Zhao, M.R. Jackson, L.A. Peluso, and L. Brewer, *MRS Bulletin*, 27 (2002), 324-329.
23. J.-C. Zhao, M.R. Jackson, L.A. Peluso, and L. Brewer, *JOM*, 54 (7) (2002), 42-45.
24. H.J. Goldschmidt and J.A. Brand, *J. Less-Common Met.*, 3 (1961), 34-43.
25. L.A. Lysenko, V.Ya. Markiv, O.V. Tsybukh, and E.I. Gladyshevskii, *Inorganic Mater.*, 7(1) (1971), 157-159.
26. U.R. Kattner: in *Binary Alloy Phase Diagrams*, 2nd ed., T.B. Massalski, ed., ASM International, Materials Park, OH, 1990.
27. J.L. Murray, in *Binary Alloy Phase Diagrams*, 2nd ed., T.B. Massalski, ed., ASM International, Materials Park, OH, 1990.
28. M.E. Schlesinger, H. Okamoto, A.B. Gokhale, and R. Abbaschian, *J. Phase Equilibria*, 14 (1993), 502.
29. M.G. Mendiratta and D.M. Dimiduk, *Scripta Metall. Mater.*, 25 (1991), 237-242.

30. B.P. Bewlay, H.A. Lipsitt, M.R. Jackson, W.J. Reeder, and J.A. Sutliff, *Mater. Sci. Eng.*, A192/193 (1995), 534-543.

31. P. Villars and L.D. Calvert, *Pearson's Handbook of Crystallographic Data for Intermetallic Phases*, 2nd ed., ASM International, Materials Park, OH, 1991.

32. C. Brukl, H. Nowotny, and F. Benesovsky, *Monatsh. Chem.*, 92 (1961), 967-980.

33. V.M. Pan, V.I. Latysheva, O.G. Kulik, A.G. Popov, and E.N. Litvinenko, *Russ. Metall.*, (4) (1984), 233-235.

34. C. Allibert, A. Wicker, J. Driole, and E. Bonnier, *J. Less-Common Met.*, 31 (1973), 221-228.

35. J.-C. Zhao, M.R. Jackson, and L.A. Peluso, to be published.

36. H. Liang and Y.A.Chang, *Intermetallics*, 7 (1999), 561.

37. Y. Yang and Y.A. Chang (University of Wisconsin – Madison), private communication, 2002.
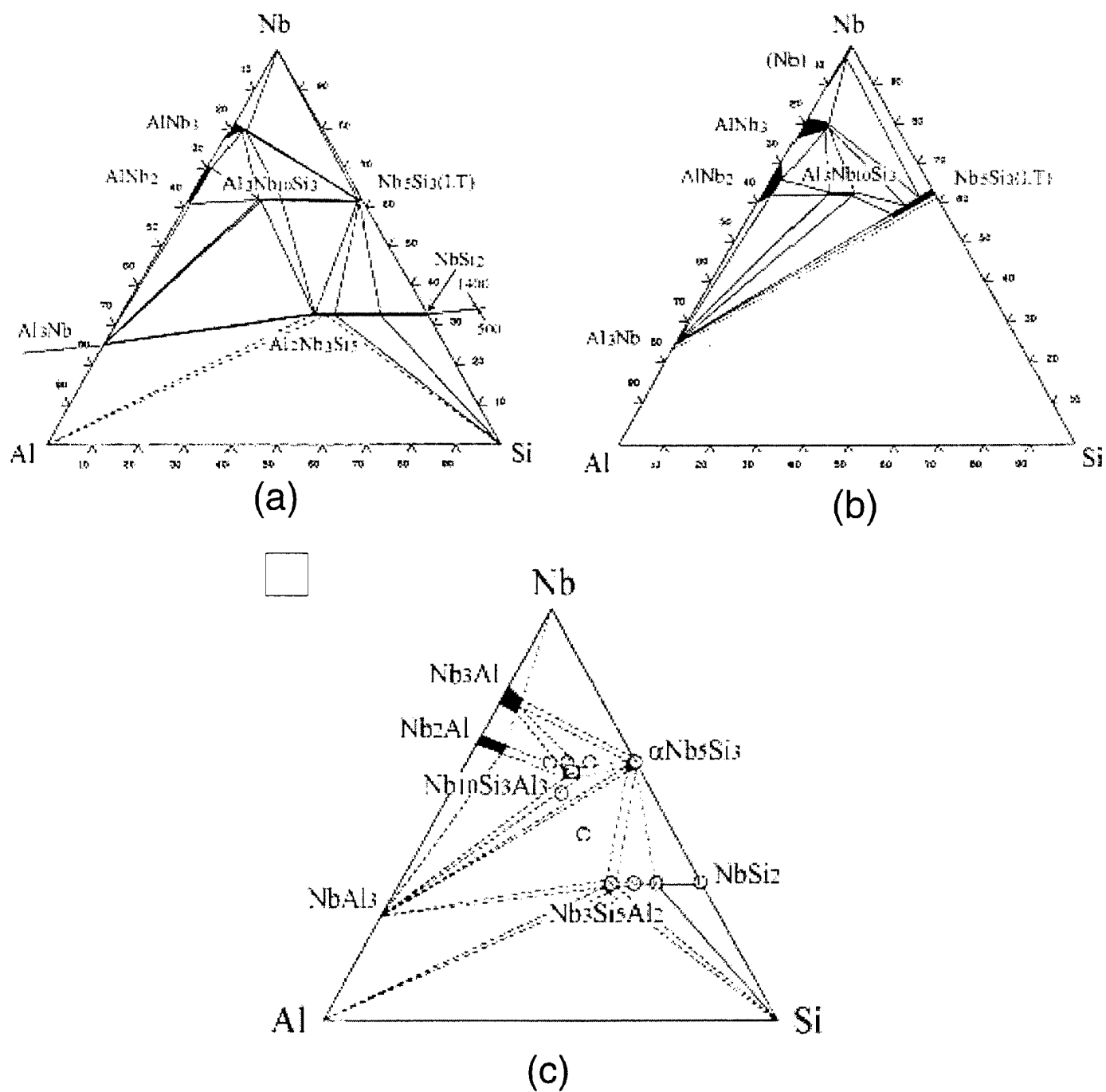
Figure 1. Isothermal sections of the Nb-Si-Al system from the literature: (a) 500 and 1400 °C (the same) results reported by Brukl *et al.* [32], (b) a partial 1500°C isothermal section of the Nb-Si-Al system by Pan *et al.* [33]; and (c) estimated 1200-1600 °C isothermal section by Murakami *et al.* [13].
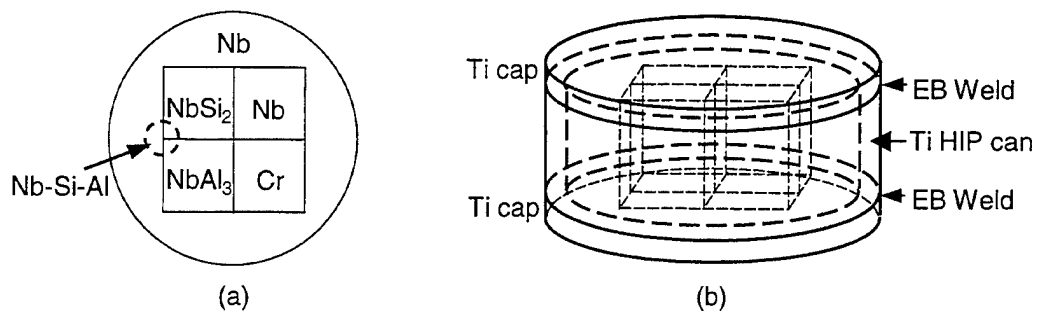
Figure 2. A diffusion multiple for efficient mapping of the Nb-Al-Si ternary phase diagram: (a) cross-sectional view; and (b) perspective view. See text for the size of the sample. The results reported in this work were all obtained from the tri-junction corner of $Nb - NbSi_2 - NbAl_3$ circled in (a).
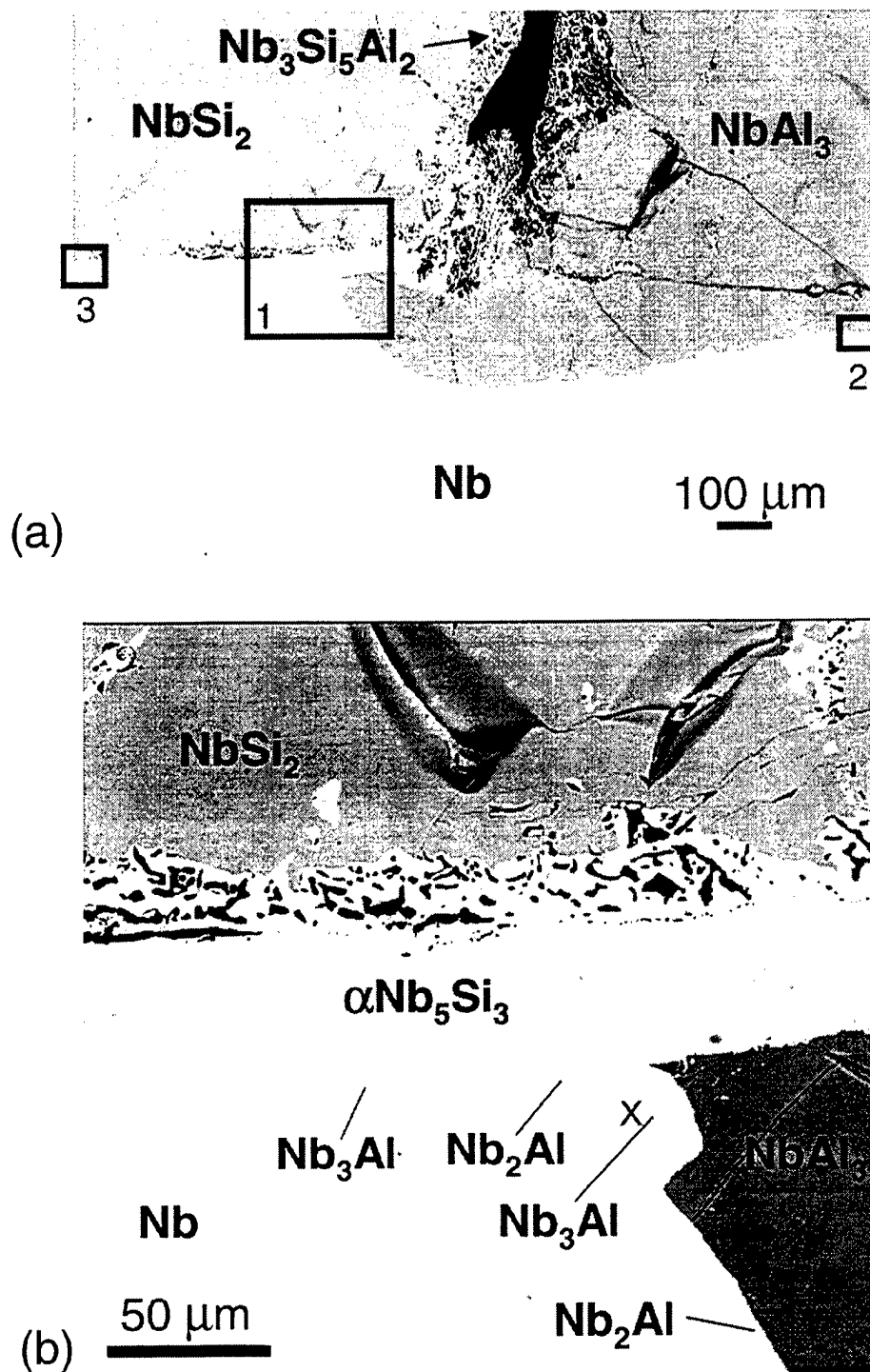
Figure 3. Backscatter electron SEM images of the Nb-NbSi$_2$-NbAl$_3$ tri-junction area of the diffusion multiple (Fig. 2) annealed at 1000°C for 2000 hrs showing the formation of many different intermetallic compounds, including one ternary compound, Nb$_3$Si$_5$Al$_2$. (a) a low-magnification image showing the overall tri-junction; (b) a high-magnification image of location 1 in (a); (c) a high-magnification image of location 2 in (a) showing the Nb$_3$Al phase; and (d) a high-magnification image of location 2 in (a) showing the disappearance of both Nb$_2$Al and Nb$_3$Al.

NbAl₃

Nb₂Al

Nb₃Al

Nb

10 μm

(c)

NbSi₂

αNb₅Si₃

Nb₃Al   Z

Y
Nb₂Al

20 μm

(d)
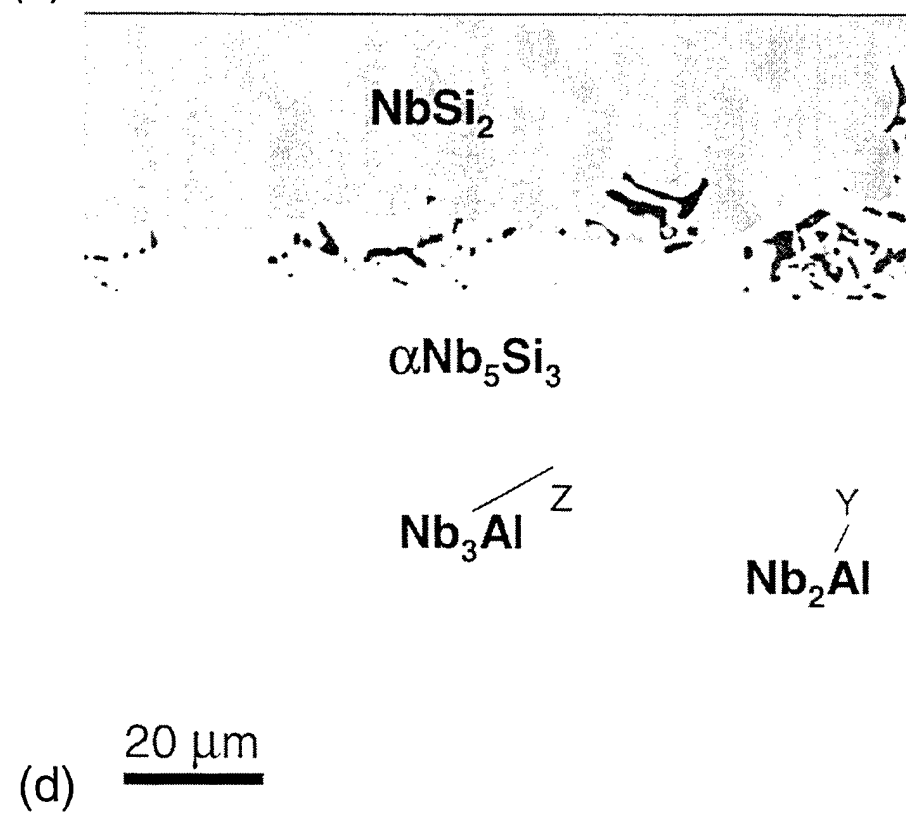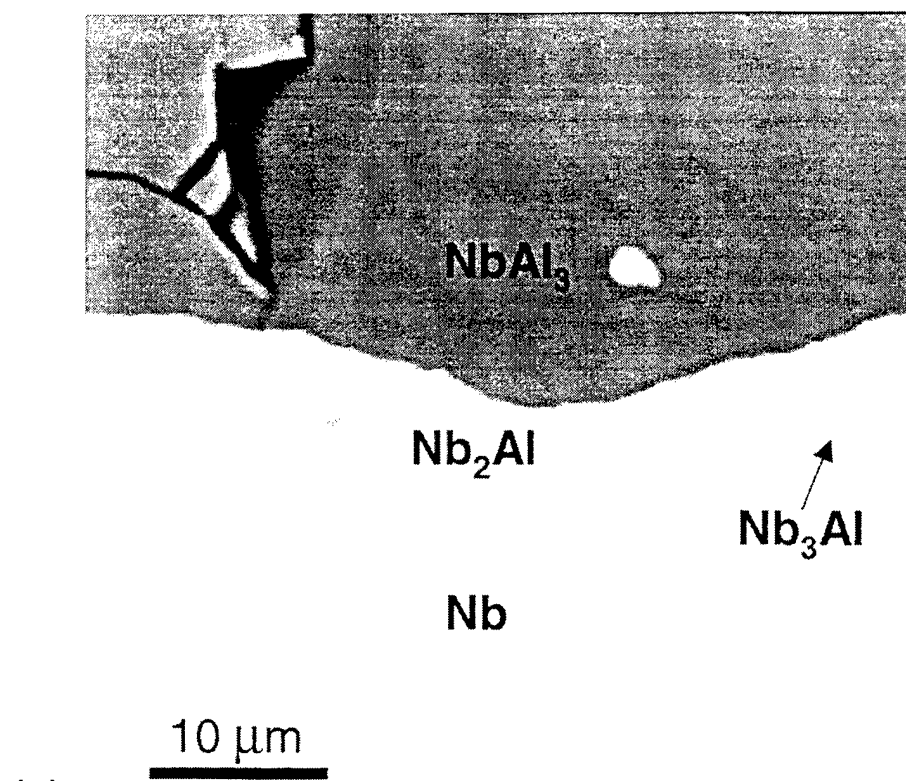
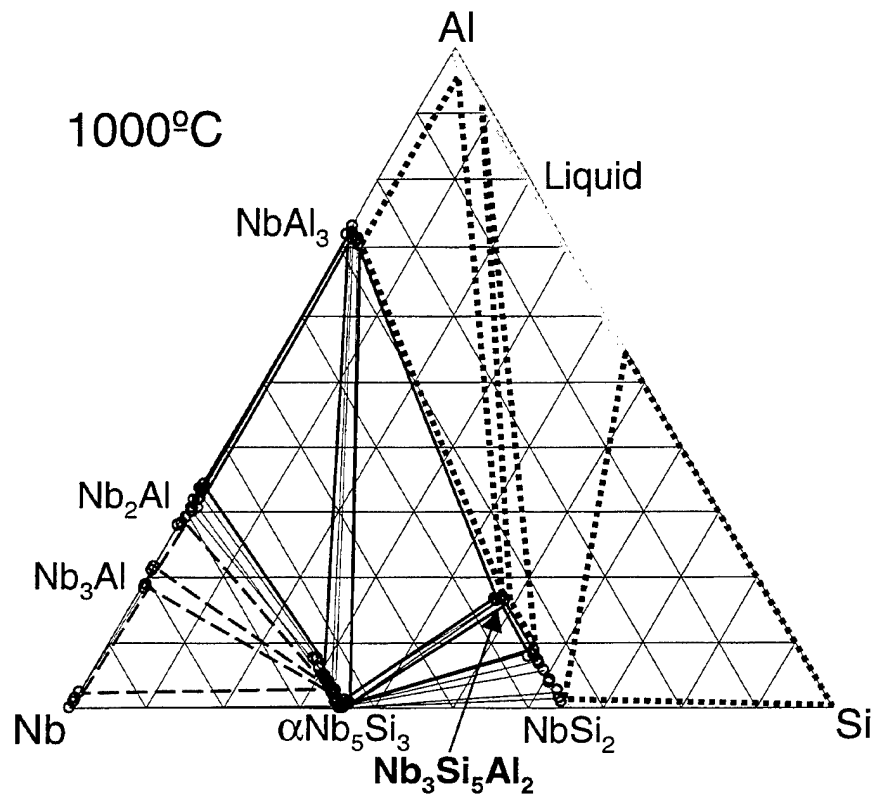Figure 3. (Continued). See previous page for figure caption.

Figure 4. The 1000°C isothermal section of the Nb-Al-Si system obtained from the tri-junction area of the diffusion multiple annealed at 1000°C for 2000 hrs. The phase diagram is plotted in atomic percent axes with the numbers removed for simplicity. The solid triangle indicates well-defined three-phase triangles and the open circles show the tie-line compositions. The tie-lines are shown with light dotted lines. The dashed tie-triangles were estimated. The heavy dotted tie-triangles were guessed three-phase equilibria based on the high temperature data of Allibert et al. [34] along with the Al-Si binary phase diagram.

Mapping of the Nb-Ti-Al Phase Diagram Using a Diffusion Multiple

J.-C. Zhao, M.R. Jackson, L.A. Peluso, and L. Tan

Mapping of the Nb-Ti-Al Phase Diagram Using a Diffusion Multiple

J.-C. Zhao, M.R. Jackson, and L.A. Peluso
General Electric Company
GE Global Research Center, P.O. Box 8, Schenectady, NY 12301, USA

and

Lizhen Tan
Department of Materials Science and Engineering
University of Wisconsin – Madison, Madison, WI 53705, USA

ABSTRACT

A high-efficiency diffusion-multiple approach was employed to map the phase diagram of the Nb-Ti-Al ternary system which is critical for the design of both niobium silicide-based composites and the gamma TiAl. A partial isothermal section at 1200°C was constructed from the results obtained from a diffusion multiple made up of Nb, Ti, TiAl$_3$ and TiSi$_2$ and annealed at 1200°C for 1000 hours. The tie-line and tie-triangles were obtained from the electron probe microanalysis (EPMA) composition profiles. Crystal structure identification was made using electron backscatter diffraction (EBSD). The 1200°C isothermal section obtained from the present study agrees well with majority of the literature results.

Keywords: Ti-Nb-Al, diffusion multiple, TiAl, phase diagram, intermetallics, composites.

1. INTRODUCTION

Niobium silicide-based composites show great promise for applications as the next generation turbine airfoil materials with significantly higher operating temperatures than current generation advanced Ni-base superalloys [1-6]. The Nb-Si binary composites have excellent creep strength, but poor oxidation resistance and poor room temperature fracture toughness [1-2]. Alloying with Ti significantly improves the oxidation resistance. The potential application of these composites at very high temperatures requires a balance of high creep resistance, high oxidation resistance, and good low-temperature damage tolerance (fracture toughness). To achieve such a property balance, elements such as Cr, Ti, Hf and Al are added to the composites and significant progress has been made in improving the properties of the composites. Some of the alloying concepts were discussed by Zhao *et al.* [7]. The advanced design of the composites requires a fair understanding of the phase equilibria in the Nb-Si-Ti-Cr-Hf-Al system. Since a reasonable definition of the Nb-Hf-Si system has been achieved [8-10], our effort has been focused on the ternary systems Nb-Cr-Si, Nb-Si-Al, Nb-Cr-Al, Ti-Si-Cr, Ti-Si-Al, Ti-Cr-Al, Nb-Ti-Si, Nb-Ti-Cr, and Nb-Ti-Al. Other ternary systems related to this six-element system such as Nb-Ti-Hf, Nb-Cr-Hf, Nb-Hf-Al, Ti-Si-Hf, Ti-Cr-Hf, and Cr-Hf-Al have either good data or are less critical for the design of the Nb silicide composites. We will report the results of the Ti-Nb-Al system in the present paper and the results of other systems will be communicated separately.

1

The Ti-Nb-Al phase diagram is also very important for the development of γTiAl since Nb is one of the most important alloying elements in TiAl-based alloys. Nb is very effective in improving both high temperature strength and oxidation resistance of γTiAl. For this reason, there have been extensive previous investigations on the phase diagrams of the Nb-Ti-Al system [11-35]. Even with these two dozens of investigations, there is still discrepancy and disagreement on the phase diagram of this ternary system. Several isothermal sections at 1200 and 1150°C are shown in Fig. 1. Significant difference can be clearly seen among these phase diagrams.

The major discrepancy in the Nb-Ti-Al system is the dispute over the existence of the γ_1-Al$_3$NbTi phase which has a relatively large solubility range. The γ_1 phase was observed at 1200 °C by Popov et al. with a stable region extended to 51 at.% Nb [35]. This phase was also reported by Zakharov et al. at 900 and 1200 °C in 1980s [33,34], but with very different lattice parameters. Zakharov et al. later disclaimed and removed the γ_1 phase from their phase diagrams [28-30]. However, the discussion around the γ_1 phase came back when Chen et al. [21] claimed its existence at 1000 to 1400°C, strangely with yet another very different set of lattice parameters. Jewett [20] questioned Chen et al.'s claim of this phase based on his own work and many other studies. Ding and Hao [18], in reply to Jewett's questioning, provided results to support the existence of the γ_1 phase. However, this phase was not observed by many other independent investigations on the alloys with compositions in the claimed γ_1 phase region. Hellwig et al. [16] provided a good review on the discrepancy around the γ_1 phase. They did not see this phase in a very comprehensive study of alloys annealed at 1000 and 1200 °C.

A high-efficiency diffusion multiple approach [36-39] was employed to map the Nb-Ti-Al phase diagram as part of our effort to map the above-mentioned nine ternary systems critical to Nb silicide composite design. This approach is ideally suited for such systems. It would take thousands of alloys to determine the nine ternary systems using the traditional one-alloy-at-a-time (equilibrated alloy) approach. For instance, it took Goldschmidt and Brand [40] about 220 alloys to map just the Nb-Cr-Si ternary system and similarly about 135 alloys were employed by Lysenko et al. [41] to determine the Ti-Cr-Si system. The comprehensive study of the Nb-Ti-Al system by Hellwig et al. [16] also took 71 alloys and 12 diffusion couples. These alloys have very high melting temperatures and are difficult to make and to homogenize. Extra effort also needs to be taken to avoid interstitial (oxygen, nitrogen, carbon, etc.) contamination during alloy casting and heat treatment. In contrast, the diffusion multiple approach needs only a few cast alloys and the samples were easy to make, and safe-guarding against the interstitial contamination can be very easily implemented as will be discussed later. The general diffusion multiple approach is discussed in detail previously [36-39] and has been successfully applied to many alloy systems.

Our data on the Nb-Ti-Al system will help judging the reliability of previous literature results on the phase equilibria of this important ternary system.

2. EXPERIMENTAL METHOD

A diffusion multiple with the cross-section view shown schematically in the Fig. 2(a) was made. The dimensions were designed so that the pieces of pure elements and compounds are much larger than the diffusion distance, thus there will be pure elements and compounds left after the long-term diffusion annealing. To avoid the low melting point of Al, we used TiAl$_3$ compound as a member of the diffusion multiple. Both this compound and TiSi$_2$ (for the Ti-Si-Al system which will be reported separately) were made by arc-melting. They were then cut into

2

square bars of 7 x 7 x 25 mm using electro-discharge machining (EDM). A 14 x 14 mm square opening was cut from a 25.4 mm diameter by 25.4 mm height cylindrical piece of pure Ti. The square opening was cut across the whole height of the Ti piece. Pieces of high purity Ti and Nb in the dimension of 7 x 7 x 25 mm were also machined using EDM. The re-cast layer on the EDM'ed surfaces was removed by mechanical grinding to make clean surfaces. The pieces were ultrasonically cleaned in methanol and then assembled into the geometry shown in Fig. 2(a). The height of all pieces was 25 mm. The assembled diffusion multiple was then loaded into hot isostatic press (HIP) cans made of commercial purity Ti, which is schematically shown in Fig. 2(b). A 25 µm layer of Ta foil was placed between the diffusion multiple and the HIP can to isolate any interstitial contaminants that may diffuse into the HIP can from the quartz capsule during long-term annealing. The top and bottom caps of the HIP can were electron beam welded. HIPing was performed at 1204°C, 200MPa for 4 hours. The HIP can containing the diffusion multiple was then encapsulated in an evacuated quartz tube backfilled with pure argon. Since Ti is susceptible to oxygen and nitrogen contamination, it is critical to keep the diffusion multiple from interstitial elements. To further absorb any oxygen that may diffuse into the quartz tube, a packet of pure yttrium was wrapped in Ta foils and was then placed inside the quartz tube. Thus, the diffusion multiple was protected from the intersitials (O, N, C, etc.) by the quartz tube, the pure yttrium absorber, the Ti HIP can, and the Ta diffusion barrier. The encapsulated sample was then annealed at 1200°C for 1000 hours. After the heat treatment, the diffusion multiple was taken from the argon furnace and cooled down to ambient temperature by breaking the quartz tube and quenching the diffusion multiple into water. The diffusion multiple was then cut into halves parallel to the ends using wire EDM, ground and polished.

The samples were first examined using scanning electron microscopy (SEM), especially the backscatter electron (BSE) imaging. Most phases could be seen (although not identified explicitly) in the BSE images due to the differences in their average atomic weight. Quantitative EPMA analysis was performed on a CAMECA (Paris, France) microprobe using 15 kV voltage, 40 nA current and a 40° take-off angle. Electron backscatter diffraction (EBSD) analysis was performed to obtain crystal structure information of the phases formed in the diffusion multiple. Phase identification was accomplished by a direct match of the diffraction bands in the experimental backscatter pattern with simulated patterns generated using known structure types and lattice parameters. A detailed discussion on this powerful EBSD technique can be found in Schwartz et al. [42].

3. RESULTS AND DISCUSSION

Backscatter electron images taken from the Nb-Ti-TiAl$_3$ tri-junction (schematically circled area in Fig. 2(a)) of the diffusion multiple annealed at 1200°C for 1000 hrs are shown in Fig. 3. During the long-term diffusion treatment, extensive interdiffusion among Nb, Ti and Al took place, and all the equilibrium phases, including the intermetallic phases, formed by interdiffusion reactions. By performing EPMA analysis in this tri-junction area, an extremely large amount of phase equilibrium information can be obtained to construct the isothermal section shown in Fig. 4. We have defined the whole isothermal section (except for the very Al-rich corner) from a corner (tri-junction) of the diffusion multiple.

The tie-lines reported on the phase diagram were defined from the EPMA line profiles by taking advantage of the local equilibrium at interfaces formed among the phases. Details of the methodology can be found elsewhere [36-39].

Our isothermal section (Fig. 4) agrees well with the majority of the phase diagram data of Hellwig et al. [16] (Fig. 1(a)), Das et al. [24] (Fig. 1(b)), Perepezko et al. [31] (Fig. 1(c)), and Kaltenbach et al. [32] (Fig. 1(d)). Overall, our results agree best with that of Hellwig et al. [16] (Fig. 1(a)). Still, the following areas show some subtle differences (Fig 1(a) vs. Fig. 4): the αTi + β + γTiAl three-phase region, the σ phase composition in the β + δ + σ three-phase region, the width of the γTiAl single-phase region, etc. Hellwig et al. [16] showed a Ti_3Al phase region in dashed lines near the Ti-rich corner (Fig. 1(a)), this phase should not exist in equilibrium according to the well-established binary Ti-Al phase diagram [43-48].

Perepezko's group reported a separate α phase island in the 1200°C isothermal sections (Fig. 1(b) and (c)). The location of this island changed significantly from their 1990 publication [31] to 1993 publication [24], Fig. 1(b) vs Fig. 1(c). We did not see indication of such an island.

The composition of the β phase in the β + σ + γTiAl three-phase region reported by Kaltenbach et al. [32], Fig. 1(d), is significantly different from our results and those of others. Figures 4 and 1(a) to (c) together indicate that this composition reported by Kaltenbach et al. may not be very reliable. The rest of their phase diagram is consistent with our results and these in the literature.

We included the 1150°C section from Chen et al. [21] in Fig. 1(e) for discussion related to the question of the γ_1 phase. They reported that this phase was stable up to 1400°C, thus it should exist at 1200°C as well. We employed EBSD to try to look for this phase. In the process, we input the three different kinds of lattice parameters of the γ_1 phase into our crystal structure database and allowed the EBSD system to match to any of these structures. No EBSD pattern matched any of the three crystal structures. Therefore, we did not see indication of this phase. Our results agree with those reported in Figs 1(a) to 1(d). Several EBSD patterns of the intermetallic compounds are shown in Fig. 5.

It seems that there were precipitate particles in certain regions of the σ (Nb_2Al) and δ (Nb_3Al) as shown in Fig. 3(d). We thought they might be the bct θ phase (space group: I41/amd, a = 0.5106 and c = 2.8168 nm) identified by Leonard et al. [12,13]. This phase is not stable at 1200°C, but exists as an equilibrium phase at lower temperatures. They can precipitate from both the σ and δ phases when the sample was cooled from 1200°C to room temperature. We were unable to get high quality EBSD patterns to confirm this phase, but the likelihood of this exists.

It can be seen that from only a corner of a diffusion multiple, we have mapped almost the entire isothermal section (except for the liquid Al phase region) of the Nb-Ti-Al system. The high efficiency of the diffusion multiple approach as compared to the individual alloys and diffusion couples is very apparent.

4. CONCLUSIONS

An isothermal section of the Nb-Ti-Al ternary system at 1200°C was obtained based on EPMA analysis from the Nb-Ti-$TiAl_3$ tri-junction region of a diffusion multiple annealed at 1200°C for 1000 hours. We employed the EBSD technique to look for the γ_1 phase which was reported in several previous investigations and disputed by others. We did not see indication of the γ_1 phase. We did not see indication of a second α phase region (island) reported by

4

Perepezko's group. Our 1200°C isothermal section agrees well with majority of the literature data at this temperature. Our results together with those reported by Hellwig et al. [16], Das et al. [24], Perepezko et al. [31] indicate that the composition of the β phase in the β + σ + γTiAl three-phase region reported by Kaltenbach et al. [32] may be very far off.

ACKNOWLEDGMENTS

REFERENCES

1. M.G. Mendiratta and D.M. Dimiduk, *Mat. Res. Soc. Symp. Proc.*, 133 (1989), 441- 446.
2. M.R. Jackson, B.P. Bewlay, R.G. Rowe, D.W. Skelly, and H.A. Lipsitt, *JOM*, 48 (1996), 39-44.
3. P.R. Subramanian, M.G. Mendiratta, and D.M. Dimiduk, *JOM*, 48 (1996), 33-38.
4. B.P. Bewlay, J.J. Lewandowski, and M.R. Jackson, *JOM*, 49 (1997), 44-45.
5. S.J. Balsone, B.P. Bewlay, M.R. Jackson, P.R. Subramanian, J.-C. Zhao, A. Chatterjee, and T. Heffernan, in *Structural Intermetallics 2001* (K. Hemker, D.M. Dimiduk, H. Clemens, R. Darolia, H. Inui, J.M. Larsen, V.K. Sikka, M. Thomas, and J.D. Whittenberger, eds.), TMS, Warrendale, PA, 2001, 99-108
6. B.P. Bewlay, M.R. Jackson, J.-C. Zhao, and P.R. Subramanian, *Metallurgical and Materials Transactions,* Accepted November 2002.
7. J.-C. Zhao, B.P. Bewlay, M.R. Jackson, and L.A. Peluso, in *Structural Intermetallics 2001* (K. Hemker, D.M. Dimiduk, H. Clemens, R. Darolia, H. Inui, J.M. Larsen, V.K. Sikka, M. Thomas, and J.D. Whittenberger, eds.), TMS, Warrendale, PA, 2001, 483-491.
8. B.P. Bewlay, R.R. Bishop, and M.R. Jackson, *Z. Metallkde.*, 90 (1999), 413-422.
9. J.-C. Zhao, B.P. Bewlay, and M.R. Jackson, *Intermetallics,* 9 (2001), 681-689.
10. Y. Yang, Y.A. Chang, J.-C. Zhao, and B.P. Bewlay, *Intermetallics,* Accepted November 2002.
11. C. Servant and I. Ansara, *CALPHAD,* 25 (2001), 509-525.
12. K.J. Leonard and V.K. Vasudevan, *Intermetallics,* 8 (2000), 1257-1268.
13. K.J. Leonard, J.C. Mishurda, B. Molloseau, M.D. Graef, and V.K. Vasudevan, *Phil. Mag. Lett.*, 80 (2000), 295-305.
14. K.J. Leonard, J.C. Mishurda, and V.K. Vasudevan, *Metall. Mater. Trans.*, 31B (2000), 1305-1321.
15. N. Saunders, in *Gamma Titanium Aluminides 1999* (Y.W. Kim, D.M. Dimiduk, and M.H. Loretto, eds.), TMS, Warrendale, PA, 1999, 183-188.
16. A. Hellwig, M. Palm, and G. Inden, *Intermetallics,* 6 (1998), 79-94.
17. M. Takeyama, Y. Ohmura, M. Kikuchi, and T. Matsuo, *Intermetallics,* 6 (1998) 643-646.
18. J.J. Ding and S.M. Hao, *Intermetallics,* 6 (1998), 329-334.
19. D. Banerjee, A.K. Gogia, T.K. Nandi, and V.A. Joshi, *Acta Metall.*, 36, (1998) 871.
20. T.J. Jewett, *Intermetallics,* 5 (1997), 157-159.
21. G.L. Chen, X.T. Wang, K.Q. Ni, S.M. Hao, J.X. Cao, J.J. Ding, and X. Zhang, *Intermetallics,* 4 (1996), 13-22.

22. K. Muraleedharan, T.K. Nandy, D. Banerjee, and S. Lele, *Intermetallics*, 3 (1995) 187-199.
23. F. Ebrahimi and B.J.G. DeAragao, *Mat. Res. Soc. Symp. Proc.*, 364 (1995), 1247-1269.
24. S. Das, T.J. Jewett, and J.H. Perepezko, in: *Structural Intermetallics*, (R. Darolia, J.J. Lewandowski, C.T. Liu, P.L. Martin, D.B. Miracle, M.V. Nathal, eds.), TMS, Warrendale, PA, 1993, 35-43.
25. U.R. Katter and W.J. Boettinger, *Mater. Sci. Eng.* A152 (1992), 9.
26. K. Muraleedharan, A.K. Gogia, T.K. Nandy, D. Banerjee, and S. Lele, *Metall. Trans.*, 23A (1992), 401-415.
27. K. Muraleedharan, T.K. Nandy, D. Banerjee, and S. Lele, *Metall. Trans.*, 23A (1992) 417-431.
28. T.P. Smirnova, A.M. Zakharov, S.V. Oleinikov, O.A. Filipyeva, *Izv. Vyssh. Uchebn. Zaved., Tsvetn. Metall.*, (1-2) (1992), 91-98.
29. A.V. Pavlov, A.M. Zakharov, G.V. Karsanov, and L.L. Vergasova, *Russ. Metall.*, (5) (1992), 117-119.
30. A.V. Pavlov, A.M. Zakharov, *Izv. Vyssh. Uchebn. Zaved., Tsvetn. Metall.*, (1-2) (1992), 98-104.
31. J.H. Perepezko, Y.A. Chang, L.E. Seitzman, J.C. Lin, N.R. Bond, R.J. Lwett, and J.C. Mishurda, in High Temperature Aluminides and Intermetallics (S.H. Wang et al., eds.), TMS, Warrendale, PA, 1990, 19.
32. K. Kaltenbach, S. Gama, D.G. Pinatti, K. Schulze, and E.-T. Henig, *Z. Metallkde.*, 80 (1989), 535-539.
33. A.M. Zakharov, G.V. Karsanov, B.S. Troitskii, and L.L. Vergasova, *Izv. Akad. Nauk. SSSR, Met.*, (1) (1984) 200-202.
34. B.S. Troitskii, A.M. Zakharov, G.V. Karsanov, and L.L. Vergasova, *Izv. Vyssh. Uchebn. Zaved., Tsvetn. Metall.*, (3) (1983), 77-80.
35. I.A. Popov and V.I. Rabezova, *Russ. J. Inorg. Chem.*, 7(2) (1962), 222-224.
36. J.-C. Zhao, *Adv. Eng. Mater.*, 3 (2001), 143-147.
37. J.-C. Zhao, *J. Mater. Res.*, 16 (2001), 1565-1578.
38. J.-C. Zhao, M.R. Jackson, L.A. Peluso, and L. Brewer, *MRS Bull.*, 27 (2002) 324-329.
39. J.-C. Zhao, M.R. Jackson, L.A. Peluso, and L. Brewer, *JOM*, 54 (7) (2002) 42-45.
40. H.J. Goldschmidt and J.A. Brand, *J. Less-Common Met.*, 3 (1961), 34-43.
41. L.A. Lysenko, V.Ya. Markiv, O.V. Tsybukh, and E.I. Gladyshevskii, *Inorg. Mater.*, 7(1) (1971), 157-159.
42. *Electron Backscatter Diffraction in Materials Science*, edited by A.J. Schwartz, M. Kumar, and B.L. Adams (Kluwer Academic / Plenum Publishers, New York, 2000).
43. J.H. Perepezko, Proc. *Intl. Symp. Intermetallic Compounds, Structure and Mechanical Properties*, (JIMIS-6), Sendai, Japan, 1991, 239-243.
44. U.R. Kattner, J.C. Lin, and Y.A. Chang, *Metall. Trans.* A23 (1992), 2081-2090.
45. C.D. Anderson, W.H. Hofmeister, R.J. Bayuzick, *Metall. Trans.* A24 (1993), 61-66.
46. P.J. Spencer, *Z. Metallkde.*, 87 (1996), 535-539.
47. H. Okamoto, *J. Phase Equil.*, 14 (1993), 120-121.
48. M.Palm, L.C. Zhang, F. Stein, and G. Sauthoff, *Intermetallics*, 10 (2002), 523 –540.
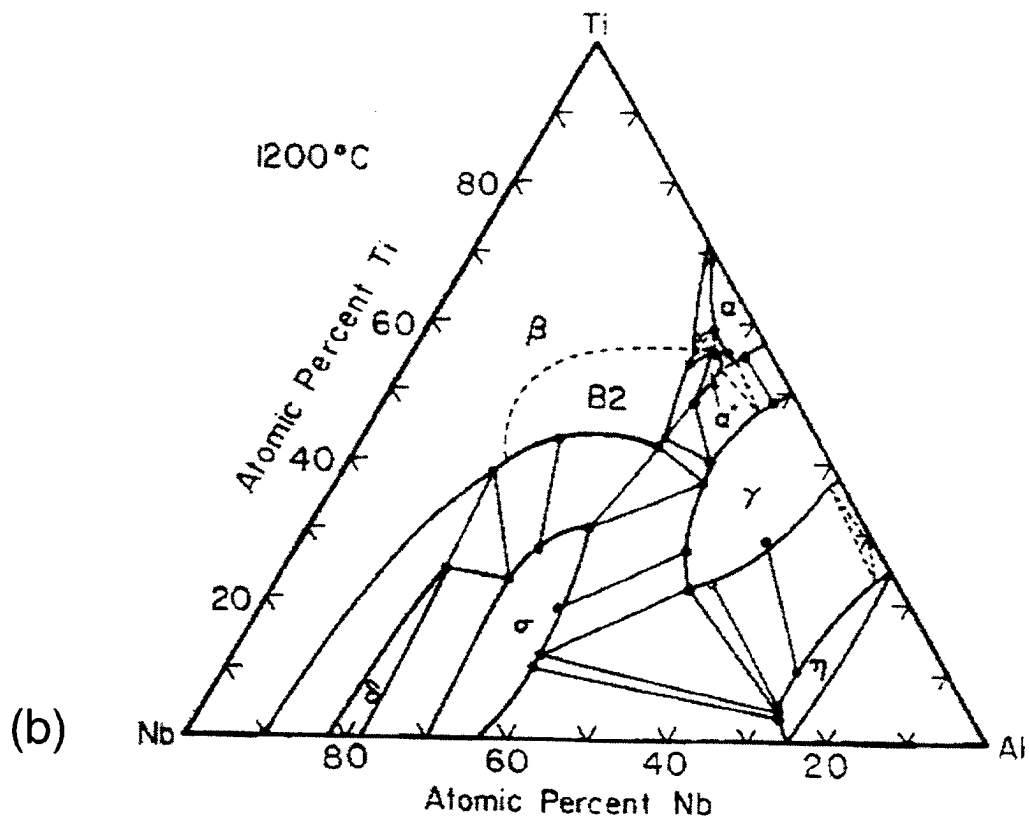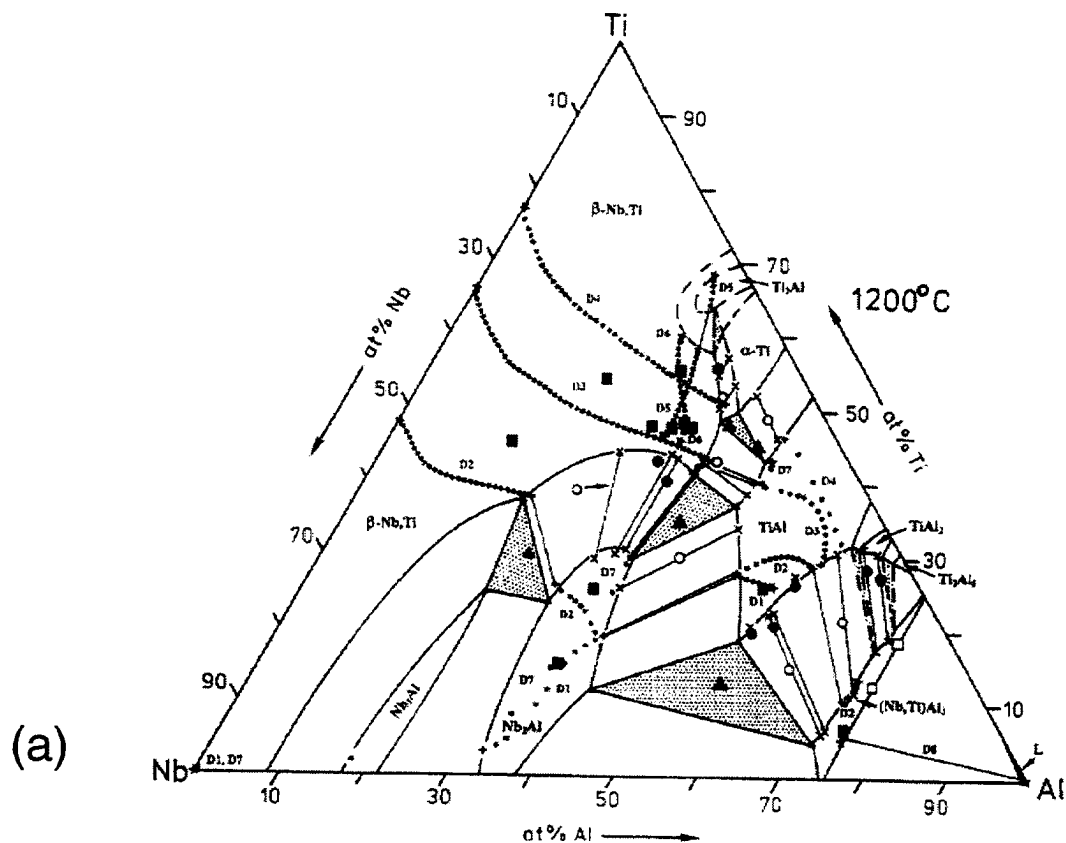
Figure 1. Several isothermal sections of the Ti-Nb-Al system at 1200 and 1150°C reported in the literature: (a) 1200°C section from Hellwig *et al.* [16], (b) 1200°C section from Das *et al.* [24], (c) 1200°C section from Perepezko *et al.* [31], (d) 1200°C section from Kaltenbach *et al.* [32], and (e) 1150°C section from Chen *et al.* [21]. It can be seen that significant discrepancy exists in the reported phase diagrams.
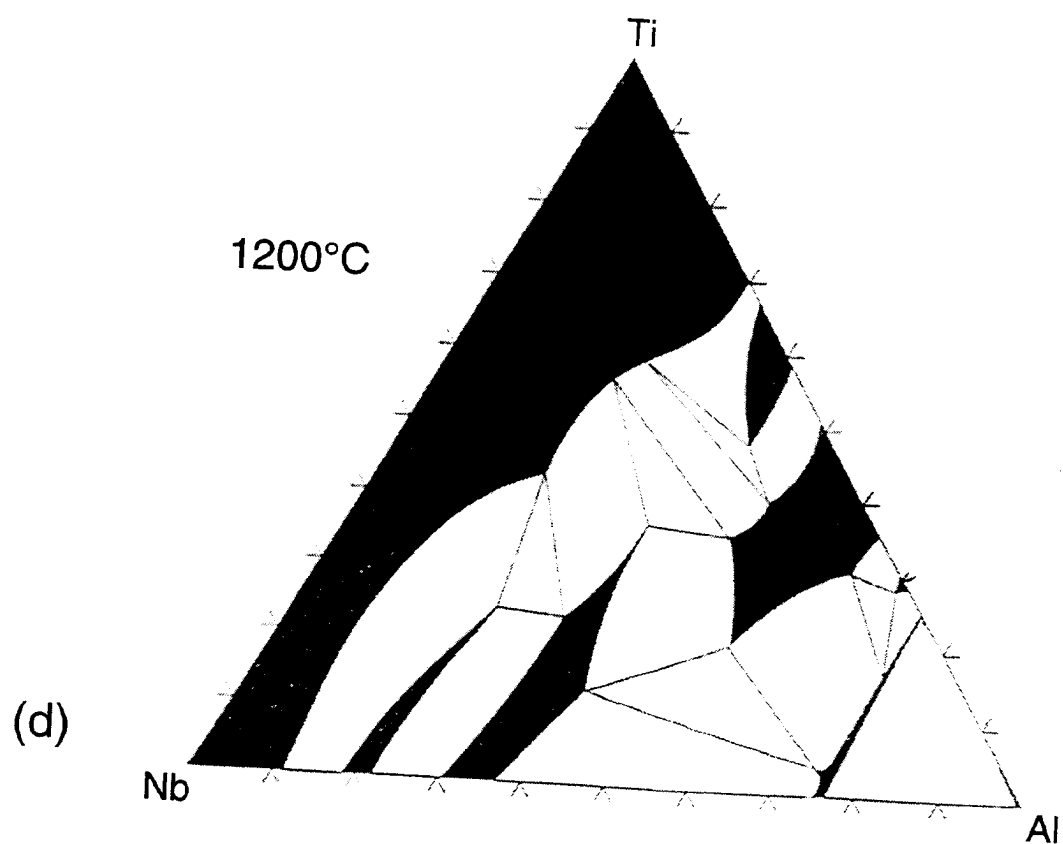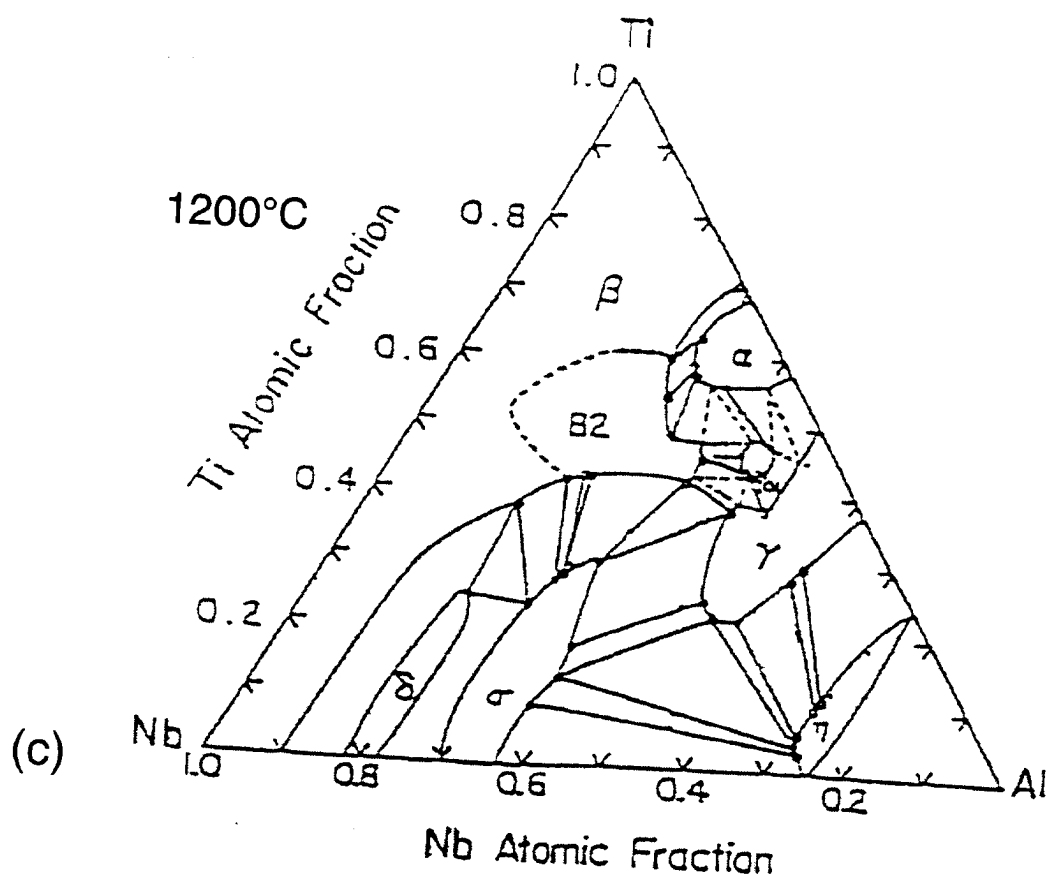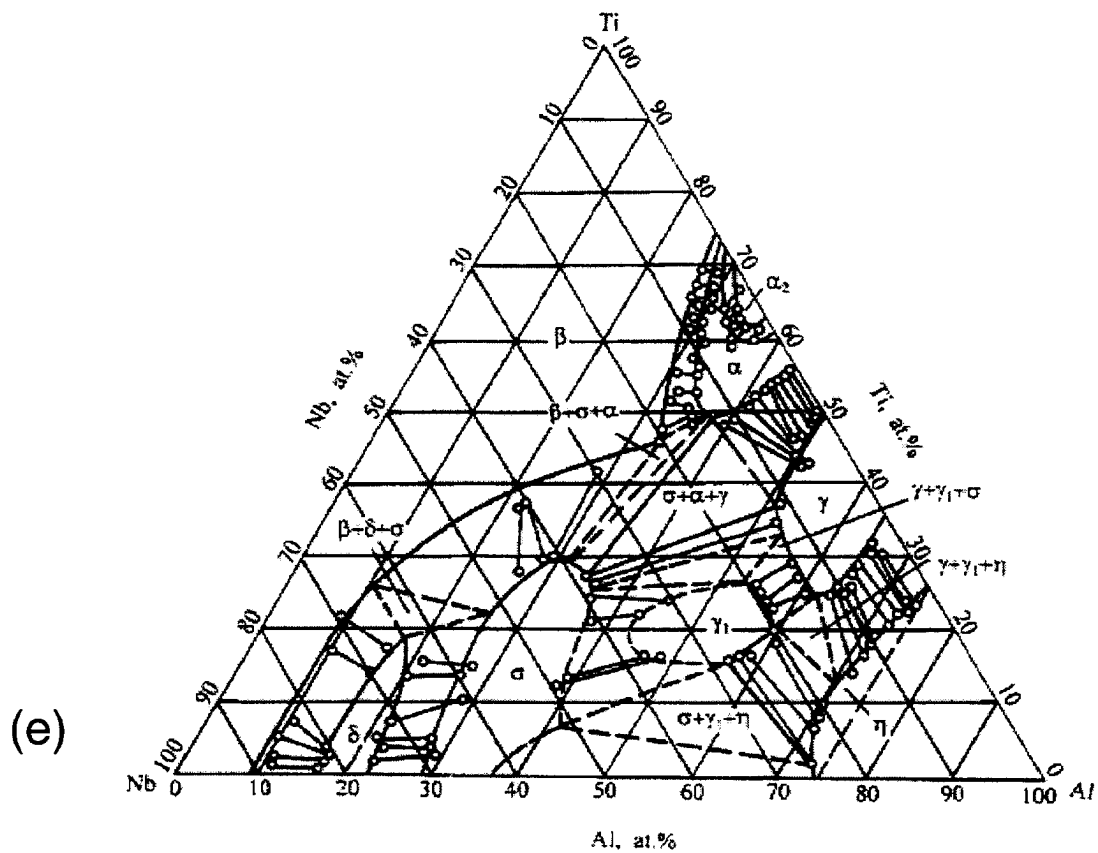
(c)

(d)

Figure 1. (Continued).

8

(e)

Figure 1. (Continued).
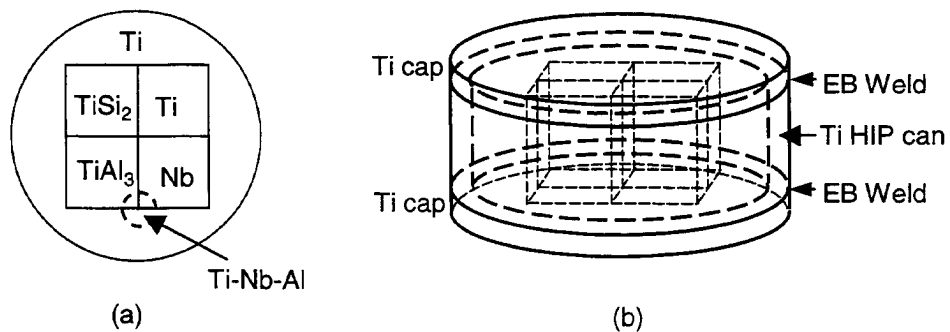
Figure 2. A diffusion multiple for efficient mapping of the Ti-Nb-Al ternary phase diagram: (a) cross-sectional view; and (b) perspective view. See text for the size of the sample. The results reported in this work were all obtained from the tri-junction corner of Ti – Nb – TiAl$_3$ circled in (a).
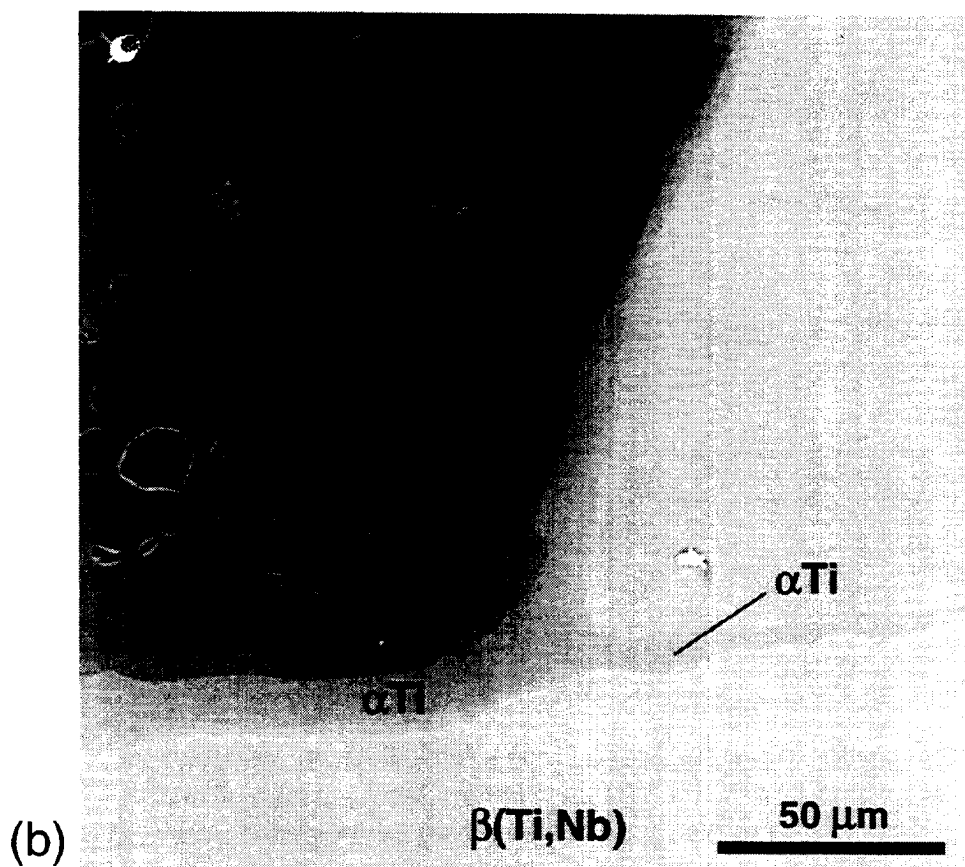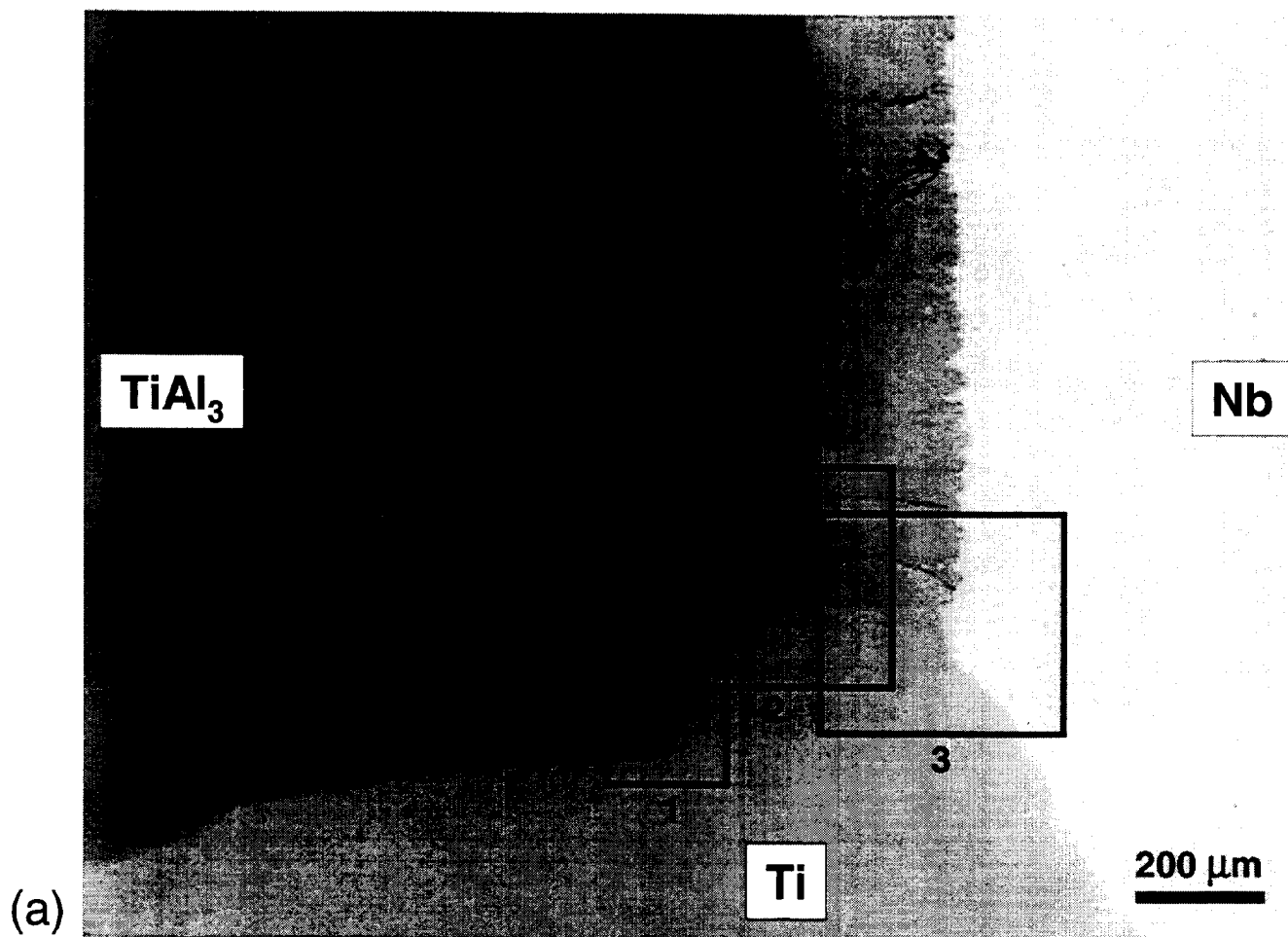
(a)

TiAl$_3$

Nb

Ti

200 μm

(b)

αTi

αTi

β(Ti,Nb)

50 μm

Figure 3. Continued with caption on next page

(c)

TiAl

β(Ti,Nb)

TiAl

αTi

100 μm

Nb₂Al (σ)

Nb₃Al (δ)
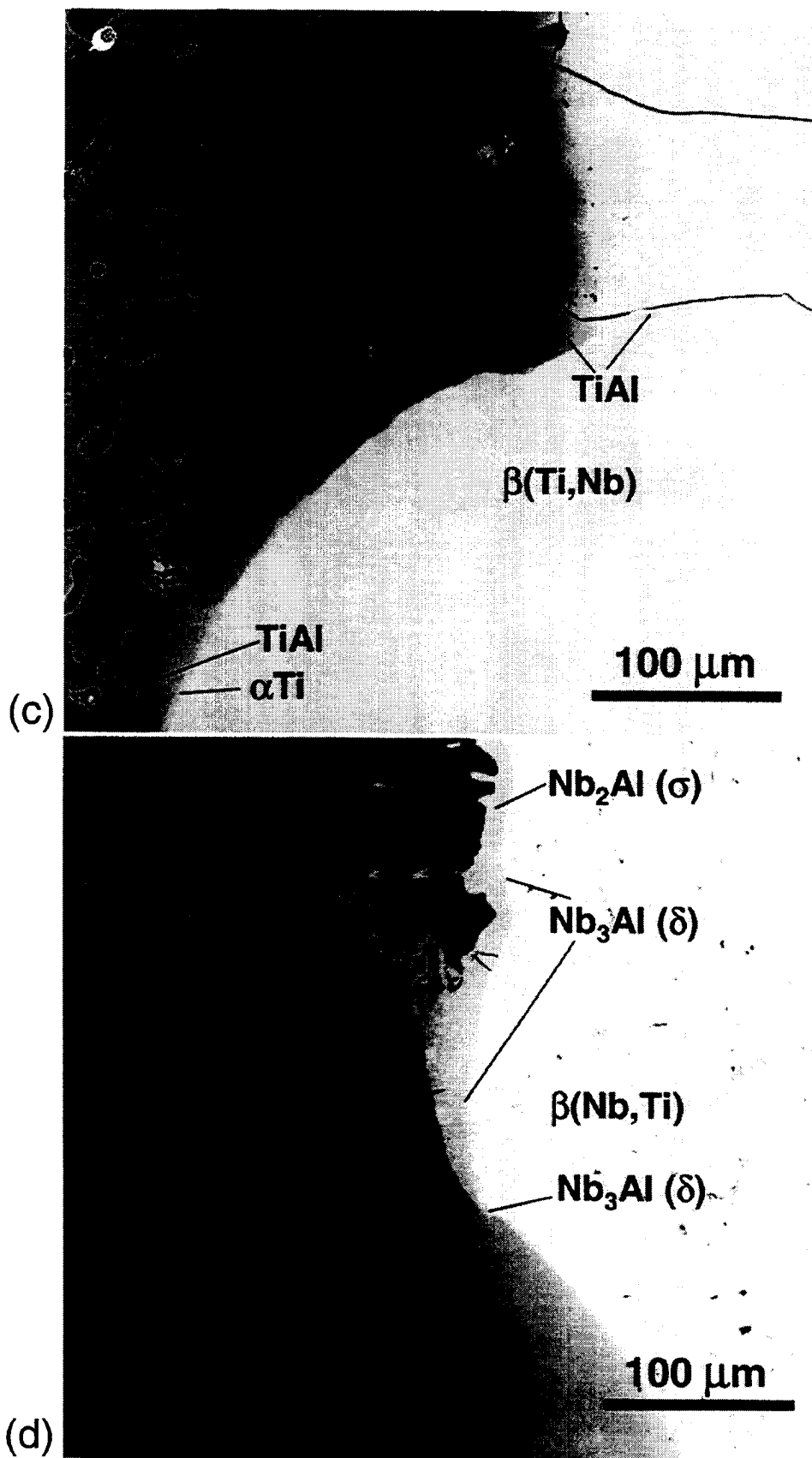
β(Nb,Ti)

Nb₃Al (δ)

100 μm

(d)

Figure 3. Backscatter electron SEM images of the Ti – Nb – TiAl₃ tri-junction area of the diffusion multiple (Fig. 2) annealed at 1200°C for 1000 hrs showing the formation of many different phases and intermetallic compounds: (a) a low-magnification image showing the overall tri-junction; (b) a high-magnification image of box 1 in (a); (c) a high-magnification image of box 2 in (a); and (d) a high-magnification image of box 3 in (a).
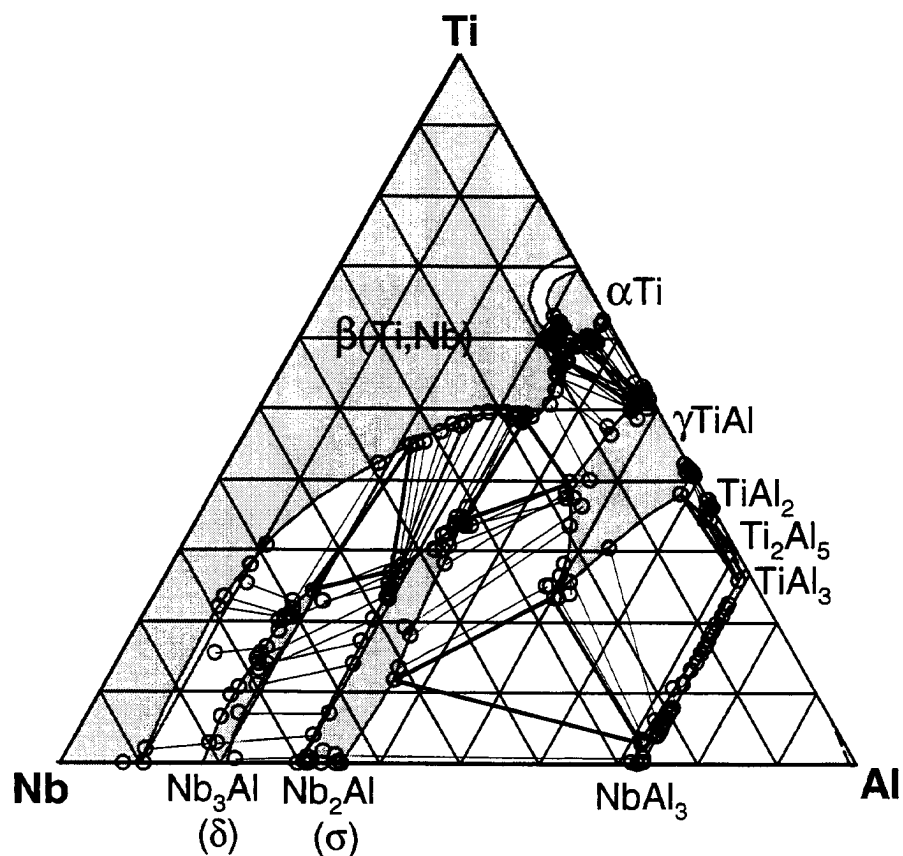
Figure 4. The 1200°C isothermal section of the Ti-Nb-Al system obtained from the Ti-Nb-TiAl₃ tri-junction area of the diffusion multiple (Fig. 2) annealed at 1200°C for 1000 hrs. The phase diagram is plotted in atomic percent axes with the numbers removed for simplicity. The solid triangle indicates well-defined three-phase triangles and the open circles show the tie-line compositions. The tie-lines are shown with light dotted lines.
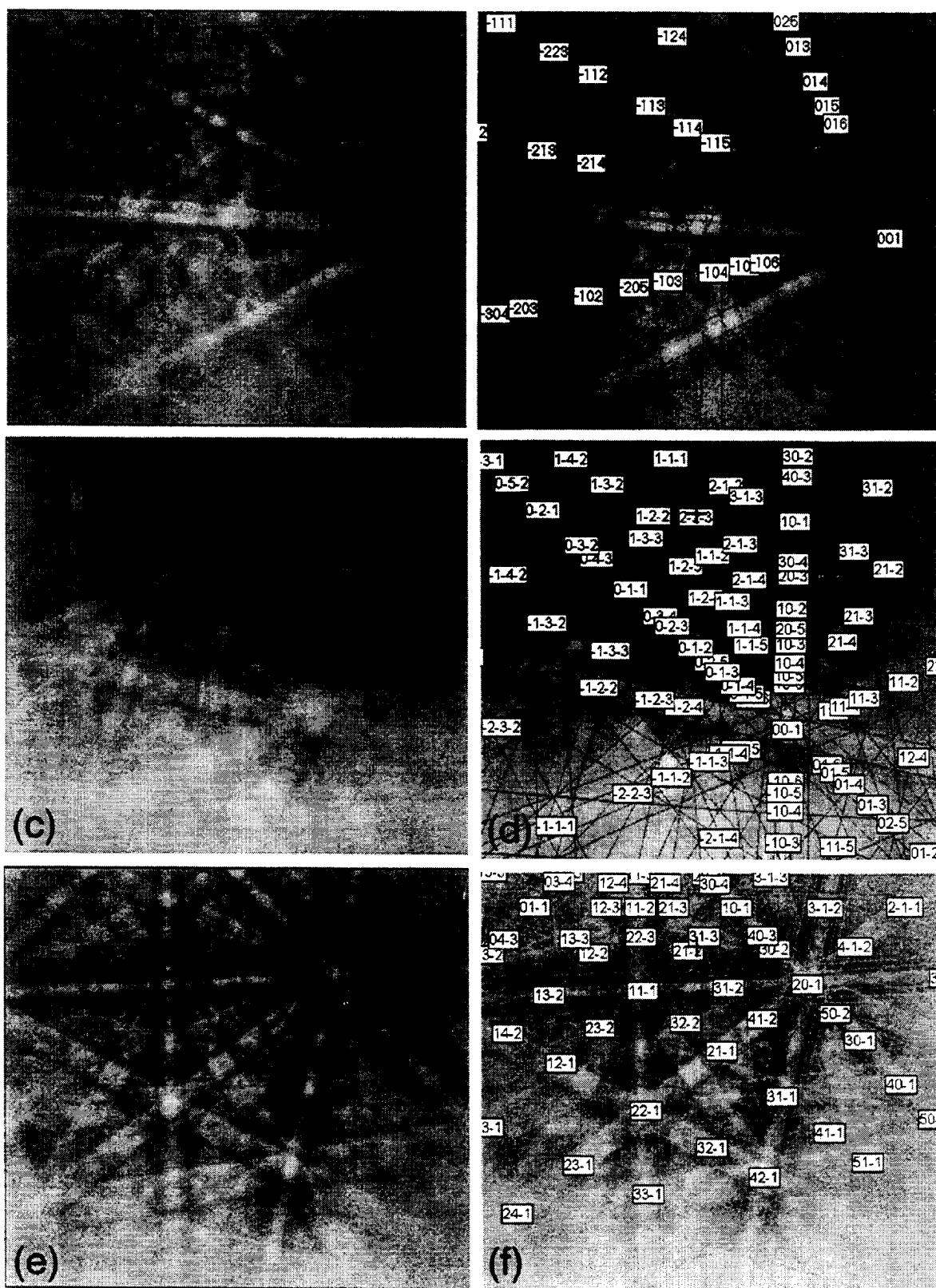
Figure 5. EBSD patterns of several intermetallic phases formed in the Nb-Ti-TiAl₃ tri-junction area of the diffusion multiple (Fig. 2) annealed at 1200°C for 1000 hrs: (a) and (b) for Nb_2Al (σ) phase; (c) and (d) for γ-TiAl; and (e) and (f) for $(Ti,Nb)Al_3$. The un-indexed patterns are shown on the left and the indexed patterns on the right.

14

Mapping of the Ti-Cr-Si Phase Diagram Using Diffusion Multiples

J.-C. Zhao, M.R. Jackson, and L.A. Peluso

Mapping of the Ti-Cr-Si Phase Diagram Using Diffusion Multiples

J.-C. Zhao, M.R. Jackson, and L.A. Peluso
General Electric Company
GE Global Research Center, P.O. Box 8, Schenectady, NY 12301, USA

ABSTRACT

A high-efficiency diffusion-multiple approach was employed to map the phase diagram of the Ti-Cr-Si ternary system which is critical for the design of niobium silicide-based composites. These composites have high potential as a replacement for Ni-base superalloys for jet engine applications. The formation of the Laves phase and alloying with Ti are critical for the high oxidation resistance of the composites and the Ti-Cr-Si system serves as the base for understanding the Laves phase formation and Ti alloying. The Ti-Cr-Si ternary system which contains up to 14 phases also serves as a model system to test the applicability of the diffusion multiple approach to such complex systems. Two isothermal sections at 1000 and 1200 °C were constructed from the results obtained from diffusion multiples using scanning electron microscopy (SEM), electron probe microanalysis (EPMA), and electron backscatter diffraction (EBSD). One ternary compound $(Cr,Ti)_6Si_5$ was observed at both temperatures, and the high-temperature $C14$-Laves phase of the Cr-Ti binary system was stabilized by Si to lower temperatures. The results compare well with literature data and some discrepancies are discussed.

Keywords: Ti-Cr-Si, diffusion multiple, Laves phase, silicide, phase diagram.

1. INTRODUCTION

Niobium silicide-based composites show great promise for applications as the next generation turbine airfoil materials with significantly higher operating temperatures than current generation advanced Ni-base superalloys [1-6]. The Nb-Si binary composites have excellent creep strength, but poor oxidation resistance and poor room temperature fracture toughness [1-2]. Alloying with Ti and Cr significantly improves the oxidation resistance. The potential application of these composites at very high temperatures requires a balance of high creep resistance, high oxidation resistance, and good low-temperature damage tolerance (fracture toughness). To achieve such a property balance, elements such as Cr, Ti, Hf and Al are added to the composites and significant progress has been made in improving the properties of the composites. Some of the alloying concepts were discussed by Zhao *et al.* [7]. The advanced design of the composites requires a fair understanding of the phase equilibria in the Nb-Si-Ti-Cr-Hf-Al system. Since a reasonable definition of the Nb-Hf-Si system has been achieved [8-10], our effort has been focused on the ternary systems Nb-Cr-Si, Nb-Si-Al, Nb-Cr-Al, Ti-Si-Cr, Ti-Si-Al, Ti-Cr-Al, Nb-Ti-Si, Nb-Ti-Cr, and Nb-Ti-Al. Other ternary systems related to this six-element system such as Nb-Ti-Hf, Nb-Cr-Hf, Nb-Hf-Al, Ti-Si-Hf, Ti-Cr-Hf, and Cr-Hf-Al have either good data or are less critical for the design of the Nb silicide composites. We will report the results of the Ti-Cr-Si system in the present paper and the results of other systems will be communicated separately.

In addition to the Nb silicide based composites, Ti_5Si_3 is also pursued as one of the candidate materials (based on its high melting point (2130 °C) and low density) for high-temperature applications with potential higher operating temperatures than those of Ni-base superalloys [11-13]. However, Ti_5Si_3 itself suffers from poor oxidation resistance. With the addition of chromium, its oxidation resistance can be improved. Theoretical calculations also showed that Cr additions to Ti_5Si_3 would enhance the bonding between atoms [14], which would improve mechanical properties of this compound. Thus, the Ti-Cr-Si phase diagram will also be very valuable for the design of Ti_5Si_3 based composites.

The high-efficiency "diffusion multiple" approach [15-18] is ideally suited for mapping phase diagrams of these ternary systems. It would take thousands of alloys to determine the above-mentioned ternary systems using the traditional one-alloy-at-a-time (equilibrated alloy) approach. For instance, it took Goldschmidt and Brand [19] about 220 alloys to map just the Nb-Cr-Si ternary system and similarly about 135 alloys were employed by Lysenko et al. [20] to determine the Ti-Cr-Si system. These alloys have very high melting temperatures and are difficult to make and to homogenize. Extra effort also needs to be taken to avoid interstitial (oxygen, nitrogen, carbon, etc.) contamination during alloy casting and heat treatment. In contrast, the diffusion multiple approach needs only a few cast alloys (no alloy for the Ti-Cr-Si system) and the samples are easy to make, and safe-guarding against the interstitial contamination can be very easily implemented as will be discussed later. The general diffusion multiple approach was discussed in detail previously [15-18] and has been successfully applied to many alloy systems.

For the ease of understanding the complex phase equilibria in the Ti-Cr-Si system, the constitutive binary phase diagrams of Cr-Si [21], Ti-Cr [22] and Ti-Si [22] are briefly discussed here. The crystal structures of the phases in the binary and the ternary system are listed in Table 1 [23].

Table 1. Crystal structure of phases in the Ti-Cr-Si ternary system [23].

System	Pearson Symbol	Space Group	Lattice Parameters			
			a	b	c	γ
αTi	$hP2$	P63/mmc	0.29512		0.46845	120°
βTi	$cI2$	Im$\underline{3}$m	0.33066			
Cr	$cI2$	Im$\underline{3}$m	0.28847			
Si	$cF8$	Fd$\underline{3}$m	0.54309			
Cr_3Si	$cP8$	Pm$\underline{3}$n	0.4555			
βCr_5Si_3	$hP16$	P6$_3$/mcm				120°
αCr_5Si_3	$tI38$	I4/mcm	0.9150		0.4639	
CrSi	$cP8$	P2$_1$3	0.4622			
$CrSi_2$	$hP9$	P6$_2$22	0.4430		0.6365	120°
αCr_2Ti	$cF24$	Fd$\underline{3}$m	0.691			
βCr_2Ti	$hP12$	P6$_3$/mmc	0.4932		0.8005	120°
γCr_2Ti	$hP24$	P6$_3$/mmc	0.4932		1.601	120°
TiSi	$oP8$	Pnma	0.6544	0.3638	0.4997	
Ti_3Si	$tP32$	P4$_2$/n	1.039		0.517	
$TiSi_2$	$oF24$	Fddd	0.82671	0.48000	0.85505	
Ti_5Si_3	$hP16$	P6$_3$/mcm	0.74610		0.51508	120°
Ti_5Si_4	$tP36$	P4$_1$2$_1$2	0.6702		1.2174	
$(Cr,Ti)_6Si_5$	$oI44$	Ibam	1.6054	0.7579	0.4915	

The Cr-Si phase diagram was well assessed by Gokhale, et al. [21] and it has four intermetallic compounds: Cr_3Si, Cr_5Si_3, $CrSi$, and $CrSi_2$. The Cr_5Si_3 phase undergoes a polymorphic transformation at 1505 °C with tetragonal structure at low temperature. Although the high-temperature crystal structure of βCr_5Si_3 has not been determined, it was assumed to be the same crystal structure as Ti_5Si_3 [24].

The Ti-Cr binary system has three Cr_2Ti-based Laves phases: the low-temperature cubic $C15$ ($cF24$) which is stable at temperatures < 1220 °C, the intermediate-temperature dihexagonal $C36$ ($hP24$) stable between 800-1270 °C, and the high-temperature hexagonal $C14$ ($hP12$) stable at temperatures > 1270 °C [22, 25,26]. The effect of Si on the stabilization of these Laves phases can be appreciated by studying the Ti-Cr-Si system.

The Ti-Si binary system [22] has five intermetallic compounds, Ti_3Si, Ti_5Si_3, Ti_5Si_4, $TiSi$, and $TiSi_2$. A thermodynamic assessment of this system was done by Seifert et al. [27].

A 1000°C isothermal section of the Ti-Cr-Si system was constructed by Lysenko et al. [20] based on 135 alloys annealed at 1000 °C for 650 to 1200 hours (depending on the alloys), and is shown in Fig. 1. The Ti_5Si_4 phase which is an equilibrium phase for the binary Ti-Si system was missing from the phase diagram reported by Lysenko et al. due to the fact that no alloys were made around the Ti_5Si_4 composition. Du et al. [28] re-determined the 1000°C isothermal section of the ternary system using 35 additional alloys. They arc melted these alloys and annealed them at 1000°C and 800°C for 505 and 1056 hours respectively. X-ray diffraction (XRD) and differential thermal analysis (DTA) were performed on these annealed alloys. They found essentially no change in the DTA signals from these two different heat treatments for all these alloys except one alloy ($Cr_{50}Ti_5Si_{45}$) for which they reported that equilibrium was not reached after 1056 hours annealing at 800°C. The phases determined from XRD from these two different heat treatments were also the same for all the alloys except for two ($Cr_{50}Ti_5Si_{45}$ and $Cr_{40}Ti_5Si_{55}$). Du et al. [28] did find the equilibrium Ti_5Si_4 phase. The results of Du et al. were essentially similar to those of Lysenko et al. Both their results will be discussed in this paper in detail later.

2. EXPERIMENTAL METHOD

A diffusion multiple with the cross-section view shown schematically in the Fig. 2(a) was made. The inner and outer circle diameters were 15.6 and 25.4 mm respectively to guarantee that the dimensions of the pure element pieces are much larger than the diffusion distance, thus there will be pure elements left after the long term diffusion anneal. High purity Nb, Cr, Si and Ti were machined into the proper shapes (quarter pies and round shells, Fig. 2(a)) by electro-discharge machining (EDM). The re-cast layer on the EDM'ed surfaces was removed by mechanical grinding to make clean surfaces. The pieces were ultrasonically cleaned in methanol and then assembled into the geometry shown in Fig. 2(a). The height of all pieces was 25 mm. The assembled diffusion multiples were then loaded into hot isostatic press (HIP) cans made of commercial purity Ti, which is schematically shown in Fig. 2(b). A 25 μm layer of Ta was placed between the diffusion multiples and the HIP cans to isolate any interstitial contaminants that may diffuse into the HIP can from the quartz capsule during long term annealing. The top and bottom caps of the HIP can were electron beam welded. HIPing was performed at 1204 °C, 200MPa for 4 hrs. The HIP cans containing the diffusion multiples were then encapsulated in evacuated quartz tubes backfilled with pure argon. Since both Nb and Ti are susceptible to oxygen and nitrogen contamination, it is critical to keep the diffusion multiples from interstitial elements. To further absorb any oxygen that may diffuse into the quartz tube, a packet of pure yttrium was wrapped in

Ta foils and was then placed inside each quartz tube. Thus, the diffusion multiples were protected from the intersitials (O, N, C, etc.) by the quartz tube, the pure yttrium absorber, the Ti HIP can, and the Ta diffusion barrier. The encapsulated samples were then annealed at two different temperatures (1200°C for 1000 hrs and 1000 °C for 4000 hrs). Two identical diffusion multiples were made and each was annealed at one temperature. After the heat treatment, the diffusion multiples were taken from the argon furnace and cooled down to ambient temperature by breaking the quartz tube and quenching the diffusion multiples into water. The diffusion multiples were then cut into halves parallel to the ends using wire EDM, ground and polished.

The samples were first examined using scanning electron microscopy (SEM), especially the backscatter electron (BSE) imaging. Most phases could be seen (although not identified explicitly) in the BSE images due to the differences in their average atomic weight. Quantitative EPMA analysis was performed on a CAMECA (Paris, France) microprobe using 15 kV voltage, 40 nA current and a 40° take-off angle. Electron backscatter diffraction (EBSD) analysis was performed to obtain crystal structure information of the phases formed in the diffusion multiple. Phase identification was accomplished by a direct match of the diffraction bands in the experimental backscatter pattern with simulated patterns generated using known structure types and lattice parameters. A detailed discussion on this powerful EBSD technique can be found in Schwartz et al. [29].

3. RESULTS AND DISCUSSION

A backscatter electron image taken from the Ti-Cr-Si tri-junction (schematically circled area in Fig. 2(a)) of the diffusion multiple annealed at 1200 °C for 1000 hrs is shown in Fig. 3. During the long-term diffusion treatment, extensive interdiffusion among Ti, Cr and Si took place, and all the equilibrium phases, including the intermetallic phases, formed by interdiffusion reactions. By performing EPMA analysis in this tri-junction area, an extremely large amount of phase equilibrium information was obtained and the 1200°C isothermal section of the Ti-Cr-Si system was constructed as shown in Fig. 4. We have defined most of the important tie-triangles (three-phase equilibria) and additional three-phase equilibria were estimated. We did not obtain some of tie-triangles due to cracking of brittle phases during sample cutting, grinding and polishing. The tie-lines are defined from the EPMA line profiles by taking advantage of the local equilibrium at interfaces formed among the phases. Details of the methodology can be found elsewhere [15-18].

The 1000°C isothermal section was also constructed from EPMA analyses of the diffusion multiple annealed at 1000°C for 4000 hours, as shown in Fig. 5. The major differences between this one and the 1200°C isothermal section are the solubilities of the elements in several phases. For instance, the solubility of Cr in the $(Ti,Cr)_5Si_3$ phase reduced from ~45 at.% (all compositions are discussed in atomic percent throughout this paper) to ~30% as temperature changed from 1200°C to 1000°C. Similarly, the solubility of Ti in the $(Cr,Ti)_5Si_3$ phase reduced from ~8% to ~5%; the solubility of Ti in $(Cr,Ti)_3Si$ reduced from ~12% to ~3%; the solubility of Si in the Laves phase reduced from ~20% to ~10%. The solubility of Si in Ti-based bcc solid-solution also changed appreciably as temperature changed from 1200°C to 1000°C. This may induce precipitation hardening of $(Ti,Cr)_5Si_3$ in the bcc phase. There is very little change of the stability (composition) range of the $(Cr,Ti)_6Si_5$ phase from 1200°C to 1000°C.

The main features of the phase diagrams obtained by Lysenko et al. [20], Fig. 1, and Du et al. [28] were confirmed from our experimental observations. These common features include the existence of $(Cr,Ti)_6Si_5$ and its composition range as well as most of the three-phase equilibria.

4

Some differences were observed: the solubility of Cr in the $(Ti,Cr)_5Si_3$ phase was ~30% at 1000°C which is quite different from ~45% reported by Lysenko et al. and Du et al. [28] at 1000°C. Their result was very close to our 1200°C data. Our result showed the solubility of Ti in the $(Cr,Ti)_3Si$ phase ~5% at 1000°C, their result was ~20% (Our result even at 1200°C is only ~12%). The solubility of Si in the Laves phase was ~10% at 1000°C based on our experimental result, while they reported ~20% (Our result at 1200°C was ~20%). Overall, their 1000°C isothermal sections, especially the one Du et al. reported (modified from Lysenko et al.) are very much like our 1200°C isothermal section.

It is very likely that many of the alloys, especially the Cr and Ti rich alloys with very high melting points, used by Lysenko et al. and Du et al. had not reached equilibrium after only 505 to 1200 hours anneal at 1000°C. Many of the high-melting alloys, such as Nb-Ti-Si alloys studied by Bewlay et al. [8, 30] and Nb-Hf-Si alloys studied by Zhao et al. [9] possess very slow kinetics, and they would not be at equilibrium after being annealed at 1000 °C for only 1200 hours. For instance, even after annealed at 1500°C for 100 hours, several Nb-Hf-Si alloys still had not reached full equilibrium [9]. It is very likely that the Cr and Ti rich Ti-Cr-Si alloys would possess similar slow kinetics as well, thus difficult to reach full equilibrium. This argument is supported by the following observations. Firstly, the single-phase region of the Laves phase sat at 40% Ti all the way to Ti-Cr binary in the phase diagram reported by Lysenko et al. (Fig. 1), which conflicts with established binary Ti-Cr phase diagram. Villars et al. [31] modified it to 35% in their ternary phase diagram handbook. Du et al. [28] did similar modification. The reason Lysenko et al. observed single phase Laves at 40% Ti might well be due to fact that the primary solidification Laves did not decompose into the equilibrium phases, thus these alloys did not reach equilibrium. Secondly, the fact the 1000°C isothermal sections by Lysenko et al. and Du et al., especially the one Du et al. reported (modified from Lysenko et al.) are very much like our 1200°C isothermal section indicates that solubility of some of phases can be very high (e.g. 45% Cr in $(Ti,Cr)_5Si_3$) at high temperature and especially from solidification. If the decomposition process did not complete due to slow kinetics, then they would show artificially high solubilities in the 1000°C isothermal sections. The likelihood of reaching equilibrium at phase interfaces is much higher in our case since we annealed the diffusion multiple at 1000°C for 4000 hours.

We argue that the diffusion multiples make it easier to form equilibrium phases especially for alloys with very sluggish decomposition kinetics. This is somewhat counter-intuitive: one would think that the equilibrated alloy method (melting, casting and heat treatment of individual alloys) is the ultimate "gold-standard" for equilibrium. However, since it involves the process of solidification and heat treatment, true equilibrium can be difficult to reach if the solid-state decomposition process is sluggish for some of the phases (as in the case of several Nb-base systems). In the diffusion multiples, there is no such problem since all the phases form by diffusion reactions at the temperature of interest (heat treatment). The phases formed should all be equilibrium phases and local equilibrium at the phase interface would give the equilibrium phase diagram. The diffusion multiple approach is not fool-proof either: in rare occasions one of the phases did not form by interdiffusion reactions. The exact reason for this is still not well understood. However, for phases with narrow stoichiometry surrounded by phases with broad stoichiometry and higher diffusivity, the phases with narrow stoichiometry may be reduced to interfacial phases (near zero thickness) for lower temperatures. Fortunately, all these instances occurred at temperatures below half of the homologous melting points. Even though the occurrence was very rare, one should always be watchful for the possibility of missing phases (especially at low temperatures) when using diffusion couples and diffusion multiples in mapping phase diagrams. In the case of Ti-Cr-Si, we are very confident that the phase diagrams (Figs. 4 and 5) we obtained are equilibrium ones since all the binary phases appeared and all the

confirmed ternary compounds were observed. It is always a good check to see whether all the binary phases and reported ternary phases appear.

As mentioned earlier, Cr_2Ti shows three types of crystal structures, cubic $C15$, hexagonal $C14$ and dihexagonal $C36$. Only $C36$ in Cr-Ti binary system and $C14$ stabilized by Si were observed in EMPA data. Unfortunately, EBSD cannot differentiate C14 from C36. The crystal structures of the Laves phases in Figs. 4 and 5, thus are our guesses based on information from the binary Ti-Cr phase diagram.

We observed the Ti_5Si_4 phase and also reasonable solubility of Cr up to ~7% (at 1000°C). Lysenko *et al.* completely missed this phase and Du *et al.* did not observe the solubility since only two alloys were prepared in the area which were not enough to find the solubility (unless EPMA was used – they did not perform EPMA analysis).

It is interesting to compare the Ti-Cr-Si system to Nb-Cr-Si [32]. The ternary $hP9$ CrNbSi compound exists in the Nb-Cr-Si system, but its analog (CrTiSi) does not exist in the Ti-Cr-Si system. Also, the $(Cr,Nb)_{11}Si_8$ phase appears in the Nb-Cr-Si, but its analog does not exist in the Ti-Cr-Si system. Both systems have the $(Cr,Ti,Nb)_6Si_5$ phase. Depending on the solubility of Ti in the NbCrSi, Ti additions to the Nb silicide based composites may de-stabilize this phase. The quaternary information obtained from the quadri-junction, the center of Fig. 2(a) where four elements met, of the diffusion multiple may provide critical data.

The phase equilibrium information of the Ti-Cr-Si system is very useful for the design of both Nb silicide composites and coatings for these composites. It is also very useful for design of Ti_5Si_3–based alloys. The phase diagrams show large flexibility of alloying Ti_5Si_3 with Cr, and can be used to predict the phases that will form in the Cr-added Ti_5Si_3 alloys. The Ti-Cr-Si system is one of the key systems for which we are performing CALPHAD modeling and will add the data into the developing thermodynamic database for Nb silicide based systems [10,33,34]. Our data provide good input to the thermodynamic modeling.

4. CONCLUSIONS

The results of this work clearly demonstrate the power and the high-efficiency of the diffusion-multiple approach to map phase diagrams of systems as complex as the Ti-Cr-Si ternary which contains 14 phases, including one ternary compound, $(Cr,Ti)_6Si_5$. Two isothermal sections at 1000 and 1200 °C were constructed from the results obtained from two diffusion multiples using scanning electron microscopy (SEM) and electron probe microanalysis (EPMA). The results were compared to the literature data and similarities and differences discussed.

ACKNOWLEDGMENTS

REFERENCES

1. M.G. Mendiratta and D.M. Dimiduk, *Mat. Res. Soc. Symp. Proc.*, 133 (1989), 441- 446.
2. M.R. Jackson, B.P. Bewlay, R.G. Rowe, D.W. Skelly, and H.A. Lipsitt, *JOM*, 48 (1996), 39-44.
3. P.R. Subramanian, M.G. Mendiratta, and D.M. Dimiduk, *JOM*, 48 (1996), 33-38.
4. B.P. Bewlay, J.J. Lewandowski, and M.R. Jackson, *JOM*, 49 (1997), 44-45.
5. S.J. Balsone, B.P. Bewlay, M.R. Jackson, P.R. Subramanian, J.-C. Zhao, A. Chatterjee, and T. Heffernan, in *Structural Intermetallics 2001* (K. Hemker, D.M. Dimiduk, H. Clemens, R. Darolia, H. Inui, J.M. Larsen, V.K. Sikka, M. Thomas, and J.D. Whittenberger, eds.), TMS, Warrendale, PA, 2001, 99-108
6. B.P. Bewlay, M.R. Jackson, J.-C. Zhao, and P.R. Subramanian, *Metallurgical and Materials Transactions,* Accepted November 2002.
7. J.-C. Zhao, B.P. Bewlay, M.R. Jackson, and L.A. Peluso, in *Structural Intermetallics 2001* (K. Hemker, D.M. Dimiduk, H. Clemens, R. Darolia, H. Inui, J.M. Larsen, V.K. Sikka, M. Thomas, and J.D. Whittenberger, eds.), TMS, Warrendale, PA, 2001, 483-491.
8. B.P. Bewlay, R.R. Bishop, and M.R. Jackson, *Z. Metallkde.*, 90 (1999), 413-422.
9. J.-C. Zhao, B.P. Bewlay, and M.R. Jackson, *Intermetallics*, 9 (2001), 681-689.
10. Y. Yang, Y.A. Chang, J.-C. Zhao, and B.P. Bewlay, *Intermetallics,* Accepted November 2002.
11. L. Zhang and J. Wu, *Acta Mater.*, 46 (1998), 3535-3546.
12. M. Yamaguchi, H. Inui and K. Ito, *Acta Mater.*, 48 (2000), 307-322.
13. J.J. Petrovic, A.K. Vasudevan, *Mate. Sci. Eng.*, A261 (1999), 1-5.
14. L.T. Zhang, Ph.D. Dissertation, Shanghai Jiao Tong University (China), 1997.
15. J.-C. Zhao, *Adv. Eng. Mater.*, 3 (2001), 143-147.
16. J.-C. Zhao, *J. Mater. Res.*, 16 (2001), 1565-1578.
17. J.-C. Zhao, M.R. Jackson, L.A. Peluso, and L. Brewer, *MRS Bulletin*, 27 (2002) 324-329.
18. J.-C. Zhao, M.R. Jackson, L.A. Peluso, and L. Brewer, *JOM*, 54 (7) (2002) 42-45.
19. H.J. Goldschmidt and J.A. Brand, *J. Less-Common Met.*, 3 (1961), 34-43.
20. L.A. Lysenko, V.Ya. Markiv, O.V. Tsybukh, and E.I. Gladyshevskii, *Inorganic Mater.,* 7(1) (1971), 157-159.
21. A.B. Gokhale and G.J. Abbaschian: in *Binary Alloy Phase Diagrams*, 2nd ed., T.B. Massalski, ed., ASM International, Materials Park, OH, 1990.
22. J.L. Murray: in *Binary Alloy Phase Diagrams*, 2nd ed., T.B. Massalski, ed., ASM International, Materials Park, OH, 1990.
23. P. Villars and L.D. Calvert, *Pearson's Handbook of Crystallographic Data for Intermetallic Phases*, 2nd ed., ASM International, Materials Park, OH, 1991.
24. Y. Du, J.C. Schuster, L. Perring, *J. Am. Ceram. Soc.*, 83 (2000), 2067-2073.
25. W. Zhuang, J. Shen, Y. Liu, L. Ling, S. Shang, Y. Du, and J.C. Schuster, *Z. Metallkd.*, 91 (2000), 121-127.
26. K.C. Chen, S.M. Allen, and J.D. Livingston, *Mat. Res. Soc. Symp. Proc.*, 364 (1995), 1401.
27. H.J. Seifert, H.L. Lukas and G. Petzow, *Z. Metallkde.*, 87 (1996), 2-13.
28. Y. Du and J.C. Schuster, *Scand. J. Metall.,* 31 (2002), 25-33.
29. *Electron Backscatter Diffraction in Materials Science*, edited by A.J. Schwartz, M. Kumar, and B.L. Adams (Kluwer Academic / Plenum Publishers, New York, 2000).
30. B.P. Bewlay, M.R. Jackson, and R.R. Bishop, *J. Phase Equilibria*, 19 (1998), 577-586.
31. P. Villars, A. Prince, and H. Okamoto, Handbook of Ternary Alloy Phase Diagrams, ASM International, Materials Park, OH, 1995.
32. J.-C. Zhao, M.R. Jackson, and L.A. Peluso, to be published.
33. H. Liang and Y.A.Chang, *Intermetallics*, 7 (1999) 561.
34. Y. Yang and Y.A. Chang (University of Wisconsin – Madison), private communication, 2002.
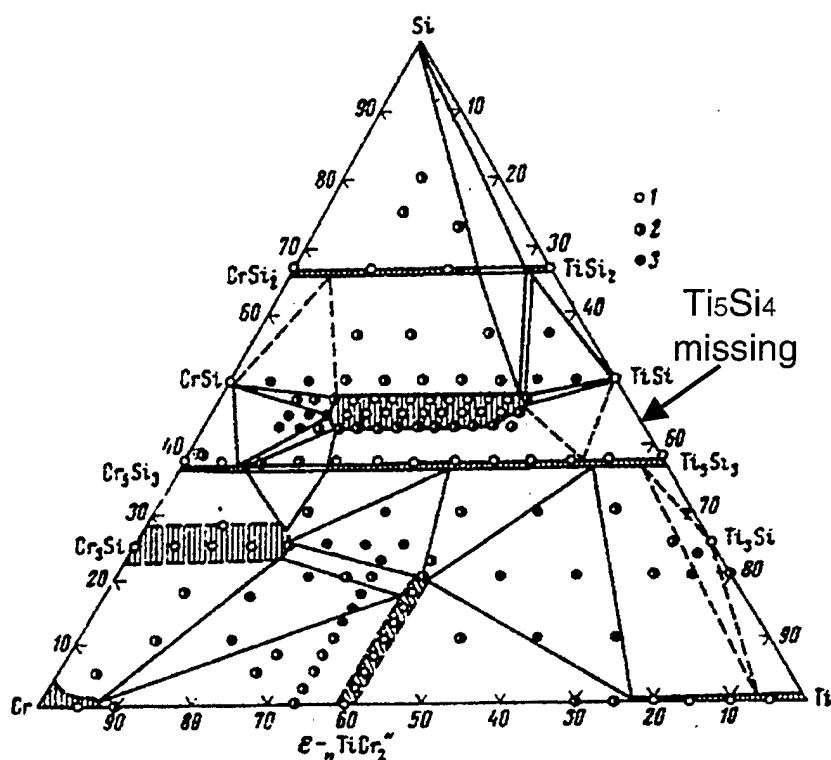
Figure 1. Isothermal section of the Ti-Cr-Si system at 1000°C constructed by Lysenko *et al.* [20] based on 135 alloys annealed at 1000°C for 650 to 1200 hours. The open circles represent single phase regions, half-filled circles denote 2-phase regions, and filled circles (dots) refer to 3-phase regions. Note the Ti_5Si_4 equilibrium phase was missing in the phase diagram. The Cr and Ti rich alloys may not have reached equilibrium as will be discussed later.
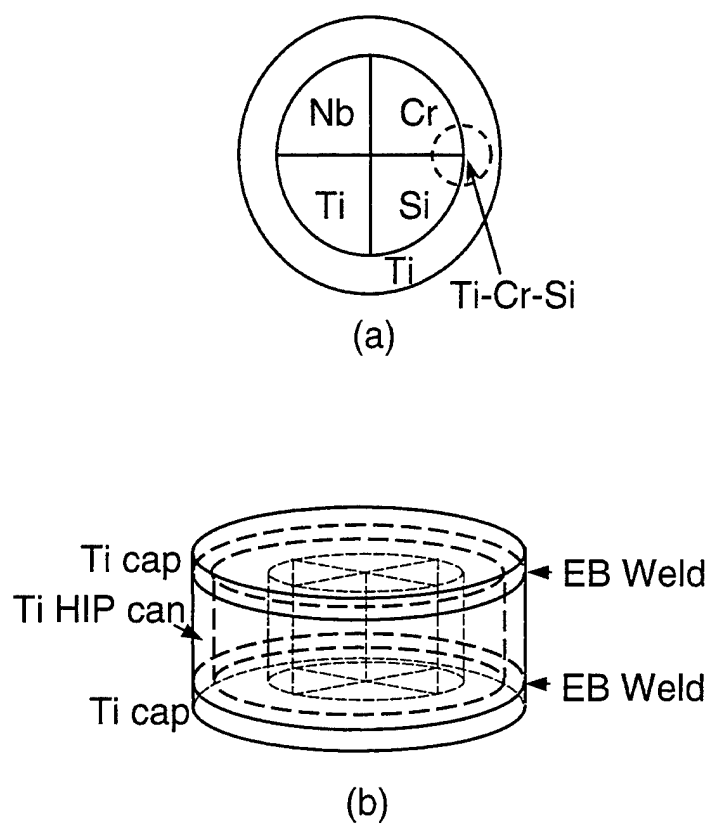
Figure 2. Diffusion multiples for efficient mapping of the Ti-Cr-Si ternary phase diagrams: (a) cross-sectional view; and (b) perspective view. See text for the size of the sample.
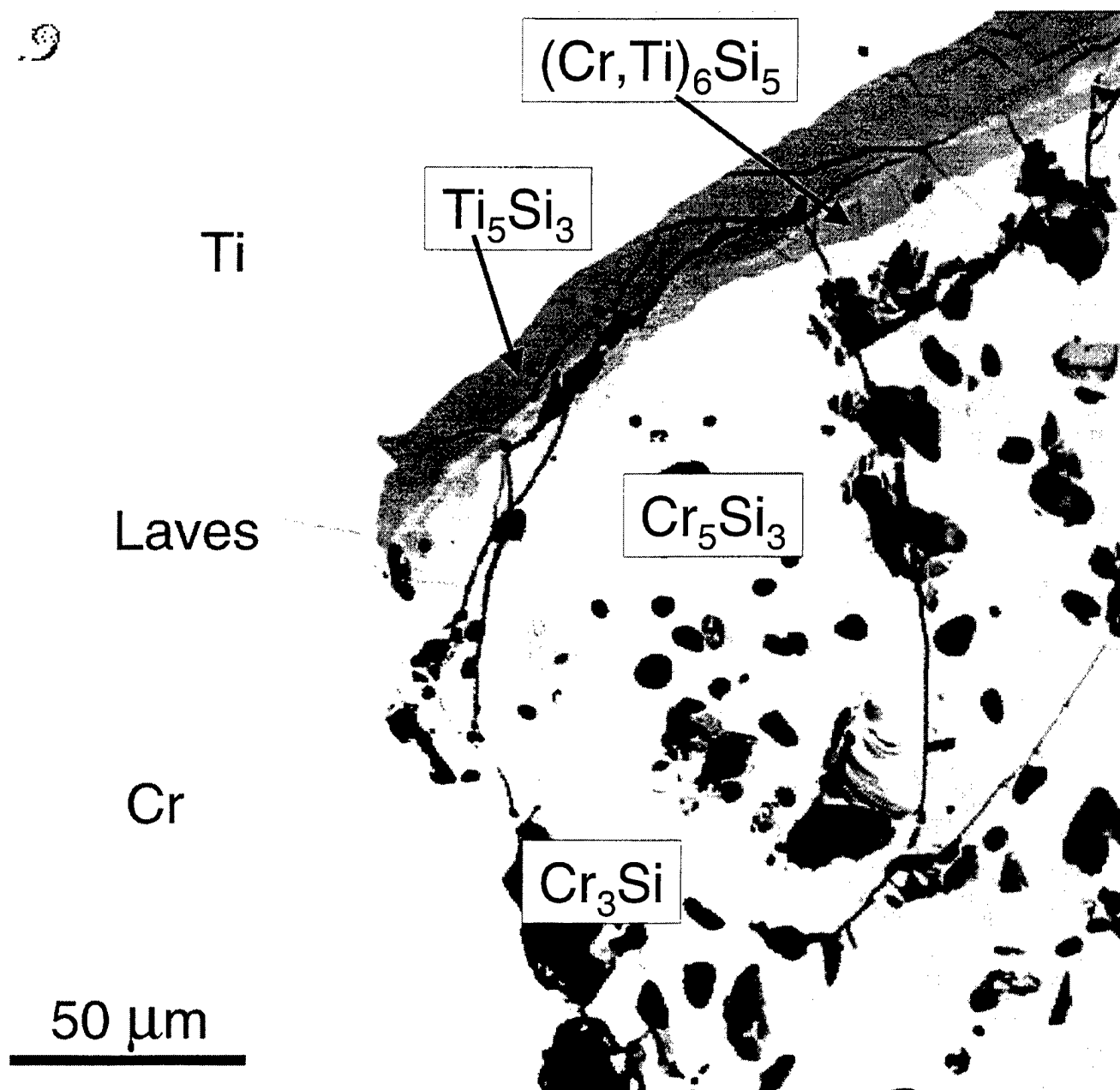
Figure 3. Backscatter electron SEM image of the Ti-Cr-Si tri-junction area of the diffusion multiple annealed at 1200°C for 1000 hrs showing the formation of many different intermetallic compounds, including the ternary compounds, $(Cr,Ti)_6Si_5$ ($oI44$).
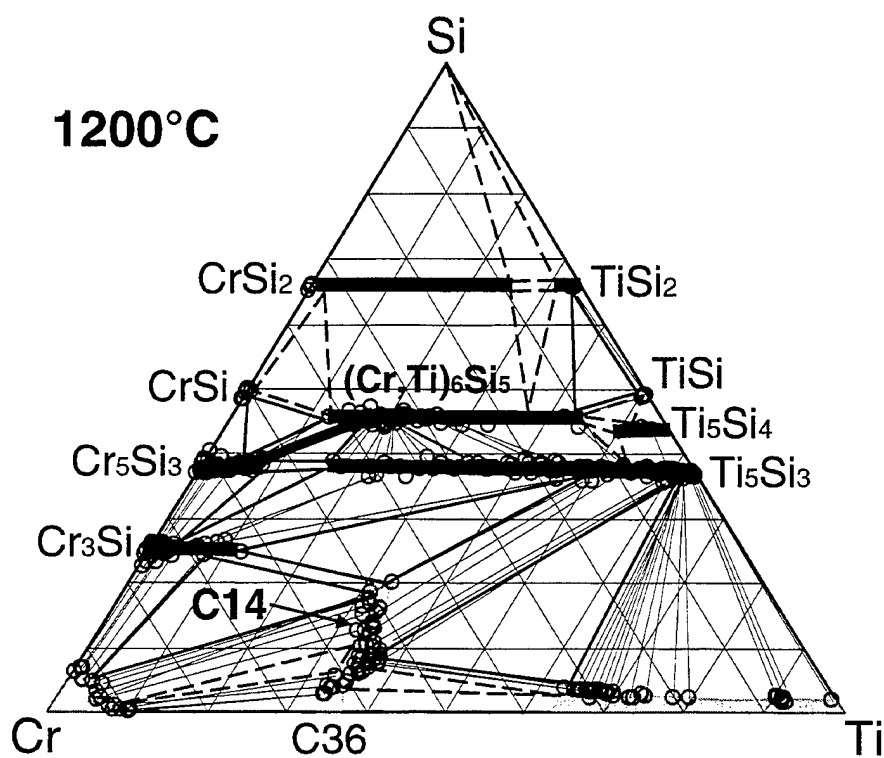
Figure 4. The 1200°C isothermal section of the Ti-Cr-Si system obtained from the tri-junction area of the diffusion multiple annealed at 1200°C for 1000 hours. The phase diagram is plotted in atomic percent axes with the numbers removed for simplicity. The solid triangle indicates well-defined three-phase triangles and the open circles show the tie-line compositions. The tie-lines are shown with dotted lines. The dashed triangles are guessed three-phase equilibria.
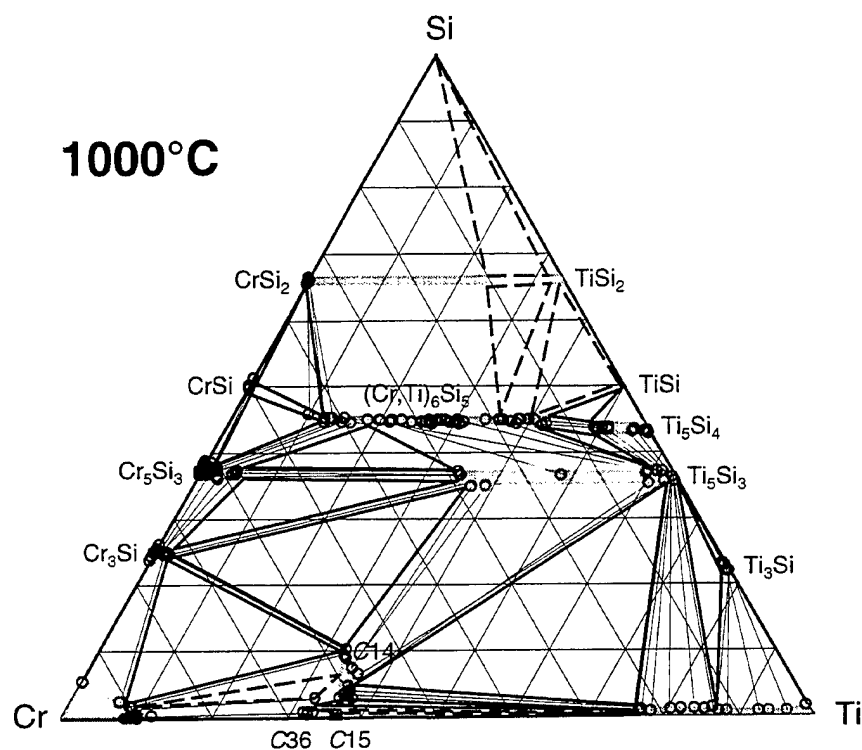
Figure 5. The 1000°C isothermal section of the Ti-Cr-Si system obtained from the tri-junction area of the diffusion multiple annealed at 1000°C for 4000 hours. The phase diagram is plotted in atomic percent axes with the numbers removed for simplicity. The solid triangle indicates well-defined three-phase triangles and the open circles show the tie-line compositions. The tie-lines are shown with dotted lines. The dashed triangles are guessed three-phase equilibria.

Mapping of the Ti-Si-Al Phase Diagram Using a Diffusion Multiple

J.-C. Zhao, M.R. Jackson, and L.A. Peluso

Mapping of the Ti-Si-Al Phase Diagram Using a Diffusion Multiple

J.-C. Zhao, M.R. Jackson, and L.A. Peluso
General Electric Company
GE Global Research Center, P.O. Box 8, Schenectady, NY 12301, USA

ABSTRACT

A high-efficiency diffusion-multiple approach was employed to map the phase diagram of the Ti-Si-Al ternary system which is critical for the design of niobium silicide-based composites. These composites have high potential as a replacement for Ni-base superalloys for jet engine applications. A partial isothermal section at 1000°C was constructed from the results obtained from diffusion multiples using scanning electron microscopy (SEM) and electron probe microanalysis (EPMA). One ternary compound $Al_2Si_5Ti_3$ was observed in the composition ranges created by interdiffusion among Ti, $TiAl_3$, and $TiSi_2$. The $Al_2Si_5Ti_3$ phase has about 35 at.% Ti and it has ~7 at.% variation of Al and Si (substitution). The Si solubility in $TiAl_3$ was found to be ~13 at.% Si at 1000°C. The Al solubility in the Ti silicides (Ti_3Si, Ti_5Si_3, Ti_5Si_4, $TiSi$, $TiSi_2$) were all very low. More information of the Ti-Si-Al system can be obtained from this diffusion multiple in the future.

Keywords: Ti-Si-Al, diffusion multiple, silicide, phase diagram.

1. INTRODUCTION

Niobium silicide-based composites show great promise for applications as the next generation turbine airfoil materials with significantly higher operating temperatures than current generation advanced Ni-base superalloys [1-6]. The Nb-Si binary composites have excellent creep strength, but poor oxidation resistance and poor room temperature fracture toughness [1-2]. Alloying with Ti significantly improves the oxidation resistance. The potential application of these composites at very high temperatures requires a balance of high creep resistance, high oxidation resistance, and good low-temperature damage tolerance (fracture toughness). To achieve such a property balance, elements such as Cr, Ti, Hf and Al are added to the composites and significant progress has been made in improving the properties of the composites. Some of the alloying concepts were discussed by Zhao *et al.* [7]. The advanced design of the composites requires a fair understanding of the phase equilibria in the Nb-Si-Ti-Cr-Hf-Al system. Since a reasonable definition of the Nb-Hf-Si system has been achieved [8-10], our effort has been focused on the ternary systems Nb-Cr-Si, Nb-Si-Al, Nb-Cr-Al, Ti-Si-Cr, Ti-Si-Al, Ti-Cr-Al, Nb-Ti-Si, Nb-Ti-Cr, and Nb-Ti-Al. Other ternary systems related to this six-element system such as Nb-Ti-Hf, Nb-Cr-Hf, Nb-Hf-Al, Ti-Si-Hf, Ti-Cr-Hf, and Cr-Hf-Al have either good data or are less critical for the design of the Nb silicide composites. We will report the results of the Ti-Si-Al system in the present paper and the results of other systems will be communicated separately.

In addition to the Nb silicide based composites, Ti_5Si_3 is also pursued as one of the candidate materials (based on its high melting point (2130 °C) and low density) for high-temperature applications with potential higher operating temperatures than those of Ni-base superalloys [11-

1

13]. However, Ti_5Si_3 itself suffers from poor oxidation resistance. With the addition of Al, its oxidation resistance may improve. The Ti-Si-Al phase diagram is also useful for potential development of intermetallics based on Ti_3Al and TiAl with Si additions [14]. Thus, the Ti-Si-Al phase diagram is very valuable for the design of high temperature composites.

The high-efficiency "diffusion multiple" approach [15-18] is ideally suited for mapping phase diagrams of the above mentioned Nb and Ti-based ternary systems. It would take thousands of alloys to determine the nine ternary systems using the traditional one-alloy-at-a-time (equilibrated alloy) approach. For instance, it took Goldschmidt and Brand [19] about 220 alloys to map just the Nb-Cr-Si ternary system and similarly about 135 alloys were employed by Lysenko et al. [20] to determine the Ti-Cr-Si system. These alloys have very high melting temperatures and are difficult to make and to homogenize. Extra effort also needs to be taken to avoid interstitial (oxygen, nitrogen, carbon, etc.) contamination during alloy casting and heat treatment. In contrast, the diffusion multiple approach needs only a few cast alloys and the samples were easy to make, and safe-guarding against the interstitial contamination can be very easily implemented as will be discussed later. The general diffusion multiple approach is discussed in detail previously [15-18] and has been successfully applied to many alloy systems.

The constitutive binary phase diagrams of the Ti-Si-Al system, i.e. Ti-Si [21], Ti-Al [21-28], and Al-Si [21] and are already available in the literature. The crystal structures of the phases in the binaries and the ternary system are listed in Table 1 [29]. The Ti-Si binary system [21] has five intermetallic compounds, Ti_3Si, Ti_5Si_3, Ti_5Si_4, TiSi, and $TiSi_2$. A thermodynamic assessment of this system was done by Seifert et al. [30]. We adopted the Ti-Al phase diagram by Okamoto [27] as our binary reference with the Al-rich part of the phase diagram recently refined by Palm et al. [28]. The Al-Si system is a simple eutectic.

Table 1. Crystal structure of phases in the Ti-Si-Al ternary system [29].

System	Conditions	Pearson Symbol	Space Group	Lattice Parameters			
				a	b	c	γ
αTi	LT	P63/mmc	$P6_3/mmc$	0.29512		0.46845	120°
βTi	HT	Im3m	Im3m	0.33066			
Al	cF4	Fm3m	Fm3m	0.40497			
Si	cF8	Fd3m	Fd3m	0.54309			
TiAl	≤ 1445°C	tP4	P4/mmm	0.4001		0.4071	
Ti_3Al	≤ 1180°C	hP8	$P6_3/mmc$	0.5780		0.4647	120°
$TiAl_2$	≤ 1180°C	tI24	$I4_1/amd$	0.3976		2.436	
$TiAl_3$	≤ 1350°C	tI8	I4/mmm	0.38537		0.85839	
Ti_2Al_5	985-1375°C	tI16	I4/mmm	0.3917		1.6524	
TiSi	≤ 1570°C	oP8	Pnma	0.6544	0.3638	0.4997	
TiSi	≤ 1920°C	oP8	Pmm2	0.3618	0.6492	0.4973	
Ti_3Si	≤ 1570°C	tP32	$P4_2/n$	1.039		0.517	
$TiSi_2$	≤ 1170°C	oF24	Fddd	0.82671	0.48000	0.85505	
Ti_5Si_3	≤ 1485°C	hP16	$P6_3/mcm$	0.74610		0.51508	120°
Ti_5Si_4	≤ 2130°C	tP36	$P4_12_12$	0.6702		1.2174	
$Al_2Si_5Ti_3$		oC12	Cmcm	0.360	1.353	0.360	
$Al_5Si_{12}Ti_7$		tI24	$I4_1/amd$	0.3576		2.715	

There were a few previous investigations on the Ti-Si-Al ternary phase diagram in the literature [31-35]. Two isothermal sections are shown in Fig. 1. These results will be discussed

in detail later. There is confusion on the phase formation. Our work will provide additional data to help better define this ternary system.

2. EXPERIMENTAL METHOD

A diffusion multiple with the cross-section view shown schematically in the Fig. 2(a) was made. The dimensions were designed so that the pieces of pure elements and compounds are much larger than the diffusion distance, thus there will be pure elements and compounds left after the long-term diffusion annealing. To avoid the low melting point of Al, we used both $TiSi_2$ and $TiAl_3$ compounds as members of the diffusion multiple. Both these compounds were made by arc-melting. They were then cut into square bars of 7 x 7 x 25 mm using electro-discharge machining (EDM). A 14 x 14 mm square opening was cut from a 25.4 mm diameter by 25.4 mm height cylindrical piece of pure Ti. The square open was cut across the whole height of the Ti piece. Pieces of high purity Ti and Cr in the dimension of 7 x 7 x 25 mm were also machined using EDM. The re-cast layer on the EDM'ed surfaces was removed by mechanical grinding to make clean surfaces. The pieces were ultrasonically cleaned in methanol and then assembled into the geometry shown in Fig. 2(a). The height of all pieces was 25 mm. The assembled diffusion multiple was then loaded into hot isostatic press (HIP) cans made of commercial purity Ti, which is schematically shown in Fig. 2(b). A 25 μm layer of Ta foil was placed between the diffusion multiple and the HIP can to isolate any interstitial contaminants that may diffuse into the HIP can from the quartz capsule during long-term annealing. The top and bottom caps of the HIP can were electron beam welded. HIPing was performed at 1204°C, 200MPa for 4 hours. The HIP can containing the diffusion multiple was then encapsulated in an evacuated quartz tube backfilled with pure argon. Since Ti is susceptible to oxygen and nitrogen contamination, it is critical to keep the diffusion multiple from interstitial elements. To further absorb any oxygen that may diffuse into the quartz tube, a packet of pure yttrium was wrapped in Ta foils and was then placed inside the quartz tube. Thus, the diffusion multiple was protected from the intersitials (O, N, C, etc.) by the quartz tube, the pure yttrium absorber, the Ti HIP can, and the Ta diffusion barrier. The encapsulated sample was then annealed at 1000°C for 2000 hours. After the heat treatment, the diffusion multiple was taken from the argon furnace and cooled down to ambient temperature by breaking the quartz tube and quenching the diffusion multiple into water. The diffusion multiple was then cut into halves parallel to the ends using wire EDM, ground and polished.

The samples were first examined using scanning electron microscopy (SEM), especially the backscatter electron (BSE) imaging. Most phases could be seen (although not identified explicitly) in the BSE images due to the differences in their average atomic weight. Quantitative EPMA analysis was performed on a CAMECA (Paris, France) microprobe using 15 kV voltage, 40 nA current and a 40° take-off angle.

3. RESULTS AND DISCUSSION

A backscatter electron image taken from the Ti-$TiSi_2$-$TiAl_3$ tri-junction (schematically circled area in Fig. 2(a)) of the diffusion multiple annealed at 1000°C for 1000 hrs is shown in Fig. 3. During the long-term diffusion treatment, extensive interdiffusion among Ti, Si and Al took place, and all the equilibrium phases, including the intermetallic phases, formed by interdiffusion reactions. By performing EPMA analysis in this tri-junction area, an extremely large amount of phase equilibrium information can be obtained. Unfortunately the EPMA analysis was halted during the run due to an equipment problem. Thus, only partial result was obtained for the

1000°C isothermal section of the Ti-Si-Al system, as shown in Fig. 4. We have defined three tie-triangles (three-phase equilibria) and additional three-phase equilibria were estimated based on the arrangement of the phases in the diffusion multiple (Fig. 3). The tie-lines are defined from the EPMA line profiles by taking advantage of the local equilibrium at interfaces formed among the phases. Details of the methodology can be found elsewhere [15-18]. If the EPMA analysis were complete, we would have obtained all the phase equilibrium information in the composition range generated by interdiffusion among Ti, $TiSi_2$ and $TiAl_3$.

. The first work on the Ti-Si-Al system was performed by Crossley and Turner [31] who studied the very Ti-rich corner at 600 to 1000°C and also two partial isopleths near the Ti-rich corner at 2 and 6 wt.% Al. Schob et al. [32] subsequently constructed an isothermal section at 1200°C as shown in Fig. 1(a). They observed one ternary compound $Ti(Si,Al)_2$ (C-49) and suggested that it had the $ZrSi_2$ type crystal structure (oC12, space group: Cmcm). They found that Ti_5Si_3 was in equilibrium with all the Ti aluminides (Ti_3Al, $TiAl$, $TiAl_3$). The other phases on binary Ti-Al and Ti-Si systems, α-Ti, $TiAl_2$ and Ti_3Si, were not considered due to the unavailability of good Ti-Al and Ti-Si binary phase diagrams at the time. The Ti_5Si_4 phase was proposed by Schob et al., but no crystal structure or related phase relations were provided in Fig. 1(a). Raman and Schubert [33] constructed a 700°C isothermal section of the Ti-Si-Al system and confirmed majority of the phase relations reported by Schob et al. They reported two ternary phases, $AlSi_3Ti_2$ and $Al_5Si_{12}Ti_7$. The $AlSi_3Ti_2$ phase is essentially the same as $Ti(Si,Al)_2$ since they have the same crystal structure and very similar lattice parameters. The $Al_5Si_{12}Ti_7$ phase was reported to have a tetragonal structure (tI24, space group: I4$_1$/amd). Villars et al. [36] revised the $AlSi_3Ti_2$ to $Al_2Si_5Ti_3$ according to the sample composition $Al_{19}Si_{50}Ti_{31}$ prepared by Raman and Schubert. We adopted their designation of the phase $Al_2Si_5Ti_3$ in our present work. The solubility of Si in $TiAl_3$ is 13 at.% Si based on our data (at 1000°C), which is about 3 at.% higher than that reported by Schob et al. for 1200°C.

Zakharov et al. [34] studied the phase equilibria of the Ti-Si-Al system in the composition region of 10 to 14 wt.% Si and 0 to 6 wt.% Ti. They constructed three partial isopleths at constant Si concentrations of 10, 12 and 14 wt.%. They claimed that the two ternary phases reported by Raman and Schubert were not confirmed. Instead, they suggested a ternary phase $Al_3Si_2Ti_2$ with a relatively narrow homogeneity range (Si: 26.4-29.7, Ti: 29.7-30.4, and Al balance, at.%), but they were unable to decipher the X-ray diffraction patterns of this phase. The existence of this phase needs to be confirmed.

We have observed one ternary compound $Al_2Si_5Ti_3$ in the composition ranges created by interdiffusion among Ti, $TiAl_3$, and $TiSi_2$. The $Al_2Si_5Ti_3$ phase has ~ 35 at.% Ti and it has ~7 at.% variation of Al and Si (substitution). The Si solubility in $TiAl_3$ was found to be ~13 at.% Si at 1000°C. The Al solubilities in the Ti silicides (Ti_3Si, Ti_5Si_3, Ti_5Si_4, $TiSi$, $TiSi_2$) were all very low. More information of the Ti-Si-Al system can be obtained from this diffusion multiple in the future.

Our work cannot confirm or un-confirm the existence of the other ternary phase $Al_5Si_{12}Ti_7$. This is because the diffusion path between $TiSi_2$ and $TiAl_3$ only passed through the $Al_2Si_5Ti_3$ phase, the $Al_5Si_{12}Ti_7$ composition is outside the composition region covered by the interdiffusion among Ti, $TiSi_2$ and $TiAl_3$.

Very recently, Azevedo and Flower studied the Ti-rich corner of the Ti-Si-Al system both experimentally and also using the CALPHAD modeling. The composition region they covered

4

did not involve the ternary phases. However, the Ti_3Si phase which is an equilibrium phase was completely missing from their analysis and modeling.

Although only partial data of the Ti-Si-Al ternary system were collected, the partial isothermal section at 1000°C provides some useful information. First of all, we confirmed the existence of the $Al_2Si_5Ti_3$ phase, which supports the work of Schob et al. as well as Raman and Schubert; and together we suggest the dismissal of this phase by Zakharov et al. maybe incorrect. Secondly, we observed two three-phase equilibria: $Al_2Si_5Ti_3$ + TiSi + $TiSi_2$ and $Al_2Si_5Ti_3$ + TiSi + $TiAl_3$, which are consistent with the work of Schob et al. (Fig. 1(a)). The phase relations are different from those reported by Raman and Schubert (Fig. 1(b)). If the result of Raman and Schubert is correct, then there must exist a four-phase reaction: ($Al_2Si_5Ti_3$ + TiSi + $TiSi_2$) + ($Al_2Si_5Ti_3$ + $Al_5Si_{12}Ti_7$ + $TiSi_2$) $\rightarrow$ ($Al_2Si_5Ti_3$ + $Al_5Si_{12}Ti_7$ + $TiSi_2$) + ($Al_2Si_5Ti_3$ + TiSi + $Al_5Si_{12}Ti_7$).

The phase equilibrium information of the Ti-Si-Al system is very useful for the design of both Nb silicide composites and coatings for these composites. It is also very useful for design of Ti_5Si_3–based alloys. Thus, this ternary system is one of the key systems for which we would like to perform CALPHAD modeling and to add the data into the developing thermodynamic database for Nb silicide based systems [10,37,38]. Our data serve as useful input to the thermodynamic modeling.

4. CONCLUSIONS

A partial isothermal section of the Ti-Si-Al ternary system at 1000°C was obtained based EPMA analysis from the Ti-$TiSi_2$-$TiAl_3$ tri-junction region of a diffusion multiple annealed at 1000°C for 2000 hours. One ternary phase, $Al_2Si_5Ti_3$, was observed which shows a constant Ti concentration of ~ 35 at.%, and ~7 at.% variation of Al and Si (substitution). The Si solubility in $TiAl_3$ was found to be ~13 at.% Si at 1000°C. The Al solubility in the Ti silicides (Ti_3Si, Ti_5Si_3, Ti_5Si_4, TiSi, $TiSi_2$) were all very low. More information of the Ti-Si-Al system can be obtained from this diffusion multiple in the future.

REFERENCES

1. M.G. Mendiratta and D.M. Dimiduk, *Mat. Res. Soc. Symp. Proc.*, 133 (1989), 441- 446.
2. M.R. Jackson, B.P. Bewlay, R.G. Rowe, D.W. Skelly, and H.A. Lipsitt, *JOM*, 48 (1996), 39- 44.
3. P.R. Subramanian, M.G. Mendiratta, and D.M. Dimiduk, *JOM*, 48 (1996), 33-38.
4. B.P. Bewlay, J.J. Lewandowski, and M.R. Jackson, *JOM*, 49 (1997), 44-45.

5. S.J. Balsone, B.P. Bewlay, M.R. Jackson, P.R. Subramanian, J.-C. Zhao, A. Chatterjee, and T. Heffernan, in *Structural Intermetallics 2001* (K. Hemker, D.M. Dimiduk, H. Clemens, R. Darolia, H. Inui, J.M. Larsen, V.K. Sikka, M. Thomas, and J.D. Whittenberger, eds.), TMS, Warrendale, PA, 2001, 99-108

6. B.P. Bewlay, M.R. Jackson, J.-C. Zhao, and P.R. Subramanian, *Metallurgical and Materials Transactions,* Accepted November 2002.

7. J.-C. Zhao, B.P. Bewlay, M.R. Jackson, and L.A. Peluso, in *Structural Intermetallics 2001* (K. Hemker, D.M. Dimiduk, H. Clemens, R. Darolia, H. Inui, J.M. Larsen, V.K. Sikka, M. Thomas, and J.D. Whittenberger, eds.), TMS, Warrendale, PA, 2001, 483-491.

8. B.P. Bewlay, R.R. Bishop, and M.R. Jackson, *Z. Metallkde.,* 90 (1999), 413-422.

9. J.-C. Zhao, B.P. Bewlay, and M.R. Jackson, *Intermetallics,* 9 (2001), 681-689.

10. Y. Yang, Y.A. Chang, J.-C. Zhao, and B.P. Bewlay, *Intermetallics,* Accepted November 2002.

11. L. Zhang and J. Wu, *Acta Mater.,* 46 (1998), 3535-3546.

12. M. Yamaguchi, H. Inui and K. Ito, *Acta Mater.,* 48 (2000), 307-322.

13. J.J. Petrovic, A.K. Vasudevan, *Mate. Sci. Eng.,* A261 (1999), 1-5.

14. J.S. Wu, P.A. Beaven, R. Wagner, Ch. Hartig, and J. Seeger, in *High Temperature Ordered Intermetallic Alloys III,* eds. C.T. Liu, A.I. Taub, N.S. Stoloff and C.C. Koch, MRS, 1989, 761..

15. J.-C. Zhao, *Adv. Eng. Mater.,* 3 (2001), 143-147.

16. J.-C. Zhao, *J. Mater. Res.,* 16 (2001), 1565-1578.

17. J.-C. Zhao, M.R. Jackson, L.A. Peluso, and L. Brewer, *MRS Bulletin,* 27 (2002) 324-329.

18. J.-C. Zhao, M.R. Jackson, L.A. Peluso, and L. Brewer, *JOM,* 54 (7) (2002) 42-45.

19. H.J. Goldschmidt and J.A. Brand, *J. Less-Common Met.,* 3 (1961), 34-43.

20. L.A. Lysenko, V.Ya. Markiv, O.V. Tsybukh, and E.I. Gladyshevskii, *Inorganic Mater.,* 7(1) (1971), 157-159.

21. J.L. Murray: in *Binary Alloy Phase Diagrams,* 2nd ed., T.B. Massalski, ed., ASM International, Materials Park, OH, 1990.

22. H.R. Ogden et al., *Trans. AIME,* 191 (1951) 1150.

23. J.H. Perepezko, Proc. *Intl. Symp. Intermetallic Compounds, Structure and Mechanical Properties,* (JIMIS-6), Sendai, Janpan, 1991, pp. 239-243.

24. U.R. Kattner, J.C. Lin, and Y.A. Chang, *Metall. Trans.* A23 (1992), 2081-2090.

25. C.D. Anderson, W.H. Hofmeister, and R.J. Bayuzick, *Metall. Trans.* A24 (1993), 61-66.

26. P.J. Spencer, *Z. Metallkde.,* 87 (1996), 535-539.

27. H. Okamoto, *J. Phase Equil.,* 14 (1993), 120-121.

28. M. Palm, L.C. Zhang, F. Stein, and G. Sauthoff, *Intermetallics,* 10 (2002), 523 –540.

29. P. Villars and L.D. Calvert, *Pearson's Handbook of Crystallographic Data for Intermetallic Phases,* 2nd ed., ASM International, Materials Park, OH, 1991.

30. H.J. Seifert, H.L. Lukas and G. Petzow, *Z. Metallkde.,* 87 (1996), 2-13.

31. F.A. Crossley and D.H. Turner, *Trans. TMS-AIME,* 212 (1958), 60-63.

32. O. Schob, H. Nowotny, F. Benesovsky, *Plansee. Pulvermetall.,* 10 (1962), 65-71.

33. A. Raman and K. Schubert, *Z. Metallkde,* 56 (1965), 44-52.

34. A.M. Zakharov, I.T. Gul'din, A.A. Arnol'd, and Yu.A. Matsenko, *Russ. Metall.,* (4) (1988), 185-189.

35. C.R.F. Azevedo and H.M. Flower, *CALPHAD,* 28 (2002), 353-373.

36. P. Villars, A. Prince, and H. Okamoto, Handbook of Ternary Alloy Phase Diagrams, ASM International, Materials Park, OH, 1995.

37. H. Liang and Y.A.Chang, *Intermetallics,* 7 (1999) 561.

38. Y. Yang and Y.A. Chang (University of Wisconsin – Madison), private communication, 2002.
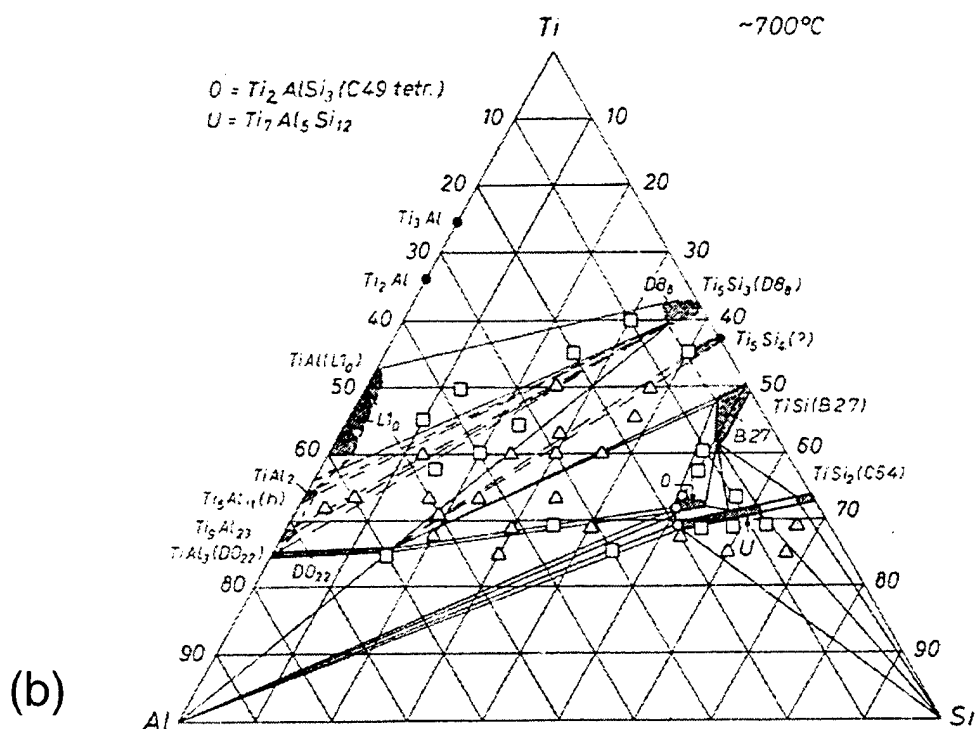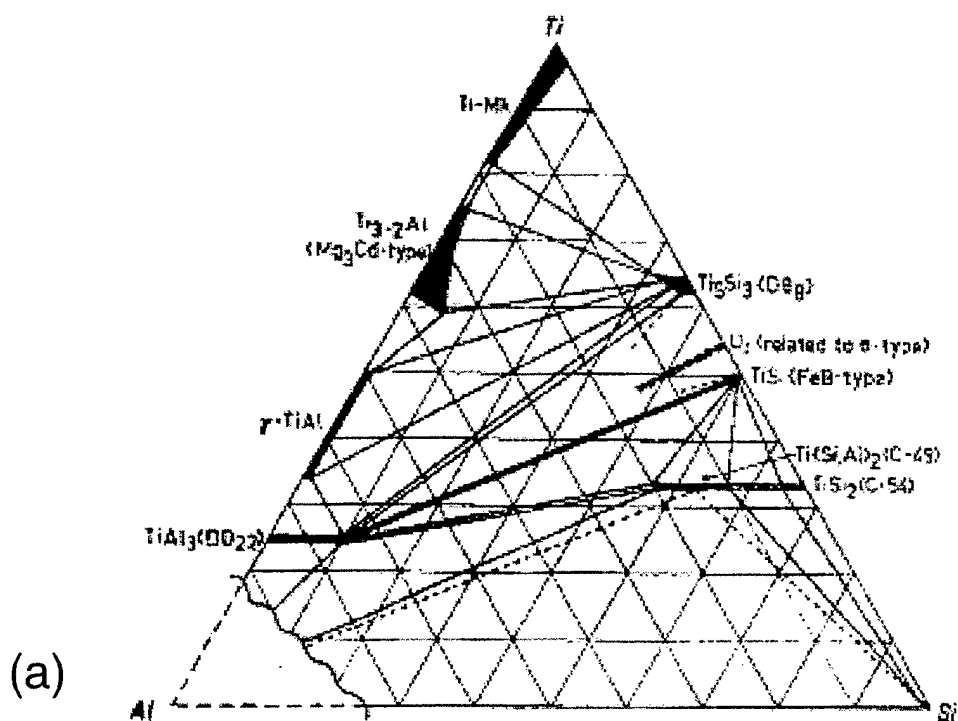
Figure 1. Isothermal sections from the literature of the Ti-Si-Al system: 1200°C isothermal section reported by Schob *et al.* [32]; and (b) 700 isothermal section reported by Raman and Schubert [33].
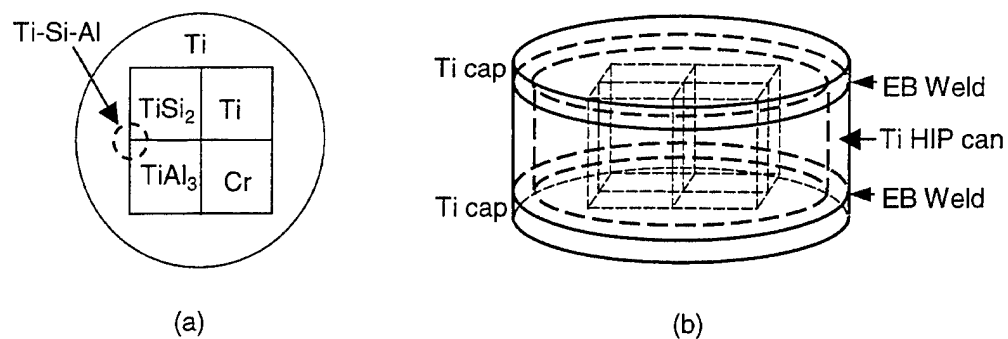
Figure 2. A diffusion multiple for efficient mapping of the Ti-Si-Al ternary phase diagram: (a) cross-sectional view; and (b) perspective view. See text for the size of the sample. The results reported in this work were all obtained from the tri-junction corner of $Ti - TiSi_2 - TiAl_3$ circled in (a).
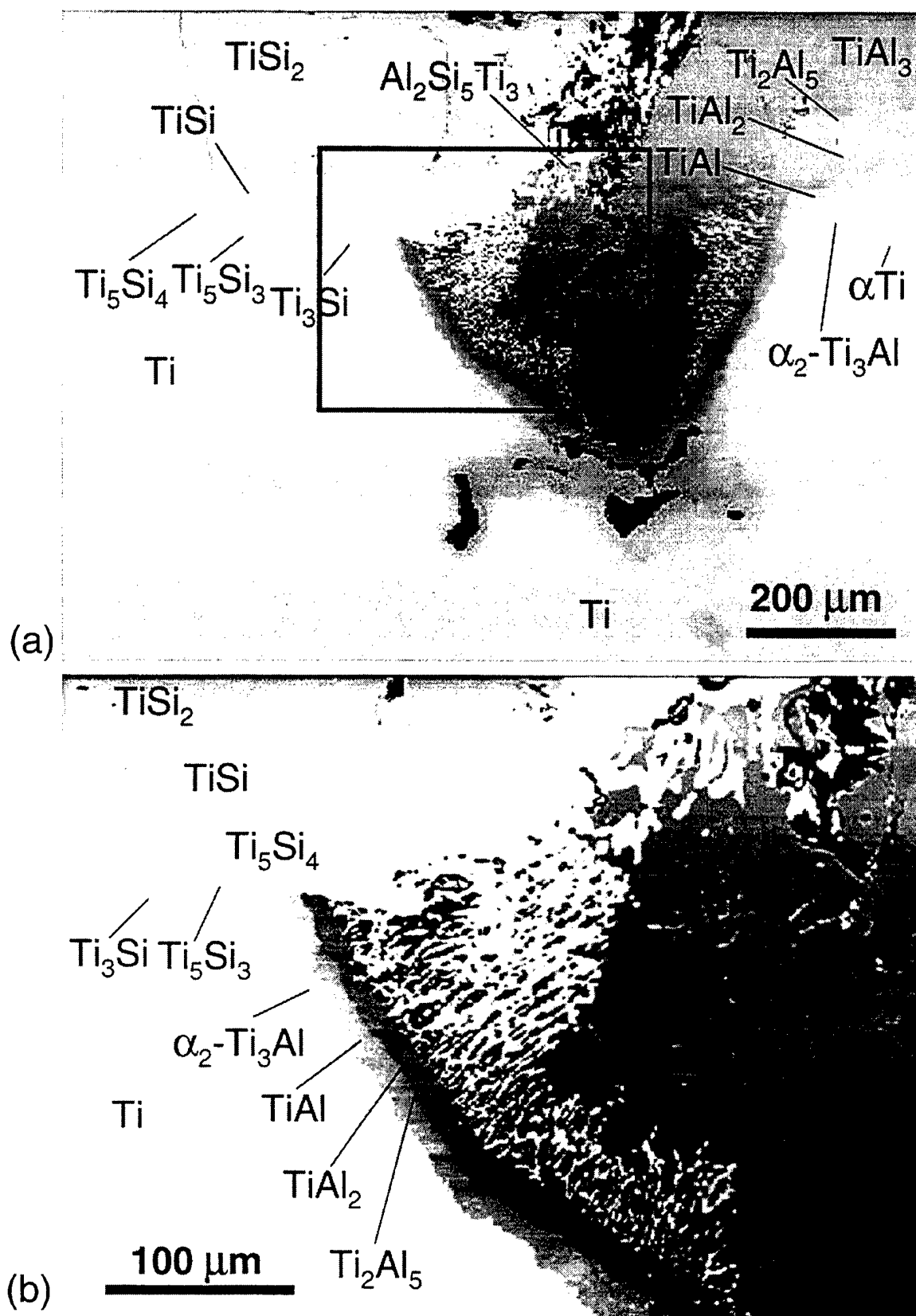
Figure 3. Backscatter electron SEM images of the Ti – TiSi$_2$ – TiAl$_3$ tri-junction area of the diffusion multiple (Fig. 2) annealed at 1000°C for 2000 hrs showing the formation of many different intermetallic compounds, including one ternary compound, Al$_2$Si$_5$Ti$_3$: (a) a low-magnification image showing the overall tri-junction; and (b) a high-magnification image of the area in (a) shown with a rectangular box.
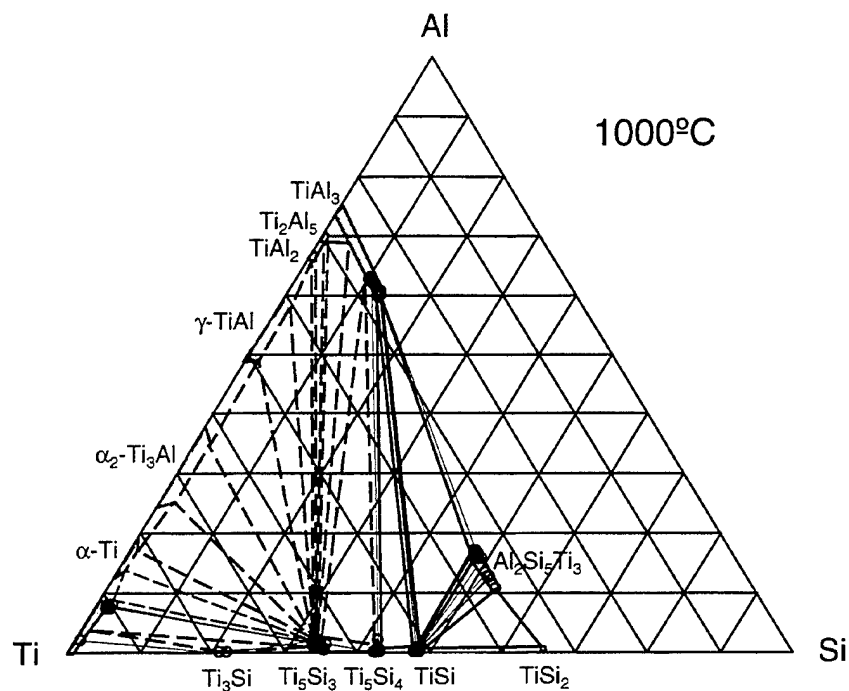
9

Figure 4. The 1000°C isothermal section of the Ti-Si-Al system obtained from the Ti - TiSi$_2$ -TiAl$_3$ tri-junction area of the diffusion multiple (Fig. 2) annealed at 1000°C for 2000 hrs. The phase diagram is plotted in atomic percent axes with the numbers removed for simplicity. The solid triangle indicates well-defined three-phase triangles and the open circles show the tie-line compositions. The tie-lines are shown with light dotted lines. The dashed triangles show estimated three-phase equilibria.

Mapping of the Nb-Cr-Ti Phase Diagram Using Diffusion Multiples

J.-C. Zhao, M.R. Jackson, and L.A. Peluso

Mapping of the Nb-Cr-Ti Phase Diagram Using Diffusion Multiples

J.-C. Zhao, M.R. Jackson, and L.A. Peluso
General Electric Company
GE Global Research Center, P.O. Box 8, Schenectady, NY 12301, USA

ABSTRACT

A high-efficiency diffusion-multiple approach was employed to map the phase diagram of the Nb-Cr-Ti ternary system which is critical for the design of niobium silicide-based composites. These composites have high potential as a replacement for Ni-base superalloys for jet engine applications. The formation of the Laves phase and alloying with Ti are critical for the high oxidation resistance of the composites and the Nb-Cr-Ti system serves as the base for understanding the Laves phase formation and Ti alloying. Three isothermal sections at 1000, 1150 and 1200 °C were constructed from the results obtained from diffusion multiples using scanning electron microscopy (SEM), electron probe microanalysis (EPMA), and electron backscatter diffraction (EBSD). The results help to define the relative stability of the C15 and C36 Laves phases in the Nb-Cr-Ti ternary system.

Keywords: Nb-Cr-Ti, diffusion multiple, Laves phase, phase diagram, composites, intermetallics.

1. INTRODUCTION

Niobium silicide-based composites show great promise for applications as the next generation turbine airfoil materials with significantly higher operating temperatures than current generation advanced Ni-base superalloys [1-6]. The Nb-Si binary composites have excellent creep strength, but poor oxidation resistance and poor room temperature fracture toughness [1-2]. Alloying with Ti and Cr significantly improve the oxidation resistance. The potential application of these composites at very high temperatures requires a balance of high creep resistance, high oxidation resistance, and good low-temperature damage tolerance (fracture toughness). To achieve such a property balance, elements such as Cr, Ti, Hf and Al are added to the composites and significant progress has been made in improving the properties of the composites. Some of the alloying concepts were discussed by Zhao *et al.* [7]. The advanced design of the composites requires a fair understanding of the phase equilibria in the Nb-Si-Ti-Cr-Hf-Al system. Since a reasonable definition of the Nb-Hf-Si system has been achieved [8-10], our effort has been focused on the ternary systems Nb-Cr-Si, Nb-Si-Al, Nb-Cr-Al, Ti-Si-Cr, Ti-Si-Al, Ti-Cr-Al, Nb-Ti-Si, Nb-Ti-Cr, and Nb-Ti-Al. Other ternary systems related to this six-element system such as Nb-Ti-Hf, Nb-Cr-Hf, Nb-Hf-Al, Ti-Si-Hf, Ti-Cr-Hf, and Cr-Hf-Al have either good data or are less critical for the design of the Nb silicide composites. We will report the results of the Nb-Cr-Ti system in the present paper and the results of other systems will be communicated separately.

In addition to the Nb silicide based composites, Laves phase based composites are also pursued as candidates of high temperature structural materials [11-15] because of their high

melting points and good retention of mechanical properties to elevated temperatures. The Nb-Cr-Ti system serves as an important base for understanding the stability of the Laves phases.

The high-efficiency "diffusion multiple" approach [16-19] is ideally suited for mapping phase diagrams of the above mentioned Nb and Ti-based ternary systems. It would take thousands of alloys to determine the nine ternary systems using the traditional one-alloy-at-a-time (equilibrated alloy) approach. For instance, it took Goldschmidt and Brand [20] about 220 alloys to map just the Nb-Cr-Si ternary system and similarly about 135 alloys were employed by Lysenko et al. [21] to determine the Ti-Cr-Si system. These alloys have very high melting temperatures and are difficult to make and to homogenize. Extra effort also needs to be taken to avoid interstitial (oxygen, nitrogen, carbon, etc.) contamination during alloy casting and heat treatment. In contrast, the diffusion multiple approach needs only a few cast alloys and the samples were easy to make, and safe-guarding against the interstitial contamination can be very easily implemented as will be discussed later. The general diffusion multiple approach is discussed in detail previously [16-19] and has been successfully applied to many alloy systems.

The constitutive binary phase diagrams of the Nb-Cr-Ti system, i.e. Nb-Cr [22], Ti-Cr [23-25], and Nb-Ti [22] and are already available in the literature. The crystal structures of the phases in the binaries are listed in Table 1 [26].

Table 1. Crystal structure of phases in the Nb-Cr-Ti ternary system [26].

System	Pearson Symbol	Space Group	Lattice Parameters		
			a (nm)	c (nm)	γ
Nb	cI2	Im$\underline{3}$m	0.33067		
Cr	cI2	Im$\underline{3}$m	0.28847		
αTi	hP2	P6$_3$/mmc	0.29512	0.46845	120°
βTi	cI2	Im$\underline{3}$m	0.33066		
Cr$_2$Nb (C14 Laves)	hP12	P6$_3$/mmc	0.4931	0.8123	120°
Cr$_2$Nb (C15 Laves)	CF24	Fd$\underline{3}$m	0.695		
β(Cr, Ti)	cI2	Im$\underline{3}$m	0.312		
αCr$_2$Ti (C15 Laves)	cF24	Fd$\underline{3}$m	0.691		
βCr$_2$Ti (C36 Laves)	hP24	P6$_3$/mmc	0.4932	0.8005	120°
γCr$_2$Ti (C14 Laves)	hP12	P6$_3$/mmc	0.4932	1.601	120°

The Nb-Cr phase diagram [22], Fig. 1(a), shows two NbCr$_2$-based Laves phases with the high-temperature hexagonal C14 (hP12) and low-temperature cubic C15 (cF24) structures. The transformation takes place at ~ 1585 to 1625 °C. The Ti-Cr binary system has three Cr$_2$Ti-based Laves phases (Fig. 1(b)): the low-temperature cubic C15 (cF24) which is stable at temperatures < 1220 °C, the intermediate-temperature dihexagonal C36 (hP24) stable between 800-1270 °C, and the high-temperature hexagonal C14 (hP12) stable at temperatures > 1270 °C [23-25]. The Nb-Ti system is a relatively simple one without any ternary compound phase [27]. The bcc phase is completely soluble at elevated temperatures.

There have been several previous investigations on the Nb-Cr-Ti ternary system [27-31]. Several isothermal sections from 1900 to 800°C were constructed and 6 isopleths were also constructed. These results were obtained from more than a hundred alloys annealed at various temperatures. The relative stability of the Laves phases is still not very clear. The present work will contribute to the understanding of this ternary system by providing more experimental data.

2. EXPERIMENTAL METHOD

Three diffusion multiples with the cross-section view shown schematically in the Fig. 2(a) were made. The inner and outer circle diameters were 15.6 and 25.4 mm respectively to guarantee that the dimensions of the pure element pieces are much larger than the diffusion distance, thus there will be pure elements left after the long term diffusion anneal. High purity Nb, Cr, Si and Ti were machined into the proper shapes (quarter pies and round shells, Fig. 2(a)) by electro-discharge machining (EDM). The re-cast layer on the EDM'ed surfaces was removed by mechanical grinding to make clean surfaces. The pieces were ultrasonically cleaned in methanol and then assembled into the geometry shown in Fig. 2(a). The height of all pieces was 25 mm. The assembled diffusion multiples were then loaded into hot isostatic press (HIP) cans made of commercial purity Ti, which is schematically shown in Fig. 2(b). A 25 μm layer of Ta was placed between the diffusion multiples and the HIP cans to isolate any interstitial contaminants that may diffuse into the HIP can from the quartz capsule during long term annealing. The top and bottom caps of the HIP can were electron beam welded. HIPing was performed at 1204 °C, 200MPa for 4 hrs. The HIP cans containing the diffusion multiples were then encapsulated in evacuated quartz tubes backfilled with pure argon. Since both Nb and Ti are susceptible to oxygen and nitrogen contamination, it is critical to keep the diffusion multiples from interstitial elements. To further absorb any oxygen that may diffuse into the quartz tube, a packet of pure yttrium was wrapped in Ta foils and was then placed inside each quartz tube. Thus, the diffusion multiples were protected from the intersitials (O, N, C, etc.) by the quartz tube, the pure yttrium absorber, the Ti HIP can, and the Ta diffusion barrier. The encapsulated samples were then annealed at three different temperatures (1200 °C for 1000 hrs, 1150°C for 2000 hrs, and 1000 °C for 4000 hrs). Three identical diffusion multiples were made and each was annealed at one temperature. After the heat treatment, the diffusion multiples were taken from the argon furnace and cooled down to ambient temperature by breaking the quartz tube and quenching the diffusion multiples into water. The diffusion multiples were then cut into halves parallel to the ends using wire EDM, ground and polished.

The samples were first examined using scanning electron microscopy (SEM), especially the backscatter electron (BSE) imaging. Most phases could be seen (although not identified explicitly) in the BSE images due to the differences in their average atomic weight. Quantitative EPMA analysis was performed on a CAMECA (Paris, France) microprobe using 15 kV voltage, 40 nA current and a 40° take-off angle. Electron backscatter diffraction (EBSD) analysis was performed to obtain crystal structure information of the Laves phases formed in the diffusion multiple. Phase identification was accomplished by a direct match of the diffraction bands in the experimental backscatter pattern with simulated patterns generated using known structure types and lattice parameters. A detailed discussion on this powerful EBSD technique can be found in Schwartz *et al.* [32].

3. RESULTS AND DISCUSSION

Backscatter electron (BSE) images taken from the Nb-Cr-Ti tri-junction (schematically circled area in Fig. 2(a)) and the Ti-Cr binary area of the diffusion multiple annealed at 1150 °C for 2000 hrs are shown in Fig. 3. During the long-term diffusion treatment, extensive interdiffusion among Nb, Cr and Ti took place, and all the equilibrium phases, including the Laves phases, formed by interdiffusion reactions. By performing EPMA analysis in this tri-junction area, diffusion profiles were obtained. The tie-lines are defined from the EPMA line profiles by taking advantage of the local equilibrium at interfaces formed among the phases.

These tie-lines were employed to construct the 1150°C isothermal section of the Nb-Cr-Ti system, Fig. 4(b). Similar isothermal sections at 1200°C and 1000°C were also constructed from EMPA analyses of the samples annealed at the respective temperature. Details of the methodology can be found elsewhere [16-19].

Since the average atomic number density of the C15 and C36 Laves phase is very similar, it is difficult to differentiate these two Laves phases using only the BSE images (Fig. 3). We could see the phase boundary between the C15- and C36-Laves phases in the high contrast BSE image taken from the Ti-Cr binary area (Fig. 3(b)) by taking advantage of twinning of the dihexagonal C36 Laves structure. EBSD patterns were collected and they confirmed the two Laves crystal structures.

It can be seen that at the three temperatures tested, the C15 Laves phase was isomorphous (completely soluble) from Nb-Cr binary to the Ti-Cr binary. The C36 Laves phase was only stable at Nb concentration < ~11 at%. Such stability information was not obtained in previous literature investigations.

Figure 5 compares the Cr solubility in the bcc(Nb,Ti) phase at three different compositions (Nb/Ti ratios). It can be seen that the results from three independent groups showed excellent agreement.

The phase equilibrium information of the Nb-Cr-Ti system is very useful for the design of both Nb silicide composites and coatings for these composites. It is also very useful for design of Laves phase based alloys. We would like to refine the thermodynamic description of this ternary system based on our new results and to add the data into the developing thermodynamic database for Nb silicide based systems [10,33,34]. Our data provide good input to the thermodynamic modeling.

4. CONCLUSIONS

Three isothermal sections at 1000, 1150 and 1250 °C of the Nb-Cr-Ti ternary system were constructed based on electron probe microanalysis and electron backscatter diffraction of three diffusion multiples annealed at these temperatures for 4000, 2000 and 1000 hours respectively. The diffusion multiples were made up of Nb, Cr, Ti and Si as shown in Fig. 2. The stability of the C15 and C36 Laves at the temperatures were defined. The C15 Laves is continuous from the Nb-Cr binary to the Ti-Cr binary, whereas the C36 Laves is only stable at Nb concentration < ~ 11 at.%. The solubility of Cr in the bcc(Nb,Ti) solid solutions was very well defined from the present work.

REFERENCES

1. M.G. Mendiratta and D.M. Dimiduk, *Mat. Res. Soc. Symp. Proc.*, 133 (1989), 441- 446.
2. M.R. Jackson, B.P. Bewlay, R.G. Rowe, D.W. Skelly, and H.A. Lipsitt, *JOM*, 48 (1996), 39-44.
3. P.R. Subramanian, M.G. Mendiratta, and D.M. Dimiduk, *JOM*, 48 (1996), 33-38.
4. B.P. Bewlay, J.J. Lewandowski, and M.R. Jackson, *JOM*, 49 (1997), 44-45.
5. S.J. Balsone, B.P. Bewlay, M.R. Jackson, P.R. Subramanian, J.-C. Zhao, A. Chatterjee, and T. Heffernan, in *Structural Intermetallics 2001* (K. Hemker, D.M. Dimiduk, H. Clemens, R. Darolia, H. Inui, J.M. Larsen, V.K. Sikka, M. Thomas, and J.D. Whittenberger, eds.), TMS, Warrendale, PA, 2001, 99-108
6. B.P. Bewlay, M.R. Jackson, J.-C. Zhao, and P.R. Subramanian, *Metallurgical and Materials Transactions,* Accepted November 2002.
7. J.-C. Zhao, B.P. Bewlay, M.R. Jackson, and L.A. Peluso, in *Structural Intermetallics 2001* (K. Hemker, D.M. Dimiduk, H. Clemens, R. Darolia, H. Inui, J.M. Larsen, V.K. Sikka, M. Thomas, and J.D. Whittenberger, eds.), TMS, Warrendale, PA, 2001, 483-491.
8. B.P. Bewlay, R.R. Bishop, and M.R. Jackson, *Z. Metallkde.*, 90 (1999), 413-422.
9. J.-C. Zhao, B.P. Bewlay, and M.R. Jackson, *Intermetallics,* 9 (2001), 681-689.
10. Y. Yang, Y.A. Chang, J.-C. Zhao, and B.P. Bewlay, *Intermetallics,* Accepted November 2002.
11. M. Yamaguchi, H. Inui, and K. Ito, *Acta Mater.*, 48 (2000), 307-322.
12. T. Taksugi and M. Yoshida, *J. Mater. Res.*, 13 (1998), 2505-2513.
13. R.L. Fleischer and R.J. Zabala, *Metall. Trans. A,* 21 (1990) 2149-2154.
14. C.T. Liu, J.H. Zhu, M.P. Brady, C.G. McKamey, and L.M. Pike, *Intermetallics*, 8 (2000), 1119-1129.
15. K.C. Chen, S.M. Allen, and J.D. Livingston, *Mater. Sci. Eng. A*, 242 (1998), 162-173.
16. J.-C. Zhao, *Adv. Eng. Mater.*, 3 (2001), 143-147.
17. J.-C. Zhao, *J. Mater. Res.*, 16 (2001), 1565-1578.
18. J.-C. Zhao, M.R. Jackson, L.A. Peluso, and L. Brewer, *MRS Bulletin*, 27 (2002) 324-329.
19. J.-C. Zhao, M.R. Jackson, L.A. Peluso, and L. Brewer, *JOM*, 54 (7) (2002) 42-45.
20. H.J. Goldschmidt and J.A. Brand, *J. Less-Common Met.*, 3 (1961), 34-43.
21. L.A. Lysenko, V.Ya. Markiv, O.V. Tsybukh, and E.I. Gladyshevskii, *Inorganic Mater.,* 7(1) (1971), 157-159.
22. M. Venkatraman and J.P. Neumann: in *Binary Alloy Phase Diagrams*, 2nd ed., T.B. Massalski, ed., ASM International, Materials Park, OH, 1990.
23. J.L. Murray: in *Binary Alloy Phase Diagrams*, 2nd ed., T.B. Massalski, ed., ASM International, Materials Park, OH, 1990.
24. W. Zhuang, J. Shen, Y. Liu, L. Ling, S. Shang, Y. Du, and J.C. Schuster, *Z. Metallkde.*, 91 (2000), 121-127.
25. K.C. Chen, S.M. Allen, and J.D. Livingston, *Mat. Res. Soc. Symp. Proc.*, 364 (1995), 1401.
26. P. Villars and L.D. Calvert, *Pearson's Handbook of Crystallographic Data for Intermetallic Phases*, 2nd ed., ASM International, Materials Park, OH, 1991.
27. K.I. Shakhova and P.B. Budberg, *Russ. Metall. Fuels*, 6 (1962), 72-78.
28. V.N. Svechnikov, Yu.A. Kocherzhinskii, and V.I. Latysheva, Sb. Nauchn. Ir. Inst. Metallofiz., Akad. Nauk Ukr. SSR., (19) (1964), 192-195.
29. I.I. Kornilov, K.I. Shakhova and P.B. Budberg, *Russ. Metall.*, 4 (1965), 119-127.
30. D.J. Thoma: Ph.D. Thesis, University of Wisconsin, Madison, WI, 1992, available from University Microfilms, Ann Arbor, MI.
31. M. Yoshida, T. Yaegashi, Y. Murakami, D. Shindo, and T. Takasugi, *J. Japan. Inst. Met.*, 65 (2001), 389-396.

32. *Electron Backscatter Diffraction in Materials Science*, edited by A.J. Schwartz, M. Kumar, and B.L. Adams (Kluwer Academic / Plenum Publishers, New York, 2000).
33. H. Liang and Y.A.Chang, *Intermetallics*, 7 (1999) 561.
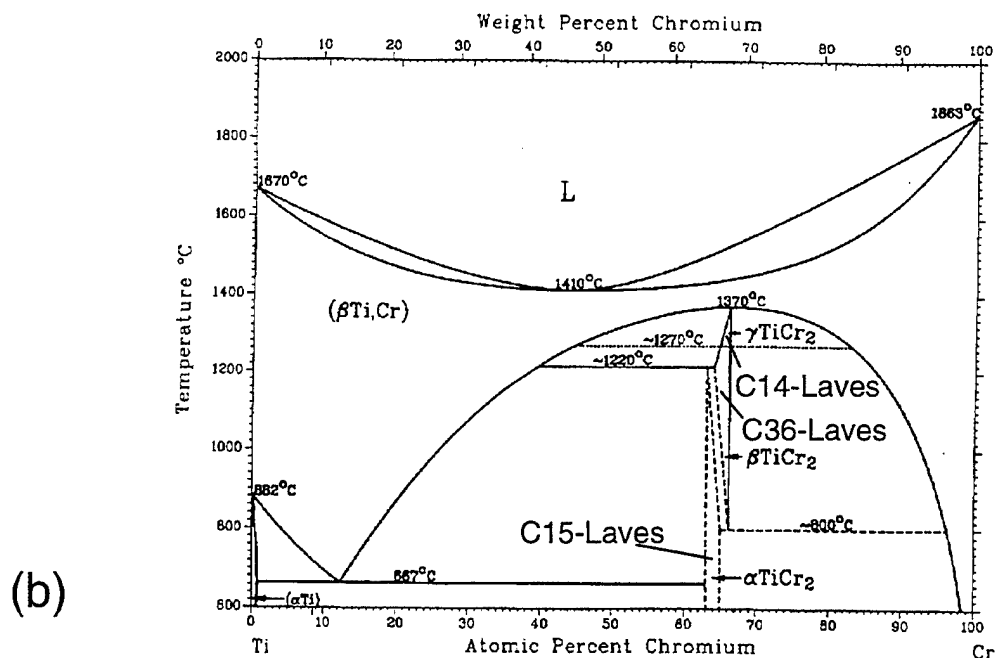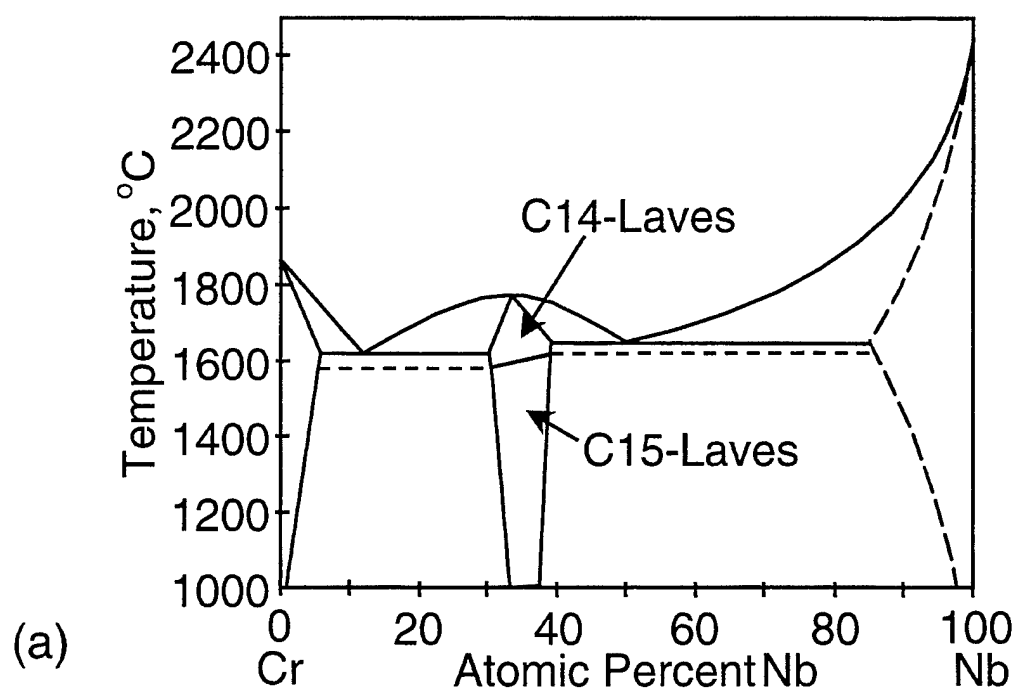34. Y. Yang and Y.A. Chang (University of Wisconsin – Madison), private communication, 2002.

Figure 1. Phase diagrams of the Nb-Cr (a) and Ti-Cr (b) binary systems showing the stability of three different Laves phases C14, C15 and C36 [22,23].
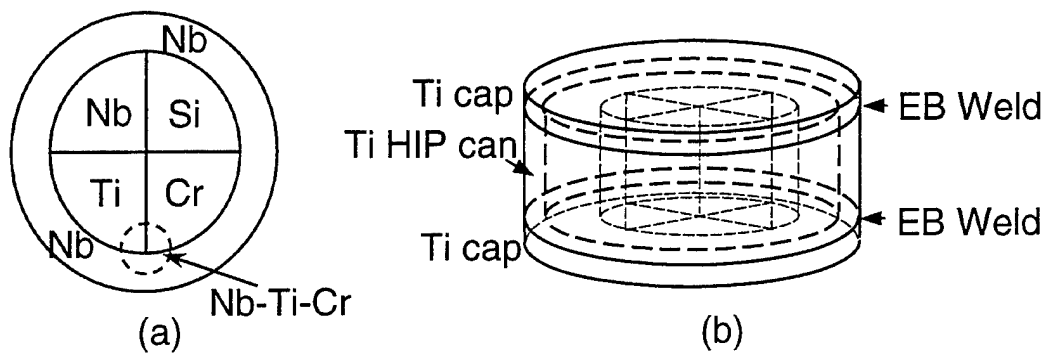
Figure 2. A diffusion multiple for efficient mapping of the Nb-Cr-Ti ternary phase diagrams: (a) cross-sectional view; and (b) perspective view. See text for the size of the sample. The results reported in this work were all obtained from the tri-junction corner of Nb – Cr – Ti circled in (a).
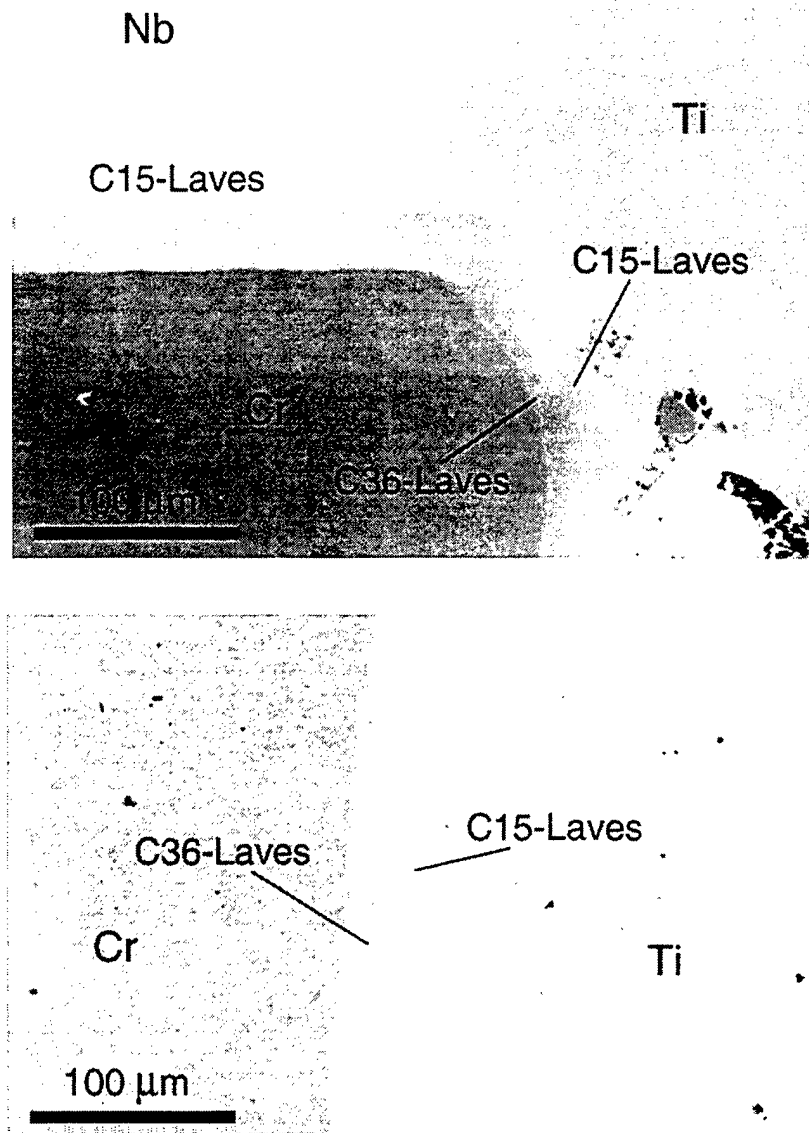
Figure 3. Backscatter electron SEM images of the Nb – Cr – Ti tri-junction area of the diffusion multiple (Fig. 2) annealed at 1150°C for 2000 hours showing the formation of the Laves phases C15 and C36: (a) the overall tri-junction; and (b) image taken from the Ti-Cr binary region of the diffusion multiple showing the formation of both C15 and C36 Laves phases.
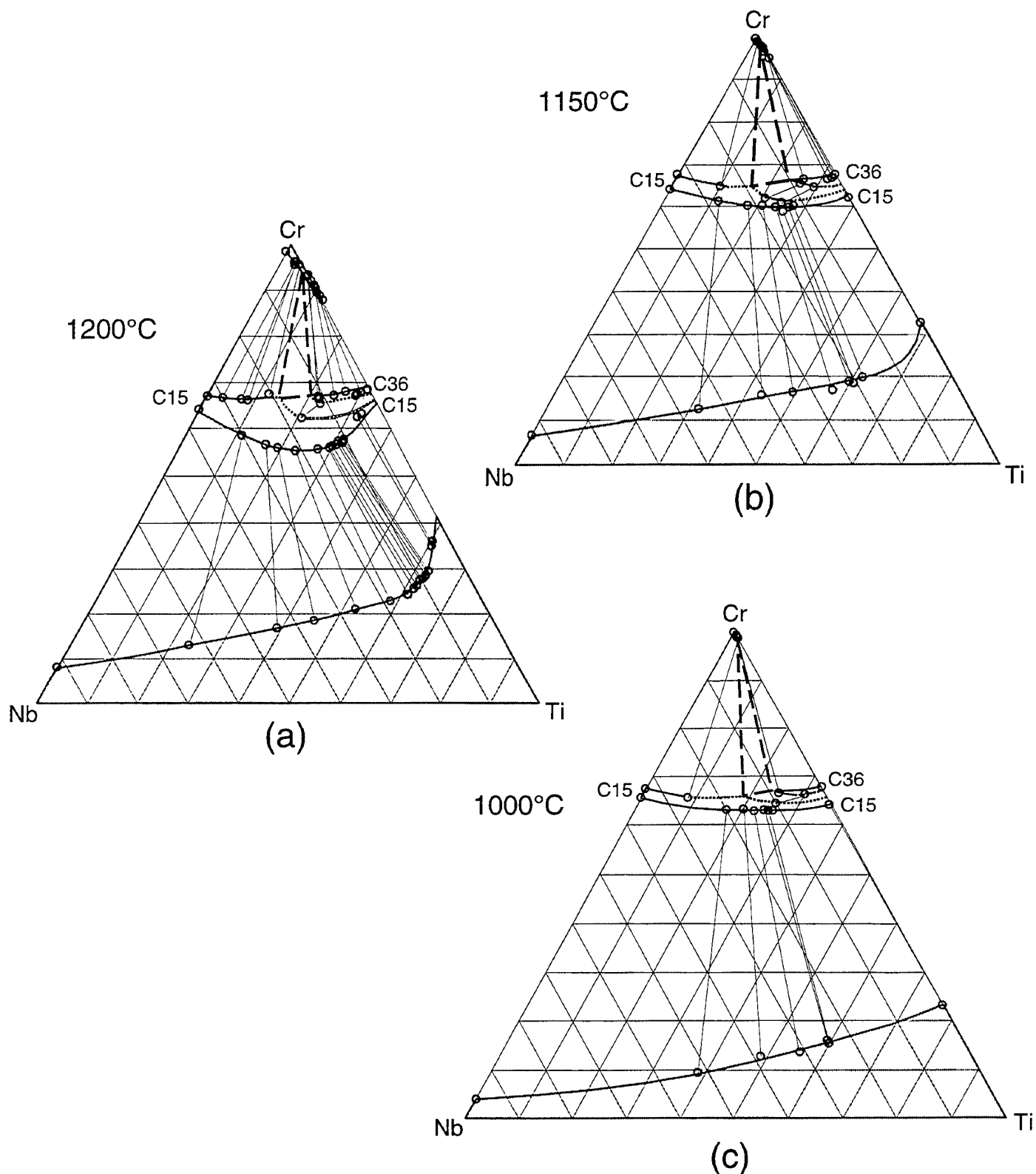
Figure 4. Isothermal sections of the Nb-Cr-Ti system obtained from the Nb-Cr-Ti tri-junction area of the diffusion multiples (Fig. 2): (a) 1200°C, (b) 1150°C, and (c) 1000°C. The phase diagrams are plotted in atomic percent axes with the numbers removed for simplicity. The dashed triangles indicate estimated three-phase equilibria and the open circles show the tie-line compositions. The tie-lines are shown with light dotted lines. The heavy dotted lines represent estimated phase boundaries.
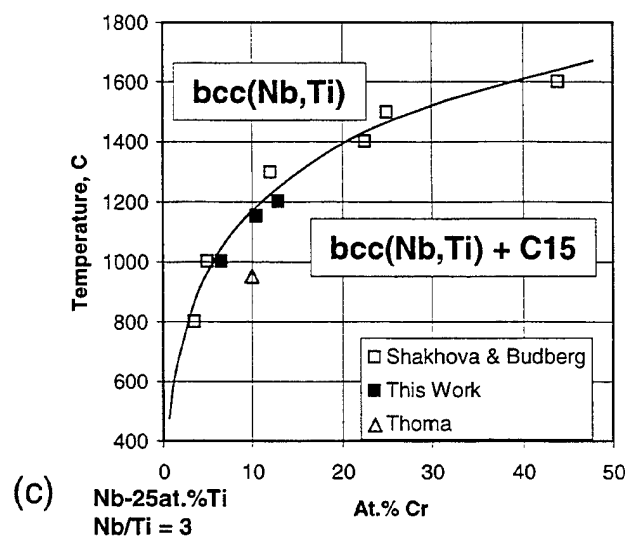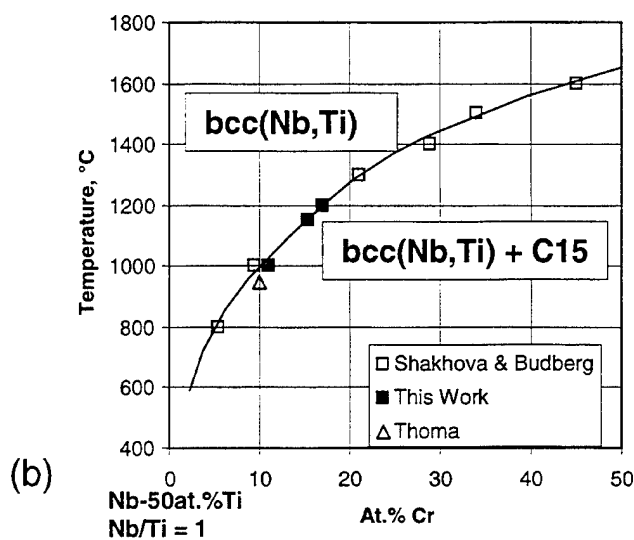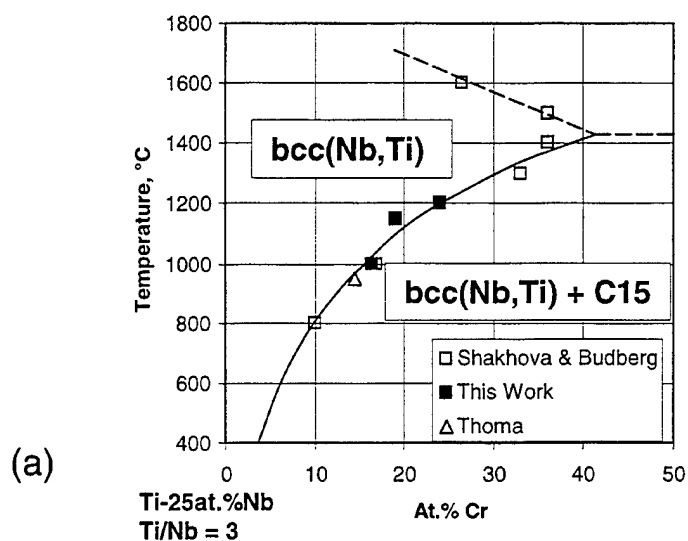
10

Figure 5. Comparison of data on the Cr solubility in bcc(Nb,Ti) solid solution of three different compositions: (a) Ti-25 at.%Nb alloy (Ti/Nb = 3), (b) Nb-50at.%Ti alloy (Nb/Ti = 1), and (c) Nb-25 at.%Ti (Nb/Ti = 3) alloy. The results from three independent investigations show excellent agreement.

11

Mapping of the Nb-Ti-Si Phase Diagram Using Diffusion Multiples

J.-C. Zhao, M.R. Jackson, and L.A. Peluso

Mapping of the Nb-Ti-Si Phase Diagram Using Diffusion Multiples

J.-C. Zhao, M.R. Jackson, and L.A. Peluso
General Electric Company
GE Global Research Center, P.O. Box 8, Schenectady, NY 12301, USA

ABSTRACT

A high-efficiency diffusion-multiple approach was employed to map the phase diagram of the Nb-Ti-Si ternary system which is critical for the design of niobium silicide-based composites. These composites have high potential as a replacement for Ni-base superalloys for jet engine applications. Titanium is one of the most important elements for oxidation resistance and fracture toughness enhancement. Three isothermal sections of Nb-Ti-Si at 1000, 1150 and 1200°C were constructed from the results obtained from diffusion multiples using scanning electron microscopy (SEM), electron probe microanalysis (EPMA), and electron backscatter diffraction (EBSD). Extremely high solubility of Nb in Ti_5Si_4 (up to ~ 46 at.%Nb at 1200°C, substituting for Ti) was observed.

Keywords: Nb-Ti-Si, diffusion multiple, silicide, phase diagram.

1. INTRODUCTION

Niobium silicide-based composites show great promise for applications as the next generation turbine airfoil materials with significantly higher operating temperatures than current generation advanced Ni-base superalloys [1-6]. The Nb-Si binary composites have excellent creep strength, but poor oxidation resistance and poor room temperature fracture toughness [1-2]. Alloying with Ti significantly improves the high temperature oxidation resistance and room temperature fracture toughness. The potential application of these composites at very high temperatures requires a balance of high creep resistance, high oxidation resistance, and good low-temperature damage tolerance (fracture toughness). To achieve such a property balance, elements such as Ti, Cr, Hf and Al are added to the composites and significant progress has been made in improving the properties of the composites. Some of the alloying concepts were discussed by Zhao *et al.* [7]. The advanced design of the composites requires a fair understanding of the phase equilibria in the Nb-Si-Ti-Cr-Hf-Al system. Since a reasonable definition of the Nb-Hf-Si system has been achieved [8-10], our effort has been focused on the ternary systems Nb-Cr-Si, Nb-Si-Al, Nb-Cr-Al, Ti-Si-Cr, Ti-Si-Al, Ti-Cr-Al, Nb-Ti-Si, Nb-Ti-Cr, and Nb-Ti-Al. Other ternary systems related to the six-element system such as Nb-Ti-Hf, Nb-Cr-Hf, Nb-Hf-Al, Ti-Si-Hf, Ti-Cr-Hf, and Cr-Hf-Al have either good data or are less critical for the design of the Nb silicide composites. We will report the results of the Nb-Ti-Si system in the present paper and the results of other systems will be communicated separately.

The high-efficiency "diffusion multiple" approach [11-14] is ideally suited for mapping phase diagrams of these ternary systems. It would take thousands of alloys to determine the nine ternary systems using the traditional one-alloy-at-a-time (equilibrated alloy) approach. For instance, it took Goldschmidt and Brand [15] about 220 alloys to map just the Nb-Cr-Si ternary

1

system and similarly about 135 alloys were employed by Lysenko et al. [16] to determine the Ti-Cr-Si system. These alloys have very high melting temperatures and are difficult to make and to homogenize. Extra effort also needs to be taken to avoid interstitial (oxygen, nitrogen, carbon, etc.) contamination during alloy casting and heat treatment. In contrast, the diffusion multiple approach needs only a few cast alloys and the samples were easy to make, and safe-guarding against the interstitial contamination can be very easily implemented as will be discussed later. The general diffusion multiple approach is discussed in detail previously [11-14] and has been successfully applied to many alloy systems.

The constitutive binary phase diagrams of the Nb-Ti-Si system, i.e. Nb-Si [7,17-19], Ti-Si [20,21], and Nb-Ti [20] and are already available in the literature. The Nb-Si phase diagram was assessed by Schlesinger et al. [17]. A slight revision, Fig. 1(a), was made [7] with the eutectoid temperature being adjusted to ~1700°C based on the result reported by Mendiratta and Dimiduk [18] and the L ↔ bcc(Nb) + Nb_3Si eutectic reaction being adjusted to 1880°C and 18.2 at.%Si to reflect the temperature and composition obtained by Bewlay et al. [19] on directionally solidified (DS) Nb-Si alloys. The Nb_5Si_3 phase forms after the decomposition of the Nb_3Si phase via an eutectoid reaction Nb_3Si ↔ bcc(Nb) + Nb_5Si_3 at ~1700°C, or as the primary solidification product in hypereutectic alloys. Two different Nb_5Si_3 phases based on the same crystal structure (tI32) with different lattice parameters were reported. The high-temperature and low-temperature phases are designated βNb_5Si_3 and αNb_5Si_3 respectively. The Ti-Si system is very similar to Nb-Si except that the Ti_3Si is stable at lower temperatures (< 1170°C) as compared to Nb_3Si which is stable between ~1700 and 1980°C. There are five intermetallic compounds, Ti_3Si, Ti_5Si_3, Ti_5Si_4, TiSi, and $TiSi_2$ in the Ti-Si binary system. Nb-Ti is a very simple system without any intermetallic compound [20]. The crystal structures of the phases in the binary system are listed in Table 1 [22].

Table 1. Crystal structure of phases in the Nb-Ti-Si ternary system [22].

System	Conditions	Pearson Symbol	Space Group	Lattice Parameters			
				a	b	c	γ
αTi	LT	hP2	P6₃/mmc	0.29512		0.46845	120°
βTi	HT	cI2	Im3m	0.33066			
Nb		cI2	Im3m	0.33067			
Si		cF8	Fd3m	0.54309			
Nb_3Si	1770-1980°C	tP32	P4₂/n	1.0224		0.5189	
βNb_5Si_3	1650-2520°C	tI32	I4/mcm	1.0040		0.5081	
αNb_5Si_3	≤ 1940°C	tI32	I4/mcm	0.6571		1.1889	
$NbSi_2$	≤ 1940°C	hP9	P6₂22	0.481		0.661	120°
TiSi	≤ 1570°C	oP8	Pnma	0.6544	0.3638	0.4997	
TiSi	≤ 1570°C		Pmm2	0.3618	0.6492	0.4973	
Ti_3Si	≤ 1170°C	tP32	P4₂/n	1.039		0.517	
$TiSi_2$	≤ 1485°C	oF24	Fddd	0.82671	0.48000	0.85505	
Ti_5Si_3	≤ 2130°C	hP16	P6₃/mcm	0.74610		0.51508	120°
Ti_5Si_4	≤ 1920°C	tP36	P4₁2₁2	0.6702		1.2174	

Since Ti is one of the most important alloying elements in Nb silicide composites, a detailed study of the Nb and Ti rich part of the Nb-Ti-Si phase diagram was carried out by Bewlay et al. [23, 24], and Subramanian et al. [25]. The results are summarized in Fig. 1(b) as a projection of a three-dimensional (3D) phase diagram. The liquidus projection was constructed by Bewlay et al. [23] by examining the microstructure of DS alloys. Isothermal sections at 1340 and 1500°C have

been measured in order to construct the whole ternary diagram [24-25]. It can been seen that Ti:
1) stabilizes Nb₃Si to lower temperatures; 2) promotes the formation of a hexagonal Ti₅Si₃ phase
(hP16); and, 3) reduces the L ↔ bcc(Nb) + Nb₃Si eutectic temperature, i.e. the melting
temperature of the composites. Although additions of Ti to the composites have very beneficial
effects on both oxidation resistance and room temperature fracture toughness [26], the amount of
the Ti addition has to be limited to < 25 at.% in order to maintain an eutectic temperature of >
1700°C, and to avoid the formation of the hP16 Ti₅Si₃ phase, which was found to be detrimental
to the creep-rupture strength of the composites [27]. It is important to maintain the melting
(eutectic) temperature of the composites above 1700°C to retain good strength to the potential use
temperatures (1200 to 1400°C).

All previous work has been focused on the Nb and Ti rich alloys with Si concentration ≤ 37.5
at.%; and most work was performed at the temperature range of 1340 and 1500°C. The present
work will provide useful data in the temperature range of 1000 to 1200°C. Our work will also
provide phase equilibrium information for higher Si concentration.

2. EXPERIMENTAL METHOD

A diffusion multiple with the cross-section view shown schematically in the Fig. 2(a) was
made. The inner and outer circle diameters were 15.6 and 25.4 mm respectively to guarantee that
the dimensions of the pure element pieces are much larger than the diffusion distance, thus there
will be pure elements left after the long term diffusion anneal. High purity Nb, Cr, Si and Ti were
machined into the proper shapes (quarter pies and round shells, Fig. 2(a)) by electro-discharge
machining (EDM). The re-cast layer on the EDM'ed surfaces was removed by mechanical
grinding to make clean surfaces. The pieces were ultrasonically cleaned in methanol and then
assembled into the geometry shown in Fig. 2(a). The height of all pieces was 25 mm. The
assembled diffusion multiples were then loaded into hot isostatic press (HIP) cans made of
commercial purity Ti, which is schematically shown in Fig. 2(b). A 25 µm layer of Ta was placed
between the diffusion multiples and the HIP cans to isolate any interstitial contaminants that may
diffuse into the HIP can from the quartz capsule during long term annealing. The top and bottom
caps of the HIP can were electron beam welded. HIPing was performed at 1204 °C, 200MPa for 4
hrs. The HIP cans containing the diffusion multiples were then encapsulated in evacuated quartz
tubes backfilled with pure argon. Since both Nb and Ti are susceptible to oxygen and nitrogen
contamination, it is critical to keep the diffusion multiples from interstitial elements. To further
absorb any oxygen that may diffuse into the quartz tube, a packet of pure yttrium was wrapped in
Ta foils and was then placed inside each quartz tube. Thus, the diffusion multiples were protected
from the intersitials (O, N, C, etc.) by the quartz tube, the pure yttrium absorber, the Ti HIP can,
and the Ta diffusion barrier. The encapsulated samples were then annealed at three different
temperatures: 1200°C for 1000 hrs, 1150°C for 2000 hrs, and 1000°C for 4000 hrs. Three
identical diffusion multiples were made and each was annealed at one temperature. After the heat
treatment, the diffusion multiples were taken from the argon furnace and cooled down to ambient
temperature by breaking the quartz tube and quenching the diffusion multiples into water. The
diffusion multiples were then cut into halves parallel to the ends using wire EDM, ground and
polished.

The samples were first examined using scanning electron microscopy (SEM), especially the
backscatter electron (BSE) imaging. Most phases could be seen (although not identified
explicitly) in the BSE images due to the differences in their average atomic weight. Quantitative
EPMA analysis was performed on a CAMECA (Paris, France) microprobe using 15 kV voltage,

40 nA current and a 40° take-off angle. Electron backscatter diffraction (EBSD) analysis was performed to obtain crystal structure information of the phases formed in the diffusion multiple. Phase identification was accomplished by a direct match of the diffraction bands in the experimental backscatter pattern with simulated patterns generated using known structure types and lattice parameters. A detailed discussion on this powerful EBSD technique can be found in Schwartz *et al.* [28].

3. RESULTS AND DISCUSSION

A backscatter electron image taken from the Nb-Ti-Si tri-junction (schematically circled area in Fig. 2(a)) of the diffusion multiple annealed at 1150°C for 2000 hrs is shown in Fig. 3. During the long-term diffusion treatment, extensive interdiffusion among Nb, Ti and Si took place, and all the equilibrium phases, including the intermetallic phases, formed by interdiffusion reactions. By performing EPMA analysis in this tri-junction area, an extremely large amount of phase equilibrium information was obtained. Based on the compositional information from EPMA, EBSD analysis was also performed to identify the crystal structure of the phases. An EBSD pattern taken from the $NbSi_2$ phase is shown in Fig. 4.

Figure 5 is a backscatter electron image taken from the Ti-Si binary area of the diffusion multiple annealed at 1150°C for 2000 hrs, showing the formation of several Ti silicides: Ti_5Si_3, Ti_5Si_4, TiSi, and $TiSi_2$. We did not see the formation of the Ti_3Si phase at this temperature, which indicates that the peritectoid reaction temperature of Ti + Ti_5Si_3 ⟺ Ti_3Si should be below 1150°C. The current Ti-Si binary phase diagram places this temperature at 1170°C. Our result clearly shows the absence of this phase at 1150°C. We did not think this is a missing phase situation since, this phase clearly appeared in the Nb-containing regions (Fig. 3) and it gradually disappeared in very Ti-rich alloys at this temperature. This phase was observed in the binary Ti-Si area in the diffusion multiple annealed at 1000°C for 4000 hrs. Therefore, the Ti + Ti_5Si_3 ⟺ Ti_3Si peritectoid reaction must be below 1150°C, but above 1000°C.

The 1000°C isothermal section constructed based on both EPMA and EBSD data is shown in Fig. 6(a). The tie-lines are defined from the EPMA line profiles by taking advantage of the local equilibrium at interfaces formed among the phases. We clearly defined phase equilibria in Si-rich (Si > 37.5 at.%) alloys for which previous data did not exist. The following three-phase equilibria were observed: $Si+NbSi_2+TiSi_2$, $NbSi_2+TiSi_2+TiSi$, $NbSi_2+TiSi+Ti_5Si_4$, $NbSi_2+Nb_5Si_3+Ti_5Si_4$, $Ti_5Si_4+Nb_5Si_3+Ti_5Si_3$, for Si > 37.5 at.%. These phase equilibria are consistent with thermodynamic prediction by Liang and Chang [28]. Very high solubility (~36 at.% at 1000°C) of Nb in Ti_5Si_4 was observed, which thermodynamic assessment cannot predict without experimental data input. The phase equilibria in the metal-rich part (Si < 37.5 at.%) of the phase diagram were consistent with the observations of Bewlay *et al.* [23, 24], and Subramanian *et al.* [25], e.g., $Nb_5Si_3+Ti_5Si_3+Ti_3Si$ and $Nb_5Si_3+ Ti_3Si+bcc(Nb,Ti)$ three-phase equilibria were observed. Since the results of Bewlay *et al.* [23, 24], and Subramanian *et al.* [25] were at 1340 and 1500°C, a direct comparison of the tie-triangles was not possible.

The isothermal sections obtained from the Nb-Ti-Si tri-junction region of the diffusion multiple heat treated at 1150 °C for 2000 hours and 1200 °C for 1000 hours are shown in Figure 6(b) and (c). The basic three-phase equilibria remained the same with some changes of solubilities with temperature. For instance, the Nb solubility in Ti_5Si_4 changed from ~36 at.%, to 45 at.% to 47 at.% as the temperature changed from 1000 to 1150 to 1200 °C. The solubility of

4

Ti in Nb_5Si_3 increased from 18 at.% to 26 at.% to 28 at.% as the temperature changed from 1000 to 1150 to 1200 °C.

The phase equilibrium information of the Nb-Ti-Si system is very useful for the design of both Nb silicide composites and coatings for these composites. This is one of the key systems in the developing thermodynamic database for Nb silicide based systems [10,29,30]. A slight modification of thermodynamic description of this Nb-Ti-Si system will be necessary to take into account the high solubility of Nb in Ti_5Si_4.

4. CONCLUSIONS

Three isothermal sections of Nb-Ti-Si at 1000, 1150 and 1200°C were constructed from the results obtained from three diffusion multiples using scanning electron microscopy (SEM), electron probe microanalysis (EPMA), and electron backscatter diffraction (EBSD). The results provide a clear definition of the phase equilibria in Si-rich (Si > 37.5 at.%) alloys for which previous experimental data were not available. The observed three phase equilibria were consistent with thermodynamic prediction made by Liang and Chang. Extremely high solubility of Nb in Ti_5Si_4 (up to ~ 46 at.%Nb at 1200°C, substituting for Ti) was observed. The following three-phase equilibria were observed: $Si+NbSi_2+TiSi_2$, $NbSi_2+TiSi_2+TiSi$, $NbSi_2+TiSi+Ti_5Si_4$, $NbSi_2+Nb_5Si_3+Ti_5Si_4$, $Ti_5Si_4+Nb_5Si_3+Ti_5Si_3$, $Nb_5Si_3+Ti_5Si_3+Ti_3Si$ and $Nb_5Si_3+Ti_3Si+bcc(Nb,Ti)$, and $Ti_5Si_3+Ti_3Si+bcc(Ti,Nb)$. Our experimental results show that the peritectoid reaction temperature of $Ti + Ti_5Si_3 \Leftrightarrow Ti_3Si$ should be below 1150°C and above 1000°C for the binary Ti-Si system (The current Ti-Si phase diagram placed this temperature at 1170°C).

REFERENCES

1. M.G. Mendiratta and D.M. Dimiduk, *Mat. Res. Soc. Symp. Proc.*, 133 (1989), 441- 446.
2. M.R. Jackson, B.P. Bewlay, R.G. Rowe, D.W. Skelly, and H.A. Lipsitt, *JOM*, 48 (1996), 39-44.
3. P.R. Subramanian, M.G. Mendiratta, and D.M. Dimiduk, *JOM*, 48 (1996), 33-38.
4. B.P. Bewlay, J.J. Lewandowski, and M.R. Jackson, *JOM*, 49 (1997), 44-45.
5. S.J. Balsone, B.P. Bewlay, M.R. Jackson, P.R. Subramanian, J.-C. Zhao, A. Chatterjee, and T. Heffernan, in *Structural Intermetallics 2001* (K. Hemker, D.M. Dimiduk, H. Clemens, R. Darolia, H. Inui, J.M. Larsen, V.K. Sikka, M. Thomas, and J.D. Whittenberger, eds.), TMS, Warrendale, PA, 2001, 99-108

6. B.P. Bewlay, M.R. Jackson, J.-C. Zhao, and P.R. Subramanian, *Metall. Mater. Trans.*, Accepted November 2002.
7. J.-C. Zhao, B.P. Bewlay, M.R. Jackson, and L.A. Peluso, in *Structural Intermetallics 2001* (K. Hemker, D.M. Dimiduk, H. Clemens, R. Darolia, H. Inui, J.M. Larsen, V.K. Sikka, M. Thomas, and J.D. Whittenberger, eds.), TMS, Warrendale, PA, 2001, 483-491.
8. B.P. Bewlay, R.R. Bishop, and M.R. Jackson, *Z. Metallkde.*, 90 (1999), 413-422.
9. J.-C. Zhao, B.P. Bewlay, and M.R. Jackson, *Intermetallics*, 9 (2001) 681-689.
10. Y. Yang, Y.A. Chang, J.-C. Zhao, and B.P. Bewlay, *Intermetallics,* Accepted November 2002.
11. J.-C. Zhao, *Adv. Eng. Mater.*, 3 (2001), 143-147.
12. J.-C. Zhao, *J. Mater. Res.*, 16 (2001), 1565-1578.
13. J.-C. Zhao, M.R. Jackson, L.A. Peluso, and L. Brewer, *MRS Bulletin*, 27 (2002) 324-329.
14. J.-C. Zhao, M.R. Jackson, L.A. Peluso, and L. Brewer, *JOM*, 54 (7) (2002) 42-45.
15. H.J. Goldschmidt and J.A. Brand, *J. Less-Common Met.*, 3 (1961), 34-43.
16. L.A. Lysenko, V.Ya. Markiv, O.V. Tsybukh, and E.I. Gladyshevskii, *Inorganic Mater.*, 7(1) (1971), 157-159.
17. M.E. Schlesinger, H. Okamoto, A.B. Gokhale, and R. Abbaschian, *J. Phase Equilibria*, 14 (1993), 502.
18. M.G. Mendiratta and D.M. Dimiduk, *Scripta Metall. Mater.*, 25 (1991), 237-242.
19. B.P. Bewlay, H.A. Lipsitt, M.R. Jackson, W.J. Reeder, and J.A. Sutliff, *Mater. Sci. Eng.*, A192/193 (1995), 534-543.
20. J.L. Murray: in *Binary Alloy Phase Diagrams*, 2nd ed., T.B. Massalski, ed., ASM International, Materials Park, OH, 1990.
21. H.J. Seifert, H.L. Lukas and G. Petzow, *Z. Metallkde.*, 87 (1996), 2-13.
22. P. Villars, L.D. Calvert, *Pearson's Handbook of Crystallographic Data for Intermetallic Phases*, 2nd ed., ASM International, Materials Park, OH, 1991.
23. B.P. Bewlay, M.R. Jackson, and H.A. Lipsitt, *J. Phase Equilibria*, 18 (1997), 264-278.
24. B.P. Bewlay, M.R. Jackson, and R.R. Bishop, *J. Phase Equilibria*, 19 (1998), 577-586.
25. P.R. Subramanian, M.G. Mendiratta, and D.M. Dimiduk, *Mat. Res. Soc. Symp. Proc.*, 322 (1994), 491- 502.
26. M.R. Jackson, R. G. Rowe, and D. W. Skelly, *Mat. Res. Soc. Symp. Proc.*, 364 (1995), 1339-1344.
27. B.P. Bewlay, M.R. Jackson, and M.F.X. Gigliotti, in *Intermetallic Compounds - Principles and Practice*, Vol. 3, Eds. R.L. Fleischer and J.H. Westbrook, John Wiley, New York, 2002, 541-560.
28. *Electron Backscatter Diffraction in Materials Science*, edited by A.J. Schwartz, M. Kumar, and B.L. Adams (Kluwer Academic / Plenum Publishers, New York, 2000).
29. H. Liang and Y.A.Chang, *Intermetallics*, 7 (1999) 561.
30. Y. Yang and Y.A. Chang (University of Wisconsin – Madison), private communication, 2002.
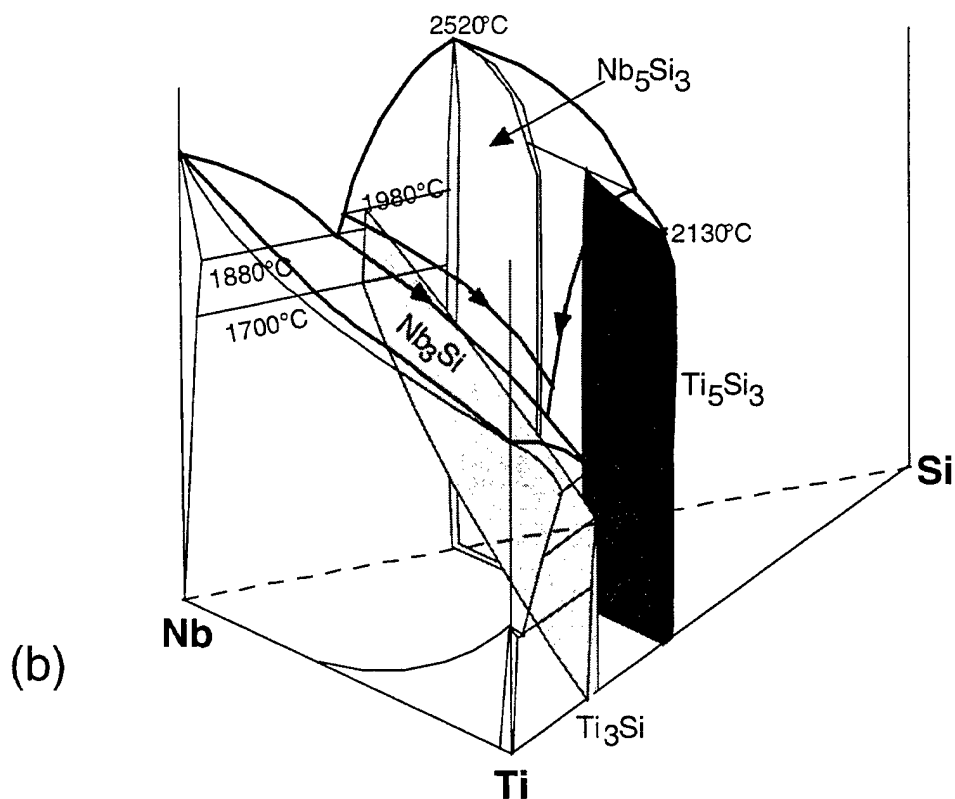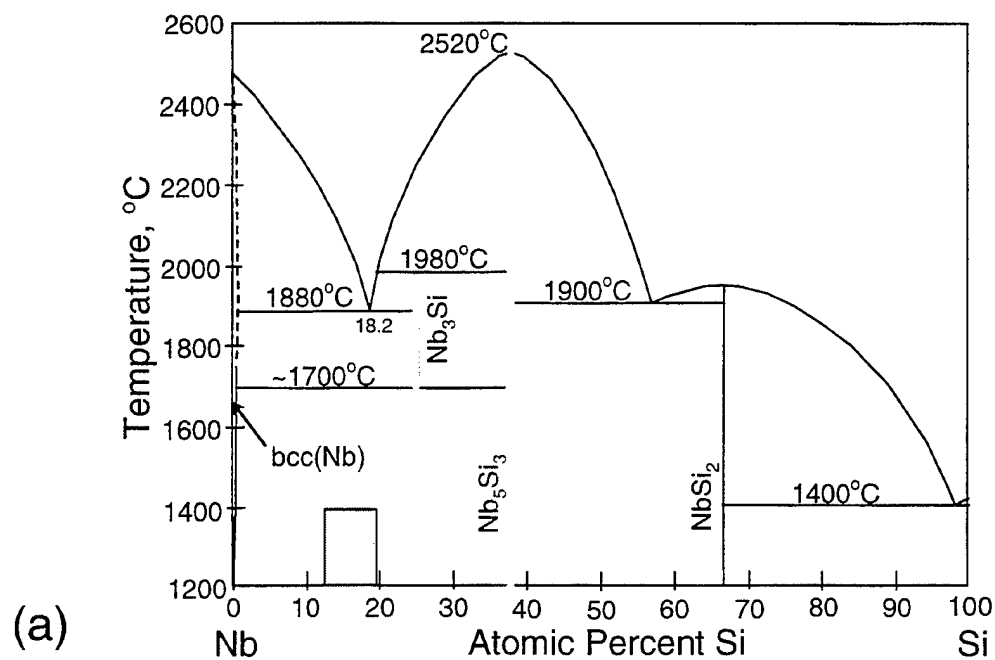
Figure 1. Phase diagrams of the Nb-Si binary (a) and the Nb-Ti-Si ternary system (b). The Nb-Si binary was based on Schlesinger *et al.* [17] and revised [7] based on results of Mendiratta and Dimiduk [18] and Bewlay *et al.* [19]. The shaded box shows the composition range and potential use temperatures of the composites. The schematic 3D phase diagram of the Nb-Ti-Si ternary system (b) was based on the work of Bewlay *et al.* [23,24].
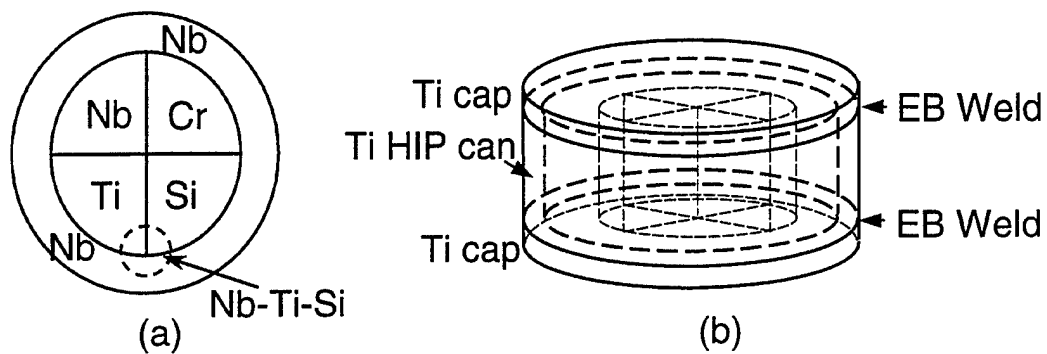
Figure 2. A diffusion multiple for efficient mapping of the Nb-Ti-Si ternary phase diagrams: (a) cross-sectional view; and (b) perspective view. See text for the size of the sample. The results reported in this work were all obtained from the tri-junction corner of Nb – Ti – Si circled in (a).
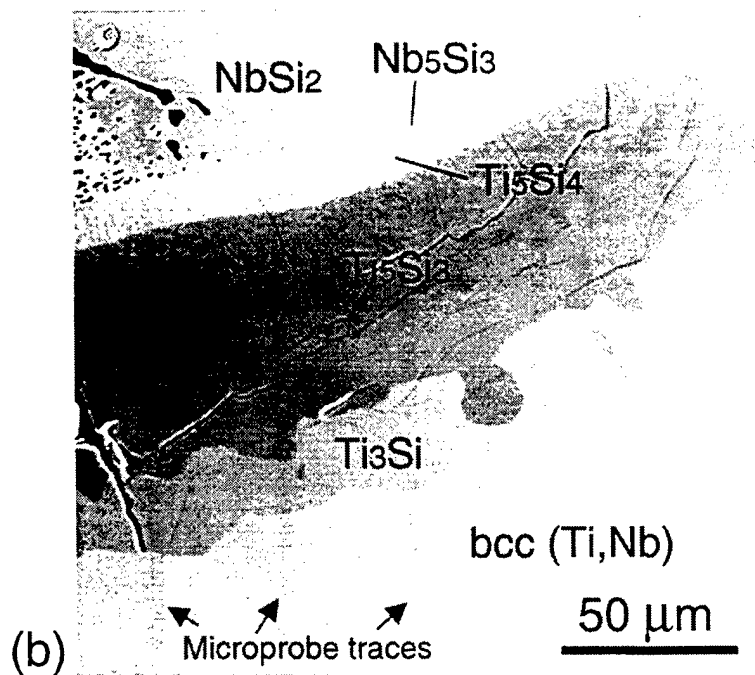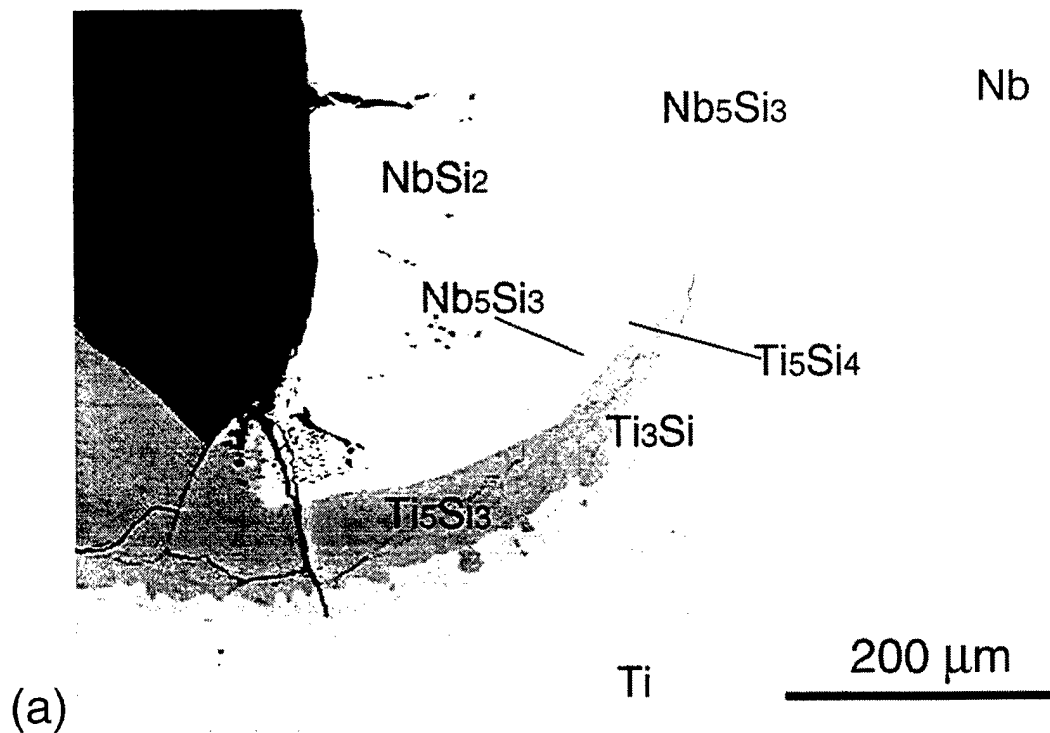
Figure 3. Backscatter electron SEM images of the Nb-Ti-Si tri-junction area of the diffusion multiple (Fig. 2) annealed at 1150°C for 2000 hrs showing the formation of many different intermetallic compounds: (a) a low-magnification image showing the overall tri-junction (the pure Si piece broke away during wire EDM cutting after the heat treatment; and (b) a high-magnification image of the location shown in (a) as a box showing the phases.
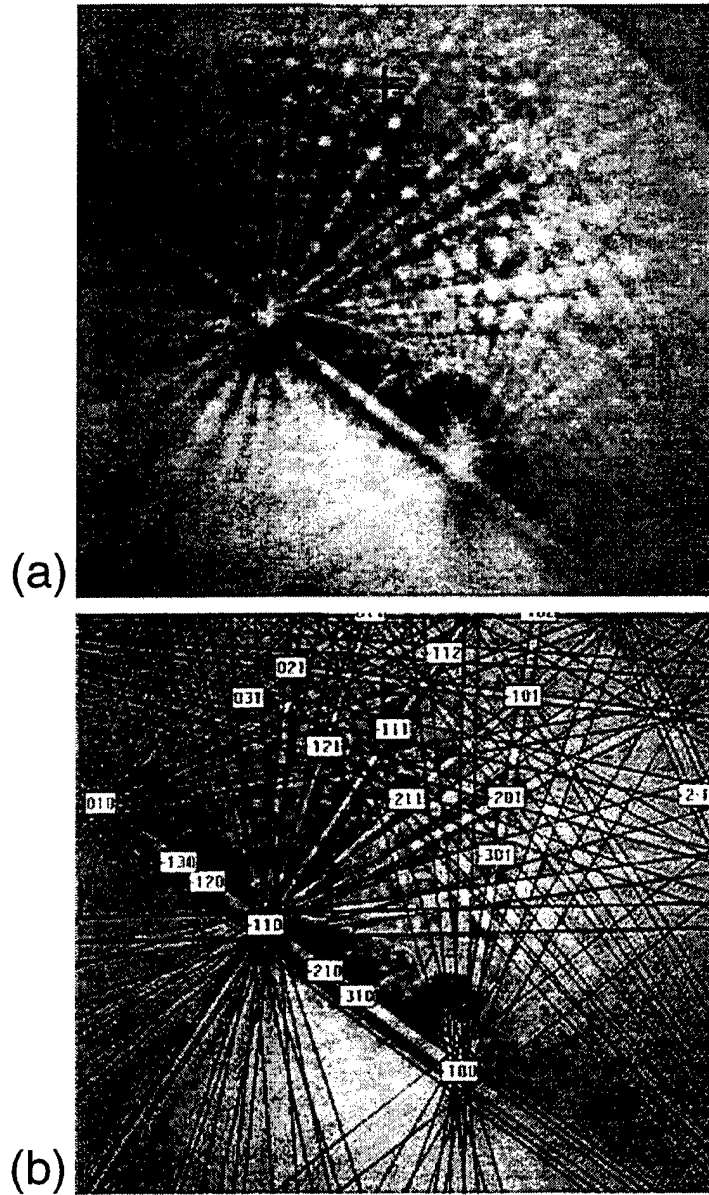
Figure 4. Un-indexed (a) and indexed (b) EBSD pattern of the $NbSi_2$ phase formed in the diffusion multiple shown in Fig. 2 at the tri-junction region of Nb-Ti-Si.
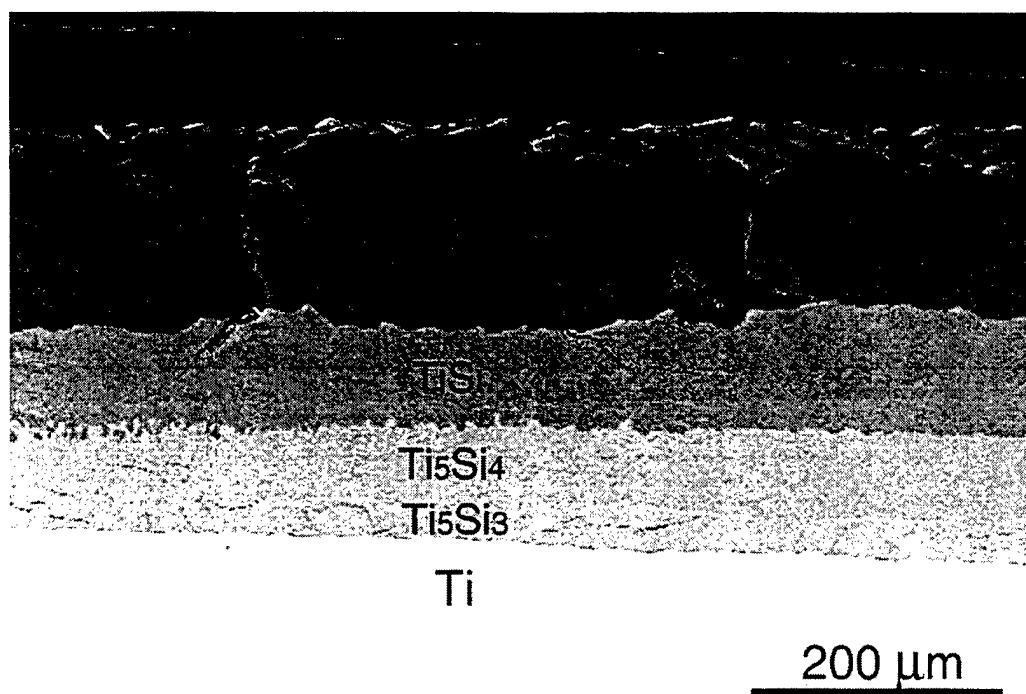
Figure 5. Backscatter electron SEM image of the Ti-Si binary area of the diffusion multiple (Fig. 2) annealed at 1150°C for 2000 hrs showing the formation of all the Ti silicides.
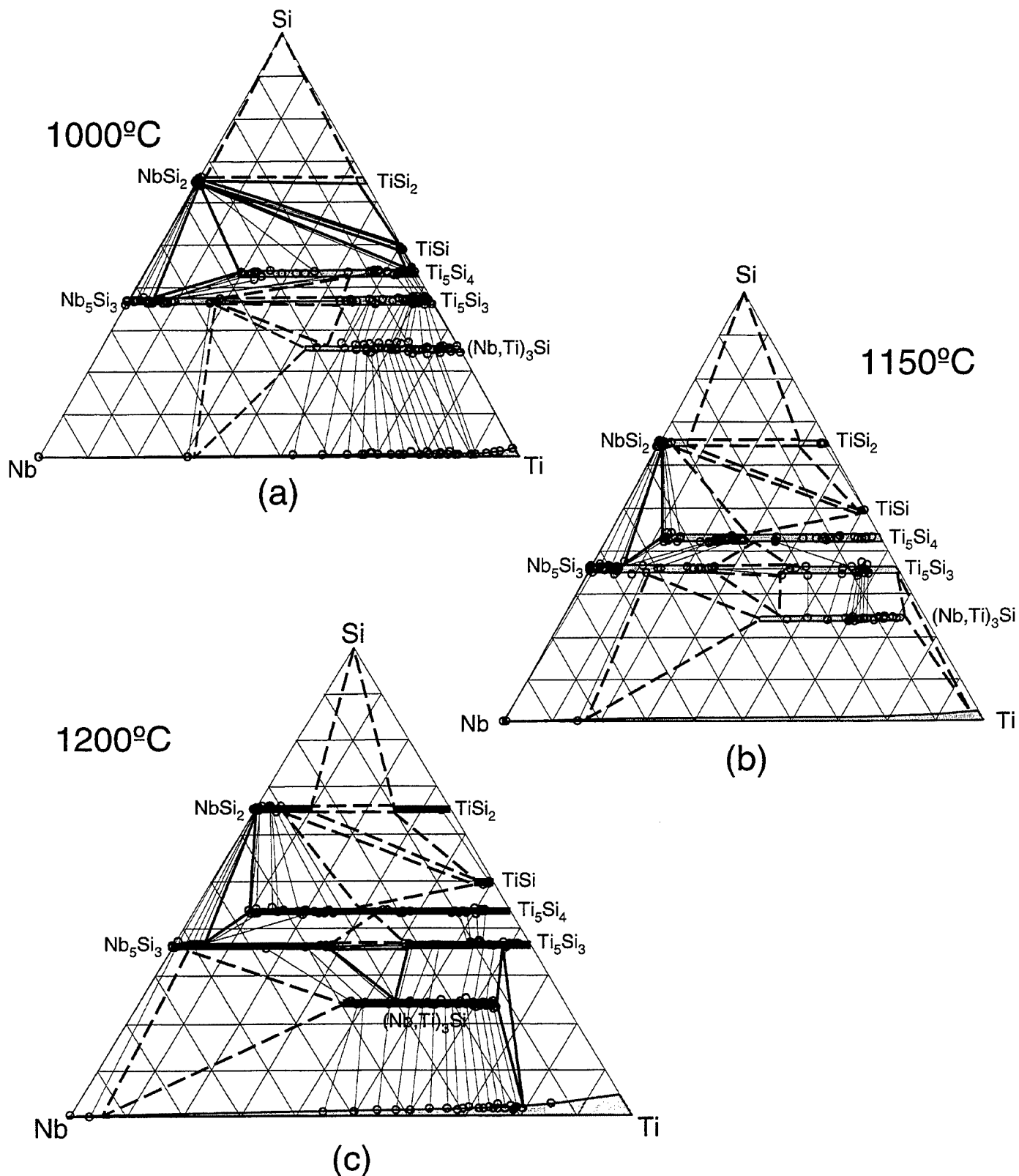
Figure 6. Isothermal sections ((a) 1200°C, (b) 1150°C, and (c) 1000°C) of the Nb-Ti-Si system obtained from the Nb-Ti-Si tri-junction area of the diffusion multiples (Fig. 2). The phase diagram is plotted in atomic percent axes with the numbers removed for simplicity. The solid triangle indicates well-defined three-phase triangles and the open circles show the tie-line compositions. The tie-lines are shown with light dotted lines. The heavy dashed tie-triangles were estimated three-phase equilibria.

12

Mapping of the Ti-Cr-Al Phase Diagram Using a Diffusion Multiple

J.-C. Zhao, M.R. Jackson, and L.A. Peluso

Mapping of the Ti-Cr-Al Ternary
Phase Diagram using a Diffusion Multiple

J.-C. Zhao, M.R. Jackson, and L.A. Peluso
General Electric Company
GE Global Research Center, P.O. Box 8, Schenectady, NY 12301, USA

ABSTRACT

A high-efficiency diffusion-multiple approach was employed to map the phase diagram of the Ti-Cr-Al ternary system which is very valuable for the design of niobium silicide-based composites. These composites have high potential as a replacement for Ni-base superalloys for jet engine applications. Ti, Cr and Al are alloying elements for these composites, thus the Ti-Cr-Al phase diagram, especially stability of the oxidation-resistant Laves phase, is important information for the composite design. In addition, the Ti-Cr-Al system is also important for the design of gamma TiAl with Cr additions. A 1000°C isothermal section was constructed from the results obtained using electron probe microanalysis (EPMA) and electron backscatter diffraction (EBSD) from a diffusion multiple made up of Ti, Cr, TiAl$_3$ and TiSi$_2$. The obtained 1000°C agrees well with the literature results.

Keywords: Ti-Cr-Al, diffusion multiple, silicide, TiAl, phase diagram, composite.

1. INTRODUCTION

Niobium silicide-based composites show great promise for applications as the next generation turbine airfoil materials with significantly higher operating temperatures than current generation advanced Ni-base superalloys [1-6]. The Nb-Si binary composites have excellent creep strength, but poor oxidation resistance and poor room temperature fracture toughness [1-2]. Alloying with Ti, Cr and Al can improve the oxidation resistance. The potential application of these composites at very high temperatures requires a balance of high creep resistance, high oxidation resistance, and good low-temperature damage tolerance (fracture toughness). To achieve such a property balance, elements such as Cr, Ti, Hf and Al are added to the composites and significant progress has been made in improving the properties of the composites. Some of the alloying concepts were discussed by Zhao *et al.* [7]. The advanced design of the composites requires a fair understanding of the phase equilibria in the Nb-Si-Ti-Cr-Hf-Al system. Since a reasonable definition of the Nb-Hf-Si system has been achieved [8-10], our effort has been focused on the ternary systems Nb-Cr-Si, Nb-Si-Al, Nb-Cr-Al, Ti-Si-Cr, Ti-Si-Al, Ti-Cr-Al, Nb-Ti-Si, Nb-Ti-Cr, and Nb-Ti-Al. Other ternary systems related to the six-element system such as Nb-Ti-Hf, Nb-Cr-Hf, Nb-Hf-Al, Ti-Si-Hf, Ti-Cr-Hf, and Cr-Hf-Al have either good data or are less critical for the design of the Nb silicide composites. We will report the results of the Ti-Cr-Al system in the present paper and the results of other systems will be communicated separately.

In addition to being valuable for the design of the Nb silicide composites, the Ti-Cr-Al ternary phase diagram is also very useful for the design of gamma TiAl (γ-TiAl) and its coatings.

Chromium addition improves the room temperature ductility and the high temperature deformability of γ-TiAl [11,12]. For this reason, there were several previous investigations on the phase diagram of this ternary system in the past decade [13-26] in addition to a few investigations in the 1950s [27-30].

The high-efficiency "diffusion multiple" approach [31-34] is ideally suited for mapping phase diagrams of the above mentioned Nb and Ti-based ternary systems. It would take thousands of alloys to determine the nine ternary systems using the traditional one-alloy-at-a-time (equilibrated alloy) approach. For instance, it took Goldschmidt and Brand [35] about 220 alloys to map just the Nb-Cr-Si ternary system and similarly about 135 alloys were employed by Lysenko et al. [36] to determine the Ti-Cr-Si system. These alloys have very high melting temperatures and are difficult to make and to homogenize. Extra effort also needs to be taken to avoid interstitial (oxygen, nitrogen, carbon, etc.) contamination during alloy casting and heat treatment. In contrast, the diffusion multiple approach needs only a few cast alloys and the samples were easy to make, and safe-guarding against the interstitial contamination can be very easily implemented as will be discussed later. The general diffusion multiple approach is discussed in detail previously [31-34] and has been successfully applied to many alloy systems.

Table 1. Crystal structure of phases in the Ti-Cr-Al ternary system. The data were taken from Villars and Calvert [53] for most phases, from Knapp [54] for Al_9Cr_4, and from Audier, et al. [44] for Al_4Cr and $Al_{11}Cr_2$.

Phase	Pearson Symbol	Space Group	Lattice Parameters			
			a (nm)	b (nm)	c (nm)	γ
Al	cF4	Fm3m	0.40497			
Cr	cI2	Im3m	0.28847			
αTi	hP2	P6₃/mmc	0.29512		0.46845	120°
βTi	cI2	Im3m	0.33066			
AlCr₂		I4/mmm	0.3005		0.8649	
Al₈Cr₅		R3m	1.2813		0.7951	120°
Al₉Cr₄		Cubic	0.9123			
Al₄Cr	hP574	P6₃/mmc	1.998		2.467	119.33°
Al₁₁Cr₂		Cmcm	1.24	3.46	2.02	122.20°
Al₇Cr		C2/m	2.5256	0.7582	1.0955	128.68°
TiAl	tP4	P4/mmm	0.4001		0.4071	
Ti₃Al	hP8	P6₃/mmc	0.5780		0.4647	120°
TiAl₂	tI24	I4₁/amd	0.3976		2.436	
TiAl₃	tI8	I4/mmm	0.38537		0.85839	
Ti₂Al₅	tI16	I4/mmm	0.3917		1.6524	
αCr₂Ti C15 Laves	cF24	Fd3m	0.691			
βCr₂Ti C36 Laves	hP24	P6₃/mmc	0.4932		0.8005	120°
γCr₂Ti C14 Laves	hP12	P6₃/mmc	0.4932		1.601	120°
τ-L1₂ (Ti₂CrAl₅)						

The constitutive binary phase diagrams of the Ti-Cr-Al system, i.e., Ti-Cr [37-39], Al-Cr [40-45] and Ti-Al [37, 46-52] are already available in the literature. There is still active research on the phase diagram of the Al-Cr binary system [42,43]. The Ti-Cr binary system has three Cr₂Ti-based Laves phases: the low-temperature cubic C15 (cF24) which is stable at temperatures <

2

1220 °C, the intermediate-temperature dihexagonal $C36$ ($hP24$) stable between 800-1270 °C, and the high-temperature hexagonal $C14$ ($hP12$) stable at temperatures > 1270 °C [37-39]. The effect of Al on the stabilization of these Laves phases can be appreciated by studying the Ti-Cr-Al system. We adopted the Ti-Al phase diagram by Okamoto [51] as our binary reference with the Al-rich part of the phase diagram recently refined by Palm *et al.* [52]. The crystal structures of the phases in the binary and the ternary system are listed in Table 1.

As mentioned earlier, there are more than a dozen investigations in the literature on the phase diagram of the Ti-Cr-Al ternary system [13-30]. The phase equilibria became clear only after the comprehensive assessments of Shao and Tsakiropoulos [19] as well as Schwanold and Inden [22], as shown in Fig. 1. However, discrepancies still exist on the phase boundaries and phase equilibria. For instance, the shape of the β(Ti,Cr,Al) single-phase region looks quite different in the two isothermal sections shown in Fig. 1. The β(Ti,Cr,Al) + α_2Ti$_3$Al + γTiAl three-phase triangle (equilibrium) also shows significant difference. Our work will help to define the ternary phase diagram, especially the 1000°C isothermal section.

2. EXPERIMENTAL METHOD

A diffusion multiple with the cross-section view shown schematically in the Fig. 2(a) was made. The dimensions were designed so that the pieces of pure elements and compounds are much larger than the diffusion distance, thus there will be pure elements and compounds left after the long-term diffusion annealing. To avoid the low melting point of Al, we used both TiSi$_2$ and TiAl$_3$ compounds as members of the diffusion multiple. Both these compounds were made by arc-melting. They were then cut into square bars of 7 x 7 x 25 mm using electro-discharge machining (EDM). A 14 x 14 mm square opening was cut from a 25 mm diameter by 25 mm height cylindrical piece of pure Ti. The square opening was cut across the whole height of the Ti piece. Pieces of high purity Ti and Cr in the dimension of 7 x 7 x 25 mm were also machined using EDM. The re-cast layer on the EDM'ed surfaces was removed by mechanical grinding to make clean surfaces. The pieces were ultrasonically cleaned in methanol and then assembled into the geometry shown in Fig. 2(a). The height of all pieces was 25 mm. The assembled diffusion multiple was then loaded into hot isostatic press (HIP) cans made of commercial purity Ti, which is schematically shown in Fig. 2(b). A 25 μm layer of Ta foil was placed between the diffusion multiple and the HIP can to isolate any interstitial contaminants that may diffuse into the HIP can from the quartz capsule during long-term annealing. The top and bottom caps of the HIP can were electron beam welded. HIPing was performed at 1204 °C, 200MPa for 4 hrs. The HIP can containing the diffusion multiple was then encapsulated in an evacuated quartz tube backfilled with pure argon. Since Ti is susceptible to oxygen and nitrogen contamination, it is critical to keep the diffusion multiple from interstitial elements. To further absorb any oxygen that may diffuse into the quartz tube, a packet of pure yttrium was wrapped in Ta foils and was then placed inside the quartz tube. Thus, the diffusion multiple was protected from the intersitials (O, N, C, etc.) by the quartz tube, the pure yttrium absorber, the Ti HIP can, and the Ta diffusion barrier. The encapsulated sample was then annealed at 1000°C for 2000 hours. After the heat treatment, the diffusion multiple was taken from the argon furnace and cooled down to ambient temperature by breaking the quartz tube and quenching the diffusion multiple into water. The diffusion multiple was then cut into halves parallel to the ends using wire EDM, ground and polished.

The samples were first examined using scanning electron microscopy (SEM), especially the backscatter electron (BSE) imaging. Most phases could be seen (although not identified explicitly) in the BSE images due to the differences in their average atomic weight. Quantitative

3

EPMA analysis was performed on a CAMECA (Paris, France) microprobe using 15 kV voltage, 40 nA current and a 40° take-off angle. Electron backscatter diffraction (EBSD) analysis was performed to obtain crystal structure information of the phases formed in the diffusion multiple. Phase identification was accomplished by a direct match of the diffraction bands in the experimental backscatter pattern with simulated patterns generated using known structure types and lattice parameters. A detailed discussion on this powerful EBSD technique can be found in Schwartz *et al.* [55].

3. RESULTS AND DISCUSSION

Backscatter electron images taken from the Ti-Cr-TiAl$_3$ tri-junction (schematically circled area in Fig. 2(a)) of the diffusion multiple annealed at 1000 °C for 2000 hrs are shown in Fig. 3. During the long-term diffusion treatment, extensive interdiffusion among Ti, Cr and Al took place, and many equilibrium phases, including the intermetallic phases, formed by interdiffusion reactions. Some of the phases which are difficult to see in Fig. 2(a) can be seen in Fig. 2(b) and (c). Some of the phases were very thin, thus we took into account overlapping and over-sampling effects when analyzing the EPMA data. Figure 4 is a backscatter electron image taken from the Ti-TiAl$_3$ binary area of the diffusion multiple, showing the formation of several Ti aluminides.

By performing EPMA analysis in this tri-junction area, a large amount of phase equilibrium information was obtained. Based on the compositional information from EPMA and by taking advantage of the local equilibrium at phase interfaces, an isothermal section of the Ti-Cr-Al system was constructed as shown in Fig. 5. Detailed procedures of phase diagram mapping using diffusion multiples can be found elsewhere [31-34].

Although the existing phase diagrams (Fig. 1) and the EPMA compositions (Fig. 5) can already differentiate all the phases in this particular Ti-Cr-Al ternary system, we performed EBSD analysis to confirm the crystal structures of the phases, especially the three different kinds of Laves phases. Unfortunately, since both C14 (*h*P12) and C36 (*h*P24) are hexagonal based structures with very similar crystal symmetry and very similar lattice parameters, EBSD usually has a hard time differentiating them. It is very easy to differentiate C15 from both C14 and C36 since C15 is cubic. When we put all the crystal structural information of the three Laves phases into the EBSD software and allowed the computer to index the phases from the diffusion multiple, we anticipated that the EBSD system would index both C14 and C36 interchangeably. To our surprise, the system seems able to differentiate C14 from C36 (maybe due to the slight symmetry differences). Based on the Ti-Cr binary phase diagram and the EBSD data, we differentiated the three Laves phases in the phase diagram shown in Fig. 5. Previous work has not been able to define the phase equilibrium between the Laves phases in this ternary system. Some EBSD patterns are shown in Fig. 6.

Due to the very stable nature of the τ-L1$_2$ (Ti$_2$CrAl$_5$) phase, the diffusion path between Cr and TiAl$_3$ passed through the τ-L1$_2$ phase. Thus, we did not obtain the phase equilibrium information at the very Al-rich end of the phase diagram (we used TiAl$_3$ instead of Al to make the diffusion multiple).

Our isothermal section (Fig. 5) agrees well with the ones constructed by Shao and Tsakiropoulos [19] as well as Schwanold and Inden [22], Fig. 1(a) and (b), although some difference was observed (There are also differences between Fig 1(a) and (b)). The excellent agreement on the odd-shaped β(Ti,Cr,Al) single-phase region between ours and that of Shao and

4

Tsakiropoulos (Fig. 1(a)) is especially dramatic, and together the results indicate that the shape shown by Schwanold and Inden may not be accurate. The obtained solubilities of Cr in α_2-Ti$_3$Al (~2.5at.%), γTiAl (4 to 6 at.%), TiAl$_2$ (~ 1 at.%), and Ti$_2$Al$_5$ (< 1 at.%) (Fig. 5) at 1000°C agree very well with the data assessed by both Shao and Tsakiropoulos and Schwanold and Inden, Fig. 1. The observed solubility of Al in the C14 Laves phase is 40 at.% which is in excellent agreement with the results in the literature, Fig. 1.

There is significant difference in the results reported in the literature on the β(Ti,Cr,Al) + α_2-Ti$_3$Al + γTiAl three-phase triangle (equilibrium), Fig. 1. Our result agrees well with that of Shao and Tsakiropoulos and is different from that of Schwanold and Inden. The observed maximum solubility of Ti in β(Cr,Al,Ti) was ~ 13 at.% (Fig. 5), which is slightly different from the results reported in the literature, ~ 19 at.% (Fig. 1).

In the isothermal section of Shao and Tsakiropoulos (Fig. 1(a)), the αTi phase was represented by a point with no variation of composition, which is inconsistent with the binary Ti-Al phase diagram. Our result showed a composition variation and is similar to that of Schwanold and Inden. Consequently, the αTi + β(Ti,Cr,Al) + α_2-Ti$_3$Al three-phase region obtained from the diffusion multiple of the present work is similar to that of Schwanold and Inden; and together it indicates that the assessment of Shao and Tsakiropoulos on this three-phase triangle may be inaccurate.

We obtained all the information in Fig. 5 from one tri-junction of a diffusion multiple, in contrast to 78 ternary alloys melted by Schwanold and Inden to construct the isothermal section shown in Fig. 1(b). Figure 1(a) was based on results from more than 50 alloys and diffusion couples. The good agreement between out results and those in the literature shows the validity and high-efficiency of the diffusion-multiple approach. Especially for a single-phase region with large solubility, the diffusion-multiple approach can provide a large amount of data quickly to map out complicated phase boundaries. The Ti-Cr-Al system provides an excellent example, e.g., the β(Ti,Cr,Al) phase boundaries.

The phase equilibrium information of the Ti-Cr-Al system is very useful for the design of both Nb silicide composites and γ-TiAl as well as their coatings. This is one of the key systems we would strongly encourage for CALPHAD modeling and for adding the data into the developing thermodynamic database for Nb silicide based systems [10, 56,57].

4. CONCLUSIONS

Using the high-efficiency diffusion-multiple approach, we mapped the 1000°C isothermal section (except the Al-rich corner) of the Ti-Cr-Al ternary system from a single sample. The results (Fig. 5) are in very good agreement with those in the literature, especially the isothermal sections by Shao and Tsakiropoulos (Fig. 1(a)) and Schwanold and Inden (Fig. 1(b)). Some differences are discussed. We have defined ten three-phase equilibria. We defined the equilibria among the three different kinds of Laves phases. The results showed significant efficiency gain using the diffusion multiple approach as compared to the traditional equilibrated alloy methods.

ACKNOWLEDGMENTS

REFERENCES

1. M.G. Mendiratta and D.M. Dimiduk, *Mat. Res. Soc. Symp. Proc.*, 133 (1989), 441- 446.
2. M.R. Jackson, B.P. Bewlay, R.G. Rowe, D.W. Skelly, and H.A. Lipsitt, *JOM*, 48 (1996), 39-44.
3. P.R. Subramanian, M.G. Mendiratta, and D.M. Dimiduk, *JOM*, 48 (1996), 33-38.
4. B.P. Bewlay, J.J. Lewandowski, and M.R. Jackson, *JOM*, 49 (1997), 44-45.
5. S.J. Balsone, B.P. Bewlay, M.R. Jackson, P.R. Subramanian, J.-C. Zhao, A. Chatterjee, and T. Heffernan, in *Structural Intermetallics 2001* (K. Hemker, D.M. Dimiduk, H. Clemens, R. Darolia, H. Inui, J.M. Larsen, V.K. Sikka, M. Thomas, and J.D. Whittenberger, eds.), TMS, Warrendale, PA, 2001, 99-108
6. B.P. Bewlay, M.R. Jackson, J.-C. Zhao, and P.R. Subramanian, *Metallurgical and Materials Transactions,* Accepted November 2002.
7. J.-C. Zhao, B.P. Bewlay, M.R. Jackson, and L.A. Peluso, in *Structural Intermetallics 2001* (K. Hemker, D.M. Dimiduk, H. Clemens, R. Darolia, H. Inui, J.M. Larsen, V.K. Sikka, M. Thomas, and J.D. Whittenberger, eds.), TMS, Warrendale, PA, 2001, 483-491.
8. B.P. Bewlay, R.R. Bishop, and M.R. Jackson, *Z. Metallkde.*, 90 (1999), 413-422.
9. J.-C. Zhao, B.P. Bewlay, and M.R. Jackson, *Intermetallics,* 9 (2001) 681-689.
10. Y. Yang, Y.A. Chang, J.-C. Zhao, and B.P. Bewlay, *Intermetallics,* Accepted November 2002.
11. T. Kawabata, M. Tadano and O. Izumi, *Scripta Met.*, 22 (1988) 1725.
12. N. Masahashi et al., *Mater. Res. Soc. Symp. Proc.*, 213 (1991) 795.
13. F.H. Hayes, *J. Phase Equil.*, 14 (1992) 79.
14. J.L. Klansky, J.P. Nic, and D.E. Mikkola, *J. Mater. Res.,* 9 (1994), 255.
15. K. Hashimoto, Y. Mizuhara, T. Hananura, and M. Kimura, in Microstruct. Prop. Relat. Titanium Alloys, Proc. Harold Marglin Symp., S. Ankem and J.A. Hall eds., TMS, Warrendale, PA, 1994, 225-234.
16. T.J. Jewett, B. Anrens, and M. Dahms, *Intermetallics*, 4 (1996), 543-556.
17. T.J. Jewett and M. Dahms, *Z. Metallkde.*, 87 (1996) 4.
18. H. Xu, Z. Jin and R. Wang, *Scripta Mater.*, 37 (1997), 1469-1473.
19. G. Shao and P. Tsakiropoulos, *Intermetallics*, 7 (1999), 579-587.
20. J.P. Nic, J.L. Klansky and D.E. Mikkola, *Mat. Sci. and Eng.*, A152 (1992), 132.
21. Y. Nakayama and H. Mabuchi, *Intermetallics*, 1 (1993), 41.
22. G. Schwanold and G. Inden, in *Materialwissenschaftliche Grundlagen*, Symp. 7, Werkstoffwoche '96, F. Aldinger and H. Mughrabi, eds, Stuttgart, 1996, 121-126.
23. R. Kainuma, I. Ohnuma, K. Ishikawa, and K. Ishida, *Intermetallics*, 8 (2000), 869-875.
24. J.K. Lee, J.Y. Park, M.H. Oh, and D.M. Wee, *Intermetallics*, 8 (2000), 407-416.
25. T. Fujita, H. Ikeda, S. Tanaka, and Z. Horita, *J. Japan Inst. Met.*, 65 (2001), 382-388.
26. J.K. Lee, M.H. Oh, and D.M. Wee, *Intermetallics*, 10 (2002), 347-352.

27. I.I. Kornilov, V.S. Mikheyev and T.S. Chernova, *Russ. J. Inorg. Chem.*, 3(3) (1958), 342-355.
28. T.V. Tagunaova, *Russ. J. Inorg. Chem.*, 3(3) (1958), 380-384.
29. J.L. Taylor and P. Duwez, *Trans. TMS-AIME.*, 197 (1953), 253-256.
30. U. Zwicker, *Z. Metallkde.*, 47 (1956) 535-548.
31. J.-C. Zhao, *Adv. Eng. Mater.*, 3 (2001), 143-147.
32. J.-C. Zhao, *J. Mater. Res.*, 16 (2001), 1565-1578.
33. J.-C. Zhao, M.R. Jackson, L.A. Peluso, and L. Brewer, *MRS Bulletin*, 27 (2002) 324-329.
34. J.-C. Zhao, M.R. Jackson, L.A. Peluso, and L. Brewer, *JOM*, 54 (7) (2002) 42-45.
35. H.J. Goldschmidt and J.A. Brand, *J. Less-Common Met.*, 3 (1961), 34-43.
36. L.A. Lysenko, V.Ya. Markiv, O.V. Tsybukh, and E.I. Gladyshevskii, *Inorganic Mater.,* 7(1) (1971), 157-159.
37. J.L. Murray: in *Binary Alloy Phase Diagrams*, 2nd ed., T.B. Massalski, ed., ASM International, Materials Park, OH, 1990.
38. W. Zhuang, J. Shen, Y. Liu, L. Ling, S. Shang, Y. Du, and J.C. Schuster, *Z. Metallkde.*, 91 (2000), 121-127.
39. K.C. Chen, S.M. Allen, and J.D. Livingston, *Mat. Res. Soc. Symp. Proc.*, 364 (1995), 1401.
40. J.L. Murray, in *Binary Alloy Phase Diagrams*, 2nd ed., T.B. Massalski, ed., ASM International, Materials Park, OH, 1990.
41. J.G.C. Neto, S. Gama, and C.A. Ribeiro, *J. Alloys Compounds*, 182 (1992), 271-280.
42. K. Mahdouk and J.C. Gachon, *J. Phase Equili.*, 21(2000), 157-166.
43. K. Mahdouk, J.C. Gachon, *Arch. Metal.*, 46 (2001), 233-238.
44. M. Audier, M. Durandcharre, E. Laclau, H. Klein, *J. Alloys Compound,* 220 (1995) 225-230.
45. X.Z. Li, K. Sugiyama, K. Hiraga, A. Sato, A. Yamamoto, H.X. Sui, and K.H. Kuo, *Z. Kristallographie*, 212 (1997), 628-633.
46. H.R. Ogden et al., *Trans. AIME*, 191 (1951) 1150.
47. J.H. Perepezko, Proc. *Intl. Symp. Intermetallic Compounds, Structure and Mechanical Properties*, (JIMIS-6), Sendai, Janpan, 1991, 239-243.
48. U.R. Kattner, J.C. Lin, and Y.A. Chang, *Metall. Trans. A23* (1992), 2081-2090.
49. C.D. Anderson, W.H. Hofmeister, R.J. Bayuzick, Liquidus Temperatures in the Ti-Al System, *Metall. Trans. A24* (1993), 61-66.
50. P.J. Spencer, *Z. Metallkde.*, 87 (1996), 535-539.
51. H. Okamoto, *J. Phase Equil.*, 14 (1993), 120-121.
52. M.Palm, L.C. Zhang, F. Stein, and G. Sauthoff, *Intermetallics*, 10 (2002), 523 –540.
53. P. Villars and L.D. Calvert, *Pearson's Handbook of Crystallographic Data for Intermetallic Phases*, 2nd ed., ASM International, Materials Park, OH, 1991.
54. A. Knapp, *Z. Metallkde.*, 33 (1941) 153.
55. *Electron Backscatter Diffraction in Materials Science*, edited by A.J. Schwartz, M. Kumar, and B.L. Adams (Kluwer Academic / Plenum Publishers, New York, 2000).
56. H. Liang and Y.A.Chang, *Intermetallics*, 7 (1999) 561.
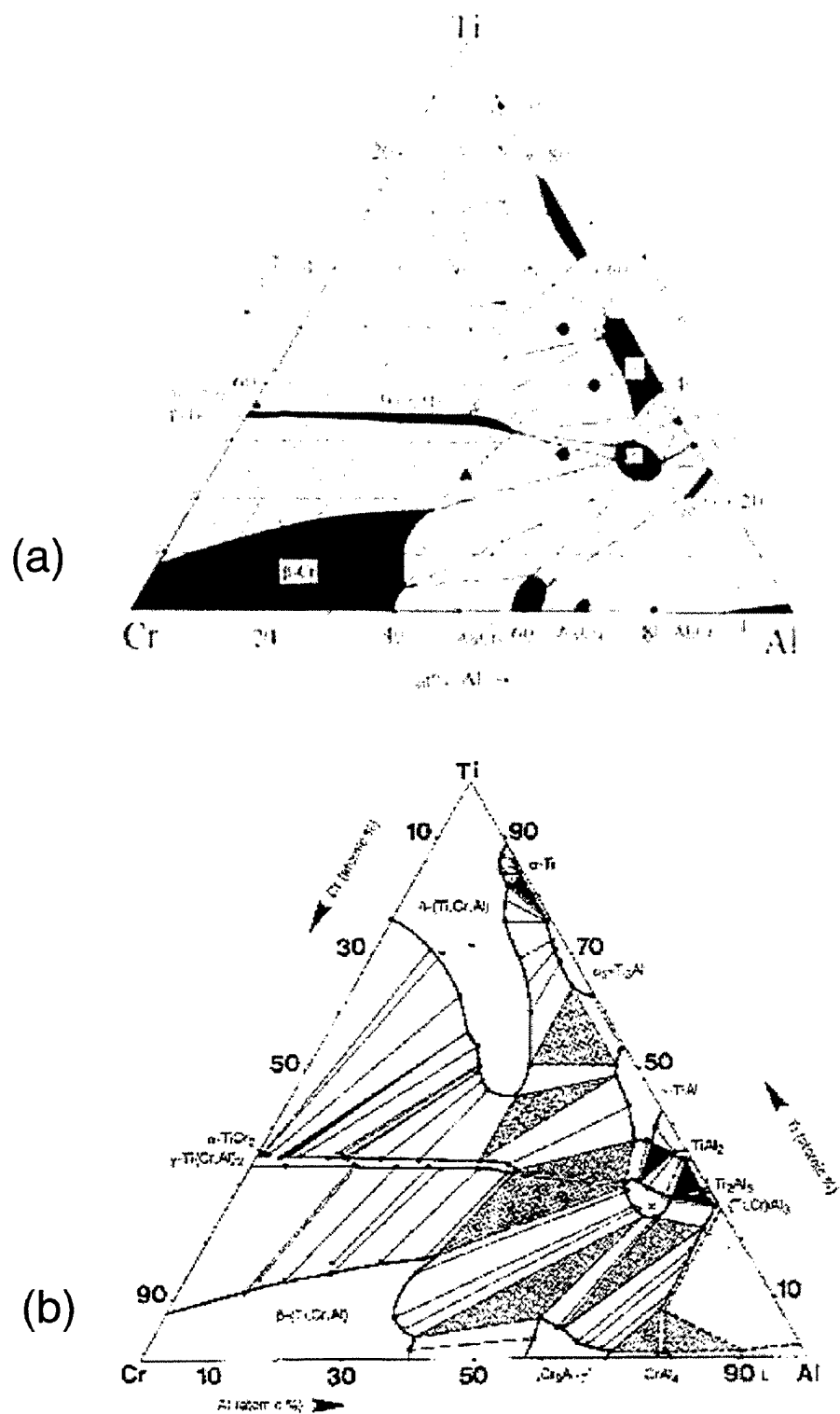57. Y. Yang and Y.A. Chang (University of Wisconsin – Madison), private communication, 2002.

Figure 1. Isothermal sections from the literature of the Ti-Cr-Al system at 1000°C: (a) constructed by Shao and Tsakiropoulos [19] based on literature results from [13,16,17], and (b) constructed by Schwanold and Inden [22] again based 78 alloys and diffusion couples.
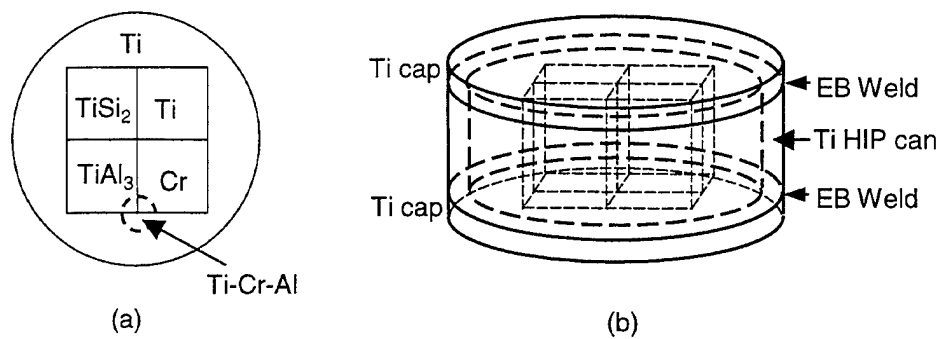
Figure 2. A diffusion multiple for efficient mapping of the Ti-Cr-Al ternary phase diagram: (a) cross-sectional view; and (b) perspective view. See text for the size of the sample. The results reported in this work were all obtained from the tri-junction corner of Ti – Cr – TiAl$_3$ circled in (a).
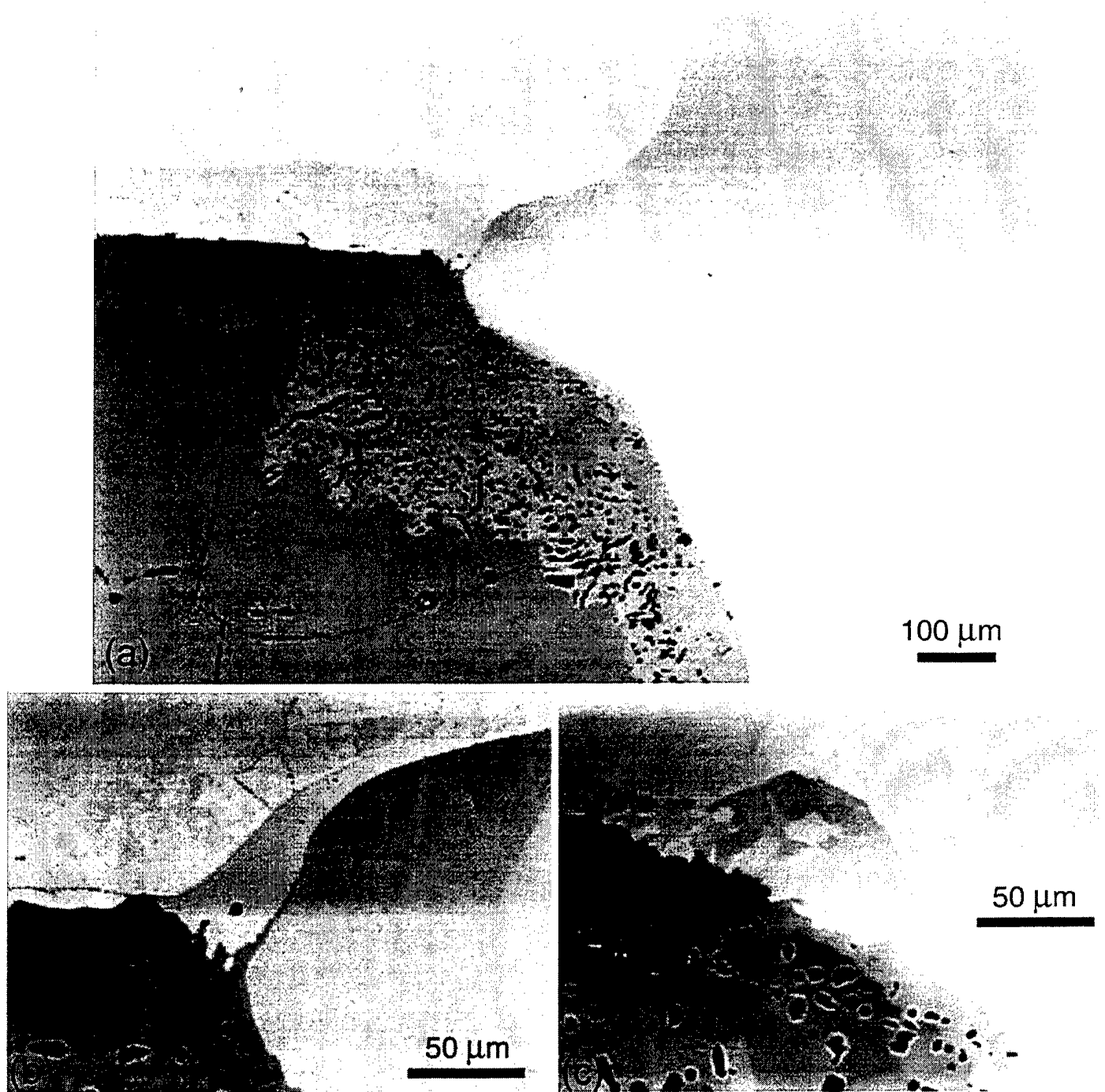
Figure 3. Backscatter electron SEM images of the Ti – Cr – $TiAl_3$ tri-junction area of the diffusion multiple (Fig. 2) annealed at 1000°C for 2000 hrs showing the formation of many different intermetallic compounds, including one ternary compound, τ-$L1_2$. (a) a low-magnification image showing the overall tri-junction; (b) a high-magnification image of location 1 in (a); and (c) a high-magnification image of location 2 in (a).

10

Figure 4. Backscatter electron SEM image of the Ti – TiAl$_3$ bi-junction (diffusion couple) area of the diffusion multiple (Fig. 2) annealed at 1000°C for 2000 hrs showing the formation of several Ti aluminides.
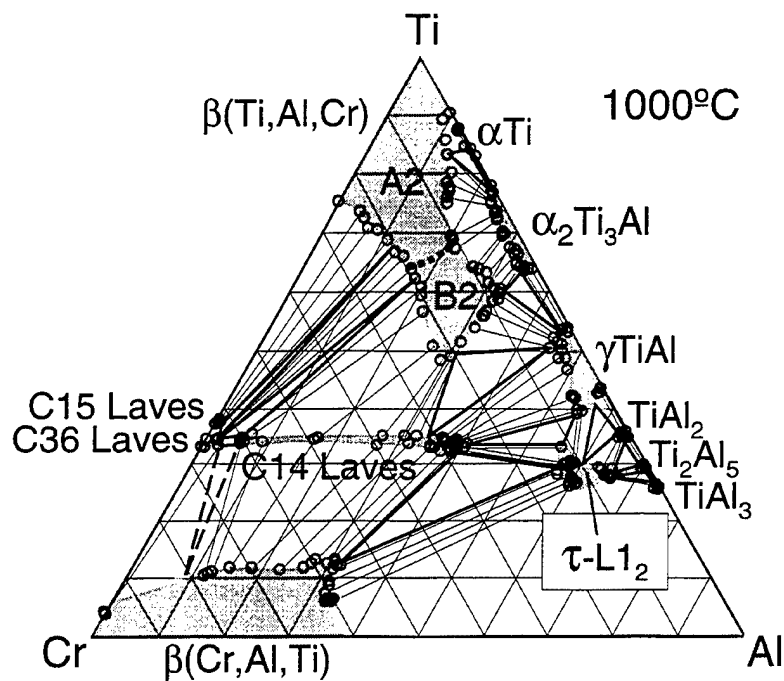
Figure 5. The 1000°C isothermal section of the Ti-Cr-Al system obtained from the Ti-Cr-TiAl$_3$ tri-junction area of the diffusion multiple (Fig. 2) annealed at 1000°C for 2000 hrs. The phase diagram is plotted in atomic percent axes with the numbers removed for simplicity. The solid triangle indicates well-defined three-phase triangles and the open circles show the tie-line compositions. The tie-lines are shown with light dotted lines. The A2 – B2 ordering transition line (shown as a heavy dotted line) was adopted from Kainuma et al. [23].
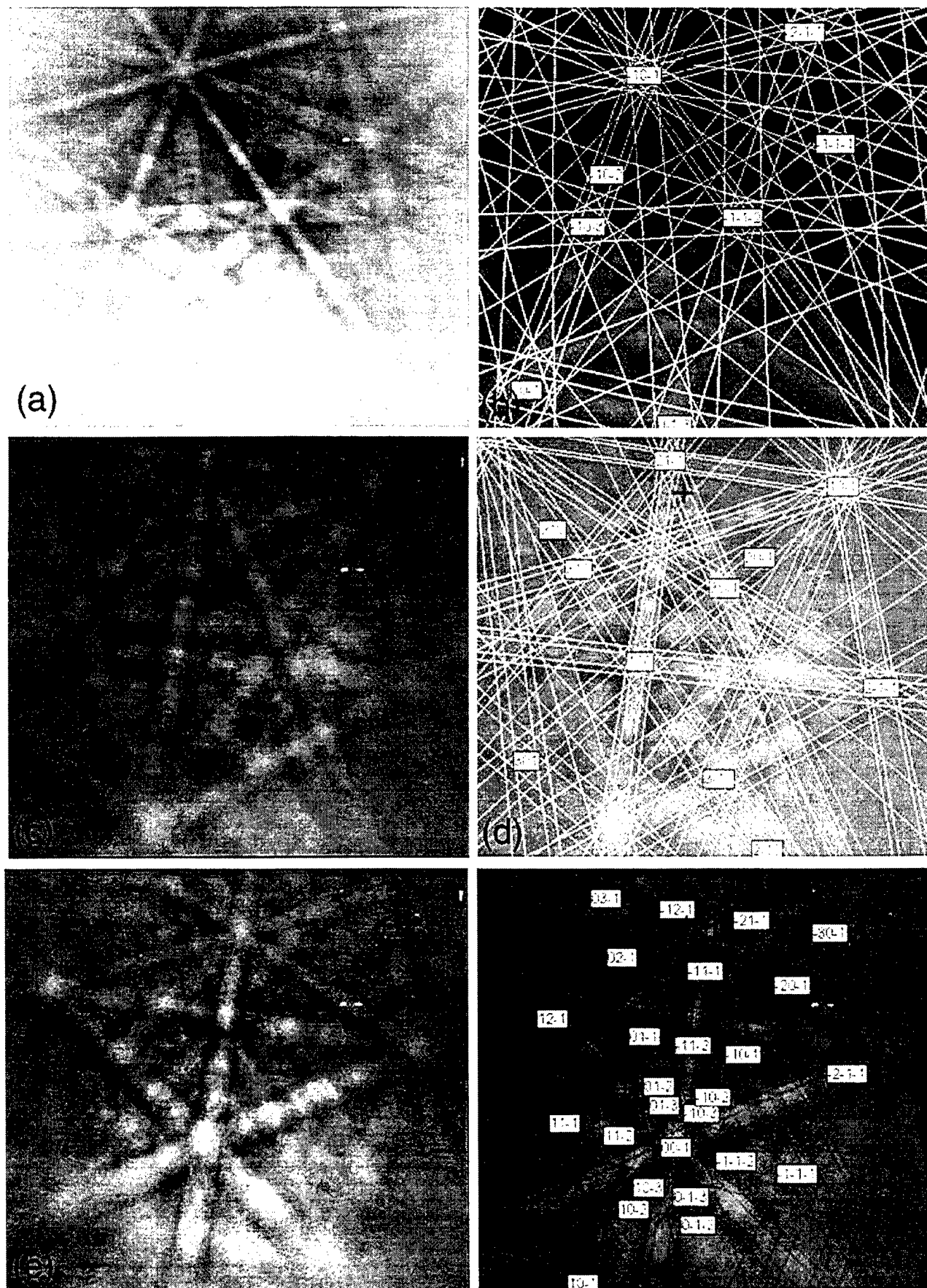
Figure 6. EBSD patterns of several intermetallic phases formed in the Ti – Cr – TiAl₃ tri-junction area of the diffusion multiple (Fig. 2) annealed at 1000°C for 2000 hrs: (a) and (b) for τ-L1₂ phase; (c) and (d) for C15 Laves; and (e) and (f) for the C36 Laves. The un-indexed patterns are shown on the left and the indexed patterns on the right.

13